MASARYKOVA
UNIVERZITA

FACULTY OF SCIENCE

Optical Emission Spectroscopy of Non-Thermal Plasma

Habilitation Thesis

ZDENĚK NAVRÁTIL

Department of Physical Electronics
Research field: Plasma Physics

Brno 2019

Abstract

Presented work contains a commented set of sixteen scientific papers of the candidate being concerned mostly with the optical diagnostics of low temperature non-thermal plasma. The first chapter is devoted particularly to the study of low pressure neon plasma sources by the method combining optical emission spectroscopy and collisional-radiative modelling; attention is also paid to the self-absorption methods of the density measurement of non-emitting particles. The second chapter deals with the diagnostics of atmospheric pressure plasma. Most of the papers commented in this part are devoted to the diagnostics of dielectric barrier discharges, the rest studied radiofrequency atmospheric pressure plasma sources. Common characteristic of both low pressure and atmospheric pressure plasma studies is their concern in rare gas plasma.

Contents

List of commented papers

The papers listed below are not ordered by the date of publication, but organically according to the topic and as they appear within the following text.

[1] Navratil Z, Trunec D, Hrachova V and Kanka A 2007 Collisional-radiative model of neon discharge: determination of E/N in the positive column of low pressure discharge *J. Phys. D: Appl. Phys.* **40** 1037.

[2] Navratil Z, Dvorak P, Brzobohaty O and Trunec D 2010 Determination of electron density and temperature in a capacitively coupled RF discharge in neon by OES complemented with a CR model *J. Phys. D: Appl. Phys.* **43** 505203.

[3] Navratil Z, Dosoudilova L, Hnilica J and Bogdanov T 2013 Optical diagnostics of a surface-wave-sustained neon plasma by collisional-radiative modelling and a self-absorption method *J. Phys. D: Appl. Phys.* **46** 295204.

[4] Vasina P, Fekete M, Hnilica J, Klein P, Dosoudilova L, Dvorak P and Navratil Z 2015 Determination of titanium atom and ion densities in sputter deposition plasmas by optical emission spectroscopy *Plasma Sources Sci. Technol.* **24** 065022.

[5] Trunec D, Navratil Z, Stahel P, Zajickova L, Bursikova V and Cech J 2004 Deposition of thin organosilicon polymer films in atmospheric pressure glow discharge *J. Phys. D: Appl. Phys.* **37** 2112.

[6] Navratil Z, Brandenburg R, Trunec D, Brablec A, Stahel P, Wagner H and Kopecky Z 2006 Comparative study of diffuse barrier discharges in neon and helium *Plasma Sources Sci. Technol.* **15** 8.

[7] Brandenburg R, Navratil Z, Jansky J, St'ahel P, Trunec D and Wagner H E 2009 The transition between different modes of barrier discharges at atmospheric pressure *J. Phys. D: Appl. Phys.* **42** 085208.

[8] Kloc P, Wagner H E, Trunec D, Navratil Z and Fedoseev G 2010 An investigation of dielectric barrier discharge in Ar and Ar/NH_3 mixture using cross-correlation spectroscopy *J. Phys. D: Appl. Phys.* **43** 345205.

[9] Dosoudilova L, Tschiersch R, Bogaczyk M, Navratil Z, Wagner H E and Trunec D 2015 Investigation of helium barrier discharges with small admixtures of oxygen *J. Phys. D: Appl. Phys.* **48** 355204.

[10] Cech J, Stahel P and Navratil Z 2009 The influence of electrode gap width on plasma properties of diffuse coplanar surface barrier discharge in nitrogen *Eur. Phys. J. D* **54** 259.

[11] Moravek T, Cech J, Navratil Z and Rahel J 2016 Pre-breakdown phase of coplanar dielectric barrier discharge in helium *Eur. Phys. J.-Appl. Phys* **75** 24706.

[12] Navratil Z, Moravek T, Rahel J, Cech J, Lalinsky O and Trunec D 2017 Diagnostics of pre-breakdown light emission in a helium coplanar barrier discharge: the presence of neutral bremsstrahlung *Plasma Sources Sci. Technol.* **26** 055025.

[13] Cech J, Navratil Z, Stipl M, Moravek T and Rahel J 2018 2D-resolved electric field development in helium coplanar DBD: spectrally filtered ICCD camera approach *Plasma Sources Sci. Technol.* **27** 105002.

[14] Navratil Z, Dosoudilova L, Josepson R, Dvorak P and Trunec D 2014 Diffuse α-mode atmospheric pressure radio-frequency discharge in neon *Plasma Sources Sci. Technol.* **23** 042001.

[15] Josepson R, Navratil Z, Dosoudilova L, Dvorak P and Trunec D 2014 Atmospheric Pressure RF Discharge in Neon and Helium *IEEE Trans. Plasma Sci.* **42** 2348.

[16] Navratil Z, Josepson R, Cvetanovic N, Obradovic B and Dvorak P 2016 Electric field development in gamma-mode radiofrequency atmospheric pressure glow discharge in helium *Plasma Sources Sci. Technol.* **25** 03LT01.

Introduction

Optical emission spectroscopy (OES) has been used for investigation of plasma sources just from its beginning in the nineteenth century. Since that time, it has helped to uncover the fundamental properties of the light and the matter; but it has also established as a standard diagnostic method in various science disciplines.

In the presented work, the OES was applied to the optical diagnostics of low temperature non-thermal plasma. The first chapter is devoted particularly to the study of several types of low pressure neon plasma sources by the author's method combining optical emission spectroscopy and collisional-radiative modelling [1–3]. Two papers utilize the self-absorption of radiation in the plasma for the density measurement of non-emitting particles [3, 4]. The second chapter deals with the optical diagnostics of atmospheric pressure plasma. Most of the papers annotated in this part are devoted to the diagnostics of dielectric barrier discharges [5–13], three papers studied atmospheric pressure radiofrequency plasma sources [14–16]. Various theoretical approaches of optical emission spectroscopy, spanning from high-resolution line profile diagnostics to continuum spectrum based diagnostics, were applied. Special attention was paid to the development of the experimental side of the diagnostics. The method of time correlated single photon counting, originally applied only for the diagnostics of filamentary air plasma, was adopted for two novel applications: radiofrequency plasma diagnostics and ultra-weak bremsstrahlung based phase resolved electric field measurement. Common characteristic of both low pressure and atmospheric pressure studies is their concern in rare gas plasma.

The most of the presented work was done at Masaryk University in Brno. However, four papers would not come into existence without a close cooperation with the University of Greifswald; two papers originate from the fruitful collaboration with the University of Belgrade and the Charles University in Prague. I want to express my gratitude to all the colleagues, who contributed to this work or helped me in some way in the course of time.

Chapter 1

Diagnostics of low pressure discharges

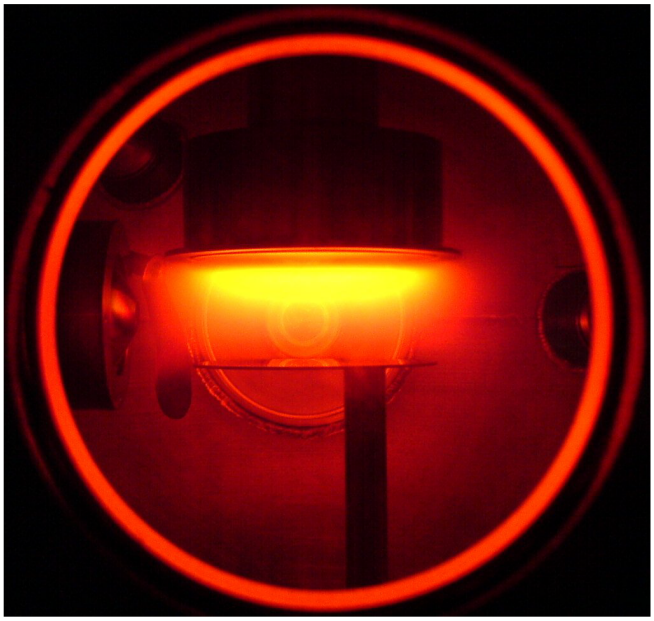

Low pressure radiofrequency capacitively coupled discharge in neon.

1.1 State of art

Methods combining optical emission spectroscopy and collisional-radiative modelling have become a well established tool in low pressure discharge diagnostics. Assuming Maxwellian electron distribution function (EDF), electron temperature is usually determined from the comparison of spectral line intensity ratios, obtained from the experiment and the simulation [17]. However, the EDF is usually non-Maxwellian in low temperature plasma with low ionization and/or at higher pressures. This happens due to the scant amount of electron-electron collisions, strong non-elastic collisions of electrons with neutral gas atoms or because of beam electrons coming from the high field regions. The diagnostics of pure rare gas discharges then often suffers from the insufficient number of excited levels (or spectral lines), useful for the measurement. As the resonance lines lie in far ultraviolet and the transitions among highly excited levels fall into near infrared, the transitions accessible for the diagnostics enable EDF mapping only in limited range of electron energies. The determined quantities as electron temperature then reflects more the high-energy electrons than the low-energy ones.

Eventually, the sensitivity of the spectra to the low energy electrons is provided by stepwise electron excitation through lower levels, e.g. through metastable states [18]. However, this introduces the dependence of the CR model on the metastable densities, which are hardly calculated from simple (0D) CR models, since the assumptions on the balance equations for the excited state densities are not fulfilled for them. This requires an independent treatment of the metastable densities, typically independent measurement.

By admixing a small amount of specific rare gas into the studied plasma, the distribution function in specific range of electron energies may be investigated [19, 20]. Using this so-called trace rare gas spectroscopy with several rare gases, non-Maxwellian character of EDF can be mapped. Similarly, 'two temperature' behaviour of the EDF can be studied, when two rare gases are naturally present in the plasma [21].

At pressure of several Pascals, an electron mean free path may be comparable with the electrode gap. The EDF is then non-local, i.e. not in the equilibrium with the local electric field. This hinders the possibility to determine the electric field from the spectra, as often performed in higher or atmospheric pressure discharges (see chapter 2 for the details).

Although the optical emission spectroscopy has been established as a measurement method for low pressure plasma for more than one and half century, there are still challenging tasks in interpretation of its outputs. Sensing the light emitted from plasma on

the plasma boundary can hide or modify important features in the emission spectrum. For example, self-absorption of the light in the plasma, typically by ground state and metastable state atoms, may play important role and needs to be considered in the modelling, see e.g. [22]. Although methods adopting movable 'optical probes' have been developed to obtain true (local) emission coefficient of the plasma, see e.g. [23], they lose the main advantage of the method – the non-intrusiveness.

Whilst the self-absorption is mostly a complication for CR modelling, methods based on this effect can serve for the precise measurement of density of non-emitting particles [24], even with the optical emission spectroscopy. The obtained values can be then used as independent inputs into CR models. Such approach was also applied in one commented paper.

1.2 Overview of the work

The work on the CR model for neon plasma started already during my doctoral study (2001 – 2006). During the years 2007 – 2013, the developed CR model for neon plasma was applied to the diagnostics of various neon discharges – DC, DC magnetron, radiofrequency and surface-wave microwave discharge [1–3]. Within this period, the model was being gradually improved; also a better understanding of the possibilities and of the drawbacks of the method was achieved.

In the papers, determination of the fundamental plasma parameters as of the electron distribution function or of the electric field from the neon optical emission spectra was demonstrated. Instead of generally used line intensity ratio, more reliable but also ambitious approach consisting in full neon spectrum fitting was chosen to obtain these quantities. Another challenge was to measure and also to calculate the absolute intensities of the neon transitions in order to fit also the electron density.

Besides the CR modelling, an attention is also paid to the application of self-absorption methods in this chapter [3, 4].

Commented papers

[1] Navratil Z, Trunec D, Hrachova V and Kanka A 2007 Collisional-radiative model of neon discharge: determination of E/N in the positive column of low pressure discharge *J. Phys. D: Appl. Phys.* **40** 1037.

[2] Navratil Z, Dvorak P, Brzobohaty O and Trunec D 2010 Determination of electron density and temperature in a capacitively coupled RF discharge in neon by OES complemented with a CR model *J. Phys. D: Appl. Phys.* **43** 505203.

[3] Navratil Z, Dosoudilova L, Hnilica J and Bogdanov T 2013 Optical diagnostics of a surface-wave-sustained neon plasma by collisional-radiative modelling and a self-absorption method *J. Phys. D: Appl. Phys.* **46** 295204.

[4] Vasina P, Fekete M, Hnilica J, Klein P, Dosoudilova L, Dvorak P and Navratil Z 2015 Determination of titanium atom and ion densities in sputter deposition plasmas by optical emission spectroscopy *Plasma Sources Sci. Technol.* **24** 065022.

1.3 Comments on articles

[1] Navratil Z, Trunec D, Hrachova V and Kanka A 2007 Collisional-radiative model of neon discharge: determination of E/N in the positive column of low pressure discharge *J. Phys. D: Appl. Phys.* 40 1037.

The first published paper on collisional-radiative modelling of neon plasma. Based on the Boltzmann kinetic equation solver for electron distribution function and solution of rate equations of thirty excited levels of neon atom, direct relation between the reduced electric field strength (E/N) and the neon line spectrum was established. Instead of line ratio method, which does not provide the possibility to check the correspondence of the model with the observed reality, full neon spectrum fitting by the least squares method was performed to obtain the electric field. The developed method was applied to the study of positive column of DC glow discharge in neon at 1.1 Torr.

The experimental part of the work drew completely from the collaboration with the colleagues from the Charles University in Prague, who were able to supply both the measured neon spectra and the electric field values determined from the independent probe measurement. This enabled the direct comparison of the obtained results; generally a close agreement of both methods were found.

As the first paper on the CR model, a lot of efforts had to be made to collect, evaluate and adopt all the atomic data needed for the model: electron collision cross sections, transition probabilities (Einstein coefficients), rate coefficients of heavy particle collisions, diffusion coefficients for metastables, escape factors for radiation etc. Less efforts were invested into the optimization of the experiment in Prague.

From the present point of view, better organization of the experiment according to the needs of the modelling could have led to further improvement. Although the radially resolved measurement provided data without average over spatially inhomogeneous regions, the axial look along the positive column enhanced the role of self-absorption (the column length was 39 cm). Although the self-absorption of radiation was included

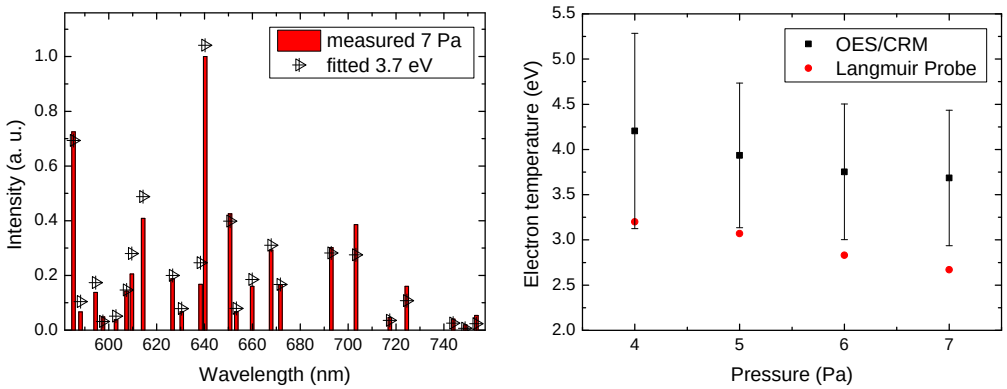

Figure 1.1: (a) Comparison of measured and fitted spectra of DC magnetron discharge. (b) Comparison of electron temperature obtained from OES/CRM method and from the probe measurement.

in the model, the used method of escape factors is always only approximate (especially for complicated geometries). Accordingly, whilst the observation along the radius could provide nearly self-absorption free data, measurement along the column could be used for metastable density measurement. This approach was used successfully later for DC magnetron discharge and surface wave driven microwave discharge [3]. On the other hand, calculation of metastable densities from 0D model was probably only approximate as well. As was shown later in [3], the correct treatment of the metastables is important especially at low electric fields, occurring just in the positive column.

The collaboration with the Charles University in Prague continued in the field of diagnostics of DC magnetron discharge in neon (assoc. prof. P. Kudrna). The first application of the CR modelling obtained a perfect agreement between the measurement and the model (see figure 1.1a) and the obtained electron temperatures nearly coincided (see figure 1.1b). However, this promising work has still not been finished.

[2] Navratil Z, Dvorak P, Brzobohaty O and Trunec D 2010 Determination of electron density and temperature in a capacitively coupled RF discharge in neon by OES complemented with a CR model *J. Phys. D: Appl. Phys.* 43 505203.

In this paper, the CR model developed previously was applied to the diagnostics of radiofrequency discharge in neon. Since the EDF was not local under the studied conditions (electrode gap 4 cm, gas pressure 10 Pa), electric field could not be determined from the measurement and only the EDF (Maxwellian, two-temperature, general etc.)

could be evaluated by the model. The metastable densities were not calculated in the model, but treated as input parameters. Simple absorption measurement provided the spatially averaged values of metastable densities in the plasma bulk. A specific attention was paid to obtain the emission coefficient of plasma unit volume from the measurement, in order to determine also the electron density. This was provided by absolute intensity measurement and by estimation of the optical fibre irradiance by the plasma. Other applied experimental and simulation techniques, Langmuir probe measurement and Particle-In-Cell/Monte-Carlo (PIC/MC) simulation, provided data for mutual comparison.

It was found, that the measurement and the CR model provided similar spectra only in the vicinity of the driven electrode, where the PIC/MC method foresaw for the EDF the Maxwellian distribution. All three methods provided similar value of the electron temperature in that region. Conversely, the light coming from the plasma bulk exhibited a spectrum, which could not be simulated by the model, even with more complicated EDF shape. As stated in the paper, this could have been caused by the specific absorption of line intensities by the metastables in outer region of the discharges chamber. Another role was attributed to the time averaging. Although a substantial effort was made to measure also the time resolved spectra of the discharge, this was disallowed by the low gating frequency of at that time available ICCD camera (30 kHz). Therefore, only a time development of the spectrally unresolved discharge emission could be obtained[1] and the spectra were finally measured using a CCD detector (and were averaged over many RF periods). Since the spectrally integrated intensity development showed only a slow variation of the light intensity during the RF period, the time dependent effects were assumed not to be crucial. On the other hand, calculation based on the CR model showed that the non-equilibrium of the excited level populations can change the ratio of line intensities in the spectrum seriously. ICCD cameras with MHz gating frequencies available nowadays would help to solve this issue easily.

[3] Navratil Z, Dosoudilova L, Hnilica J and Bogdanov T 2013 Optical diagnostics of a surface-wave-sustained neon plasma by collisional-radiative modelling and a self-absorption method *J. Phys. D: Appl. Phys.* 46 295204.

The third paper of this series was devoted to the collisional radiative modelling based diagnostics of surface-wave driven (microwave) discharge in coaxial tube configuration.

[1] To illustrate this difficulty, the spectrally unresolved measurement was accumulated over the whole night, providing only the data in figure 7 of the publication [2].

This kind of discharge had been developed at the University of Sofia and the stay of T. Bogdanov from Sofia in Brno provided a possibility to realize the experiment just according to the needs of the modelling. Several improvements of the method were made in comparison with the previous work.

Firstly, a large attention was paid to the independent measurement of the mestastable densities. Three different methods were tested: a white light absorption method [25], self-absorption method according to [24] and method of effective branching fractions (EBF) [22][2], see [26]. A suitable discharge configuration enabled OES measurement both in axial and secant direction, providing self-absorption influenced and self-absorption free spectra. Whilst both were used for the self-absorption method, self-absorption free spectra measured in secant direction, but spatially resolved along the column, were fitted by the CR model.

Secondly, since the pressure in the tube was set up to 700 Pa, some heavy particle induced reactions, as two-body excitation transfer between 3p states, were included in the model. Though, their role was found negligible at the studied conditions.

The sensitivity of the fitting at low electric field values (approx. 8 V/cm) were improved by direct calculation of the sum of squares (instead of Levenberg-Marquardt algorithm) for a wide range of conditions (T_e or E/N) and adopting the values with the lowest sum as the result.

Boltzmann solver for EDF with the effective field approximation (the AC voltage frequency was 2.45 GHz) was included into the model to obtain the reduced electric field E/N as the result. In order to determine the electric field strength E, gas temperature had to be evaluated. Fitting the rotationally unresolved structure of molecular bands of nitrogen in self-absorption free spectra revealed the gas temperature variation along the plasma column. This variation affected the reduced electric field frequency (ω/N). Since the temperature was decreasing along the column, ω/N decreased too and the electron heating became more efficient. This resulted in a decrease of reduced electric field E/N along the column. Without taking into account the spatially variable gas heating, the reduced field would seem to be constant along the plasma column.

[2]Finally only the results of Jolly's method [24] were published in the paper.

[4] Vasina P, Fekete M, Hnilica J, Klein P, Dosoudilova L, Dvorak P and Navratil Z 2015 Determination of titanium atom and ion densities in sputter deposition plasmas by optical emission spectroscopy *Plasma Sources Sci. Technol.* 24 065022.

The self-absorption method used in the previous work greatly simplified the measurement of the neon metastables. External light source and look through setup needed by absorption methods were avoided, the metastable densities were obtained simply by analysis of optical emission spectra. We realized soon, that these methods, especially the method of effective branching fractions[3], which needs only a single spectrum measurement, has a wider application potential than the original measurement of argon metastable densities [22]. A requirement to diagnose the sputtering of titanium atoms during the magnetron deposition process came at the right time. Since both titanium neutral atom and ion have resonance lines in UV/VIS region, their absolute densities could be obtained simultaneously, enabling also determination of the ionization fraction. Several case studies including the determination of the titanium atom density in a DC sputtering experiment, of titanium atom and ion densities for transition from DC to HiPIMS mode (high power impulse magnetron sputtering), and of the temporal evolution of titanium atom and ion densities during the HiPIMS pulse, were studied. Later comparison of some of these measurements with laser absorption experiment exhibited an excellent agreement between both methods [27]. The requirement of processing of large amount of data led to the development of a special purpose software, program *EBF Fit*, which was made free for use.

[3]The EBF method is based on fitting of theoretically calculated branching fractions (of lines originating from the same upper level) to measured ratios of the relative intensities in optical emission spectra.

Chapter 2

Diagnostics of atmospheric pressure discharges

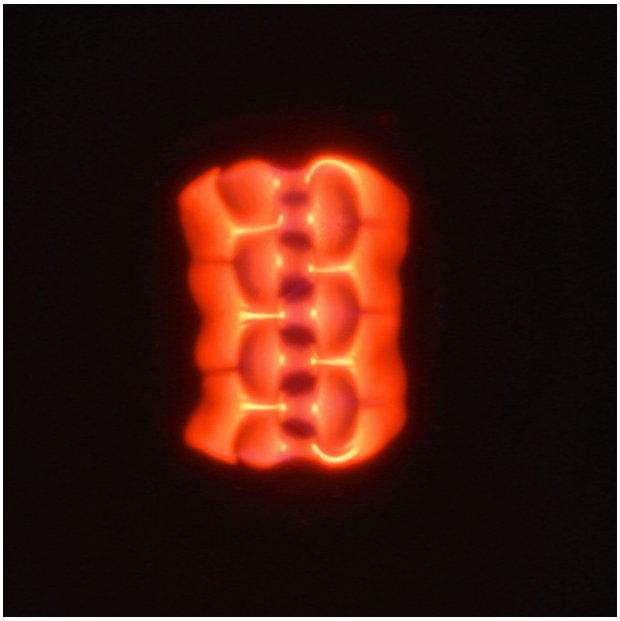

Atmospheric pressure filamentary coplanar barrier discharge in neon.

2.1 State of art

Among various non-thermal atmospheric pressure plasmas suitable for plasma processing applications, dielectric barrier discharges (DBDs) and radiofrequency (RF) plasmas are of the particular scientific interest. Whilst the DBDs are typically operated with AC high voltage at the frequency of several kHz, radiofrequency plasma sources use frequencies of several MHz (e.g. 13.56 MHz). Moreover, the DBDs rely on the dielectric barrier, arranged in some way in the electrode gap. According to this, we can resolve volume, surface and coplanar DBD configuration. It is worth mentioning that the coplanar configuration is a variant to a certain degree between volume and surface discharge [28], with the applied field dominant along the dielectric in the gap, but perpendicular above the electrodes.

An important difference between RF and DBD atmospheric pressure plasma lies in the way how the non-thermal character of the plasma is achieved. The most often observed mode of the DBD is the filamentary mode, consisting of a number of thin filaments (or microdischarges) realizing the local gas breakdown. The transferred electric charge by the filament is accumulated on the dielectric barrier. The electric field induced by the charge then stops locally the discharge development. Together with the AC power supply a self-pulsing operation is obtained [29].

On the other hand, the high frequency of RF discharges traps the ions in the gap, suppressing the role of secondary emission. The RF period (74 ns for frequency of 13.56 MHz) is short enough to ensure a continuous operation. The electrons are heated at oscillating sheath edges or by ohmic heating [30, 31]. The breakdown occurs at lower voltage [32] and the discharge operates in a diffuse, so-called α-mode, characterized by a weak ionization and a nearly room temperature. At higher voltage the breakdown in the RF sheath occurs, secondary emission supplies new charge carriers and the discharge transits into so-called γ-mode with the higher gas ionization and the gas temperature [33]. The discharge is substantially brighter, constricted to a limited area of the electrode, but the current density is still substantially lower than that of the arc discharge.

Diffuse barrier discharges in rare gases

Besides the filamentary regime, the DBD can be operated in a diffuse (or uniform) mode under special conditions. 'Uniform or diffuse means that the surface cross section is covered by the discharge more or less entirely, although the plasma is not necessarily homogeneous in axial direction' [29]. It was shown first, that such diffuse mode can be generated in volume barrier discharge in helium and nitrogen [34, 35], but the discharges

in both gases exhibited a different nature (i.e. of atmospheric pressure glow-like or Townsend-like discharge). The homogeneity of the helium discharge was explained by the high ionization coefficient and sufficient gas preionization by Penning ionization of gas impurities by metastables. The breakdown then occurs slowly at low electric field providing electrons the time to diffuse in the gap. On the other hand, the existence of diffuse discharge in nitrogen was attributed to the production of electrons by secondary emission of electrons from the dielectric, caused by heavy particles as metastables.

The helium discharge typically operates in glow-like mode with pronounced cathode fall region and positive column [36]. It was shown later, that the helium discharge can operate also in the Townsend mode with maximum ionization at the anode, when the gap is small (2 mm). The glow-like mode can be still established in such a gap when voltage waveform with a steeper slope than that of harmonic one is applied [37].

Since the 'diffuse breakdown' occurs simultaneously in the whole gap, the discharge is manifested by a single current peak per half period. More current peaks can be observed in a half-period, when the applied voltage is further increased and dielectric surface regions outward the covered area are deposited by the charge from new discharges [38]. Between the discharge peaks, the deposited surface charge (and its density) stays nearly constant, as expected from the electrical measurements [34] and later proved by direct surface charge measurement utilizing the Pockel's effect [39].

In contrast to the air DBD plasma, where a method of band ratio for the determination of the reduced electric field was soon developed [40], optical diagnostics of the diffuse rare gas barrier discharges was for a long time limited to a simple imaging by ICCD cameras or by a time resolved optical emission spectroscopy. The situation improved, when a method of Stark polarization spectroscopy, utilizing the Stark shift of helium lines, was introduced for atmospheric pressure discharges to measure directly the electric field [41]. This method proved the existence of the cathode fall region in helium volume diffuse discharge. It was later applied also to the diagnostics of helium DBD plasma jets to determine the electric field in so-called plasma bullets [42, 43]. Another approach to the measurement of the electric field, based on the collisional-radiative modelling and utilizing the line ratio of helium lines, provided sensitivity at lower electric fields (> 3 kV/cm). It was utilized for the direct observation of the cathode fall formation in helium diffuse DBD [44]. Another line-ratio method was developed for electron density measurement in argon atmospheric pressure discharges [45].

Atmospheric pressure radio-frequency discharges in rare gases

The radiofrequency discharges generated at atmospheric pressure between bare metal electrodes rely mostly on use of rare gas as a working gas. Among them, plasma jets are of the largest interest, since they provide plasmas that are not spatially bound or confined by electrodes as required by various applications [46]. The existence of a non-equilibrium RF atmospheric pressure glow discharge (RF APGD) in helium was published already in [47]. It should be noted, that the term 'RF APGD' is used to address a discharge different from barrier APGD. The word 'glow' is meant here to describe a visually diffuse discharge, different from arc discharge.

The RF APGD discharge in helium in planar electrode gap has been a subject of numerous experimental and theoretical investigations, see e.g. [30, 31, 33, 48–50]. It was found, that whilst the ionization in α mode is mostly volumetric and the discharge is sustained by electrons heated at sheath edges, it is dominated by electron avalanches in the RF sheaths seeded by secondary electron emission in the higher current density γ-mode [30]. Concerning the electric field, a space resolved distributions were obtained from the numerical modelling, showing large differences between the discharge modes [48] or revealing high values of the electric field in the atmospheric pressure discharge RF bulk [31]. However, facing the sheath thicknesses of about 100 μm, no attempt had been made to measure the electric field directly using OES methods. This stimulated our research on electric field measurement in these discharges [16].

2.2 Overview of the work

My professional interest in atmospheric pressure plasma diagnostics was ignited soon after the start of my doctoral study in 2001. The research on dielectric barrier discharges, especially on their application to plasma treatment and plasma enhanced chemical vapour deposition had been just launched at our department [5, 51–53]. The demand of homogeneous plasma treatment led to the interest in the known diffuse modes of barrier discharges. The discovery of a diffuse mode in neon by prof. D. Trunec and co-workers [54] invoked the basic research of these discharges at our department and led subsequently to a fruitful long-term collaboration on this topic with the University of Greifswald (group of Dr. H.-E. Wagner), where a unique diagnostics of barrier discharges by the method of cross correlation spectroscopy, based on single photon counting, had been just launched [40]. Starting from the comparison of the diffuse modes in neon and helium [6], our interest was then focused on the effect of gas admixtures on the diffuse mode stability [7–9, 55].

The research on barrier discharges were later extended to coplanar barrier discharge, which became available due to the development of this technology by prof. M. Černák and his co-workers. The great advantage of the coplanar discharge geometry is the possibility to observe the whole discharge development 'in one plane'. A single electrode pair variant of this configuration in a chamber with a controlled atmosphere [10] provided a well-defined experimental setup for the basic research. A milestone for our work on the diagnostics of atmospheric pressure plasmas was the purchase of the time correlated single photon counter at our department in 2013. Using this instrument, e.g. a presence of ultra-weak bremsstrahlung radiation in the dark phase of the helium diffuse coplanar barrier discharge during the charge relaxation event could be discovered [11, 12]. For this type of discharge, a novel method of 2D resolved mapping of electric field, based on helium line ratio method [44] and ICCD camera filtered by interference filters was developed [13].

Besides the barrier discharges, an attention has been also paid to the diagnostics of rare gas atmospheric-pressure radiofrequency (RF) discharges. Short after the start of the investigations in 2013, the diffuse α-mode RF APGD in neon was discovered [14, 15]. It was soon realized that the time correlated single photon counter (TCSPC) is a marvellous instrument for the diagnostics of radiofrequency discharges. The pioneer application of the TCSPC method provided the electric field in the sheath of the γ-mode RF helium discharge [16].

Commented papers

[5] Trunec D, Navratil Z, Stahel P, Zajickova L, Bursikova V and Cech J 2004 Deposition of thin organosilicon polymer films in atmospheric pressure glow discharge *J. Phys. D: Appl. Phys.* **37** 2112.

[6] Navratil Z, Brandenburg R, Trunec D, Brablec A, Stahel P, Wagner H and Kopecky Z 2006 Comparative study of diffuse barrier discharges in neon and helium *Plasma Sources Sci. Technol.* **15** 8.

[7] Brandenburg R, Navratil Z, Jansky J, St'ahel P, Trunec D and Wagner H E 2009 The transition between different modes of barrier discharges at atmospheric pressure *J. Phys. D: Appl. Phys.* **42** 085208.

[8] Kloc P, Wagner H E, Trunec D, Navratil Z and Fedoseev G 2010 An investigation of dielectric barrier discharge in Ar and Ar/NH_3 mixture using cross-correlation spectroscopy *J. Phys. D: Appl. Phys.* **43** 345205.

[9] Dosoudilova L, Tschiersch R, Bogaczyk M, Navratil Z, Wagner H E and Trunec D 2015 Investigation of helium barrier discharges with small admixtures of oxygen *J. Phys. D: Appl. Phys.* **48** 355204.

[10] Cech J, Stahel P and Navratil Z 2009 The influence of electrode gap width on plasma properties of diffuse coplanar surface barrier discharge in nitrogen *Eur. Phys. J. D* **54** 259.

[11] Moravek T, Cech J, Navratil Z and Rahel J 2016 Pre-breakdown phase of coplanar dielectric barrier discharge in helium *Eur. Phys. J.-Appl. Phys* **75** 24706.

[12] Navratil Z, Moravek T, Rahel J, Cech J, Lalinsky O and Trunec D 2017 Diagnostics of pre-breakdown light emission in a helium coplanar barrier discharge: the presence of neutral bremsstrahlung *Plasma Sources Sci. Technol.* **26** 055025.

[13] Cech J, Navratil Z, Stipl M, Moravek T and Rahel J 2018 2D-resolved electric field development in helium coplanar DBD: spectrally filtered ICCD camera approach *Plasma Sources Sci. Technol.* **27** 105002.

[14] Navratil Z, Dosoudilova L, Josepson R, Dvorak P and Trunec D 2014 Diffuse α-mode atmospheric pressure radio-frequency discharge in neon *Plasma Sources Sci. Technol.* **23** 042001.

[15] Josepson R, Navratil Z, Dosoudilova L, Dvorak P and Trunec D 2014 Atmospheric Pressure RF Discharge in Neon and Helium *IEEE Trans. Plasma Sci.* **42** 2348.

[16] Navratil Z, Josepson R, Cvetanovic N, Obradovic B and Dvorak P 2016 Electric field development in gamma-mode radiofrequency atmospheric pressure glow discharge in helium *Plasma Sources Sci. Technol.* **25** 03LT01.

2.3 Comments on articles

[5] Trunec D, Navratil Z, Stahel P, Zajickova L, Bursikova V and Cech J 2004 Deposition of thin organosilicon polymer films in atmospheric pressure glow discharge *J. Phys. D: Appl. Phys.* 37 2112

In this work, atmospheric pressure barrier discharge in nitrogen at atmospheric pressure with a small admixture of monomer (hexamethyldisiloxane, hezmatehyldisilazane) was used for the deposition of thin organic films. The discharge was studied by electrical measurements and optical emission spectroscopy. The deposited films were studied by a

number of diagnostic techniques (atomic force microscopy, x-ray photoelectron spectroscopy, infrared absorption measurements, ellipsometry, indentation technique and contact angle measurements).

Firstly, the work proved the necessity of sustainment of diffuse APTD mode in nitrogen DBD in order to produce homogeneous films. Whilst the films from APTD were smooth, the films deposited in filamentary discharge contained sharp asperities. Secondly, the low (nearly room) temperature provided only minor decomposition of the monomer, leaving polymer films on the substrate with $(CH_3)_x$-Si-O-groups and lower hardness (0.3 to 0.6 GPa). In order to obtain harder SiO_x-like films, the substrate temperature had to be increased, as was proved by the research team during the later work [56].

For the purpose of precise control of surface energy measurement, own diagnostic apparatus called 'See System' was developed during this work. In order to improve the reliability of the surface energy determination, a two-dimension regression version of Acid-Base method of surface energy determination was introduced [57]. The method proved to provide stable surface energy results, avoiding misleading results when incorrect set of testing liquids were measured. The instrument was later commercialized and a spin-off company for production of the instrument was established. More than 120 pieces have been sold worldwide so far.

To finish with the plasma diagnostics, presence of CN molecular violet system (B-X) and its intensity variation with the monomer density was observed in the experiments. The production of excited CN in the DBD was later investigated by Dilecce *et al* [58]. According to that work, the excited CN is formed in reaction of N and CH in active discharge and by three-body recombination of C and N atoms in the post discharge. This suggests, that some organosilicon molecules were decomposed into atomic fragments also in our low-temperature deposition process.

[6] Navratil Z, Brandenburg R, Trunec D, Brablec A, Stahel P, Wagner H E and Kopecky Z 2006 Comparative study of diffuse barrier discharges in neon and helium *Plasma Sources Sci. Technol.* 15 8

The aim of the paper was to undertake an optical diagnostics of the diffuse mode of neon barrier discharge and to compare the discharge to the well known diffuse mode of helium barrier discharge [34, 38]. In the original paper, where the discovery of the diffuse mode of the neon discharge was reported [54], only classical photography and electrical measurements were performed. A TCSPC setup located at University of Greifswald was used for this purpose.

The performed measurements revealed, that the discharges in neon and helium are remarkably similar. The spatial structures of both diffuse discharges were nearly the same, consisting of a formed cathode fall and a region resembling the positive column – when the electrode gap was decreased from 5 to 2.2 mm, the cathode region of the neon discharge remained the same, but the 'positive column' disappeared. Other similarities, as the existence of pseudoglow regime with several current peaks per the half period, was found. The existence of the diffuse mode in helium and neon, but not in argon, was explained by high excitation energy of helium and neon metastables, sufficient for Penning ionization of nitrogen molecules. The Penning process provides a sufficient preionization, leading to the overlapping and a coalescence of electron avalanches.

It is interesting from the present point of view (see the discussion of paper [12]), that a continuum spectrum was observed in UV spectral region in the neon DBD. At that time, a hypothesis of bremsstrahlung as the source of the continuous emission was considered improbable, e.g. due to the light emission delayed from the discharge current. Although maximum of bremsstrahlung intensity delayed from the current can be somehow expected, when the maximum of the bremsstrahlung spectrum moves to far UV at high electric field, such delay should be then followed by the change of the continuum shape. A small variation of the measured continuum spectral shape, published in [55], then more likely supports the original conclusion. Molecular continua, as of H_2 ($a\,^3\Sigma_g^+ \rightarrow b\,^3\Sigma_u^+$) below 400 nm [59], were probably better candidates. However, as will be shown later, the bremsstrahlung emission can occur in barrier discharges [12].

[7] Brandenburg R, Navratil Z, Jansky J, Stahel P, Trunec D and Wagner H E 2009 The transition between different modes of barrier discharges at atmospheric pressure *J. Phys. D: Appl. Phys.* 42 085208

In order to use the diffuse barrier discharges industrially, a detailed knowledge of the effect of a gas impurity (or a controlled admixture) on the diffuse mode is needed. For example, the high admixture of a precursor during plasma enhanced chemical vapour deposition (PECVD) in nitrogen BD led to the disruption of the homogeneous mode and onset of the filaments, depositing rough coatings in our experiments [5]. Therefore, we focused mainly in this paper on the impact of gas admixtures into diffuse nitrogen, helium and neon barrier discharges. The experiments were done both in Greifswald and Brno.

We have shown, that the operational area of the homogeneous discharge largely depends on the main gas and the gas admixture. In case of hydrogen admixture into ni-

trogen, several per cent of hydrogen disrupted the homogeneous mode totally. Contrary, 90 vol % admixture of helium into nitrogen still allowed to generate the atmospheric pressure Townsend-like discharge (APTD). In order to generate a stable atmospheric pressure glow-like discharge (APGD), the nitrogen content had to be below 0.1 vol %. As we explained in the article, such differences are due to the different impact of the admixture on the nitrogen or the rare gas metastables, which are vital for the generation of APTD and APGD diffuse mode, respectively.

An important achievement of the presented work was the explanation of the oscillatory current peak of nitrogen APTD observed when hydrogen was admixed. The model developed by the colleagues J. Jánský and D. Trunec showed, that the quenching of nitrogen metastables by hydrogen diminishes the mostly constant secondary electron emission flux by metastables, responsible for the smooth current peak. Concurrent processes of secondary electron production as the photoionization then prevail, exhibiting due to their dependence on the ionization in the gap a multi-peak structure.

[8] Kloc P, Wagner H E, Trunec D, Navratil Z and Fedoseev G 2010 An investigation of dielectric barrier discharge in Ar and Ar/NH_3 mixture using cross-correlation spectroscopy *J. Phys. D: Appl. Phys.* 43 345205

After the study of the disruption of the diffuse modes in nitrogen, helium and neon by gas admixtures, our work was concerned with the opposite role of the admixture, i.e. in establishing the diffuse mode in purely filamentary plasma gases. The example of such a filamentary plasma gas is argon with metastable states $1s_3$ and $1s_5$ with energies (11.7 and 11.5 eV, respectively) insufficient for Penning ionization of the nitrogen molecules (15.5 eV). Since the efficient Penning effect is thought to be vital for the sufficient gas preionization and the homogeneous breakdown, by 'replacing' the intrinsic nitrogen impurity by species with a lower ionization energy (e.g. NH_3, 10.4 eV), the generation of the diffuse mode is supported. This had been already observed by other teams (see the citations in the paper).

In this work, the discharge in argon-ammonia mixture was studied by electrical measurements and so-called Cross-Correlation Spectroscopy utilizing TCSPC apparatus with two independent optical pathways [40]. The most of the experimental work was done during the stay of my colleague P. Kloc (and of mine) at the University of Greifswald. The diffuse mode exhibiting both diffuse light emission and broad current peak was indeed observed when the ammonia content was higher than 3 vol. %. Even a smaller admixture of ammonia (around 0.1 vol.%) caused an abrupt decrease of

the breakdown voltage, as expected for the Penning gas mixture. It also considerably slowed down the discharge development (having originally a streamer character in pure argon). To sum up, the carried out experiments complied with the developing theory of the diffuse barrier discharges.

Similar behaviour was expected from the admixture of acetylene into argon. This gas mixture was indeed later studied at our department and it was also applied for a homogeneous deposition of carbon nanotubes in high temperature atmospheric pressure barrier discharge [60].

[9] Dosoudilova L, Tschiersch R, Bogaczyk M, Navratil Z, Wagner H E and Trunec D 2015 Investigation of helium barrier discharges with small admixtures of oxygen *J. Phys. D: Appl. Phys.* 48 355204

The cooperation between the Masaryk University and the University of Greifswald weakened in the discussed topic after the work described above. Whilst my attention was then occupied by CR modelling of low pressure plasma (see section 1), being later drawn back by the diagnostics of atmospheric pressure plasma, but of coplanar barrier or radiofrequency discharges, the group of Dr. Wagner in Greifswald continued in the investigation of volume barrier discharges (e.g. in He/N_2 mixtures [61, 62]) and did a marvellous work in applying Pockel's effect for the measurement of the surface charge deposited on the dielectric. Erasmus stay of Ph.D. student L. Dosoudilová in Greifswald enabled again to take part in the on-going experiments and to use this technique also for the investigations of He/O_2 mixtures.

In the work, the diffuse discharge in He/O_2 mixtures was operated in APTD, occurring in helium when the electrode gap is only 1 mm [63]. Range of conditions (values of transition vs. burning voltage) of diffuse mode operation was determined as in the previous work [7]. It was found, that already the oxygen concentration of 0.025 vol. % destroyed the diffuse mode, owing to the quenching of helium metastables. The role of oxygen could be well followed from the changes of pseudoglow current patterns. The admixture of oxygen led to the decrease of the current peak decay times and favoured the first current peak in one half-period. The total transferred charge increased, in agreement with the surface charge measurement.

Although the work did not bring any revolutionary finding, it proved the role of oxygen as the strong quenching agent, having the essential influence on the discharge mode and its characteristics. The oxygen enriched helium plasmas are considered as promising tools for the applications in plasma chemistry and biomedicine.

[10] Cech J, Stahel P and Navratil Z 2009 The influence of electrode gap width on plasma properties of diffuse coplanar surface barrier discharge in nitrogen *Eur. Phys. J. D* 54 259

Following studies were focused on coplanar barrier discharge. The aim of this work was to perform an application-oriented optical diagnostics of filamentary plasma in a coplanar barrier discharge in nitrogen and to analyse plasma parameters crucial for the plasma treatment. The attention was paid to the spectroscopy-based gas temperature measurement. Instead of classical on-ceramic-printed large electrode, a special single-electrode setup, which provided also a possibility to change the gap, was used for those studies. The placement of the electrode system into the chamber enabled to perform the experiments in a controlled atmosphere.

The most important result was the finding of very different gas temperatures in the gap centre and above the electrodes (e. g. 650 K vs. 300 K). By reduction of the electrode gap width the filamentary part of the discharge could be suppressed and the rotational temperature was lowered substantially. Such temperature manipulation can be utilized to ensure a safe plasma treatment of temperature sensitive samples.

[11] Moravek T, Cech J, Navratil Z and Rahel J 2016 Pre-breakdown phase of coplanar dielectric barrier discharge in helium *Eur. Phys. J.-Appl. Phys* 75 24706

As mentioned in the introductory part, the coplanar barrier discharge represents a perfect configuration for the simultaneous observation of the phenomena within the whole discharge. That is why the coplanar barrier discharge (generated in experimental setup from the previous paper [10]) was chosen for investigations within the research project of 'Spectroscopic studies of dielectric barrier discharge surface charge recombination' (of Czech Science Foundation, project leader J. Ráheľ). Another reasoning was based on knowledge of recombination processes between opposite charges located at the same side of the dielectric [64]. It was found soon, that a diffuse mode with a very stable active discharge phase is needed in order to study the processes in the dark phase. This stimulated an investigation of the coplanar barrier discharge in rare gas atmospheres.

The first important finding, presented in this first paper on this topic, was that the diffuse mode of helium barrier discharge can be establish also in coplanar configuration (and this holds true also for neon). Conversely, the coplanar discharge in nitrogen was filamentary in the previous study [10], although homogeneous Townsend-like discharge can be easily generated in volume configuration [35]. The ICCD imaging of the diffuse mode in helium revealed the existence of both cathode and anode ionization waves, similarly to air, but running under very different conditions.

Interestingly, an extremely weak luminosity wave was registered by the ICCD imaging in dark phase of the discharge, just before the start of Townsend avalanching. Such emission had not been yet observed in volume nor coplanar barrier discharge. An appearance of the emission within the time region around the AC voltage reversal led us to the hypothesis of a charge relaxation event, in which electrons loosened from the anode dielectric propagate in the residual electric field and recombine with the positive charges at the former cathode (somewhat similar to backward discharge, known from surface barrier discharges [28] or from pulsed discharges [29]).

Since the helium molecular ions He_2^+ as the most abundant ions in pure helium atmospheric pressure plasma recombine dissociatively, recombination radiation from the helium discharge should exhibit a helium atomic line spectrum. In contrast to these expectations, attempts to sense the light (by ICCD camera) at various wavelengths found always a similar but hardly detectable enhancement of the light intensity during the event.

[12] Navratil Z, Moravek T, Rahel J, Cech J, Lalinsky O and Trunec D 2017 Diagnostics of pre-breakdown light emission in a helium coplanar barrier discharge: the presence of neutral bremsstrahlung *Plasma Sources Sci. Technol.* 26 055025.

The aim of this paper was to analyse the charge relaxation event observed in the previous work [11] by the optical emission spectroscopy. Due to its very weak intensity, detectors as CCD or ICCD were ruled out from the use behind the monochromator and ICCD PROES measurement was utilized only to monitor the total light intensity development of the charge relaxation event. It was found, that at early stages of the development, the light was observed already at the anode; then it moved towards the cathode and intensified. This suggested (in agreement with the presented hypothesis), that even the phenomenon appears mainly at the cathode, the anode with the deposited negative charge plays the important role.

In order to measure the spectrum of this ultra-weak event, a method of phase resolved single photon counting was applied. In addition to the afterglow light left by the active discharge, the spectrum measured during the charge relaxation event contained continuum spreading over all measured wavelengths. The neutral bremsstrahlung hypothesis, applied to model the continuum, fit well the spectrum and provided also an estimate of the electric field during this event.

The spatially resolved investigations performed recently (not presented in the paper) have revealed, that the measured electric field does not vary with the position within the

cathode region. The interpretation of this fact requires a precise measurement of a surface charge distribution on the dielectric.

[13] Cech J, Navratil Z, Stipl M, Moravek T and Rahel J 2018 2D-resolved electric field development in helium coplanar DBD: spectrally filtered ICCD camera approach *Plasma Sources Sci. Technol.* 27 105002.

The interpretation of the dark phase diagnostics of the coplanar barrier discharge presented in the previous paper lacked the knowledge of plasma parameters during the active discharge development. For example, the electric field obtained from the fit of the dark phase bremsstrahlung spectrum could not be compared to the value in the active phase. Also, no assumption of the surface charge density spatial variation could be made without the knowledge of the active discharge spatial development. Therefore, further diagnostics of the coplanar barrier discharge was focused on the active discharge phase.

In this paper, electric field strength in the active discharge, i.e. in the ionizing wave, was measured by the optical emission spectroscopy. Since the Stark polarization spectroscopy, applied previously by the author to the atmospheric pressure RF discharge diagnostics [16] (see below) was not simply applicable due to the inhomogeneous electric field in coplanar barrier discharge, helium line ratio method developed in [44] was utilized. The approach based on a direct observation of the discharge by ICCD camera through two interference filters provided true 2D spatially resolved distribution of the electric field.

The obtained electric field developments were qualitatively similar to that observed in coplanar discharge in air, resembling cathode and anode directed ionizing waves [65], but of much lower speed ($\approx$ 4 km/s) and much lower peak electric field value (32 kV/cm max. in the cathode directed wave). On the other hand, the values were similar to that so far measured or simulated in helium plasma jets [42, 43, 66].

Although the method seemed to be straightforward for the use first, the performed tests showed, that only a small misalignment, introduced e.g. by a slow drift of the discharge or by an imperfection in the image alignment can cause severe deviations of the obtained electric field values. These issues were solved e.g. by a 4-point image matching or by a precise time synchronization of subsequently measured frame stacks of both lines according to the simultaneously performed observation through a binocular optical system. Such complications do not arise in Stark polarization spectroscopy, where both lines are measured simultaneously and a temporal resolution can be even omitted due to the emission of the light on the forbidden line only in the high electric field region [43].

[14] Navratil Z, Dosoudilova L, Josepson R, Dvorak P and Trunec D 2014 Diffuse α-mode atmospheric pressure radio-frequency discharge in neon *Plasma Sources Sci. Technol.* 23 042001

The exclusivity of helium and neon as the only rare gases, in which homogeneous mode of barrier discharge can be generated, raised for us a question, whether this holds true also in different types of atmospheric pressure plasma. Besides the dielectric barrier discharges, radiofrequency plasma sources are often used, especially in the form of plasma jets [46]. Whilst helium is one of the most often used gas in the jets, we found surprisingly, that the generation of a similar discharge in neon had not been yet studied. Therefore, first we focused our attention on radiofrequency discharge in neon at atmospheric pressure.

Using ICCD imaging through optical filters (PROES), measurement of electrical parameters and classical optical emission spectroscopy we were able to show, that as in the case of the barrier discharges [67], the radiofrequency discharges are very similar in both gases, having similar I-V curves, spatial profiles of atomic lines being constrained to the sheath regions and similar spatio-temporal developments of various emitters. As in case of helium, the RF discharge in neon can be operated in the diffuse α or in the constricted γ mode. The generation of the discharge in neon was again easier due to the lower voltage needed for the breakdown.

Nevertheless, the correspondence between the two homogeneous discharge regimes (DBD versus α-RF) is not straightforward. As discussed in the text, the homogeneous α mode is a specialty of the RF power, as the discharge is sustained by electrons heated at sheath edges or in low conductive bulk under high electric field. The gas ionization takes place mostly through the ionization of impurities. In glow-like barrier discharge, Townsend theory of the cathode fall formation presumes the role of the γ processes. When the γ processes are involved in RF discharges, the regime is changed abruptly to the constricted γ mode. Still, this γ mode is stable in both helium and neon, though at higher temperature, but the feed of argon into the chamber led to the quick overheating and destruction of the electrode system. Even though, generation of homogeneous mode in argon has been also reported [68].

[15] Josepson R, Navratil Z, Dosoudilova L, Dvorak P and Trunec D 2014 Atmospheric Pressure RF Discharge in Neon and Helium *IEEE Trans. Plasma Sci.* 42 2348

Another comparison of both α-mode discharges in neon and helium was performed in this article using a phase resolved color ICCD photography. ICCD images of both dis-

charges were recorded through three wide band RGB filters and were assembled into colour frames. The resulting images were not only breath-taking, but they also provided an insight into the large differences in excitation of the impurity species in both discharges. Whilst the red emission from helium atoms in RF sheaths was replaced by violet emission from N_2^+ in times, when the region was flooded by plasma, such behaviour was not observed in neon. In case of neon, the emission from N_2^+ was low (as expected from neon metastable energies) and the emission from N_2 formed rather a homogeneous background.

[16] Navratil Z, Josepson R, Cvetanovic N, Obradovic B and Dvorak P 2016 Electric field development in gamma-mode radiofrequency atmospheric pressure glow discharge in helium *Plasma Sources Sci. Technol.* 25 03LT01

After the comparative studies of the discharges in neon and helium, our attention was drawn by the helium discharge as by the discharge with a higher applicability.[1] As mentioned in the State of Art, there had been a number of published modelling studies, but a substantially less work on the optical diagnostics of basic plasma parameters. In this paper, the method of Stark polarization spectroscopy [41, 70], based on the line profile measurement of 492 nm helium line, was used to measure the electric field in the sheath of the γ-mode RF discharge. In contrast to the α-mode, where the electric field can be determined from the electrical measurements, the electric field in the γ-mode is hardly accessible, since the current density, needed in the calculations, may be only estimated in the constricted discharge. For the time resolved measurement of the line profile, the time correlated single photon counting device was utilized. This provided a higher time resolution (0.8 ns) than typically offered by ICCD cameras, higher dynamic range and a better spectral resolution (0.075 nm). The measured profiles were analyzed by the colleagues from the University of Belgrade (N. Cvetanović, B. Obradović) who developed a novel method of the line profile fitting for this specific application.

At first surprising for us, the obtained temporal development of the electric field did not follow a harmonic dependence, but had an almost rectangular profile. However, the sheath model developed by my colleague P. Dvořák provided a clear explanation for that – since the secondary avalanches developing in the γ-mode sheath are efficiently amplified under the high electric field, the sheath conductivity strongly increases, preventing the sheath voltage from further growth.

[1] The lower applicability of neon, given by the higher price, even worsened due to the conflict in Ukraine in 2015, where a majority of the neon worldwide supplies had been produced [69]. Not only the conflict caused 10-30$\times$ rise in price of the gas, but it also led to the elimination of neon from the applications.

The low sheath thickness of about 45 μm estimated by the model disallowed the spatial resolution of the sheath electric field around hemispherical electrodes. On the other hand, the hemispherical electrodes helped us to stabilize the discharge spatially. Asymmetrical electrode design was successfully tried out, but it has been still waiting for the measurement.

Conclusion

In conclusion, I tried to show that the optical emission spectroscopy is vital to uncover the most fundamental properties of both low and atmospheric pressure plasmas. The most often obtained plasma parameters were those describing the electron distribution function. For example, electron temperature was obtained in [2, 3]. Absolute electron density measurement was performed in [2]. When the EDF was found local, reduced electric field strength could be extracted from the measured data [1, 3, 12, 13].

As was shown in this work, very different approaches may be adopted to reveal the plasma properties, spanning from highly spectrally resolved atomic line profile measurement through atomic line ratio or full spectrum fit to low resolved continuum measurement. Measuring techniques utilizing classical CCD, time-resolved ICCD, time correlated single photon counting or phase resolved single photon counting were applied. Some of them were run on the edge of the present capabilities, requiring high spectral resolution in pm range, sub-ns temporal resolution, high spatial resolution or sensitivity on the single photon level. Sometimes such requirements were needed simultaneously as well. On the other hand, temporal and spatial stability of the discharge itself limited the performed diagnostics in some cases. Therefore, not only the development of novel measurement techniques, but also the improvement of present plasma sources is needed to push further the boundaries of the optical plasma diagnostics.

References

[1] Navratil Z, Trunec D, Hrachova V and Kanka A 2007 *J. Phys. D: Appl. Phys.* **40** 1037.

[2] Navratil Z, Dvorak P, Brzobohaty O and Trunec D 2010 *J. Phys. D: Appl. Phys.* **43** 505203.

[3] Navratil Z, Dosoudilova L, Hnilica J and Bogdanov T 2013 *J. Phys. D: Appl. Phys.* **46** 295204.

[4] Vasina P, Fekete M, Hnilica J, Klein P, Dosoudilova L, Dvorak P and Navratil Z 2015 *Plasma Sources Sci. Technol.* **24** 065022.

[5] Trunec D, Navratil Z, Stahel P, Zajickova L, Bursikova V and Cech J 2004 *J. Phys. D: Appl. Phys.* **37** 2112.

[6] Navratil Z, Brandenburg R, Trunec D, Brablec A, Stahel P, Wagner H and Kopecky Z 2006 *Plasma Sources Sci. Technol.* **15** 8.

[7] Brandenburg R, Navratil Z, Jansky J, St'ahel P, Trunec D and Wagner H E 2009 *J. Phys. D: Appl. Phys.* **42** 085208.

[8] Kloc P, Wagner H E, Trunec D, Navratil Z and Fedoseev G 2010 *J. Phys. D: Appl. Phys.* **43** 345205.

[9] Dosoudilova L, Tschiersch R, Bogaczyk M, Navratil Z, Wagner H E and Trunec D 2015 *J. Phys. D: Appl. Phys.* **48** 355204.

[10] Cech J, Stahel P and Navratil Z 2009 *Eur. Phys. J. D* **54** 259.

[11] Moravek T, Cech J, Navratil Z and Rahel J 2016 *Eur. Phys. J.-Appl. Phys* **75** 24706.

[12] Navratil Z, Moravek T, Rahel J, Cech J, Lalinsky O and Trunec D 2017 *Plasma Sources Sci. Technol.* **26** 055025.

[13] Cech J, Navratil Z, Stipl M, Moravek T and Rahel J 2018 *Plasma Sources Sci. Technol.* **27** 105002.

[14] Navratil Z, Dosoudilova L, Josepson R, Dvorak P and Trunec D 2014 *Plasma Sources Sci. Technol.* **23** 042001.

[15] Josepson R, Navratil Z, Dosoudilova L, Dvorak P and Trunec D 2014 *IEEE Trans. Plasma Sci.* **42** 2348.

[16] Navratil Z, Josepson R, Cvetanovic N, Obradovic B and Dvorak P 2016 *Plasma Sources Sci. Technol.* **25** 03LT01.

[17] Boffard J B, Lin C C and DeJoseph, Jr. C A 2004 *J. Phys. D: Appl. Phys.* **37** R143–R161.

[18] Boffard J B, Jung R O, Lin C C and Wendt A E 2010 *Plasma Sources Sci. Technol.* **19** 065001.

[19] Malyshev M V and Donnelly V M 1999 *Phys. Rev. E* **60** 6016–6029.

[20] Donnelly V M 2004 *J. Phys. D: Appl. Phys.* **37** R217.

[21] Zhu X M, Pu Y K, Celik Y, Siepa S, Schuengel E, Luggenhoelscher D and Czarnetzki U 2012 *Plasma Sources Sci. Technol.* **21** 024003.

[22] Boffard J B, Jung R O, Lin C C and Wendt A E 2009 *Plasma Sources Sci. Technol.* **18** 035017.

[23] Zhu X M, Tsankov T V and Czarnetzki U 2015 *Plasma Sources Sci. Technol.* **24** 035023.

[24] Jolly J and Touzeau M 1975 *J. Quant. Spectrosc. Radiat. Transf.* **15** 863–872.

[25] Wamsley R C, Mitsuhashi K and Lawler J E 1993 *Rev. Sci. Instrum.* **64** 45–48.

[26] Dosoudilová L. Absorpční metody při optické diagnostice plazmatu. Master's thesis Masaryk University Brno, the Czech Republic 2011.

[27] Fekete M, Hnilica J, Vitelaru C, Minea T and Vasina P 2017 *J. Phys. D: Appl. Phys.* **50** 365202.

[28] Gibalov V I and Pietsch G J 2012 *Plasma Sources Sci. Technol.* **21** 024010.

[29] Brandenburg R 2017 *Plasma Sources Sci. Technol.* **26** 053001.

[30] Shi J and Kong M 2005 *J. Appl. Phys.* **97** 023306.

[31] Hemke T, Eremin D, Mussenbrock T, Derzsi A, Donko Z, Dittmann K, Meichsner J and Schulze J 2013 *Plasma Sources Sci. Technol.* **22** 015012.

[32] Park J, Henins I, Herrmann H and Selwyn G 2001 *J. Appl. Phys.* **89** 15.

[33] Moon S, Rhee J, Kim D and Choe W 2006 *Phys. Plasmas.* **13** 033502.

[34] Massines F, Rabehi A, Décomps P, Ben Gadri R, Séguer P and Mayoux C 1998 *J. Appl. Phys.* **83** 2950–2957.

[35] Gherardi N, Gouda G, Gat E, Ricard A and Massines F 2000 *Plasma Sources Sci. Technol.* **9** 340–346.

[36] Massines F, Sarra-Bournet C, Fanelli F, Naude N and Gherardi N 2012 *Plasma Process. Polym.* **9** 1041.

[37] Bogaczyk M, Nemschokmichal S, Wild R, Stollenwerk L, Brandenburg R, Meichsner J and Wagner H E 2012 *Contrib. Plasma Phys.* **52** 847.

[38] Mangolini L, Orlov K, Kortshagen U, Heberlein J and Kogelschatz U 2002 *Appl. Phys. Lett.* **80** 1722–1724.

[39] Bogaczyk M, Wild R, Stollenwerk L and Wagner H E 2012 *J. Phys. D: Appl. Phys.* **45** 465202.

[40] Kozlov K V, Wagner H E, Brandenburg R and Michel P 2001 *J. Phys. D: Appl. Phys.* **34** 3164–3176.

[41] Obradovic B M, Ivkovic S S and Kuraica M M 2008 *Appl. Phys. Lett.* **92** 191501.

[42] Sretenovic G B, Krstic I B, Kovacevic V V, Obradovic B M and Kuraica M M 2014 *J. Phys. D: Appl. Phys.* **47** 102001.

[43] Sobota A, Guaitella O, Sretenovic G B, Krstic I B, Kovacevic V V, Obrusnik A, Nguyen Y N, Zajickova L, Obradovic B M and Kuraica M M 2016 *Plasma Sources Sci. Technol.* **25** 065026.

[44] Ivkovic S S, Sretenovic G B, Obradovic B M, Cvetanovic N and Kuraica M M 2014 *J. Phys. D: Appl. Phys.* **47** 055204.

[45] Zhu X M, Pu Y K, Balcon N and Boswell R 2009 *J. Phys. D: Appl. Phys.* **42** 142003.

[46] Laroussi M and Akan T 2007 *Plasma Process. Polym.* **4** 777.

[47] Park J, Henins I, Herrmann H, Selwyn G and Hicks R 2001 *J. Appl. Phys.* **89** 20.

[48] Shi J and Kong M 2005 *IEEE Trans. Plasma Sci.* **33** 624.

[49] Liu D W, Iza F and Kong M G 2009 *Appl. Phys. Lett.* **95** 031501.

[50] Niemi K, Waskoenig J, Sadeghi N, Gans T and O'Connell D 2011 *Plasma Sources Sci. Technol.* **20** 055005.

[51] Bursikova V, St'ahel P and Janca J 2002 *Czech. J. Phys.* **52** 866.

[52] Sira M, Trunec D, Stahel P, Bursikova V, Navratil Z and Bursik J 2005 *J. Phys. D: Appl. Phys.* **38** 621.

[53] Sira M, Trunec D, St'ahel P, Bursikova V and Navratil Z 2008 *J. Phys. D: Appl. Phys.* **41** 015205.

[54] Trunec D, Brablec A and Buchta J 2001 *J. Phys. D: Appl. Phys.* **34** 1697.

[55] Navratil Z, Trunec D, Brablec A, St'Ahel P, Brandenburg R and Wagner H 2004 *Czech. J. Phys.* **54** C550.

[56] Trunec D, Zajickova L, Bursikova V, Studnicka F, Stahel P, Prysiazhnyi V, Perina V, Houdkova J, Navratil Z and Franta D 2010 *J. Phys. D: Appl. Phys.* **43** 225403.

[57] Navratil Z, Bursikova V, St'ahel P, Sira M and Zverina P 2004 *Czech. J. Phys.* **54** C877.

[58] Dilecce G, Ambrico P F, Scarduelli G, Tosi P and De Benedictis S 2009 *Plasma Sources Sci. Technol.* **18** 015010.

[59] Fantz U, Schalk B and Behringer K 2000 *New J. Phys.* **2** 7.

[60] Elias M, Kloc P, Jasek O, Mazankova V, Trunec D, Hrdy R and Zajickova L 2015 *J. Appl. Phys.* **117** 103301.

[61] Bogaczyk M, Wild R, Stollenwerk L and Wagner H E 2012 *J. Phys. D: Appl. Phys.* **45**.

[62] Tschiersch R, Bogaczyk M and Wagner H E 2014 *J. Phys. D: Appl. Phys.* **47** 365204.

[63] Bogaczyk M, Nemschokmichal S, Wild R, Stollenwerk L, Brandenburg R, Meichsner J and Wagner H E 2012 *Contrib. Plasma Phys.* **52** 847.

[64] Wild R, Benduhn J and Stollenwerk L 2014 *J. Phys. D: Appl. Phys.* **47** 435204.

[65] Hoder T, Synek P, Chorvat D, Rahel J, Brandenburg R and Cernak M 2017 *Plasma Phys. Control. Fusion* **59** 074001.

[66] Boeuf J P, Yang L L and Pitchford L C 2013 *J. Phys. D: Appl. Phys.* **46** 015201.

[67] Navrátil Z, Brandenburg R, Trunec D, Brablec A, Sťahel P, Wagner H E and Kopecký Z 2006 *Plasma Sources Sci. Technol.* **15** 8–17.

[68] Laimer J and Stoeri H 2006 *Plasma Process. Polym.* **3** 573.

[69] Corbett M, Thirsk M and Tuan A. Semiconductor industry neon capacity disruption continues. `http://www.semi.org/en/node/57646`. Accessed: 2018-06-30.

[70] Kuraica M and Konjevic N 1997 *Appl. Phys. Lett.* **70** 1521.

Appendix

Copy of scientific papers

INSTITUTE OF PHYSICS PUBLISHING JOURNAL OF PHYSICS D: APPLIED PHYSICS

J. Phys. D: Appl. Phys. **40** (2007) 1037–1046 doi:10.1088/0022-3727/40/4/018

Collisional–radiative model of neon discharge: determination of E/N in the positive column of low pressure discharge

Z Navrátil[1,2], D Trunec[1], V Hrachová[3] and A Kaňka[3]

[1] Faculty of Science, Department of Physical Electronics, Masaryk University, Kotlářská 2, 611 37 Brno, Czech Republic
[2] Faculty of Science, Department of General Physics, Masaryk University, Kotlářská 2, 611 37 Brno, Czech Republic
[3] Faculty of Mathematics and Physics, Department of Electronics and Vacuum Physics, Charles University in Prague, V Holešovičkách 2, 182 00 Prague, Czech Republic

E-mail: zdenek@physics.muni.cz

Received 10 October 2006, in final form 4 December 2006
Published 2 February 2007
Online at stacks.iop.org/JPhysD/40/1037

Abstract

A method for the determination of the reduced electric field strength (E/N) in a neon discharge from the optical emission spectra was developed. This method is based on a collisional–radiative model, which was used to calculate the emission spectra of the neon plasma. In the model, populations of 30 excited levels of the neon atom were studied. Various elementary collision processes were taken into account: electron impact excitation, de-excitation and ionization of neon atoms, emission and absorption of radiation, metastable–metastable collisions, metastable and radiative dimer production, Penning ionization, etc. To determine the rates of electron collisions, the Boltzmann kinetic equation for the electron distribution function (EDF) was solved for given E/N, and thus the dependence of the emission spectra on E/N could be determined. The EDF was expanded in terms of Legendre polynomials and the first two terms of this approximation were taken into account. The theoretical emission spectra were fitted by the non-linear least-squares method to the measured spectra with respect to the unknown parameter E/N.

The method was applied to the study of low pressure dc glow discharge in neon. In such a discharge the calculated reduced electric field strength could be compared with the independent results of simultaneously performed electric probe measurements of E/N. Generally, close agreement of the calculated values with the experimental data was achieved.

(Some figures in this article are in colour only in the electronic version)

1. Introduction

Collisional–radiative models represent an important method in plasma studies. Basically, using the elementary data (cross sections, rate constants and transition probabilities) they enable the determination of population distributions of atoms, molecules and ions over their excited states. The knowledge of population distribution and its dependence on plasma parameters can be used in various ways: in diagnostics to determine the parameters of the studied plasma, in simulations, for example, to determine the discharge emission of radiation over a large range of conditions, or in atomic physics to study the elementary processes, which are responsible for population and depopulation of atomic excited levels.

A large number of collisional–radiative models has been reported in the literature, so only some of them are mentioned here. A very useful overview of collisional–radiative models was presented in [1]. A collisional–radiative

model with the Boltzmann solver was used to determine the stepwise excitation cross sections of rare-gas atoms in [2]. An extensive collisional–radiative model for argon [3, 4] enabled the investigation of population mechanisms of excited levels in various argon discharges. The method of electron temperature measurement, based on a collisional–radiative model, was reported in [5]. Collisional–radiative modelling was also employed in optical diagnostic methods used for the investigation of collisional processes governing the populations of the lowest 15 levels of the neon atom [6]. A collisional–radiative model for the study of positive columns of low pressure discharge in neon, argon and xenon was reported in [7].

In this paper the collisional–radiative model is used to develop the diagnostic method of reduced electric field strength (E/N) determination in neon discharges. Based on optical emission spectroscopy and on comparison of the measured spectra with the spectra calculated by the model, this method is entirely non-invasive and can be used under conditions when the electric probe measurement is not applicable or strongly disrupts the plasma (e.g. in atmospheric pressure discharges). However, in order to check the possibilities and limitations of this method, the model was applied to the study of the positive column of low pressure dc glow discharge in neon first. In such a discharge an independent electric probe measurement is possible and the results of both methods can be compared.

The paper is organized as follows: the collisional–radiative model and the method of determination of the reduced electric field strength is described in section 2. Details of the experimental apparatus, used for spectroscopy and probe measurements, are given in section 3. The results of both experimental and theoretical studies are presented, compared and discussed in section 4. Conclusions are presented in section 5.

2. Principles

The principal scheme of the method is shown in figure 1. An electron distribution function (EDF) was determined for a given E/N by a solution of the Boltzmann kinetic equation. After that, rate coefficients of electron collisions, which are responsible for the population (and the depopulation) of excited levels, could be determined. These rate coefficients, together with the rate coefficients and transition probabilities of other incorporated processes (e.g. electron impact ionization of neon atoms, emission and absorption of radiation, metastable–metastable collisions, three-body ion conversion, metastable and radiative dimer production and Penning ionization), served to build up the rate equations for concentrations of excited states of neon atoms. The steady state values of excited state concentrations, commonly determined just by the solution of algebraic balance equations [1], were found by a more robust fourth-order Runge–Kutta method with an adaptive step size according to [8]. This method was used to calculate the time development of the excited state concentrations from the initial guess to the steady state values from the rate equations. The calculated steady state populations allowed us to determine the optical emission spectrum for a given E/N, which was fitted by the least-squares method to the measured spectrum in order to determine the E/N in the discharge.

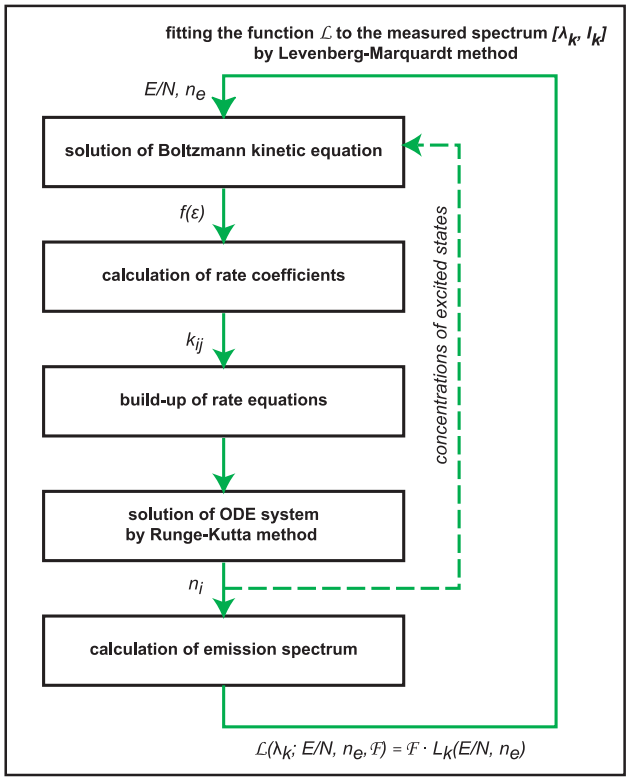

Figure 1. Principal scheme of method used for the determination of reduced electric field strength E/N. For explanation see the text.

In the following subsections more detailed descriptions of the above-mentioned procedures are given.

2.1. Electron distribution function

In order to obtain a distribution function of electrons in the positive column of a dc glow discharge a stationary Boltzmann kinetic equation was solved. Provided that the electric field is spatially uniform, EDF f is rotationally symmetric in the velocity space around the direction of the electric field and it may be expanded in terms of Legendre polynomials of cos θ (θ is the angle between the velocity and the electric field strength):

$$f(v, \theta) = f_0(v) + f_1(v) \cos\theta + \ldots, \tag{1}$$

where v denotes the magnitude of velocity. A common Lorentz approximation takes into account only the first two terms of the expansion: an isotropic part f_0 of EDF and an anisotropic perturbation f_1. Since functions f_0 and f_1 depend only on the magnitude of velocity, they can be simply expressed as the functions of the electron energy ε (in eV). Thus, $f_0(\varepsilon)$ was determined numerically by solving the equation

$$\begin{aligned}
&\frac{1}{3}\left(\frac{E}{N}\right)^2 \frac{\mathrm{d}}{\mathrm{d}\varepsilon}\left(\frac{\varepsilon}{\sigma_\mathrm{m}(\varepsilon)}\frac{\mathrm{d}f_0(\varepsilon)}{\mathrm{d}\varepsilon}\right) \\
&\quad + \frac{2m_\mathrm{e}}{M}\frac{\mathrm{d}}{\mathrm{d}\varepsilon}\left(\varepsilon^2\sigma_\mathrm{m}(\varepsilon)\left(f_0(\varepsilon) + \frac{k_\mathrm{b}T_\mathrm{n}}{e}\frac{\mathrm{d}f_0(\varepsilon)}{\mathrm{d}\varepsilon}\right)\right) \\
&\quad + \sum_{a,i,j}\frac{n_a}{N}[(\varepsilon+\varepsilon_{ij})f_0(\varepsilon+\varepsilon_{ij})\sigma_{ij}(\varepsilon+\varepsilon_{ij}) \\
&\quad - \varepsilon f_0(\varepsilon)\sigma_{ij}(\varepsilon)] = 0,
\end{aligned} \tag{2}$$

where E denotes the electric field, N is the concentration of neutral gas atoms, M their mass, m_e the electron mass, σ_m the momentum transfer cross section, k_b the Boltzmann constant, e the elementary charge and T_n the temperature of neutral atoms. n_a is the concentration of particles a, colliding inelastically with electrons (ground-state and excited atoms). ε_{ij} is the energy difference between the initial (ith) and final (jth) states of the colliding particles, which is positive in the case of excitation or ionization collisions and negative in the case of de-excitation collisions (superelastic electron collisions). σ_{ij} is the cross section of the collisions.

The binary excitation and ionization electron collisions with the ground-state neon atoms and excitation, ionization and de-excitation collisions with the neon atoms in $2p^5 3s$ states were taken into account as inelastic electron collisions. Details of the cross-section data being used are given in section 2.3. Assuming the following normalization of the EDF

$$\int_0^\infty f_0(\varepsilon)\varepsilon^{1/2}\,\mathrm{d}\varepsilon = 1, \tag{3}$$

the rate coefficient k of electron collisions with the cross-section σ can be calculated as

$$k = \sqrt{\frac{2e}{m_e}}\int_0^\infty \sigma(\varepsilon) f_0(\varepsilon)\varepsilon\,\mathrm{d}\varepsilon. \tag{4}$$

In such a way the rate coefficients of excitation and ionization electron collisions can be determined. The rate coefficients of electron de-excitation collisions were determined on the basis of a detailed balance between the two levels. Assuming σ for excitation cross section, the rate coefficient of inverse de-excitation collisions is

$$k = \sqrt{\frac{2e}{m_e}}\frac{g_j}{g_i}\int_{\varepsilon_{ij}}^\infty \sigma(\varepsilon) f_0(\varepsilon-\varepsilon_{ij})\varepsilon\,\mathrm{d}\varepsilon, \tag{5}$$

where ε_{ij} is the electron energy gain in de-excitation collisions and g_i, g_j are the statistical weights of upper and lower states of the colliding atom.

2.2. Excited levels

The 30 lowest excited states of the neon atom were incorporated in the collisional–radiative model. These states are listed, together with their notation, statistical weights and excitation energies, in table 1; their structure is schematically shown in figure 2. The ground state of the neon atom is a closed shell, $1s^2\,2s^2\,2p^6$. The four lowest excited states arise from the $2p^5 3s$ configuration. The states $1s_2$ and $1s_4$ (labelled in Paschen notation) are resonance levels with short radiative lifetimes. The spectral lines originating from transitions from these levels lie in the deep UV region (73.6 and 74.3 nm) and thus they are not measurable with the common UV-VIS optical spectrometers. The other states $1s_3$ and $1s_5$ are metastable with radiative lifetimes in the order of a second [9]. The next ten levels, $2p_1 - 2p_{10}$, are radiative states arising from the $2p^5 3p$ configuration. They are depopulated by intensive radiative transitions to $1s_2$–$1s_5$ states with wavelengths in the range 540–808 nm. These transitions are generally usable for optical diagnostics, since they occur even at low electric field strengths. Higher states $2s_i$, $3s_i$ and $3d_i$ arising from configurations $2p^5 4s$ and $2p^5 3d$ are upper states only for the transitions directed to the ground state and to the states of the $2p^5 3p$ configuration due to the selection rules. Under the conditions being considered the lines corresponding to these transitions are too weak or in the deep UV region to be used for diagnostics. Similar results were also obtained for higher excited states. Thus, only transitions $2p_i \to 1s_j$ were studied in the experiment. Inclusion of the states of $2p^5 4s$ and $2p^5 3d$ configurations in the model thus serves only to take into account the cascade contributions to $2p_i$ state excitations.

Table 1. The ground state and excited states of the neon atom, which were incorporated in the model. The individual columns show the effective level number i, describing the level in this paper, the $nlpqr$ number, the Racah and Paschen notation, statistical weight g_i and excitation energy $\mathcal{E}_i^{\mathrm{excit}}$ (according to [10]). The levels 26 and 27 are effective, both consisting of two real levels due to their unresolved excitation cross-section data.

Level i	Notation $nlpqr$	Racah	Paschen	g_i	$\mathcal{E}_i^{\mathrm{excit}}$ (eV)
1	21000	$2p^6$	$1p_0$	1	0.00000
2	30332	$3s\,[3/2]_2^o$	$1s_5$	5	16.61907
3	30331	$3s\,[3/2]_1^o$	$1s_4$	3	16.67083
4	30110	$3s'[1/2]_0^o$	$1s_3$	1	16.71538
5	30111	$3s'[1/2]_1^o$	$1s_2$	3	16.84805
6	31311	$3p\,[1/2]_1$	$2p_{10}$	3	18.38162
7	31353	$3p\,[5/2]_3$	$2p_9$	7	18.55511
8	31352	$3p\,[5/2]_2$	$2p_8$	5	18.57584
9	31331	$3p\,[3/2]_1$	$2p_7$	3	18.61271
10	31332	$3p\,[3/2]_2$	$2p_6$	5	18.63679
11	31131	$3p'[3/2]_1$	$2p_5$	3	18.69336
12	31132	$3p'[3/2]_2$	$2p_4$	5	18.70407
13	31310	$3p\,[1/2]_0$	$2p_3$	1	18.71138
14	31111	$3p'[1/2]_1$	$2p_2$	3	18.72638
15	31110	$3p'[1/2]_0$	$2p_1$	1	18.96596
16	40332	$4s\,[3/2]_2^o$	$2s_5$	5	19.66403
17	40331	$4s\,[3/2]_1^o$	$2s_4$	3	19.68820
18	40110	$4s'[1/2]_0^o$	$2s_3$	1	19.76060
19	40111	$4s'[1/2]_1^o$	$2s_2$	3	19.77977
20	32310	$3d\,[1/2]_0^o$	$3d_6$	1	20.02464
21	32311	$3d\,[1/2]_1^o$	$3d_5$	5	20.02645
22	32374	$3d\,[7/2]_4^o$	$3d'_4$	9	20.03465
23	32373	$3d\,[7/2]_3^o$	$3d_4$	7	20.03487
24	32332	$3d\,[3/2]_2^o$	$3d_3$	5	20.03675
25	32331	$3d\,[3/2]_1^o$	$3d_2$	3	20.04039
26	32352	$3d\,[5/2]_2^o$	$3d''_1$	5	20.04821
	32353	$3d\,[5/2]_3^o$	$3d'_1$	7	20.04843
27	32152	$3d'[5/2]_2^o$	$3s''''_1$	5	20.13611
	32153	$3d'[5/2]_3^o$	$3s'''_1$	7	20.13630
28	32132	$3d'[3/2]_2^o$	$3s''_1$	5	20.13751
29	32131	$3d'[3/2]_1^o$	$3s'_1$	3	20.13946

2.3. Considered elementary processes

Various collisional, radiative and also diffusion processes, governing the populations of the considered 30 excited neon states, were taken into account[4].

(i) Electron impact excitation out of the ground state and the $2p^5 3s$ states:

$$\mathrm{Ne}(i) + \mathrm{e}^- \xrightarrow{k_{ij}} \mathrm{Ne}(j) + \mathrm{e}^-,$$
$$i = 1, \ldots 5, \qquad j = 2, \ldots 29, \qquad i < j. \tag{6}$$

[4] The neon excited states are distinguished in the following list by a level number i, which is written in parentheses after the element symbol (see table 1).

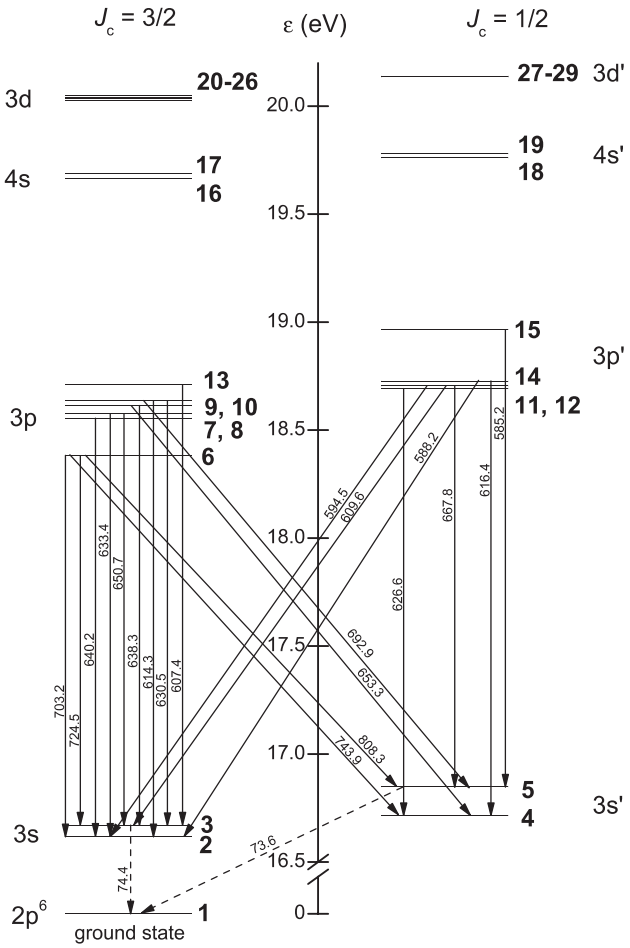

Figure 2. The scheme of excited levels of the neon atom showing the levels incorporated in the model and the main radiative transitions from 3s and 3p states. The number in bold face denotes the effective level number.

(ii) Electron impact de-excitation to the ground state and the $2p^5 3s$ states:

$$\mathrm{Ne}(i) + \mathrm{e}^- \xrightarrow{k_{ij}} \mathrm{Ne}(j) + \mathrm{e}^-, \quad i = 2, \ldots 29, \quad j = 1, \ldots 5, \quad i > j. \tag{7}$$

(iii) Spontaneous emission of radiation:

$$\mathrm{Ne}(i) \xrightarrow{A_{ij}} \mathrm{Ne}(j) + h\nu, \quad i = 2, \ldots 29, \quad i > j. \tag{8}$$

Symbol A_{ij} denotes the Einstein coefficient of spontaneous emission.

(iv) Absorption of radiation:

$$\mathrm{Ne}(i) + h\nu \xrightarrow{(1-\Lambda_{ji})A_{ji}} \mathrm{Ne}(j), \quad i = 1, \ldots 28, \quad i < j. \tag{9}$$

Symbol Λ_{ji} denotes the escape factor (see section 2.4).

(v) Electron impact ionization of the ground-state and metastable atoms:

$$\mathrm{Ne}(1) + \mathrm{e}^- \xrightarrow{k_{\mathrm{ion}}} \mathrm{Ne}^+ + \mathrm{e}^- + \mathrm{e}^-, \tag{10}$$

$$\mathrm{Ne}(2,4) + \mathrm{e}^- \xrightarrow{k_{\mathrm{ionmet}}} \mathrm{Ne}^+ + \mathrm{e}^- + \mathrm{e}^-. \tag{11}$$

(vi) Chemoionization:

$$\mathrm{Ne}(2,4) + \mathrm{Ne}(2,4) \xrightarrow{k_{\mathrm{met}}} \mathrm{Ne}(1) + \mathrm{Ne}^+ + \mathrm{e}^-. \tag{12}$$

(vii) Associative ionization:

$$\mathrm{Ne}(2,4) + \mathrm{Ne}(2,4) \xrightarrow{k_{\mathrm{met}}} \mathrm{Ne}_2^+ + \mathrm{e}^-. \tag{13}$$

(viii) Collision-induced emission:

$$\mathrm{Ne}(2,4) + \mathrm{Ne}(1) \xrightarrow{k_{2\mathrm{b}}} 2\mathrm{Ne}(1) + h\nu. \tag{14}$$

(ix) Three-body production of dimers:

$$\mathrm{Ne}(2,4) + \mathrm{Ne}(1) + \mathrm{Ne}(1) \xrightarrow{k_{3\mathrm{b_m}}} \mathrm{Ne}_2^* + \mathrm{Ne}(1), \tag{15}$$

$$\mathrm{Ne}(3) + \mathrm{Ne}(1) + \mathrm{Ne}(1) \xrightarrow{k_{3\mathrm{b_3}}} \mathrm{Ne}_2^m + \mathrm{Ne}(1), \tag{16}$$

$$\mathrm{Ne}(5) + \mathrm{Ne}(1) + \mathrm{Ne}(1) \xrightarrow{k_{3\mathrm{b_5}}} \mathrm{Ne}_2^m + \mathrm{Ne}(1). \tag{17}$$

(x) Penning ionization of impurities (concentrations according to the gas supplier specification):

$$\mathrm{Ne}(2\text{–}5) + \mathrm{H}_2 \xrightarrow{k_{\mathrm{H}_2^+}} \mathrm{H}_2{}^+ + \mathrm{Ne}(1) + \mathrm{e}^-, \tag{18}$$

$$\mathrm{Ne}(2\text{–}5) + \mathrm{H}_2 \xrightarrow{k_{\mathrm{NeH}^+}} \mathrm{NeH}^+ + \mathrm{H} + \mathrm{e}^-, \tag{19}$$

$$\mathrm{Ne}(2\text{–}5) + \mathrm{N}_2 \xrightarrow{k_{\mathrm{N}_2^+}} \mathrm{N}_2{}^+ + \mathrm{Ne}(1) + \mathrm{e}^-, \tag{20}$$

$$\mathrm{Ne}(2\text{–}5) + \mathrm{N}_2 \xrightarrow{k_{\mathrm{NeN}_2^+}} \mathrm{NeN}_2{}^+ + \mathrm{e}^-, \tag{21}$$

$$\mathrm{Ne}(2\text{–}5) + \mathrm{O}_2 \xrightarrow{k_{\mathrm{O}_2^+}} \mathrm{O}_2{}^+ + \mathrm{Ne}(1) + \mathrm{e}^-. \tag{22}$$

These processes were incorporated for generality. However, we assume a negligible influence on the calculated spectra.

(xi) Diffusion of metastable-state atoms to the wall.

The rate coefficients for excitation of neon atoms by electron impact k_{ij} ($i < j$) were calculated according to (4). The cross-section data in [11] were adapted for the direct excitation of the ground-state neon atoms into both metastable states $1s_3$, $1s_5$ of the $2p^5 3s$ configuration. The data for direct excitation into radiative states $1s_2$, $1s_4$ of the $2p^5 3s$ configuration were taken from [12, 13]. To calculate the direct excitation into the states of $2p^5 3p$, $2p^5 4s$ and $2p^5 3d$ configurations the data published in [14] and [15], respectively, were used.

The experimental values of cross sections in [16] were used for the excitation out of states of the $2p^5 3s$ configuration. However, in this work only the cross sections (given in absolute values) for excitation out of the state $1s_5$ (effective number 2) into states $2p_9$ (7), $2p_8$ (8), $2p_6$ (10) and $2p_4$ (12) were published. The cross sections for other states were presented, e.g. in [2, 17, 18][5], but the reported values differ considerably for some transitions from the recent data published in [16].

[5] The average cross section for excitation among the states $2p^5$ 3s–$2p^5$ 3p was published in [18].

Table 2. Rate coefficients of the processes considered in the model. The number in parentheses, if appropriate, denotes the level, for which the value is valid.

Denomination	Value	References
k_{ij}	calculated	[11–14,16]
k_{ion}	calculated; (1)	[11]
k_{ionmet}	calculated; (2, 4)	[22]
k_{met}	6.40×10^{-16} m^3 s^{-1}; (2, 4)	[24]
$k_{2\mathrm{b}}$	1.55×10^{-21} m^3 s^{-1}; (2, 4)	[24]
$k_{3\mathrm{b_m}}$	5.00×10^{-46} m^6 s^{-1}; (2, 4)	[25]
$k_{3\mathrm{b_3}}$	7.04×10^{-45} m^6 s^{-1}; (3)	[26]
$k_{3\mathrm{b_5}}$	6.45×10^{-46} m^6 s^{-1}; (5)	[26]
$k_{\mathrm{H_2^+}}$	1.79×10^{-17} m^3 s^{-1}; (2–5)	[27]
$k_{\mathrm{NeH^+}}$	0.51×10^{-17} m^3 s^{-1}; (2–5)	[27]
$k_{\mathrm{N_2^+}}$	7.52×10^{-17} m^3 s^{-1}; (2–5)	[27]
$k_{\mathrm{NeN_2^+}}$	0.48×10^{-17} m^3 s^{-1}; (2–5)	[27]
$k_{\mathrm{O_2^+}}$	2.50×10^{-16} m^3 s^{-1}; (2–5)	[27]
D_2N	5.1×10^{20} m^{-1} s^{-1}; (2, 300 K)	[25]
D_4N	5.8×10^{20} m^{-1} s^{-1}; (4, 300 K)	[25]

According to [19], the cross sections scale with the oscillator strengths also at low electron energies, where the Born approximation of excitation cross section is not valid. Thus, the excitation function for the $1s_5$–$2p_9$ transition published in [16] was scaled with the oscillator strength ratio to obtain a consistent set of excitation cross sections for optically allowed transitions among the states $2p^53s$–$2p^53p$. Two different sets of cross sections for the $2p^53s$–$2p^53p$ excitations were tested: the set consisting of the four cross sections from [16] (Set 1) and the set expanded with the cross sections for other transitions determined by scaling the cross section for the $1s_5$–$2p_9$ excitation (Set 2). The cross sections for optically forbidden transitions, which could not be determined in this way, were assumed to be zero.

The rate coefficients for de-excitation of neon atoms by electron impact k_{ij} $(i > j)$ were calculated according to (5) from the same excitation cross-section data. The rate coefficients for ionization of neon atoms by electron impact k_{ion} (ground-state atoms) and k_{ionmet} (metastables) were determined again from (4). The cross section for direct ionization by electron impact was taken from [11], where early measurements in [20, 21] were combined. Ionization of neon metastables was characterized by cross-section data published in [22]. The same cross-section values for both metastable states were assumed as in this reference.

The Einstein coefficients for spontaneous emission A_{ij} were taken primarily from [10]. The transition probability data, which were not included in this database, were taken from [23]. The transition probabilities of effective levels 26 and 27 were determined as

$$A_{\{i\}j} = \frac{\sum_i g_i A_{ij}}{\sum_i g_i}, \qquad i \in \{i\}, \tag{23}$$

in which A_{ij} is the Einstein coefficient, g_i the statistical weight and i indexes the levels grouped into an effective level $\{i\}$.

The rate coefficients for collisions, in which heavy particles (e.g. neon ground-state atoms and metastables) participate, are given with their references in table 2.

The rate equation for the concentration of excited state i of the neon atom has generally the form

$$\begin{aligned}\frac{\mathrm{d}n_i}{\mathrm{d}t} &= k_{1i}n_\mathrm{e}n_1 - k_{i1}n_\mathrm{e}n_i + \delta_{i\,3\mathrm{p}}\left(\sum_{j=2}^{5} k_{ji}n_\mathrm{e}n_j - \sum_{j=2}^{5} k_{ij}n_\mathrm{e}n_i\right) \\ &+ \delta_{i\,3\mathrm{s}}\left(-\sum_{j=6}^{15} k_{ij}n_\mathrm{e}n_i + \sum_{j=6}^{15} k_{ji}n_\mathrm{e}n_j\right) - \sum_{j=1}^{i-1} \Lambda_{ij}A_{ij}n_i \\ &+ \sum_{j=i+1}^{29} \Lambda_{ji}A_{ji}n_j = 0, \end{aligned} \tag{24}$$

where n_e and N denote the concentration of electrons and neutral atoms, respectively, $\delta_{i\,3\mathrm{p}}$ equals unity for $2p^53p$ levels $(i = 6$–$15)$ and zero otherwise and $\delta_{i\,3\mathrm{s}}$ is defined similarly for $2p^53s$ levels $(i = 2$–$5)$. The concentration of neutral atoms was determined from the thermodynamic equation of state. The rate equations for $2p^53s$ states and particularly for metastable states are more complicated, incorporating other, in some cases also non-linear, processes as mentioned above.

2.4. Radiation trapping

The radiation emitted by a single atom in the discharge can be absorbed and re-emitted by surrounding atoms many times before the radiation reaches the walls of the discharge chamber. This repeated absorption–re-emission process, known as radiation trapping, changes the apparent radiative lifetimes of states and transition probabilities. The radiation trapping is crucial in the case of resonance transitions, but it may be important also in the case of transitions with a metastable lower state. In collisional–radiative models the local effect of absorption of radiation is approximately described by so-called escape factors, which are calculated by solving the Holstein equation [28] for various discharge geometries and line shapes. In our calculations a technique described in [29] was adapted. In this work trapping factors g (inverse value to escape factor) were published for Doppler (g^D), Lorentz (g^L) and Voigt (g^V) line shapes and cylindrical and spherical geometries:

$$\begin{aligned} g^\mathrm{D}(k_0R) &= 1 + \frac{1}{m_j^\mathrm{D}}k_0R\sqrt{\ln\left(\frac{k_0R}{2} + \mathrm{e}\right)} \\ &- \frac{c_{0,j}^\mathrm{D}k_0R\ln(k_0R) + c_{1,j}^\mathrm{D}k_0R + c_{2,j}^\mathrm{D}(k_0R)^2}{1 + c_{3,j}^\mathrm{D}k_0R + c_{4,j}^\mathrm{D}(k_0R)^2}, \\ g^\mathrm{L}(k_0R) &= \frac{1}{m_j^\mathrm{L}}\sqrt{\pi k_0R + (m_j^\mathrm{L})^2} \\ &- \frac{c_{0,j}^\mathrm{L}k_0R\ln k_0R + c_{1,j}^\mathrm{L}k_0R + c_{2,j}^\mathrm{L}(k_0R)^2}{1 + c_{3,j}^\mathrm{L}k_0R + c_{4,j}^\mathrm{L}(k_0R)^2}, \\ g^\mathrm{m}(k_0R) &= 1 - \frac{1.5}{a+1}\left(\frac{k_0R}{k_0R + \alpha m_j^\mathrm{D}/m_j^\mathrm{L}}\right. \\ &\left. - \frac{k_0R}{k_0R + \beta m_j^\mathrm{D}/m_j^\mathrm{L}}\right), \\ g^\mathrm{B}(k_0R) &= 1 + \frac{1}{a}\sqrt{\pi\ln(k_0R + \mathrm{e})m_j^\mathrm{L}/m_j^\mathrm{D}}, \end{aligned}$$

Table 3. Constants for calculation of the trapping factor for discharge with cylindrical geometry (according to [29]).

i	0	1	2	3	4
$c^{\mathrm{D}}_{i,0}$	-4.447×10^{-3}	2.464×10^{-1}	-2.139×10^{-4}	1.650×10^{-2}	6.570×10^{-6}
$c^{\mathrm{L}}_{i,0}$	1.204×10^{-1}	8.738×10^{-1}	-3.321×10^{-3}	1.877	1.166×10^{-1}
m^{D}_0	8.889×10^{-1}				
m^{L}_0	1.1227				
α	4				
β	12				

$$g^{\mathrm{A}}(k_0R) = g^{\mathrm{L}}\left(\frac{k_0R}{a\sqrt{\pi}}\right) \Big/ g^{\mathrm{B}}(k_0R),$$

$$\frac{1}{g^{\mathrm{V}}(k_0R)} = \frac{\mathrm{e}^{-g^{\mathrm{A}^2}(k_0R)}}{g^{\mathrm{D}}(k_0R)}\left(1 - \frac{\sqrt{\pi}}{2}\frac{g^{\mathrm{A}}(k_0R)}{(1+k_0R/m^{\mathrm{D}}_j)^2}\right) + \frac{\mathrm{erf}[g^{\mathrm{A}}(k_0R)]}{g^{\mathrm{L}}[k_0R/(a\sqrt{\pi})]g^{\mathrm{m}}(k_0R)},$$

$$\Lambda^{\mathrm{V}}(k_0R) = \frac{1}{g^{\mathrm{V}}(k_0R)}. \tag{25}$$

In these equations k_0 is the absorption coefficient at the line centre, R the discharge radius and a the damping constant. $c^X_{i,j}$ and m^X_j are coefficients associated with the eigenfunction (or mode j) constituting the spatial dependence of the concentration of the excited state. The coefficients for the lowest mode ($j = 0$), as the only one, which was taken into account, and for cylindrical geometry, are listed in table 3. Constants α and β were determined by discharge geometry (see also table 3). In our calculations the Voigt profile was assumed and the damping constant a was calculated from the FWHMs (full widths at half of the maximum) of Doppler, Stark, natural and resonance broadening.

2.5. Comparison of the spectra

The measured spectrum and the spectra calculated for various values of E/N were compared in order to determine the E/N. Usually, for the determination of E/N the ratio of two spectral line intensities is used to avoid difficulties in absolute intensity measurements [30]. However, in order to achieve a reasonable sensitivity of this intensity ratio to the plasma parameters, a large difference in the excitation energies of the upper states of the two spectral lines used is needed. This requirement is in contrast to the availability of reliable cross-section data for highly excited levels. Moreover, under conditions studied in this paper (low reduced electric field strength) the lines originating from highly excited levels were not present in the measured spectrum and only the lines from $2p_i$ states with a small energy spread of 0.6 eV could be studied. Thus, more lines ($n = 16$–20) were taken in the analysis. Assuming I_k and L_k for the measured and calculated intensity of line k, respectively, the spectra were compared on the basis of the least-squares sum

$$\mathcal{S} = \sum_{k=1}^{n}(\mathcal{F}\cdot L_k(E/N, n_{\mathrm{e}}) - I_k)^2, \tag{26}$$

where $\mathcal{F}$ is the scaling factor, adjusting the relative intensities of the spectra. If we define a function $\mathcal{L}$ as

$$\mathcal{L}(\lambda_k;\, E/N, n_{\mathrm{e}}, \mathcal{F}) = \mathcal{F}\cdot L_k(E/N, n_{\mathrm{e}}), \tag{27}$$

then the parameters E/N, n_{e} and $\mathcal{F}$ can be found by fitting the function $\mathcal{L}$ to the data

$$\{[\lambda_k, I_k],\ k = 1, \ldots, n\}. \tag{28}$$

The number of lines n ranged from 14 for the spectrum measured at a high electric field to 20 lines at a low electric field. The Marquardt–Levenberg algorithm of the least-squares method was used for fitting in order to minimize the time of calculation.

3. Experimental set-up

The measurements were carried out in a U-shaped Pyrex discharge tube with a total length of 590 mm. The central part of the discharge tube, 390 mm long, was equipped with Pyrex head-on-windows. The inner diameter of this part was 24 mm. The discharge tube was filled up to the working pressure of 1.1 Torr with spectrally pure neon produced by Moravské Chemické Závody Ostrava. The amount of impurities was below 10 ppm.

The U-shaped discharge tube enabled us to investigate the spectral line intensities of the discharge in the central part of the tube at the tube axis. The emitted light, averaged over the central part, was imaged by a positive lens onto a quartz fibre and analysed by a Jobin Yvon-Spex Triax 550 monochromator (focal length 550 mm) equipped with a plane grating (1200 grooves mm^{-1}) and a thermoelectrically cooled MTE CCD 1024×256-16 detector. The spectra were measured in the spectral range 300–850 nm for six values of discharge current.

The axial electric field strength was measured by a double probe method. The fixed probes were made from a platinum wire 100 μm in diameter and 3 mm in length. The active region of the probes was immersed into the positive column perpendicularly to the axis of the central part of the tube at the distance of 15 mm. The probe technique was also used to determine the electron concentration.

The optical system was calibrated with a Pencil style 6035 Hg(Ar) lamp produced by Oriel Instruments, operating in the dc mode at 18 mA. The irradiances of selected lines were taken from [31]. Due to the practically constant dependence of the quantum efficiency of our instrument on the wavelength (with error no more than 4%) in the measured range 560–750 nm, this calibration was extended to wavelengths higher than that provided by the lamp. Therefore, the relative intensities of the neon lines were determined with uncertainties of about 15% and even higher at wavelengths above 600 nm.

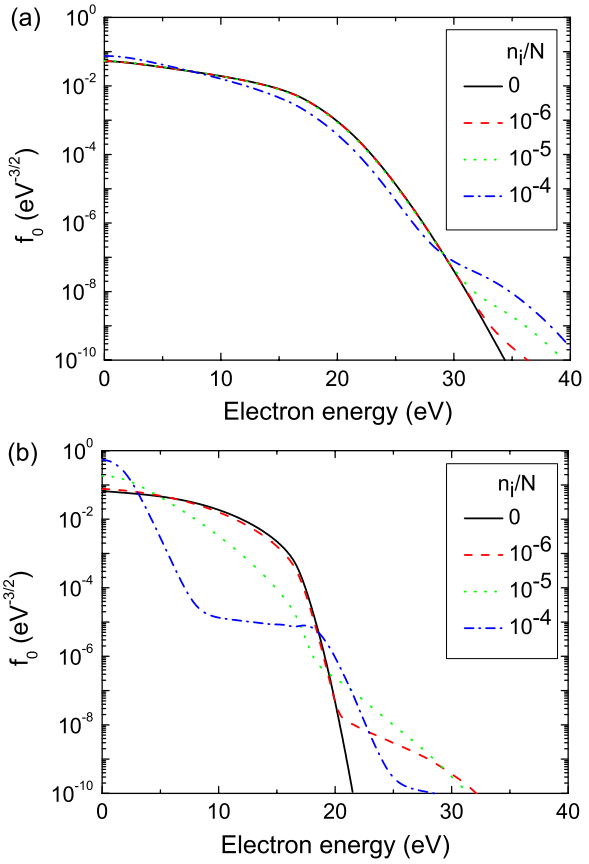

Figure 3. The isotropic part of EDF for reduced electric field strengths (*a*) $E/N = 12$ Td and (*b*) $E/N = 2$ Td and various relative concentrations n_i/N of individual $2p^53s$ states. The concentrations of all states of $2p^53s$ configuration are assumed to have the same value.

4. Results and discussion

The isotropic part of the EDF $f_0(\varepsilon)$ is shown for reduced electric field strengths 12 and 2 Td in figure 3. The effect of processes, in which neon atoms in the excited states of the $2p^53s$ configuration participate, on the EDF is documented by plots of the EDF for various concentrations of excited states. Since the de-excitation collisions accelerate the electrons, the increase in the concentration of the excited atoms is manifested in the increase in the number of energetic electrons in the tail of the EDF. In contrast, the excitation collisions of electrons with the atoms in $2p^53s$ states (of large collision cross sections) and ionization collisions with the metastables further increase the proportion of low energetic electrons in the EDF in comparison with the inclusion of excitation and ionization collisions out of the ground state only. As can be seen in the figure, the EDF seems to be much more sensitive to these processes at a lower value of reduced electric field strength. However, at a low electric field the relative concentrations of excited states, which were used in the calculations, are hardly attainable. The influence of electron–electron collisions on the EDF was found to be negligible under our experimental conditions (ionization degree $\sim 10^{-8}$, $n_e \sim 10^8$ cm^{-3}). These results are in agreement with the calculations presented for argon in [32] or for helium in [33].

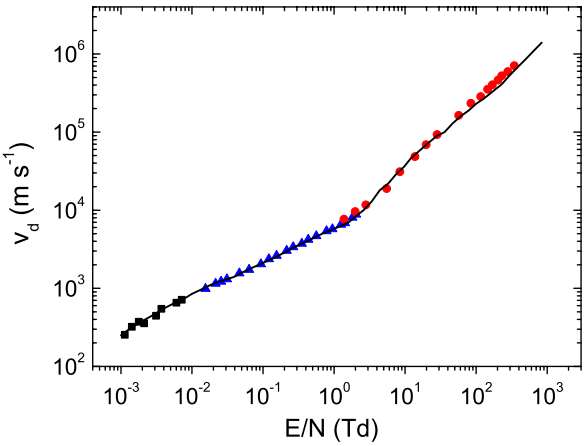

Figure 4. Calculated drift velocity v_d plotted as a function of reduced electric field strength E/N. The calculated curve (——) is compared with the experiments (■) [34], (▲) [35] and (●) [36].

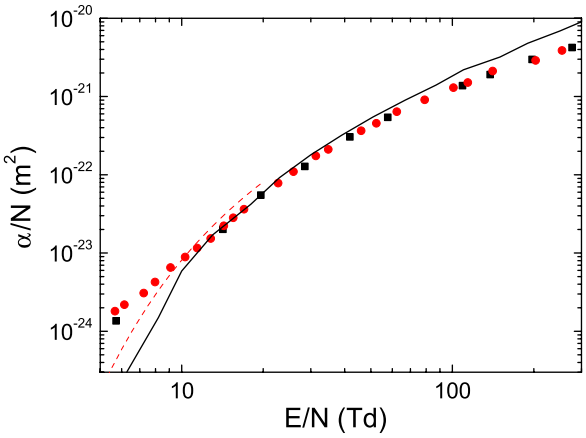

Figure 5. The calculated reduced Townsend ionization coefficient α/N as a function of the reduced electric field strength E/N for two different solutions of the Boltzmann kinetic equation: (——) without incorporation of excited states, (- - - -) with incorporation of excited states. The calculated curves are compared with the experiments (■) [37] and (●) [38].

The accuracy of the calculated EDF and of the used cross-section data was tested by a comparison of the transport parameters (calculated as the moments of EDF) with their experimental values. The dependence of drift velocity v_d on the reduced electric field strength is shown in figure 4. Close agreement of the calculated curve with the experimental data can be observed. However, as noted already in [11] and verified again by changing the cross-section set (not shown here), the drift velocity is less sensitive to excitation cross-section data.

A similar comparison of the reduced Townsend ionization coefficient, which was calculated as $\alpha/N = k_{ion}/v_d$, is shown in figure 5. The calculations are in agreement with the experimental data at middle reduced electric field strengths (10–100 Td). The discrepancy at higher values is particularly due to the limited electron energy range (up to 200 eV) of the used excitation cross sections, but such a discrepancy is unimportant for the diagnostics of the positive column plasma being studied in this paper. The discrepancy in the Townsend ionization coefficient at a low reduced electric field may be improved, aside from the explanation based on the

Table 4. Comparison of the calculated values of E/N determined from Fit 1 (cross-section set No. 1) and Fit 2 (cross-section set No. 2) with the results of probe measurement. The error estimates were calculated for the confidence level of 68.3 %.

Spectrum no.	Current (mA)	E/N (Td)		
		Measured	Fit 1	Fit 2
1	5	12.9 ± 1.2	12.4 ± 5.5	8.5 ± 4.3
2	10	8.1 ± 0.8	10.7 ± 3.9	5.6 ± 2.5
3	15	6.6 ± 0.7	8.6 ± 2.8	3.3 ± 3.1
4	20	6.2 ± 0.6	8.5 ± 2.7	4.7 ± 3.1
5	25	5.8 ± 0.6	8.7 ± 2.7	7.0 ± 3.2
6	30	5.3 ± 0.5	8.3 ± 2.5	6.9 ± 3.1

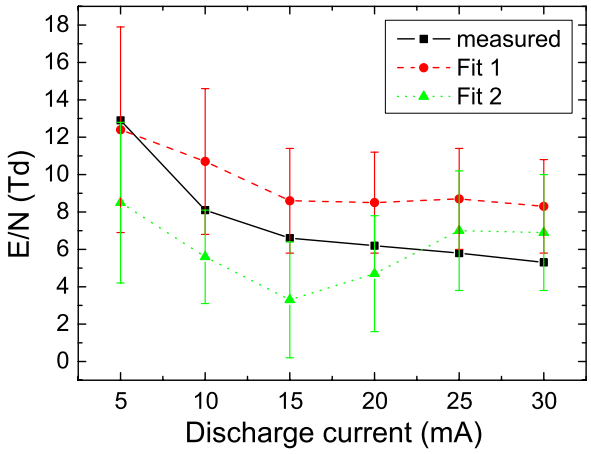

Figure 6. The reduced electric field strength versus the discharge current determined from Fit 1 and Fit 2 with different cross-section sets in comparison with the experimental data from the probe measurement.

overestimation of experimental data [11], by using the EDF, which was calculated with the excited states taken into account (see the dashed curve in figure 5). However, the collisional–radiative model is needed to determine the concentrations of excited atoms in such calculations.

The calculated values of the reduced electric field strength, determined from Fit 1 and Fit 2 with different cross-section sets No. 1 and No. 2 (described in section 2.3), are given together with the experimental data in table 4 and they are shown as functions of the discharge current in figure 6. The electron concentration was not found from the fits, since the ratios of the line intensities in the calculated spectra did not depend on the electron concentration significantly. The electron concentration acted only as another scaling factor and thus it was strongly correlated with the scaling factor $\mathcal{F}$. The measured values of the electric field strength generally lie within the confidence intervals determined from both fits, which were calculated for the probability level of 68.3%. Comparing the two fits, Fit 1 gives closer agreement with the experimental values, particularly at higher electric field (12 Td). At lower electric fields the agreement is worse, since the direct excitation becomes less intensive at a lower electric field and the model used thus becomes less sensitive. This was improved by the inclusion of the stepwise excitation through the states of the $2p^5 3s$ configuration in Fit 2. However, it was found that the total sum of the squares determined from Fit 2 was not reduced substantially and in some cases the sum was

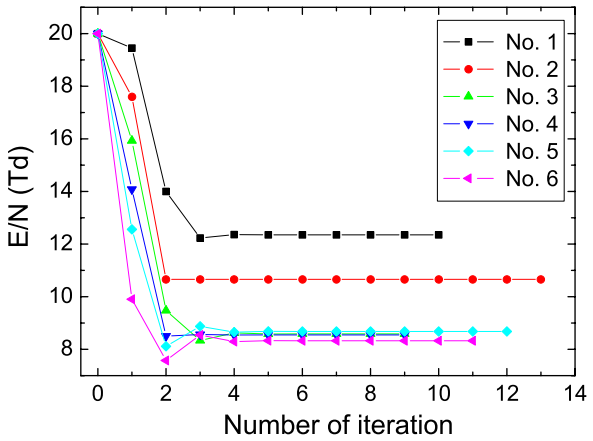

Figure 7. The example of the reduced electric field strength development during the iterations of the Marquardt–Levenberg algorithm on different spectra no. 1–6.

even higher than that of Fit 1. This result may be caused by various factors. The uncertainty of the collision cross sections of the $2p^5 3s$–$2p^5 3p$ excitation measured in [16] is about ±30% and the results of various authors differ even by a factor of 3. (The error of direct excitation cross sections is up to ±36% [14].) Furthermore, the omission of optically forbidden excitations may play some role, since these optically forbidden excitations may be due to the excitation functions with sharp maxima at low electron energies of significant importance at a low electric field. Finally, the uncertainty of the populations of $2p^5$ 3s states is also included in the calculated spectra through the stepwise excitation. For example, the error of cross sections for excitation from the ground state to the $1s_4$ and $1s_2$ states was estimated to be ±20% [13] and the other uncertainty is caused, e.g., by errors in Einstein coefficients and approximate description of resonance radiation trapping.

The example of the development of electric field strength during the iterations of the Marquardt–Levenberg algorithm on different spectra is shown in figure 7. The initial value of E/N was set in all cases to 20 Td; the electron concentration was fixed at 10^8 cm^{-3} according to the experimental data. The iteration mostly tended to the resultant value after several (≈10) steps of the Marquardt–Levenberg algorithm. The examples of the fitted spectra are shown in figure 8. The solid line represents the measured spectrum, corrected in accordance with the spectrometer sensitivity, and the arrows denote the results of Fit 1. The fitted and measured intensities of spectral lines are generally in close agreement, with the exception of the lines in the red end of the spectrum. Since the lines 703.24, 724.52 and 743.89 nm start in the same upper state $2p_{10}$, their intensities should be approximately in the proportion of their Einstein coefficients. Since this is not observed in the measured spectrum, the discrepancy in the measured and calculated intensities is probably due to the overestimation of the measured intensities in the spectrum correction. The measured and the calculated intensity of the spectral line at 614.34 nm are obviously different as well. The upper level of the 614.34 nm transition was also populated by excitation out of the $1s_5$ level, so a large calculated intensity may arise, e.g., from an overestimation of the metastable atoms density (which can be expected due to the not fully included depopulation, e.g., by heavy-particle collisions).

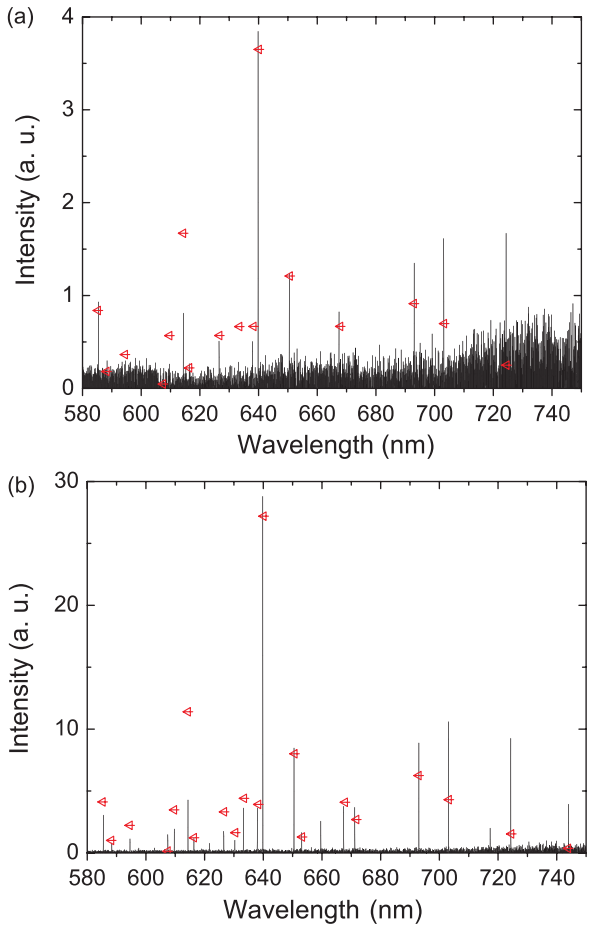

Figure 8. The examples of the measured spectra and the results of the fitting procedure shown by arrows (⋖–). (*a*) Spectrum no. 1 and (*b*) spectrum no. 5.

5. Conclusion

The collisional–radiative model of the neon discharge was developed in order to determine the reduced electric field strength in the positive column of the low pressure dc glow discharge. The optical emission spectra, which were compared by the least-squares fitting method with the resultant spectra of the collisional–radiative model, were measured in the positive column of the discharge for six values of the discharge current. Furthermore, independent measurements of the electric field by electric probes were performed.

In the collisional–radiative model populations of 30 excited levels of the neon atom were studied. A number of elementary processes were taken into account: electron impact excitation, de-excitation and ionization of neon atoms, emission and absorption of radiation, metastable–metastable collisions, metastable and radiative dimer production, Penning ionization, etc. The electrons were characterized by the EDF in the two-term approximation, which was determined for a given E/N by the solution of the Boltzmann kinetic equation. The steady state values of populations of excited states were found by the solution of their rate equations by the Runge–Kutta method. The calculated spectra were fitted by the Marquardt–Levenberg least-squares algorithm to the measured spectrum in order to determine the E/N in the discharge.

The comparison of calculated and experimental results of E/N in the positive column of the low pressure dc glow discharge shows agreement of the measured and the calculated values. The calculated E/N values ranged from 3 to 12 Td depending on the discharge current. The model sensitivity to the E/N was found to be higher for higher E/N. The aim of the next work will be to apply this method to the study of discharges, at which the determination of the E/N by electric probe diagnostics is not possible (e.g. atmospheric pressure discharges).

Acknowledgments

The work was supported by the research project MSM0021622411 of the Ministry of Education of the Czech Republic and by grants nos 202/06/0776, 202/05/0777 and 202/06/1473 of the Czech Science Foundation. VH and AK acknowledge the support of the research project MSM 0021620834.

References

[1] van der Sijde B, van der Mullen J J A M and Schram D C 1984 Collisional radiative models in plasmas *Beitr. Plasmaphys.* **24** 447–73
[2] Behnke J F, Deutsch H and Scheibner H 1985 Investigation about stepwise excitation cross sections in rare gases *Contrib. Plasma Phys.* **25** 41
[3] Vlček J 1989 A collisional–radiative model applicable to argon discharges over a wide range of conditions: I. Formulation and basic data *J. Phys. D: Appl. Phys.* **22** 623–31
[4] Bogaerts A, Gijbels R and Vlček J 1998 Collisional–radiative model for an argon glow discharge *J. Appl. Phys.* **84** 121
[5] Kano K, Suzuki M and Akatsuka H 2000 Spectroscopic measurements of electron temperature and density in argon plasmas based on collisional–radiative model *Plasma Sources Sci. Technol.* **9** 314–22
[6] Smith D J, Whitehead C J and Stewart R 2002 Complementary optical diagnostics for determination of rate coefficients and electron temperature in noble gas discharges *Plasma Sources Sci. Technol.* **11** 115–26
[7] Bezanahary T, Zissis G and Salo S A S 2003 A collisional radiative model applied to the study of pure rare gas electrical discharge *IEEE Trans. Plasma Sci.* **31** 587–95
[8] Dormand J R and Prince P J 1980 A family of embedded Runge–Kutta formulae *J. Comput. Appl. Math.* **6** 19–26
[9] Van Dyck R S Jr, Johnson C E and Shugart H A 1972 Lifetime lower limits for the $3P_0$ and $3P_2$ metastable states of neon, argon, and krypton *Phys. Rev.* A **5** 991–3
[10] Martin W C *et al* 2004 NIST Atomic Spectra Database http://physics.nist.gov/asd.
[11] Puech V and Mizzi S 1991 Collision cross sections and transport parameters in neon and xenon *J. Phys. D: Appl. Phys.* **24** 1974–85
[12] Tsurubuchi S, Arakawa K, Kinokuni S and Motohashi K 2000 Electron-impact cross sections of Ne *J. Phys. B: At. Mol. Opt. Phys.* **33** 3713–23
[13] Tsurubuchi S 2003 Electron-impact cross sections of Ne, private communication
[14] Chilton J E, Stewart M D Jr and Lin C C 2000 Electron-impact excitation cross sections of neon *Phys. Rev.* A **61** 052708-1
[15] Stewart M D Jr, Chilton J E, Boffard J B and Lin C C 2002 Use of radiation trapping for measuring electron-impact excitation cross sections for higher resonance levels of rare-gas atoms *Phys. Rev.* A **65** 032704-1
[16] Boffard J B, Keeler M L, Piech G A, Anderson L W and Lin C C 2001 Measurement of electron-impact excitation

cross sections out of the neon $^3P_2$ metastable level *Phys. Rev.* A **64** 032708
[17] Leveau J, Valignat S and Deigat F 1977 Destruction par chocs électroniques des atomes métastables et pseudo-métastables de néon dans une colonne positive *J. Physique Lett.* **38** L385
[18] Hyman H A 1981 Electron impact excitation cross sections for the transition $(n-1)p^5\,ns \rightarrow (n-1)p^5\,np$ in the rare gases *Phys. Rev.* A **24** 1094–5
[19] Boffard J B 2005 Electron-impact excitation cross sections out of the neon $1s_3$ and $1s_5$ level Private communication
[20] Rapp D and Englander-Golden P 1965 Total cross sections for ionization and attachment in gases by electron impact: I. Positive ionization *J. Chem. Phys.* **43** 1464–79
[21] Wetzel R C, Baiocchi F A, Hayes T R and Freund R S 1987 Absolute cross sections for electron-impact ionization of the rare-gas atoms by the fast-neutral-beam method *Phys. Rev.* A **35** 559–77
[22] Johnston M, Fujii K, Nickel J and Trajmar S 1996 Ionization of metastable neon by electron impact *J. Phys. B: At. Mol. Opt. Phys.* **29** 531–43
[23] Seaton M J 1998 Oscillator strength in Ne I *J. Phys. B: At. Mol. Opt. Phys.* **31** 5315–36
[24] Bogaerts A and Gijbels R 1997 Comparison of argon and neon as discharge gases in a direct-current glow discharge: a mathematical simulation *Spectrochim. Acta B* **52** 553–65
[25] Phelps A V 1959 Diffusion, de-excitation and three-body collision coefficients for excited neon atoms *Phys. Rev.* **114** 1011–25
[26] Leichner P K 1973 Time and pressure dependence of the vacuum-ultraviolet radiation in neon *Phys. Rev.* A **8** 815–22
[27] Ricard A 1996 *Reactive Plasmas* (Paris: SFV)
[28] Holstein T 1947 Imprisonment of resonance radiation in gases *Phys. Rev.* **72** 1212–33
[29] Molisch A F, Oehry B P, Schupita W and Magerl G 1993 Radiation-trapping in cylindrical and spherical geometries *J. Quant. Spectrosc. Radiat. Transfer* **49** 361–70
[30] Boffard J B, Lin C C and DeJoseph C A Jr 2004 Application of excitation cross sections to optical plasma diagnostics *J. Phys. D: Appl. Phys.* **37** R143–61
[31] Reader J, Sansonetti C J and Bridges J M 1996 Irradiances of spectral lines in mercury pencil lamps *Appl. Opt.* **35** 78–83
[32] Hagelaar G J M and Pitchford L C 2005 Solving the Boltzmann equation to obtain electron transport coefficients and rate coefficients for fluid models *Plasma Sources Sci. Technol.* **14** 722–33
[33] Capriati G, Colonna G, Gorse C and Capitelli M 1992 A parametric study of electron distribution functions and rate and transport coefficients in nonequilibrium helium plasmas *Plasma Chem. Plasma Process.* **12** 237–60
[34] Pack J L and Phelps A V 1961 Drift velocities of slow electrons in helium, neon, argon, hydrogen and nitrogen *Phys. Rev.* **121** 798–806
[35] Robertson A G 1972 The momentum transfer cross section for low energy electrons in neon *J. Phys. B: At. Mol. Phys.* **5** 648–64
[36] Kücükarpaci H N, Saelee H T and Lucas J 1981 Electron swarm parameters in helium and neon *J. Phys. D: Appl. Phys.* **14** 9–25
[37] Chanin L M and Rork G D 1963 Measurements of the first Townsend ionization coefficient in neon and hydrogen *Phys. Rev.* **132** 2547–53
[38] Kruithof A A and Penning F M 1937 *Physica* **4** 430

IOP PUBLISHING JOURNAL OF PHYSICS D: APPLIED PHYSICS

J. Phys. D: Appl. Phys. **43** (2010) 505203 (11pp) doi:10.1088/0022-3727/43/50/505203

Determination of electron density and temperature in a capacitively coupled RF discharge in neon by OES complemented with a CR model

Z Navrátil[1], P Dvořák[1], O Brzobohatý[2] and D Trunec[1]

[1] Department of Physical Electronics, Faculty of Science, Masaryk University, Kotlářská 2, 611 37 Brno, Czech Republic

[2] Institute of Scientific Instruments of the ASCR, v.v.i., Academy of Sciences of the Czech Republic, Královopolská 147, 612 64 Brno, Czech Republic

E-mail: zdenek@physics.muni.cz

Received 21 July 2010, in final form 19 October 2010
Published 2 December 2010
Online at stacks.iop.org/JPhysD/43/505203

Abstract

A method of determination of electron temperature and electron density in plasmas based on optical emission spectroscopy complemented with collisional–radiative modelling (OES/CRM) was studied in this work. A radiofrequency (13.56 MHz) capacitively coupled discharge in neon at 10 Pa was investigated by intensity calibrated optical emission spectroscopy. The absolute intensities of neon transitions between 3p and 3s states were fitted with a collisional–radiative (CR) model in order to determine the electron temperature and electron density. Measuring techniques such as imaging with an ICCD camera were adopted for supplementary diagnostics. The obtained results were compared with the results of compensated Langmuir probe measurement and one-dimensional particle-in-cell/Monte Carlo (PIC/MC) simulation.

The results of OES/CRM and PIC/MC method were in close agreement in the case of electron temperature in the vicinity of a driven electrode. The determined value of electron temperature was about 8 eV. In bulk plasma, the measured spectra were not satisfactorily fitted. In the case of electron density only relative agreement was obtained between OES/CRM and Langmuir probe measurement; the absolute values differed by a factor of 5. The axial dependence of electron density calculated by PIC/MC was distinct from them, reaching the maximum values between the results of the other two methods. The investigation of power dependence of plasma parameters close to the driven electrode showed a decrease in electron temperature and an increase in electron density together with increasing incoming RF power. The calculated spectra fitted very well the measured spectra in this discharge region.

(Some figures in this article are in colour only in the electronic version)

1. Introduction

Radiofrequency (RF) capacitively coupled discharges are widely used in industrial applications for thin film deposition, etching, cleaning, surface modification, in high power lasers, as analytical sources, light sources, etc [1]. However, precise measurement of the basic plasma parameters such as electron density and electron temperature or electron distribution function is still demanded. Although the use of Langmuir probe in RF discharges is well established, it is still limited to low-pressure plasmas, risking the plasma disturbance and suffering with low signal-to-noise ratio for highly energetic electrons, which have a low concentration but high impact on plasma processes. On the other hand, optical emission spectroscopy (OES) seems to overcome all these drawbacks. However, in order to derive the plasma parameters

from the measured optical emission spectra, a relatively complicated collisional–radiative (CR) modelling is generally needed.

In the case of rare gases, the capacitively coupled RF discharge has been extensively studied in helium and argon, but less often in neon. Electron distribution function (EDF) has previously been measured with a Langmuir probe in argon and helium [2]. Anisotropy of electron energy distribution function was measured by an electrostatic energy analyser in asymmetric helium RF discharges [3]. Thomson light scattering was adopted for low electron temperature and density measurement in helium RF discharges [4]. Transition between α and γ mode of RF discharges in argon was investigated in [5]. Time-averaged axial potential profile was measured with the electrostatic probe in symmetric RF discharge in neon [6]. Paper [7] compared EDFs measured in a discharge centre at different pressures (0.1–0.8 Torr) in neon, argon and xenon. EDF in capacitive RF discharges in molecular gases was also investigated (see e.g. [8, 9] for nitrogen).

The cited papers show the necessity of knowledge of EDF for understanding capacitive discharges, including understanding of heating mechanisms and prediction of reactions induced by electron collisions. Further important information concerning the physics of capacitively coupled discharges can be obtained by methods that enable measurements with a high temporal resolution. Uncompensated electric probes enable measurement of plasma potential changes occurring during one RF period [10, 11]. OES with a high temporal resolution brings an illustrative look into the processes occurring in each RF period, including discharge heating in α and γ modes [12], generation of electron beams by sheath expansion [13] and field reversal during sheath collapse [14]. Despite the fact that these measurements brought numerous facts on the time development of capacitive discharges, they did not provide information concerning EDFs, electron concentration or temperature. Therefore, measurement of EDFs based on OES, which is noninvasive and potentially enables a high temporal resolution, is still desired.

Computer simulation, especially CR modelling, has become widely used for diagnostics of various types of discharges [15–17]. The method of electron temperature measurement based on a CR model for argon was reported, e.g., in [18]. Trace rare gases optical emission spectroscopy (TRG-OES), based on the addition of a small admixture of rare gas into the studied plasma and evaluation of plasma parameters from the best fit between the measured and CR model calculated relative emission intensities, was reviewed in [19]. Comparative diagnostics of helium and argon microwave plasmas at a pressure of 1–5 Torr utilizing CR model, OES and probe measurement was published in [20]. Statistical analysis of reconstruction of EDF in the positive column of neon dc discharge from the emission spectra was presented in [21]. Application of particle-in-cell/Monte Carlo method (PIC/MC) for investigation of plasma was published in [22–24].

In this work a method of the determination of electron temperature and density from temporally averaged optical emission spectra is developed for neon plasma and compared with the results from Langmuir probe measurement and PIC/MC simulation. The paper is organized as follows: details of experimental apparatus, OES and Langmuir probe diagnostics are given in section 2. CR model and PIC/MC approach are described in sections 3 and 4, respectively. The results obtained with the above mentioned methods are presented, compared and discussed in section 5. Conclusions are given in section 6.

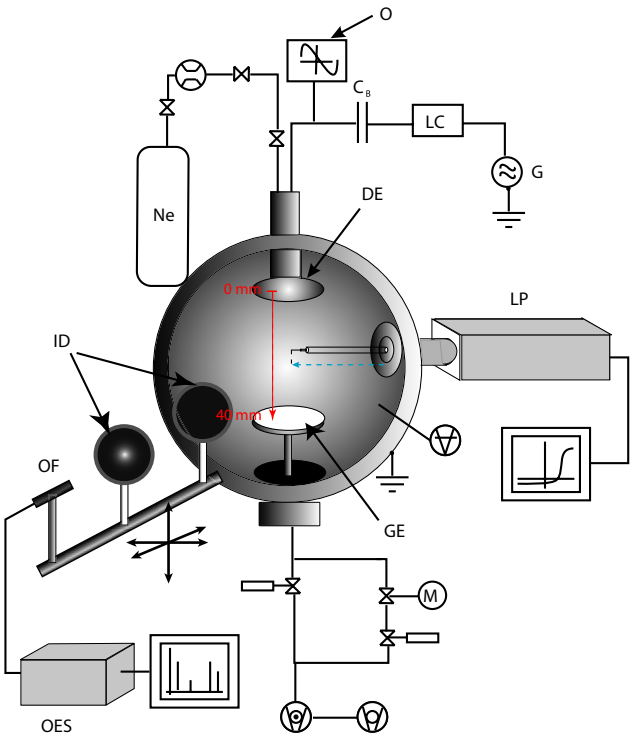

Figure 1. The scheme of experimental set-up: DE and GE—driven and grounded movable electrode, G—13.56 MHz generator, O—oscilloscope, OF—optical fibre, ID—iris diaphragms, OES—Jobin Yvon FHR 1000 spectrometer, LP—Langmuir probe.

2. Experimental set-up

The schematic of the experimental set-up is displayed in figure 1. The RF discharge was generated in a grounded stainless-steel vacuum chamber with an inner diameter of 33 cm. Two parallel plate circular electrodes with a diameter of 80 mm were placed 40 mm apart. The upper electrode (located at position 0 mm), embedded in a grounded ring, was capacitively coupled to a RF sinusoidal voltage generator (13.56 MHz, maximum power 50 W, maximum applied voltage 470 V_{pp}). The lower electrode (located at position 40 mm) was grounded. The dc self-bias on the powered electrode varied within −130 to −300 V showing an asymmetry of the discharge.

The vacuum chamber was pumped down using a turbomolecular pump to an ultimate pressure of 5×10^{-5} Pa and then filled with neon gas of research purity 5.0 up to pressures of 5–15 Pa. The discharge was sustained in flowing regime with gas flow rate approximately 5 sccm. The butterfly valve

between the chamber and the pump controlled the pumping speed, allowing the pressure to be set independently of the flow rate. The pressure in the chamber was measured by a MKS Baratron. A large window, with diameter 7 cm, enabled the observation of the discharge.

2.1. Langmuir probe measurement

Electron energy distribution function, electron concentration, mean electron energy and mean (dc) plasma potential were measured using a compensated Langmuir probe (ESPion, Hiden Analytical). The probe consisted of a 1 cm long platinum wire, radius 190 μm, connected to a control unit and computer. RF voltage including higher harmonic frequencies was passively compensated [25]. Eventual disturbance of plasma potential due to high sheath resistivity was compensated by means of a reference probe [26]. Electron energy distribution functions were calculated from a second derivative of the probe characteristics by the well-known Druywestein formula. If EDFs had Maxwellian shape, the electron concentration and mean energy were calculated from a linear fit to a logarithm of measured probe characteristics in order to exclude the impact of noise produced by numerical calculation of the second derivative. Analogically, when it was possible to describe EDF by so-called general distribution, an appropriate function was fitted to the logarithm of the measured data. The general distribution f_g is described by the relation

$$f_g(E) = C_g\, n_e\, E^{1/2} \exp\left\{-\frac{E^\kappa}{2\kappa\, E_p^\kappa}\right\}$$

where n_e, E and E_p are the electron concentration, energy and the most probable energy, respectively. C_g is a constant depending only on E_p and κ. κ describes the shape of the EDF. For $\kappa = 1$ or $\kappa = 2$ the general distribution is identical to Maxwellian or Druywestein distribution, respectively. When EDFs had another shape, electron concentration and mean energy were calculated by integration of EDFs obtained by the Druywestein formula. At the pressure 10 Pa the measured EDFs were similar to Maxwellian EDF. The statistical error of electron temperature and density determined from repeated probe measurement was below 5% and 4%, respectively.

2.2. Optical emission spectroscopy

The emission of radiation from the discharge was studied by optical spectroscopy in the UV/VIS spectral range (300–750 nm). The spatial resolution of the measurement was achieved by two iris diaphragms, mounted with optical fibre on a movable table in front of the chamber window. The light coming from a narrow cone going through the whole discharge diameter, but with a distinct axial position between the electrodes, was taken out with the diaphragms and optical fibre and analysed with a Jobin Yvon FHR 1000 spectrometer with a CCD detector (focal length 1 m, grating 2400 gr mm^{-1}). The spectra were integrated over many periods of RF signal. An Oriel tungsten halogen lamp was used to calibrate the fibre irradiance. Original uncertainty of the lamp intensity was 2%. A new recalibration with 5% uncertainty revealed as much as 10% difference in the calibrations.

The emission coefficient ϵ_{ij} of specific transition $i \to j$, integrated over the lineshape, was derived from the fibre irradiance. If the cylindrical symmetry of plasma with uniform radial profile for region between the electrodes can be assumed

$$\epsilon_{ij}(r) = \begin{cases} \epsilon_{ij}, & r \leqslant R, \\ 0, & r > R, \end{cases}$$

where ϵ_{ij} is the emission coefficient of unit discharge volume defined as

$$\epsilon_{ij} = \frac{1}{4\pi} n_i A_{ij} \Lambda_{ij} \hbar\omega_{ij},$$

where n_i is the population of excited state i, A_{ij} and Λ_{ij} Einstein coefficient and so-called escape factor of spontaneous emission, respectively, and $\hbar\omega_{ij}$ is the corresponding photon energy, then the irradiance of the optical fibre ('detector') is

$$I_{ij} = \frac{1}{S_{det}} \int_{V_{pl}} \int_{S_{det}} \frac{\epsilon_{ij}(r)}{\rho^2} \mathrm{Acc}(\theta)\, \mathrm{d}V_{pl}\, \mathrm{d}S_{det},$$

where ρ is the distance of the plasma element $\mathrm{d}V_{pl}$ from the detector part $\mathrm{d}S_{det}$, θ is the angle of incidence and $\mathrm{Acc}(\theta)$ represents the fibre acceptance function, determined experimentally. The escape factor Λ_{ij} approximates the reduction of emitted photons due to reabsorption [27, 28]. Under the above-mentioned considerations the emission coefficient can be taken out from the integral. In our case, the plasma region contributing through the iris diaphragms to the irradiation of fibre aperture was assumed to have a cylindrical shape with length $2R = 110$ mm and diameter 5 mm. Constant value of emission coefficient along this length and diameter was assumed and taken into calculations.

Supplementary temporally and spatially resolved, but spectrally unresolved, measurement of discharge emission of radiation was carried out with an intensified CCD camera PI-MAX 1024RB-25-FG-43, controlled by a ST-133 controller and working in image mode. The temporal resolution was 5 ns and the spatial resolution 0.3 mm.

3. Collisional–radiative model

The CR model used in this work was described in detail in [29], where a method of determination of reduced electric field strength in the positive column of neon dc glow discharge was developed. Basically, comparing the measured spectra of the discharge with the spectra calculated with the CR model by the least-squares method, the plasma parameters as reduced electric field strength, electron temperature or electron density may be determined from the best fit.

In this work, Maxwellian electron distribution function (Maxwellian EDF) was assumed for calculation of rates of collisional processes. Other distribution functions, such as, so-called, bi-Maxwellian EDF, general EDF f_g, or product of PIC/MC simulation could be included in the calculations. The comparison between the measured and calculated spectra was performed on the basis of $1/I$-weighted sum of squares, where I stands for intensity. Since the measured spectra

were determined in absolute values of emission coefficient (in $\mathrm{W\,m^{-3}\,sr^{-1}}$), no scaling factor between the measured and calculated intensities was needed. In contrast, a strong dependence of absolute intensity on the electron density increased the sensitivity of the fit to the electron density. Twenty-six transitions of neon were taken for fitting.

In the CR model 30 excited states of neon, arising from $2p^5 3s$, $2p^5 3p$, $2p^5 4s$ and $2p^5 3d$ configurations, were considered. Various collisional, radiative and also diffusion processes were taken into account: electron impact excitation out of the ground state and 3s states and de-excitation to these states, electron impact excitation transfer between 3s levels, spontaneous emission of radiation, radiation trapping, electron impact ionization of the ground-state and metastable atoms, chemoionization, associative ionization, two-body and three-body collisions with ground-state neon atoms or diffusion of metastable-state atoms to the wall. The radiation trapping was incorporated by means of so-called trapping factors (or escape factors, respectively). In their calculations, Voigt profile with Doppler, Stark, natural and resonance broadening components was assumed for lineshapes.

The Einstein coefficients, cross-sections, rate coefficients and other data were taken primarily from [29]. The rate constants for electron impact-induced excitation transfer between 3s states were adopted from [30]. The original sources of Einstein coefficients and oscillator strengths were [31] and [32], respectively. For 3s–3p transitions, the accuracy of Einstein coefficients was below 10% (class B), the calculated oscillator strengths differed from experimental data no more than 10%, mostly they were 3% higher [32]. This is in agreement with our comparison of both data sources. However, for 3p–3d transitions, with only indirect influence on fitted 3s–3p lines, the differences between the data sources reach 30–40%. Accuracy up to 50% (class D) is reported in [31].

4. Particle-in-Cell/Monte Carlo model

One-dimensional (1D) electrostatic PDP1 code [33, 34] was modified and employed for the study of various plasma parameters of the RF discharge in neon, e.g. of spatial distribution of plasma density and EDF. The PDP1 code applied the approach of PIC/MC methods. Motion of the charged particles in the electric field was solved using the PIC method [22, 23] incorporating a self-consistent solution of the Newton motion equations

$$m_i \boldsymbol{a}_i = q_i \boldsymbol{E}, \qquad i = 1, \ldots, N,$$

where m_i, $\boldsymbol{a}_i$, q_i, $\boldsymbol{E}$ and N denote the particle mass, acceleration, charge, electric field strength and the number of charged particles in the system, respectively, together with the Poisson equation

$$\nabla^2 \varphi = -\rho/\varepsilon_0,$$

in which φ and ρ stand for the electric field potential and the charge density, respectively. The equations of motion were solved numerically employing the well-known leap-frog (explicit) method. To reduce a huge number of charged particles in the studied plasma the so-called computer particles were brought into play [22]. The number of such computer super-particles was then $\approx 10^4$.

Collisions of charged particles with the neutral atoms were considered in our model using a MC method [24, 33]. Free flight time of charged particles was calculated using the null-collision method. The initial velocities of particles, e.g. after ionization collisions, were also generated using the MC method. Elastic, excitation and ionization collisions were considered for the electrons and the elastic and charge transfer collisions for the ions. The methods briefly described above are nowadays well utilized in computer simulations of plasma [35–37].

The model system was set in accordance with the experimental set-up. It consisted of two parallel electrodes having the same diameter of 8 cm. The distance between the electrodes was set at 40 mm. One electrode was powered by RF voltage, the second electrode was grounded. The frequency f of the power source was 13.56 MHz, the voltage amplitude V_0 was 300 V. The pressure p of the neutral gas was 10 Pa or 15 Pa, respectively. Since with the 1D model a negative self-bias could not be modelled, it was introduced into the model as a boundary condition [38].

The boundaries of our computer model were given with the electrodes, where secondary electron emission and recombination occurred. Generally, secondary electron yields for incident electrons and ions, γ_e and γ_+, respectively, differ. A secondary electron yield γ_e depends on electron energy and incident angle. On the other hand a secondary electron yield γ_+ for low energetic ions, i.e. in the case of Auger emission, is dependent only on the type of ion [39, 40]. Assuming constant values γ for ions and electrons (independent of projectile energy and incident angle) the problem was simplified in our model. The distribution of initial velocities of the secondary electrons was chosen arbitrarily as half-Maxwellian with the temperature $kT = 1$ eV. The performed tests proved that this choice of initial secondary electron temperature ($kT \in 0.5$–3 eV) did not influence the results significantly (not presented in this paper).

5. Results and discussion

5.1. Axial dependence

The axial electron temperature dependences determined in the discharge at pressure 10 Pa and RF power 50 W from OES/CRM method, Langmuir probe measurement and PIC/MC simulation are shown in figure 2. In the case of OES/CRM method, two dependences are shown: with metastable densities determined from the CR model and with densities set to fixed values $1.4 \times 10^{15}\,\mathrm{m^{-3}}$ and $7.0 \times 10^{15}\,\mathrm{m^{-3}}$ for $1s_3$ and $1s_5$ states, respectively, according to absorption measurement of $1s_5$ population (not presented in this paper). The Maxwellian distribution function was assumed in these calculations. Since PIC/MC simulation generally predicted non-Maxwellian EDF, both effective temperature T_{eff} calculated as two-thirds of the mean electron kinetic energy, and T_{high} from a slope of EDF at electron

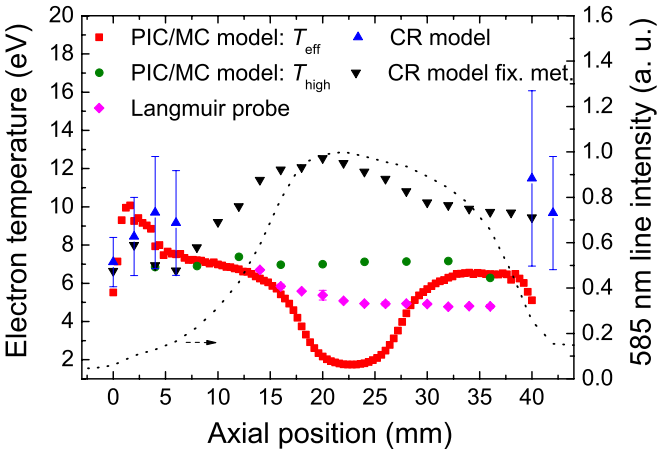

Figure 2. The electron temperature versus axial position for pressure 10 Pa as determined by various methods: PIC/MC T_{eff}, T_{high}—effective temperature determined from mean electron kinetic energy and slope of EDF at electron energies above 16 eV, respectively, Langmuir probe measurement, CR model with metastable density determined from the model, CR model with metastable density set according to absorption measurement. Axial profile of intensity of the 585 nm line (dotted line) is shown to clarify the axial position: 0 mm—driven electrode, 40 mm—grounded electrode.

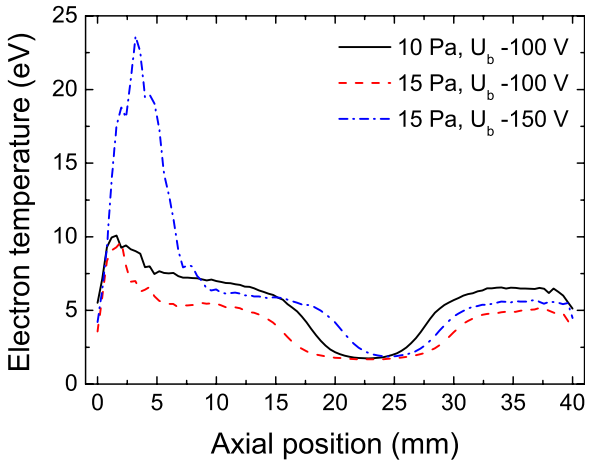

Figure 3. The electron temperature determined from PIC/MC model for pressures 10 Pa and 15 Pa and bias −100 V and −150 V, respectively. The temperature is only effective and it is calculated from the mean electron kinetic energy.

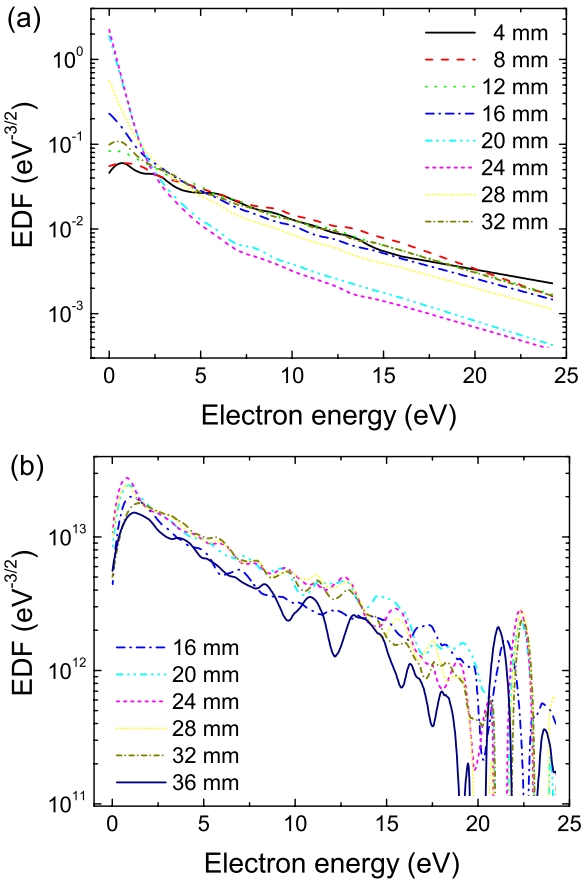

Figure 4. EDF at different axial positions, as determined from (*a*) 1D PIC/MC simulation for pressure 10 Pa and bias −100 V and (*b*) Langmuir probe measurement. The EDF determined in PIC/MC simulation was Maxwellian at the electrodes and deviated from this distribution going into the bulk plasma. The measured EDF was Maxwellian at all measured positions.

energies above 16 eV are displayed. There is obviously good agreement between OES/CRM method and PIC/MC simulation close to the driven electrode (axial position 0–7 mm in the plots). Both dependences of the OES/CRM method gave similar values of electron temperature within the error, since calculated and fixed metastable densities were of the same order. There was also a perfect agreement between the spectra measured with OES and the spectra calculated with the CR model (see section 5.2 for more information). The Langmuir probe could not be used in the RF sheath. However, going into the bulk plasma, considerable discrepancy between the measurement and simulations was observed. According to PIC/MC simulations, T_{eff} decreases to about 2 eV at positions 20–25 mm, while T_{high} stays constant at approximately 7 eV. Neither the result of OES/CRM nor of the Langmuir probe were in agreement with this prediction. Although the Langmuir probe registers particularly the development of T_{eff}, the temperature determined from the probe changes only slowly around 5 eV. The optical spectra depend mostly on T_{high}, but the electron temperature values determined from the OES/CRM method were considerably higher. Also the calculated spectra did not satisfactorily fit the measured spectra in the bulk plasma. Although PIC/MC simulation predicts electrons with a temperature about 10–20 eV under similar discharge conditions due to stochastic heating (see figure 3 and also next), they are expected just conversely close to the driven electrode.

The differences between Langmuir probe measurement and the PIC/MC model can be understood by directly comparing the EDFs (see figure 4). The PIC/MC simulation generally predicts bi-Maxwellian, or a more complicated EDF. Close to the electrode, PIC/MC expects only electrons with higher temperature, $T_{high} \approx 7$ eV, and the EDF is Maxwellian. Going into the bulk plasma a group of low energetic electrons with temperature ≈0.7 eV appears, but T_{high} remains the same, though the density of electrons with this temperature decreases. This behaviour of EDF is responsible for the development of T_{eff} observed in figure 2: T_{eff} approaches T_{high} at the

electrodes, but decreases in the middle. The EDF measured by the Langmuir probe was almost Maxwellian at all measured positions (see figure 4(*b*)). An only weakly steeper low-energy part of EDF was observed at the discharge centre (positions 20–28 mm). Consequently, the probe measurements did not confirm the bi-Maxwellian character of the EDF. However, the determination of the low-energy part of EDF by a Langmuir probe is known to suffer from several problems [2]. A large number of low-energy electrons, present in the bulk plasma, may be unregistered by the probe. For these reasons, the temperature determined from the probe measurement (see figure 2) does not follow the axial dependence of T_{eff} from PIC/MC simulation with pronounced temperature minimum in the bulk plasma.

The bi-Maxwellian EDF was first observed by Godyak *et al* [41] in argon, employing the Langmuir probe. The origin of bi-Maxwellian EDF is relatively simple. The high-temperature group of electrons gain their energy in the so-called stochastic heating process, in which interactions of electrons with the oscillating plasma sheaths are crucial. This group of electrons has enough energy to enter into inelastic collisions with neutral atoms; furthermore, these electrons can easily overcome the ambipolar potential barrier interacting, therefore, more frequently with the oscillating sheath edges [41].

On the other hand, electrons created in the ionization collisions inside the bulk of the plasma belong to the group of low-temperature electrons. These electrons oscillate in a very weak electric field presented in the bulk of the plasma and hence cannot gain energy to overcome the ambipolar potential barrier on the boundary of plasma sheath and plasma bulk, where there exists a maximal electric field and where stochastic heating takes place [39, 41–43]. Thermalization of these electrons occurs only due to the elastic collisions with neutral atoms, which become important at higher pressures.

5.1.1. Influence of EDF type. It is interesting that OES/CRM and PIC/MC methods gave similar temperature values only in the electrode region, where EDF was Maxwellian according to PIC/MC simulations. Considerable attention was therefore paid to describe the electrons of the bulk plasma in the CR model by more sophisticated EDFs. Bi-Maxwellian, general distribution function and also directly the EDF produced by PIC/MC were tested in the CR model to explain the discrepancy between the measured optical spectra and the spectra calculated for temperature expected by other methods. However, no substantial improvement was obtained. Bi-Maxwellian EDF gave a similar value of electron temperature in the high-energy region to Maxwellian EDF. Moreover, it was not possible to let the fitting algorithm change low energy temperature independently, since optical spectra are less sensitive to this parameter through stepwise excitation and de-excitation processes. General distribution function was found to describe the electrons better (evaluated by sum of squared differences in measured and fitted spectra), but only in electrode vicinity, where the deviation from Maxwellian distribution was small. As expected, the use of EDF from PIC/MC simulation did not produce optical spectra similar to the spectra observed by OES.

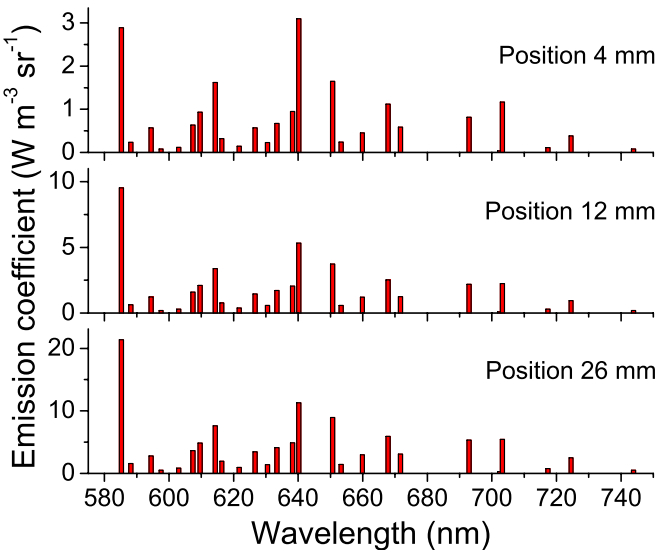

Figure 5. The dependence of measured optical spectra of neon RF discharge at pressure 10 Pa and incoming power 50 W on axial position. The line intensities were integrated over their lineshapes. Note the different scales of vertical axes.

5.1.2. Influence of metastables. In agreement with our previous work [29], the calculated intensities of 3p–3s transitions depended considerably on the populations of metastables. The influence of metastables (and of all states of 3s configuration) on the populations of 3p states is through a stepwise electron impact excitation and it is crucial at low electron energies. At higher electron energies the direct excitation from the ground state becomes the most important. This provides a sensitivity of the spectra to the electron temperature, although excitation energies of 3p states differ by 0.6 eV at most. On the other hand, this requires a reliable cross-sectional data for electron impact excitation out of the ground state to 3s states and out of 3s states. In this work a cross-section for $1s_5$–$2p_9$ transition from [44] was scaled with oscillator strength to obtain a consistent cross-section set for all optically allowed excitations out of 3s states [29]. The uncertainty of the collision cross-sections is about ±30% as determined in [44], but the results of various authors differ by as much as a factor of 3 (compare [44–46]). Moreover, reliable calculation of self-absorption of resonant lines and also of lines originating from transitions between 3p and 3s states is needed.

The dependence of the optical spectra on the axial position is shown in figure 5. Going into the bulk plasma the intensities of individual lines increase at different growth rates. Whilst at axial position 4 mm the line at 640 nm is the most intensive, the line at 585 nm dominates in the spectrum at larger axial distances. Since the upper state of the line at 585 nm ($2p_1$ in Paschen notation) is populated mainly by direct electron impact excitation from the ground state and the upper state of the line at 640 mm ($2p_9$) is populated substantially also by stepwise excitation, the increase in intensity ratio 585 nm/640 nm is interpreted by the CR model as enhancement of electron energies in the discharge middle. However, this is in strong contrast with the decrease in electron temperature predicted by the PIC/MC simulation.

The high values of electron temperature determined by the OES/CRM method in the discharge middle suggest that the relative intensities in the spectra are influenced by other processes. For example, the spectra may be influenced by the absorption of light in the outer regions of the discharge and in the vacuum chamber. Metastable atoms diffuse to the chamber wall and can selectively absorb intensities of transitions ending in metastable states. Since these transitions in the opposite direction are also stimulated by electron impact, their absorption may be misinterpreted as enhancement of direct excitation against the stepwise excitation. A simulation of spatial distribution of metastables in the discharge chamber is needed to analyse the effect of absorption. However, this distribution cannot be determined using the local CR model. For measured metastable densities the escape factor of line 640 nm is ≈0.7. The local CR model predicts even higher metastable densities and the escape factor can reach values ≈0.1. Such small values of escape factors show a large influence of the metastables on the line intensities.

5.1.3. Limitations of PIC/MC code. The 1D PIC/MC model is generally valid in cases where the separation between the electrodes is much smaller than the electrode diameters. In our case the separation was 40 mm and the diameters of the electrodes were only 80 mm. Furthermore, the 1D model is symmetric (both electrodes have the same area) and therefore no self-bias can be observed. This drawback of our PIC/MC simulation code was overcome by introducing the bias voltage artificially. The value of the bias was set to −100 V for pressure 10 Pa in simulations, which was below the experimental value. At −220 V the simulation was unstable. However, as can be seen from figure 3, the bias mostly affects the maximal electron temperature[3] of the beam electrons, but the temperature in the bulk remains approximately the same, and the minimum only shifts in the axial direction.

The discrepancy between measured and simulated EDFs in bulk plasma (the measured EDF was Maxwellian, but the simulated EDF was bi-Maxwellian) may be due to simple incorporation of inelastic collisions. Only total-excitation into 3s state was considered in the model from excitations. For example, superelastic collisions can reasonably modify the shape of EDF. However, the influence of higher excited states on EDF is usually negligible. For better agreement with the experimental data a more complex 2D or 3D model should be employed.

The comparison of determined electron density in the discharge at pressure 10 Pa is shown as a function of axial position in figure 6. The density dependence is different from the intensity development due to spatially varying electron temperature. The relative axial dependences of electron density determined by OES/CRM and the Langmuir probe are rather similar. However, they differ approximately 5× in their absolute values. This can be due to complicated estimation of spatial dependence of emission coefficient. According to optical and probe measurements of radial dependences of involved parameters (electron temperature and density,

[3] We keep using effective temperature ($k_bT = 2/3E_{mean}$), although E_{mean} would be more appropriate in this discussion.

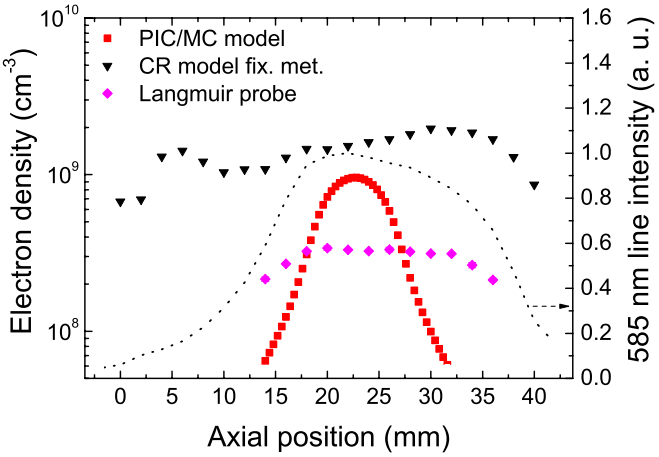

Figure 6. The electron density versus axial position as determined by various methods: PIC/MC simulation, OES/CRM method with metastable density set according to the absorption measurement and Langmuir probe measurement. Axial profile of intensity of the 585 nm line (dotted line) is shown to clarify the axial position: 0 mm—driven electrode, 40 mm—grounded electrode.

discharge intensity) a constant radial profile was assumed for the emission coefficient of plasma region of diameter 110 mm (electrode diameter was 80 mm). However, this assumption is only approximate and at 10 Pa there is still some radiation produced outside this region, which increases the measured intensity and thus also the calculated electron density. The slow decrease in electron density in the sheath observed by the OES/CRM method may also be influenced by this, as well as by reflection of light in the vacuum chamber. Another source of error in the electron concentration determination can be the overestimated absorption of radiation by overestimated concentration of 3s states (see the discussion in section 5.1.2).

The electron density simulated by the PIC/MC method reaches values between the OES/CRM and Langmuir probe results in the bulk plasma. The spatial profile of electron density simulated by the PIC/MC method is sensitive to the self-bias, which is given due to the asymmetry of the electrodes. Better agreement would be achieved by employing a more complex 2D code.

5.1.4. Influence of temporal development. The axially and temporally resolved, but spectrally unresolved, light emission of the discharge measured with the ICCD camera is displayed in figure 7. The light emission is axially and temporally inhomogeneous, although the variation of light intensity through the period is substantially smaller in neon at 10 Pa than at lower pressures [13, 14] or in other gases [14]. In our case the light emission lasted nearly the whole period. Since the light emitted from the discharge was accumulated on the CCD detector over many periods of the RF signal, the obtained results of OES/CRM were averaged over the whole period. For example, the values of electron temperature and density measured at positions close to the electrode do not reflect the conditions in the sheath only, but rather the plasma flooding the region when the sheath collapses. However, the electron temperature and density calculated from temporally integrated

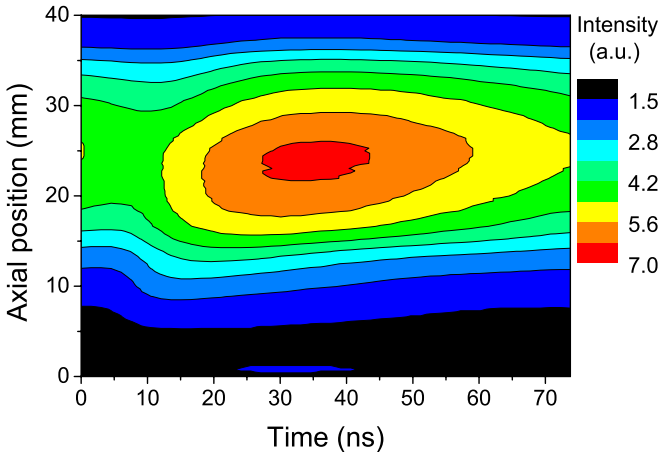

Figure 7. The axially and temporally resolved light emission of RF discharge in neon at 10 Pa, measured with ICCD camera during RF voltage period. The intensity was measured at the discharge centre. The driven electrode is at position 0 mm, grounded electrode at position 40 mm.

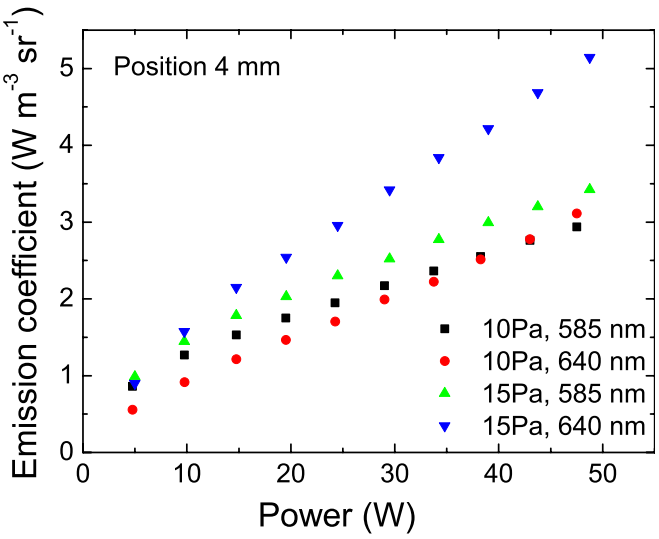

Figure 8. The intensity dependences of two lines at 585 and 640 nm on RF power at position 4 mm from the driven electrode.

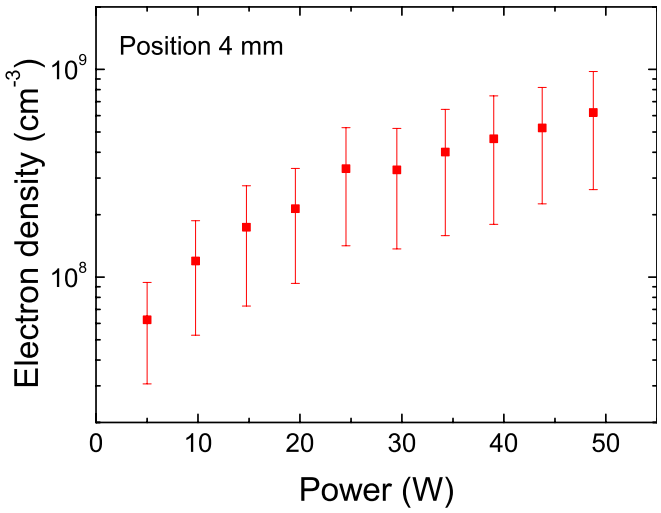

Figure 9. The electron density determined from the spectra taken at position 4 mm from the driven electrode as a function of RF power.

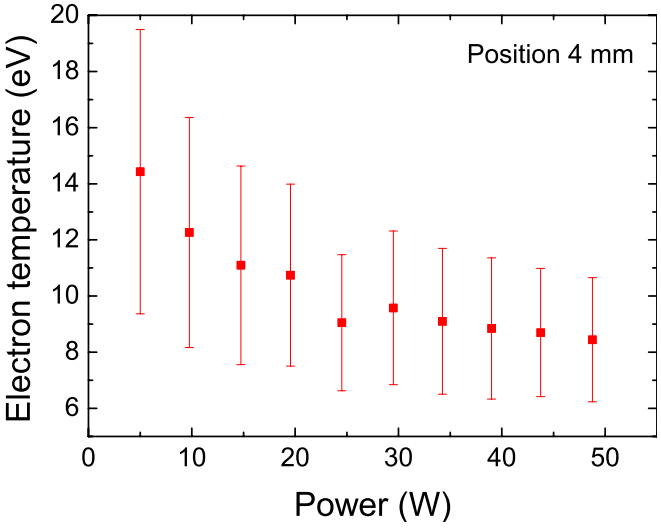

Figure 10. The electron temperature determined from the spectra taken at position 4 mm from the driven electrode as a function of RF power.

intensities need not be simply equal to their temporal mean values, determined, e.g., in PIC/MC simulations.

5.2. Power dependence

The agreement of measured and calculated spectra and OES/CRM and the PIC/MC method at positions close to the driven electrode was further analysed by decreasing the incoming RF power. The optical emission spectra were measured at position 4 mm from the driven electrode, the RF power was changed in the range 5–50 W. The metastable density was calculated from the CR model.

The intensities of spectral lines increased monotonically with increasing power. However, they increased in a different way. The dependences of two lines at 585 and 640 nm on RF power are displayed for pressures 10 and 15 Pa in figure 8. It can be seen that whilst the 640 nm line increases nearly linearly with power, the increase in 585 nm line slightly decelerates. This behaviour can be understood considering figures 9 and 10, in which dependences of electron density and electron temperature determined from the spectra are shown (taken at the same axial position 4 mm). It can be seen that with increasing power the electron density increases. This is why intensities of the spectral lines increase. Due to the increasing conductivity of the plasma, electrons gain less energy, which probably causes the decrease in electron temperature. Then, a further decrease in electron temperature affects the excitation of those higher excited states, which are not populated by stepwise excitation through the metastable levels but mostly by direct excitation. This is the case of, e.g., $2p_1$ state, from which the 585 nm line originates.

The examples of fitted spectra for pressure 10 Pa and input RF power 10 W and 50 W, are shown in figures 11 and 12, respectively. Obviously, the agreement between the calculated and measured spectra is appreciably good. This is evidence of

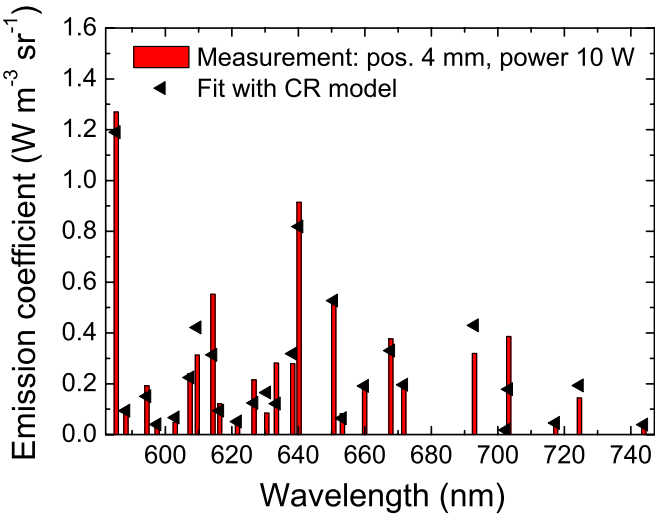

Figure 11. The example of spectra fit at position 4 mm and input RF power 10 W. The electron temperature and density determined from the fit were 12.2 eV and 1.2×10^8 cm^{-3}, respectively.

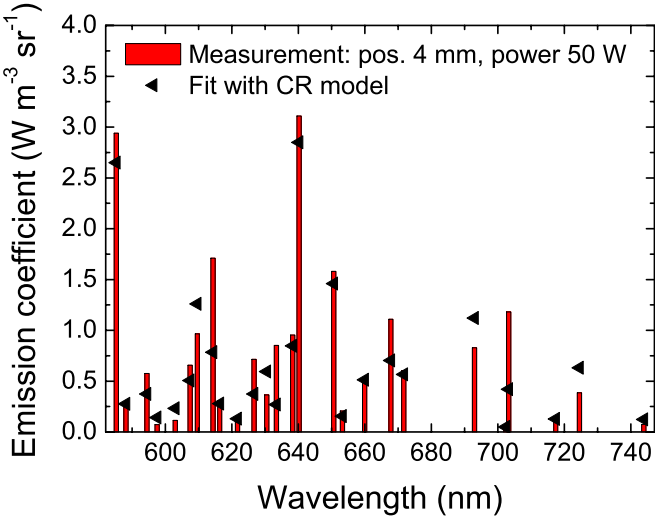

Figure 12. The example of spectra fit at position 4 mm and input RF power 50 W. The electron temperature and density determined from the fit were 8.4 eV and 6.2×10^8 cm^{-3}, respectively.

a valid assumption of Maxwellian EDF and correct description of kinetics in this region.

6. Conclusion

In this work several methods, optical emission spectroscopy with collisional–radiative modelling, Langmuir probe and particle-in-cell/Monte Carlo simulation were applied to the study of a capacitively coupled RF discharge in neon at 10 Pa. The electron density and electron temperature were determined independently by these methods as functions of axial position.

The results of the OES/CRM and the PIC/MC method were in close agreement in the case of electron temperature in the vicinity of the driven electrode. The determined value of electron temperature was about 8 eV. In the bulk plasma, the measured spectra were not satisfactorily fitted. In the case of electron density only relative agreement was obtained between OES/CRM and Langmuir probe measurements; the absolute values differed by a factor of 5. The axial dependence of electron density calculated by PIC/MC was distinct from them, reaching the maximum values between the results of the other two methods. The investigation of power dependence of plasma parameters close to the driven electrode showed a decrease in electron temperature and an increase in electron density with increasing incoming RF power. The measured and calculated spectra agreed very well in this region.

The obtained results suggest that the determination of electron density based on OES with absolute intensity measurement and CR modelling suffers from serious problems. Complicated geometry, unknown radial intensity profile, reflection of light in the chamber, etc—all these attributes make the estimation of absolute emission coefficient and thus also of electron density difficult. On the other hand, the electron temperature is determined mainly from the relative shape of the optical spectra, which is sensitive mostly to the high energetic region of the EDF. Although this sensitivity in the low energetic region of the EDF is increased by the stepwise excitation, fitting problems appear when more free parameters are used to describe the shape of the EDF.

A very important topic is the correct determination of absolute value and spatial profile of neon metastables (or all 3s states). They are not only the initial states, out of which the low energetic electrons populate the studied 3p levels, but they can also alter the spectrum measured by the spectrometer due to radiation trapping. This is in contrast, e.g., with the TRG-OES method, in which the studied emissions may be assumed to be under optically thin conditions [19].

Acknowledgments

The work was supported by the research project MSM 0021622411 of the Ministry of Education of the Czech Republic, grants No 202/09/0800 and No 202/07/1669 of the Czech Science Foundation and by project No KAN 101630651 of the Academy of Sciences of the Czech Republic.

References

[1] Raizer Y P, Shneider M N and Yatsenko M A 1995 *Radio-Frequency Capacitive Discharges* (Boca Raton, FL: CRC Press)

[2] Godyak V A, Piejak R B and Alexandrovich B M 1992 Measurement of electron energy distribution in low-pressure RF discharges *Plasma Sources Sci. Technol.* **1** 36

[3] Okuno Y, Ohtsu Y, Komatsu C and Fujita H 1993 Measurements of electron energy distribution function in an asymmetric radio-frequency discharge plasma *J. Appl. Phys.* **73** 1612

[4] Wesseling H J and Kronast B 1996 Thomson light scattering measurements of electron temperature and density in the α–γ transition of a capacitive rf discharge in helium *J. Phys. D: Appl. Phys.* **29** 1035

[5] Deegan C, Goss J, Vender D and Hopkins M 1999 Measurement of the electron energy distribution function in an argon radio-frequency discharge in the gamma mode *Appl. Phys. Lett.* **74** 1969–71
[6] Kaneda T, Kubota T, Ohuchi M and Chang J S 1990 Time-averaged electric potential profiles in a capacitive-coupling parallel-plate electrode neon gas RF discharge plasma *J. Phys. D: Appl. Phys.* **23** 1642
[7] Kimura T and Ohe K 1997 Pressure dependences of electron energy distribution and power dissipation in symmetrical RF discharges of inert gases *Japan. J. Appl. Phys.* **36** 1274–81
[8] Turner M and Hopkins M 1992 Anomalous sheath heating in a low-pressure RF discharge in nitrogen *Phys. Rev. Lett.* **69** 3511–4
[9] Tatarova E, Stoykova E, Bachev K and Zhelyazkov I 1998 Effects of nonlocal electron kinetics and transition from alpha to gamma regime in an RF capacitive discharge in nitrogen *IEEE Trans. Plasma Sci.* **26** 167–74
[10] Sobolewski M 1995 Electrical characteristics of argon radio frequency glow discharges in an asymmetric cell *IEEE Trans. Plasma Sci.* **23** 1006–22
[11] Dvořák P 2010 Measurement of plasma potential waveforms by an uncompensated probe *Plasma Sources Sci. Technol.* **19** 025014
[12] Schulze J, Donkó Z, Luggenhöelscher D and Czarnetzki U 2009 Different modes of electron heating in dual-frequency capacitively coupled radio frequency discharges *Plasma Sources Sci. Technol.* **18** 034011
[13] Schulze J, Heil B G, Luggenhölscher D, Mussenbrock T, Brinkmann R P and Czarnetzki U 2008 Electron beams in asymmetric capacitively coupled radio frequency discharges at low pressures *J. Phys. D: Appl. Phys.* **41** 042003
[14] Schulze J, Donkó Z, Heil B G, Luggenhölscher D, Mussenbrock T, Brinkmann R P and Czarnetzki U 2008 Electric field reversals in the sheath region of capacitively coupled radio frequency discharges at different pressures *J. Phys. D: Appl. Phys.* **41** 105214
[15] Vlček J 1989 A collisional–radiative model applicable to argon discharges over a wide range of conditions: I. Formulation and basic data *J. Phys. D: Appl. Phys.* **22** 623–31
[16] Golubovskii Y B, Kozakov R V, Nekuchaev V O and Skoblo A Y 2008 Nonlocal electron kinetics and radiation of a stratified positive column of discharge in neon *J. Phys. D: Appl. Phys.* **41** 105205
[17] Zhu X M, Pu Y K, Balcon N and Boswell R 2009 Measurement of the electron density in atmospheric-pressure low-temperature argon discharges by line-ratio method of optical emission spectroscopy *J. Phys. D: Appl. Phys.* **42** 142003
[18] Kano K, Suzuki M and Akatsuka H 2000 Spectroscopic measurements of electron temperature and density in argon plasmas based on collisional–radiative model *Plasma Sources Sci. Technol.* **9** 314–22
[19] Donnelly V M 2004 Plasma electron temperatures and electron energy distributions measured by trace rare gases optical emission spectroscopy *J. Phys. D: Appl. Phys.* **37** R217
[20] Mizuochi J, Sakamoto T, Matsuura H and Akatsuka H 2010 Evaluation of electron energy distribution function in microwave discharge plasmas by spectroscopic diagnostics with collisional–radiative model *Japan. J. Appl. Phys.* **49** 036001
[21] Dodt D, Dinklage A, Fischer R, Bartschat K, Zatsarinny O and Loffhagen D 2008 Reconstruction of an electron energy distribution function using integrated data analysis *J. Phys. D: Appl. Phys.* **41** 205207
[22] Birdsall C K and Langdon A B 1991 *Plasma Physics via Computer Simulation* (Bristol: Adam Hilger)
[23] Hockney R W and Eastwood J W 1988 *Computer Simulation using Particles* (Bristol: Adam Hilger)
[24] Nanbu K 2000 Probability theory of electron–molecule, ion–molecule, molecule–molecule, and Coulomb collisions for particle modeling of materials processing plasmas and gases *IEEE Trans. Plasma Sci.* **28** 971–90
[25] Hopkins M 1995 Langmuir probe measurements in the Gaseous Electronic Conference RF reference cell *J. Res. Natl Inst. Stand. Technol.* **100** 415–25
[26] Kleber J and Overzet L 1999 Sheath resistance measurements in the GEC reference reactor *Plasma Sources Sci. Technol.* **8** 534–43
[27] Holstein T 1947 Imprisonment of resonance radiation in gases *Phys. Rev.* **72** 1212–33
[28] Molisch A F, Oehry B P, Schupita W and Magerl G 1993 Radiation-trapping in cylindrical and spherical geometries *J. Quant. Spectrosc. Radiat. Transfer* **49** 361–70
[29] Navrátil Z, Trunec D, Hrachová V and Kaňka A 2007 Collisional–radiative model of neon discharge: determination of E/N in the positive column of low pressure discharge *J. Phys. D: Appl. Phys.* **40** 1037
[30] Ivanov V A 1998 Electron-impact-induced excitation transfer between 3s levels of the neon atom *J. Phys. B: At. Mol. Opt. Phys.* **31** 1765
[31] Martin W C *et al* 2004 *NIST Atomic Spectra Database* http://physics.nist.gov/asd
[32] Seaton M J 1998 Oscillator strength in Ne I *J. Phys. B: At. Mol. Opt. Phys.* **31** 5315–36
[33] Vahedi V, DiPeso G, Birdsall C K, Lieberman M A and Rognlien T D 1993 Capacitive RF discharges modelled by particle-in-cell Monte Carlo simulation: I. Analysis of numerical techniques *Plasma Sources Sci. Technol.* **2** 261–72
[34] Verboncoeur J P, Alves M V, Vahedi V and Birdsall C K 1993 Simultaneous potential and circuit solution for 1D bounded plasma particle simulation codes *J. Comput. Phys.* **104** 321–8
[35] Vahedi V, Birdsall C K, Lieberman M A, DiPeso G and Rognlien T D 1993 Capacitive RF discharges modelled by particle-in-cell Monte Carlo simulation: II. Comparisons with laboratory measurements of electron energy distribution functions *Plasma Sources Sci. Technol.* **2** 273–8
[36] Longo S 2000 Monte Carlo models of electron and ion transport in non-equilibrium plasmas *Plasma Sources Sci. Technol.* **9** 468–76
[37] Hagelaar G and Kroesen G 2000 A Monte Carlo modelling study of the electrons in the microdischarges in plasma addressed liquid crystal displays *Plasma Sources Sci. Technol.* **9** 605–14
[38] Nagayama K, Farouk B and Lee Y 1998 Particle simulation of radio-frequency plasma discharges of methane for carbon film deposition *IEEE Trans. Plasma Sci.* **26** 125–34
[39] Lieberman M A and Lichtenberg A J 1994 *Principles of Plasma Discharges and Material Processing* (New York: Wiley)
[40] Lide D R 1999 *CRC Handbook of Chemistry and Physics* (Boca Raton, FL: CRC Press)
[41] Godyak V and Piejak R 1990 Abnormally low electron-energy and heating-mode transition in a low-pressure argon RF discharge at 13.56 MHz *Phys. Rev. Lett.* **65** 996–9
[42] Brzobohatý O and Trunec D 2006 Influence of the Ramsauer minimum on the plasma characteristics studied via computer simulation *Czech. J. Phys. (Suppl. B)* **56** B665–71
[43] Brzobohatý O, Buršíková V, Nečas D, Valtr M and Trunec D 2008 Influence of substrate material on plasma in

deposition/sputtering reactor: experiment and computer simulation *J. Phys. D: Appl. Phys.* **41** 035213

[44] Boffard J B, Keeler M L, Piech G A, Anderson L W and Lin C C 2001 Measurement of electron-impact excitation cross sections out of the neon $^3P_2$ metastable level *Phys. Rev.* A **64** 032708

[45] Behnke J F, Deutsch H and Scheibner H 1985 Investigation about stepwise excitation cross sections in rare gases *Contrib. Plasma Phys.* **25** 41

[46] Leveau J, Valignat S and Deigat F 1977 Destruction par chocs électroniques des atomes métastables et pseudo-métastables de néon dans une colonne positive *J. Phys.—Lett.* **38** L385

IOP Publishing Journal of Physics D: Applied Physics

J. Phys. D: Appl. Phys. **46** (2013) 295204 (9pp) doi:10.1088/0022-3727/46/29/295204

Optical diagnostics of a surface-wave-sustained neon plasma by collisional–radiative modelling and a self-absorption method

Z Navrátil[1], L Dosoudilová[1], J Hnilica[1] and T Bogdanov[1,2]

[1] Department of Physical Electronics, Faculty of Science, Masaryk University, Kotlářská 2, 611 37 Brno, Czech Republic

[2] Faculty of Physics, University of Sofia, 5 James Bourchier Blvd., BG-1164 Sofia, Bulgaria

E-mail: zdenek@physics.muni.cz

Received 21 January 2013, in final form 14 May 2013
Published 1 July 2013
Online at stacks.iop.org/JPhysD/46/295204

Abstract

A surface-wave-sustained microwave discharge in a coaxial tube configuration in neon at low pressure (300–700 Pa) was studied by optical emission spectroscopy. Spectra of the discharge were analysed by a self-absorption method and a collisional–radiative model. The self-absorption method was used to determine the densities of neon metastable states. The collisional–radiative model, using these densities, was applied to determine the axially resolved electron temperature and the reduced electric field strength in the discharge from the optical spectra. Two types of electron distribution functions were used in the calculations—a Maxwellian distribution function and a solution of electron Boltzmann kinetic equation.

The spatially averaged neon metastable densities were in the range (0.12–0.53) $\times 10^{16}$ m^{-3} and (3.4–4.1) $\times 10^{16}$ m^{-3} for $1s_3$ and $1s_5$ states, respectively. The axial profile of the electron temperature was found to be approximately constant around 1.3–1.6 eV depending on the pressure. The reduced electric field strength decreased along the plasma column in the range 16.5–6.0 Td depending on the pressure. A large influence of gas cooling along the plasma column on the determined reduced electric field strengths was observed.

(Some figures may appear in colour only in the online journal)

1. Introduction

Microwave discharges sustained by surface wave have been found applicable in a wide range of processing applications such as thin-film deposition, gas decontamination, surface modification, sterilization, and biological applications [1–6]. The main advantages of these plasma sources are an easy operation in a wide range of conditions (pressure, frequency, type of gas), a low electromagnetic interference with electronics and a high efficiency [7]. Surface-wave-sustained discharges (SWDs) have also been studied theoretically, e.g. [8–14], and experimentally [15–20]. Several papers studied discharges in neon [21–25]. Most of these papers investigated the neon discharge at atmospheric pressure, which differs significantly from the low-pressure plasma due to the discharge contraction and filamentation [19, 26].

SWD in a coaxial tube structure was proposed in [27, 28]. In this configuration, the plasma is produced in the interspace between two coaxial dielectric tubes. A sourced metal rod is placed at the common tube axis in air at normal pressure. The interspace between the tube is evacuated and filled with working gas at low pressure. The plasma is sustained by an electromagnetic wave propagating along the tube–plasma interface. The plasma properties strongly depend on the geometry factors such as the tube radius, tube wall thickness, metal rod radius, as well as on the gas pressure. These dependences have been studied theoretically [29, 30], but have not been confirmed experimentally.

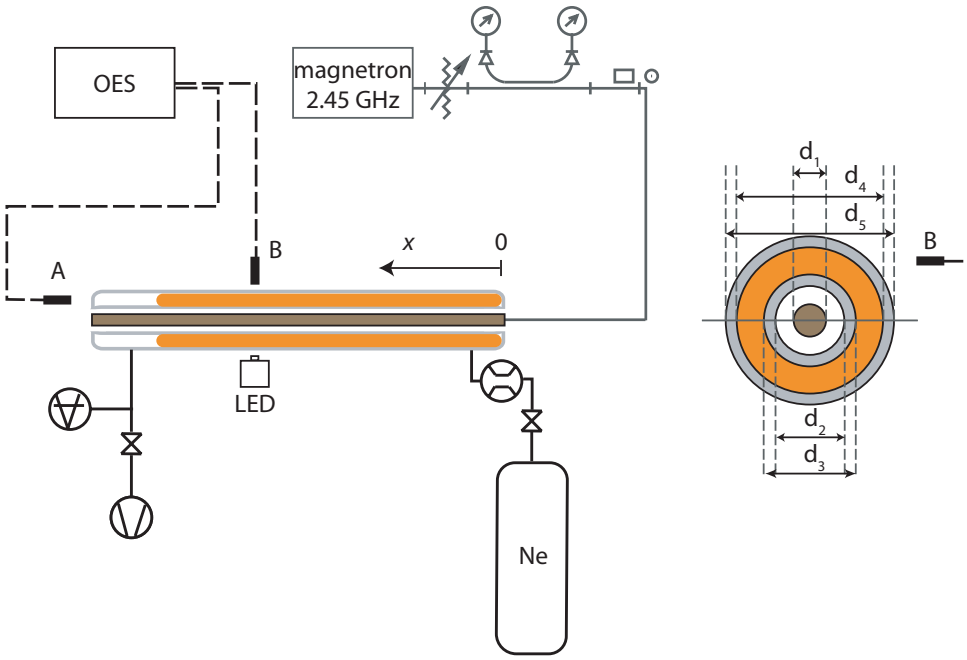

Figure 1. Scheme of the experimental set-up. The dimensions of the metal rod antenna and the tubes were $d_1 = 5$ mm, $d_2 = 7$ mm, $d_3 = 11$ mm, $d_4 = 20$ mm and $d_5 = 24$ mm. The length of the tube was 320 mm.

Collisional–radiative (CR) modelling has become widely used in plasma diagnostics for the determination of the electron temperature, electron density or even the type of electron distribution function (EDF), see e.g. [31–35]. Using a 0D CR model, it is possible to evaluate the plasma parameters of the SWD from the measured optical spectra without electrodynamic modelling, when the balance equations for populations of excited states do not contain spatial terms. This condition is not fulfilled e.g. for metastables [36], which can carry the quanta of energy from place to place in the discharge. This may be overcome by dropping the balance equation for the metastables and by replacing the missing equations with independently measured metastable densities [34, 37]. SWDs in relatively long tube with a small radius are suitable for investigations with a self-absorption technique [38], since both self-absorbed and absorption-free spectra can be simply recorded.

In this work an SWD in neon in the coaxial tube configuration is investigated with the CR modelling and a self-absorption method. Whilst the self-absorption method is used to determine the average metastable densities along the plasma column, the CR model, using these densities, is applied to determine the axially resolved plasma parameters from the absorption-free spectra. The paper is organized as follows: the experimental apparatus is described in section 2, details of the self-absorption method are given in section 3, the CR model is described in section 4. The obtained results are presented with discussion in section 5. The conclusions are given in section 6.

2. Experimental set-up

The schematic of the experimental set-up is displayed in figure 1. Microwave energy from a magnetron power generator with input power of 60 W was fetched via a coaxial cable into a metal rod-shaped antenna, forming the so-called Goubau transmission line. The antenna, made of copper and 5 mm in diameter, was placed at an axis of a two-cylinder quartz tube. The total length of the tube was 320 mm, the outer diameters of the inner and outer walls were 11 mm and 24 mm, respectively. Whilst the antenna passing through the tube centre was surrounded by air at atmospheric pressure, the interspace between the cylindrical walls was pumped with a rotary oil pump down to ultimate pressure 10 Pa and filled with neon gas of research purity 5.0 to a pressure of 300–700 Pa. The discharge was sustained in a flowing regime with a gas flow rate of approximately 5–30 sccm. A throttling valve between the tube and the pump controlled the pumping speed and allowed to set the pressure independently of flow rate. The pressure in the chamber was measured by a Leybold capacitance gauge.

The emission of radiation from the plasma was studied by optical emission spectroscopy with a Jobin Yvon HR 640 spectrometer with a CCD detector cooled with LN_2 (focal length 640 mm, grating 1200 gr mm^{-1}). The spectra were measured in two different directions: at the tube end in an axial (or longitudinal) direction, sensing the light from the whole plasma column (see A in figure 1) and in an azimuthal direction, collecting the light only from a small plasma region (B in figure 1). In the latter case, the optical fibre was placed on a movable holder 5 cm far from the tube, and by moving it along the tube (described with x coordinate in figure 1 with $x = 0$ denoting the column beginning) axially dependent spectra were recorded. Due to the coaxial structure of the tubes only radially averaged spectra were measured. The spatial resolution in the axial direction was about 1 cm.

An extra light-emitting diode (LED) light source was placed opposite the fibre on the other side of the tube for

supporting absorption measurements. An Oriel tungsten halogen lamp calibrated by the Czech Metrology Institute with 5% uncertainty of intensity was used to determine the spectral sensitivity of the spectrometer.

3. The self-absorption method

A self-absorption method [38] was applied to determine the densities of neon metastable states. The method is based on the comparison of total intensities of two partially self-absorbed lines and needs a measurement of their ratio over both optically thin and thick dimensions. The spectra were, therefore, measured in A and B directions, respectively (see figure 1). Whilst self-absorption was observed through the plasma column with a length of 12–17 cm (A), the absorption in the azimuthal direction could be neglected (B).

Assuming an axially constant absorption coefficient $k(\nu)$ and an emission coefficient linearly dependent on the axial position

$$j(\nu, x) = j(\nu) \cdot (ax + b), \tag{1}$$

with constants a and b determined from the experiment, the ratio of total intensities, integrated over a line profile and a plasma column of length l in the presence and absence of absorption, respectively, is

$$I/I' = \frac{1}{k_{\mathrm{tot}}(al^2/2 + bl)} \int_{\mathrm{profile}} \left[\left(b - \frac{a}{k_{\mathrm{tot}} P(\nu)} \right) \times \left(1 - \mathrm{e}^{-k_{\mathrm{tot}} P(\nu) l} \right) + al \right] \mathrm{d}\nu. \tag{2}$$

The same spectral profile $P(\nu)$ calculated as Gaussian due to the Doppler broadening mechanism is assumed for emission and absorption. k_{tot} is the total absorption coefficient integrated over the line profile.

Taking two spectral lines (indexed with 1, 2) with the same lower level (i.e. metastable level, for which the density is being determined), the ratio of their intensity ratios

$$r = \frac{I_1/I_1'}{I_2/I_2'} \tag{3}$$

can be compared with the measured value in order to determine the metastable density. When I_1 denotes the intensity of line with a higher oscillator strength, the ratio r ranges from 0 to 1 depending on the optical thickness and thus on the metastable density (see figure 2).

Whilst the axial dependence of the emission coefficient was simply measurable by sensing the light (of neon 3p → 3s transitions) at different axial positions, a similar measurement of the absorption coefficient was not possible, since the discharge was optically thin in the direction B. Therefore, an axially constant absorption coefficient was assumed in the calculations and the metastable densities were averaged over the plasma column.

The assumption of optical thin condition in the direction B was proved with an additional 'white-light' absorption experiment. Using an LED diode, placed opposite the optical fibre and radiating through the discharge tube in the azimuthal direction, and the so-called subtraction method [39], plasma transmittance in the direction B was found to be close to the absorption-free value.

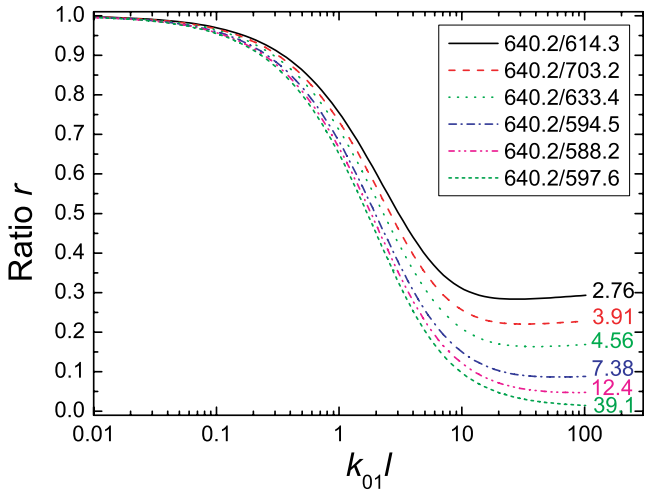

Figure 2. Dependence of the intensity ratio r on the optical thickness $k_{01}l$ calculated for various pairs of spectral lines. k_{01} is the absorption coefficient of the line with a higher oscillator strength in the line centre. The ratio of line oscillator strengths is indicated on the right. The emission coefficient $j(x)$ was assumed to decrease linearly along the tube axis.

4. The collisional–radiative model

The CR model used in this work has already been described in [37, 40], so only basic information will be given here. Thirty excited states of neon of $2p^5 3s$, $2p^5 3p$, $2p^5 4s$ and $2p^5 3d$ configurations are studied in the model. The model includes elementary processes such as electron impact excitation out of the ground state and $2p^5 3s$ states and de-excitation from upper states to these levels, electron impact excitation transfer between 3s levels, spontaneous emission of radiation, radiation trapping, electron impact ionization of the ground-state and metastable atoms, chemoionization, associative ionization, two-body and three-body collisions of metastables with ground-state neon atoms and diffusion of 3s state atoms to the wall. However, the densities of metastable states n_{1s_3}, n_{1s_5} were set constant in this work for all axial positions according to the axially averaged result of the self-absorption measurement (see section 3). Experiments with discharges in argon showed only a small variation of $1s_i$ densities along the plasma column [18]. The processes of two-body collisional deactivation and excitation transfer between neon $2p^5 3p$ states were included using the rate coefficients published in [41]. The radiation trapping of $2p^6$–$2p^5 3s$ and $2p^5 3s$–$2p^5 3p$ transitions was described by means of escape factors. The neutral gas kinetic temperature was assumed to vary along the tube. The rotational temperature of the N_2 $C\,^3\Pi_u$ state was used as the approximation of the neutral gas temperature.

Maxwellian electron distribution function (Maxwellian EDF) and a solution of Boltzmann kinetic equation were used for the calculation of rates of electron collisional processes. The Boltzmann kinetic equation for the stationary EDF under a high-frequency electric field was solved assuming the well-known two-term approximation with an effective electric field [42, 43]. The binary excitation and ionization electron collisions with the ground-state neon atoms were considered as inelastic collisions. The used code calculated the EDF as a

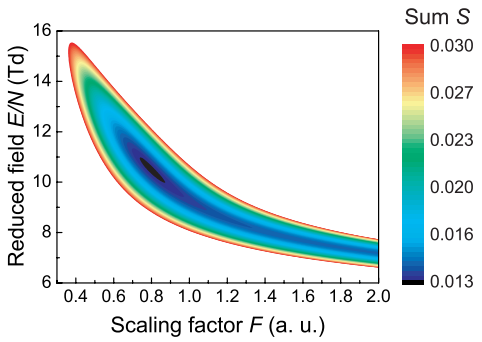

Figure 3. Example of the sum of squares $\mathcal{S}$ map calculated for a spectrum measured at 320 Pa at the axial position of 1 cm for a wide range of reduced electric field strengths and scaling factors. The assumed neutral gas temperature was 300 K.

function of the reduced electric field strength amplitude E/N and reduced electric field frequency ω/N.

In order to determine the electron temperature or the reduced electric field strength, the measured and calculated spectra (spectral lines with upper levels from $2p^5\,3p$ and $2p^5\,3d$ configurations, number of lines was 27) were compared on the basis of a weighted least-squares sum:

$$\mathcal{S} = \sum_{i,j} \frac{(\mathcal{F} \cdot I_{ij}^{\mathrm{cr}}(T_\mathrm{e} \text{ or } E/N, n_\mathrm{e}, n_{1s_3}, n_{1s_5}) - I_{ij}^{\mathrm{exp}})^2}{I_{ij}^{\mathrm{exp}}}, \tag{4}$$

where $\mathcal{F}$ is a scaling factor, I_{ij}^{exp} is the measured total intensity of transition ij, corrected for the instrument spectral sensitivity. I_{ij}^{cr} denotes the calculated total intensity of transition ij and n_{1s_3}, n_{1s_5} are the metastable densities.

For each measured spectrum, the sum of squares $\mathcal{S}$ was calculated for a wide range of conditions (T_e or E/N) and scaling factors. In this way, a map of $\mathcal{S}$ values versus, e.g., E/N and $\mathcal{F}$ was obtained (see figure 3). The parameter with the lowest $\mathcal{S}$ value was taken as the result for the measured spectrum.

In the above-mentioned calculations, an estimation of the electron density value is needed. At a low ionization ratio, the dependence of relative intensities in the spectra on electron density is only weak and can even be neglected [33]. This is valid in corona equilibrium, when the electron density scales only the electron impact excitation from the ground state. Our estimation of electron density 10^{12}–10^{13} cm^{-3} according to the literature [18] is far from the local thermodynamic equilibrium condition

$$n_\mathrm{e} \gg 1.6 \times 10^{12} \sqrt{T_\mathrm{e}} (\mathcal{E}_{ij})^3 \,\mathrm{cm}^{-3} \approx 2.7 \times 10^{15} \mathrm{cm}^{-3},$$
$$[T_\mathrm{e}] = K, \quad [\mathcal{E}_{ij}] = eV,$$

determined for the calculated electron temperature T_e and the largest energy difference of levels $\mathcal{E}_{ij}$ [44]. However, since the system of levels can also be partially in the excitation saturation phase, the validity of this assumption was tested in the calculations.

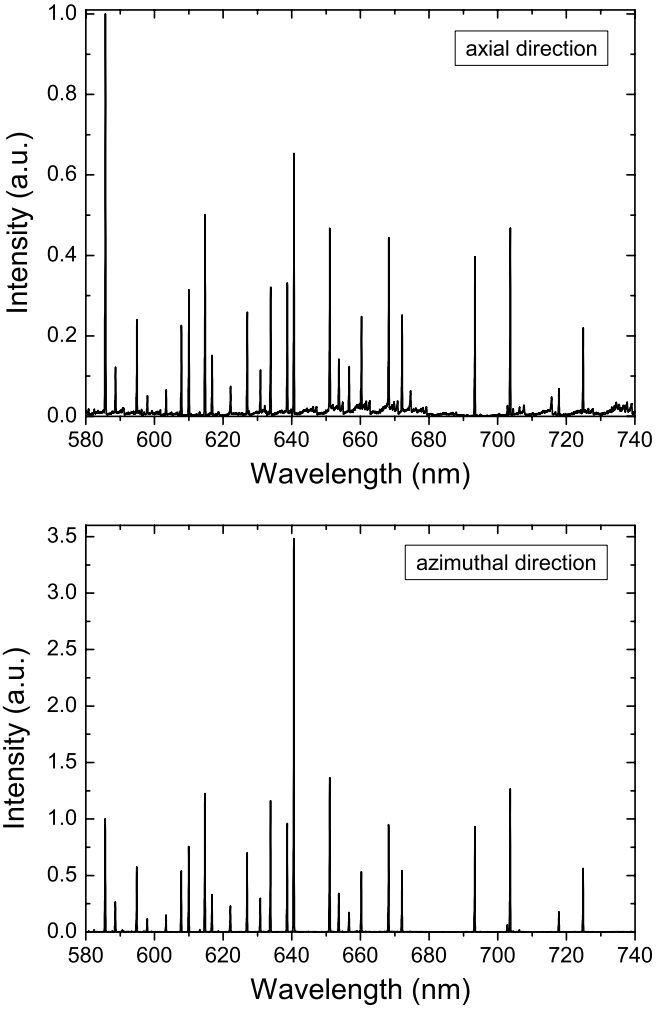

Figure 4. Comparison of spectra measured in (*a*) axial and (*b*) azimuthal directions at the pressure of 320 Pa and microwave power of 60 W. The spectrum sensed in the azimuthal direction was measured at the axial position of 2.5 cm. The spectra were corrected for the instrument spectral sensitivity and normalized according to the 585.2 nm line.

5. Results and discussion

5.1. The self-absorption method

A comparison of two spectra measured in axial (A) and azimuthal (B) directions is shown in figures 4(*a*) and (*b*), respectively. The spectra were normalized according to a 585.2 nm line. The relative intensities in both spectra substantially differ. Although some differences may appear due to a possible variation of plasma parameters along the plasma column, the main reason for the line intensity variation is the self-absorption of radiation in the axial direction. This is manifested in the strong attenuation of the transitions with a large Einstein coefficient, i.e. at 614.3, 640.2 and 703.2 nm, ending in the metastable state $1s_5$.

The typical axial dependence of the spectral line intensity and that of the intensity ratio of two lines ending in the same lower state ($1s_5$) with different oscillator strengths ($f_1/f_2 = 4.3$) are shown in figure 5. The intensities were measured in the azimuthal direction (B) at various axial positions. Whereas the

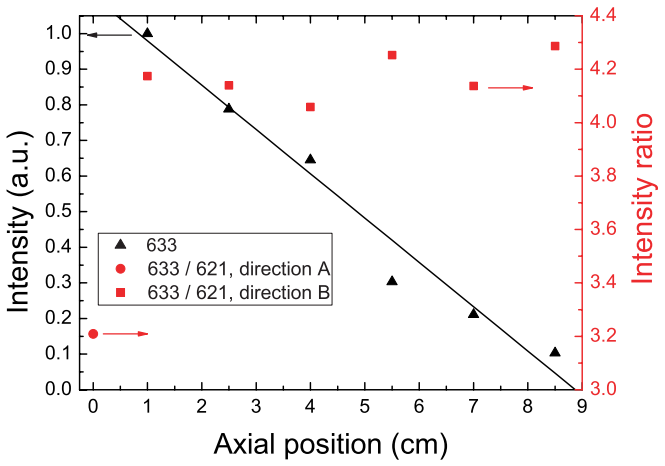

Figure 5. Axial dependence of the intensity of the 633.4 nm line (on the left axis) and axial dependence of the intensity ratio of 633.4 and 621.7 nm lines (on the right axis) from the azimuthal measurements at pressure 320 Pa. The value of the same intensity ratio, but measured in the axial direction along the whole column, is indicated by a red circle plotted at the position of 0 cm.

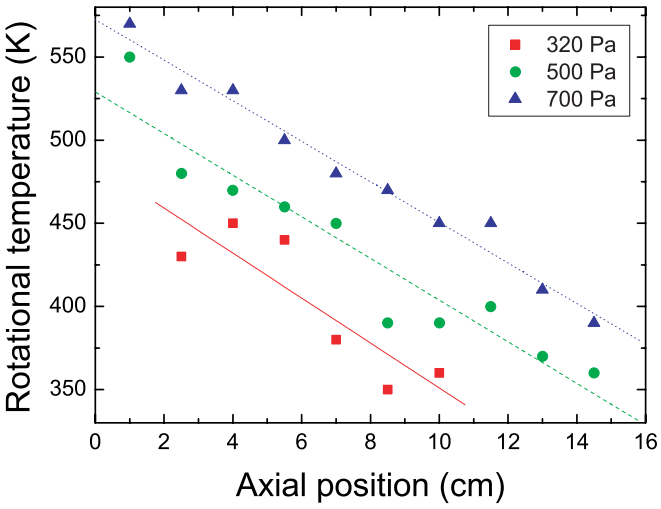

Figure 6. Rotational temperature of N_2 molecule in the $C\ ^3\Pi_u$ state as a function of the axial position. The microwave power was 60 W in all cases.

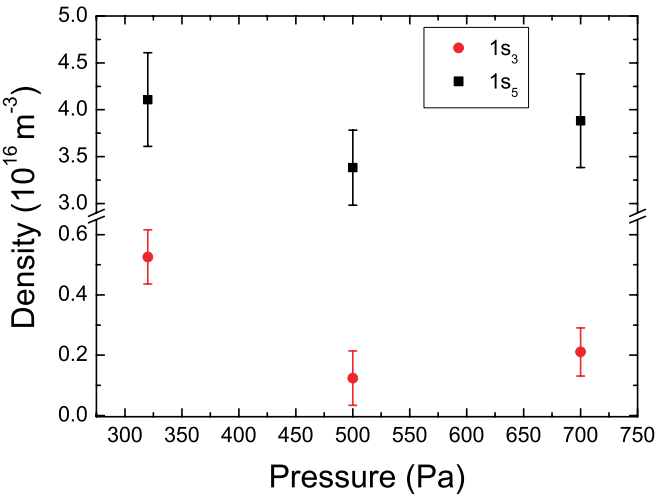

Figure 7. Densities of $1s_3$ and $1s_5$ metastable neon states calculated using the self-absorption method for average nitrogen rotational temperatures. The metastable densities are also averaged over the plasma column. The error bars were determined from the uncertainty of intensity and temperature measurement.

intensity of the 633.4 nm line decreases with the axial position, the intensity ratio of 633.4 nm and 621.7 nm is stable along the plasma column, defining well the optically thin value. The intensity ratio of the same lines, but measured in the axial direction (A), is plotted in the graph at the position of 0 cm. From its difference from the optically thin value, the density of the $1s_5$ state could be inferred using the self-absorption method.

The neutral gas temperature, needed in the calculation of spectral line profiles in (2), was estimated from the rotational temperature of nitrogen molecules in the N_2 $C\ ^3\Pi_u$ state. The emission spectra of the second positive system of N_2 ($C\ ^3\Pi_u \rightarrow B\ ^3\Pi_g$, $v' - v'' = -2$) with an unresolved rotational structure were simulated using the software Specair [45] and compared with the measured spectra with the least-squares method. The determined axial dependences are shown in figure 6. The temperatures decreased linearly with increasing axial position and also increased with pressure, as expected in the simulations [13]. However, the systematic error of their absolute values can be large, since the rotational temperature generally differs from the kinetic gas temperature in non-equilibrium plasmas [46]. Due to the low sensitivity of the spectrometer in the UV spectral region, a comparative measurement of the commonly used rotational temperature of OH radicals was not possible.

In order to simplify the evaluation of the intensity ratio r only average temperatures determined from the dependences in figure 6 were taken into the calculations—400 K, 430 K and 480 K, for pressures 320 Pa, 500 Pa and 700 Pa, respectively. The determined densities of neon $1s_3$ and $1s_5$ states as a function of pressure are displayed in figure 7. The $1s_5$ density was determined from the pair of lines with the highest ratio of oscillator strengths 640.2/597.6 ($f_1/f_2 = 39.1$), the $1s_3$ density was obtained from the only one suitable line pair 626.7/743.9 ($f_1/f_2 = 7.65$). The density of the $1s_3$ state slightly decreased with gas pressure, but this decrease is obviously comparable to the experimental error. More investigations would be needed to analyse the metastable density–pressure dependence. When the temperature of 300 K is used in the calculation of spectral profiles, the systematic error of metastable densities reaches maximally about 20%.

The critical evaluation of the obtained values is complicated due to the lack of experimental and theoretical data under similar tube geometries and discharge conditions. The axial dependence of metastable densities was studied experimentally and theoretically for a discharge generated in argon in a single dielectric tube with inner diameter 9 mm, surrounded by a metallic cylinder with a diameter of 20 mm [18]. The metastable densities were approximately constant along the plasma column and for pressure 370 Pa the densities reached 1.3×10^{17} m^{-3} and 4.1×10^{17} m^{-3} for $1s_3$ and $1s_5$ states, respectively, i.e. an order of magnitude higher values than ours. Theoretical calculations for a similar configuration and discharge conditions [13] (inner diameter of the single tube, 4 mm, diameter of the metallic cylinder, 40 mm and pressure, 133 Pa) provided values 0.4×10^{18} m^{-3} and $1.2 \times$

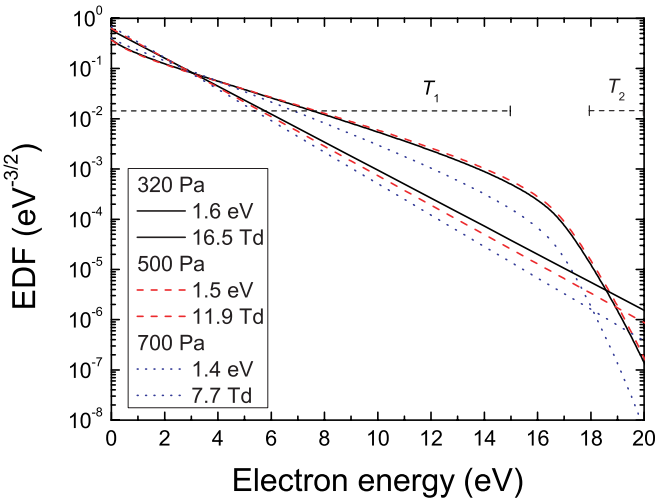

Figure 8. EDFs calculated from the Maxwell distribution and the Boltzmann kinetic equation and selected according to the least-squares sum as a result of the fitting procedure on the measured spectra. The final values of the electron temperature (as $k_b T_e/e$) and of the reduced electric field strength, for which the EDFs were calculated, are listed in the legend for three pressures and the axial position 1 cm. For explanation of regions T_1 and T_2 see the text.

10^{18} m^{-3} for $1s_3$ and $1s_5$ states, respectively. These results were about twice as high as the findings in [18] for the same pressure. The SWD in neon, studied in [25] by the self-absorption technique for a homogeneous column, was generated at atmospheric pressure (inside a capillary tube with an inner diameter of 2.5 mm); the determined volume-averaged metastable density was two orders larger than ours, 2.1×10^{17} m^{-3}.

5.2. The collisional–radiative model

5.2.1. EDF & spectra. The EDFs determined from the fit of the calculated to the measured spectra are shown for three pressures in figure 8. Two different EDF shapes were taken into the calculations: Maxwellian EDF and solution of the Boltzmann kinetic equation. For the determined reduced electric field strengths of 7.7–16.5 Td, the EDFs were non-Maxwellian due to the inelastic electron collisions with the neutral gas. This is in agreement with the observations carried out in argon [47]. The determined values of field strengths are also in accordance with the self-consistent simulations of the SWD in a single dielectric tube in argon [13]. The field strength amplitude reached ≈8 V cm^{-1} compared with the 6–10 V cm^{-1} in the cited paper.

Since electron–electron (e–e) collisions responsible for Maxwellization of the EDF were not taken into account in the solution of the Boltzmann equation, the obtained results were compared with that using the Maxwellian EDF (being the extreme case). Using the Boltzmann EDF, the temperature determined as the slope from the linear fit of the final EDF in the log plot was 2.1–2.5 eV with electron energies below 15 eV (temperature T_1) and 0.33–0.43 eV in the range of electron energies 18–20 eV (temperature T_2). Using the Maxwellian EDF, the final temperatures 1.4–1.6 eV were lower than T_1 values, since they have to direct the EDF also in the high electron energy region of T_2. Thus, the use of the Maxwellian EDF in the calculations provides only a rough estimate of the mean electron energy. The determined T_2 values could be compared with the excitation temperatures 0.4–0.5 eV from the Boltzmann plot of intensities with the same spectral lines as used in the CR model. However, although the spectral lines in the Boltzmann plot produce a relatively straight line, the excitation temperature determined from the plot represents well the electron temperature only in local thermodynamic equilibrium [36]. Moreover, the result of the CR model reflects both regions of T_1 and T_2 of the EDF, since the model (with externally determined metastable densities) balances the direct excitation out of the ground state with the stepwise excitation out of the 3s states [37].

The measured spectra at the axial position of 1 cm for pressures of 320 and 700 Pa are plotted with their fitted values in figures 9(*a*) and (*b*), respectively. The measured spectra were normalized according to the maximal intensity of the spectral line 640.2 nm. Although the fitted intensity differs for some lines from the measured one, the overall sum of squares, determined from (4), is minimized at different pressures for different values of the reduced electric field strength. This reflects the particularity of the measured spectra: e.g. the stronger intensity of the 585.3 nm line implies a higher field strength, since its upper level $2p_1$ (in Paschen notation) is excited primarily by direct excitation from the ground state.

A larger discrepancy between the measured and calculated intensities is found in the case of spectral lines 703.2, 724.5 and 743.9 nm originating from the neon excited state $2p_{10}$, and of the 640 nm line from the neon $2p_9$ state. Whilst the calculated intensities of lines from $2p_{10}$ are lower than that in the measured spectrum, the calculated intensity of the 640 nm line is conversely higher. This difference was attributed according to [41] to the excitation transfer between neon $2p^5 3p$ states induced by ground-state atoms. However, incorporation of the collisional deactivation and excitation transfer processes into the model with the coefficients published in [41] improved the correspondence of the spectra only partially (see figure 9). The model is still unable to simulate the measured spectra of high-pressure plasmas (as of atmospheric-pressure plasmas), in which the transitions from the $2p_{10}$ state dominate.

The fixed value of the electron density of 10^{12} cm^{-3} was used in the above-mentioned calculations, since a weak dependence of the final result on the electron density was assumed (see section 4). The validity of this assumption was tested by varying the entered value of the electron density and observing the output of the model. The result of this procedure for the Maxwellian EDF is displayed in figure 10. It can be seen that in the range 10^{12}–10^{13} cm^{-3}, the electron density does not substantially influence the resulting electron temperature. Alternatively, the electron temperature can be about 15% higher when two orders lower electron density is expected. A decreasing trend of electron temperature in the wide electron density range cannot be simply interpreted, since the metastable densities are kept fixed at the externally determined values during the variation of the electron density.

In order to evaluate the impact of measurement uncertainty of the metastable densities on the outputs of the CR model,

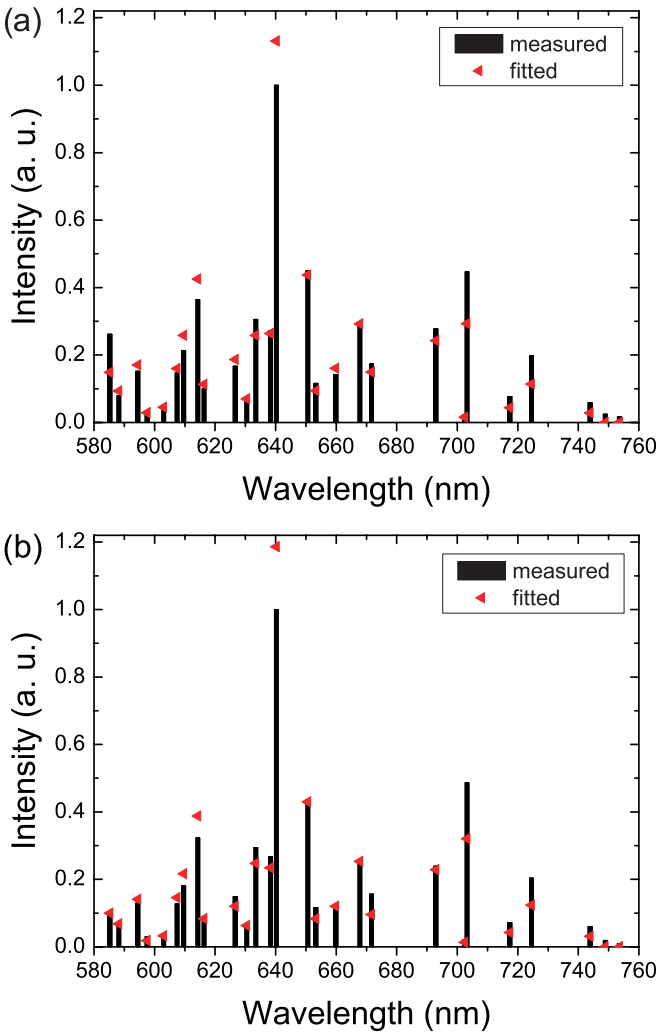

Figure 9. Measured and fitted spectra at the axial position of 1 cm for pressures (*a*) 320 Pa and (*b*) 700 Pa. The fitted spectra were calculated with the solution of the Boltzmann kinetic equation as the EDF.

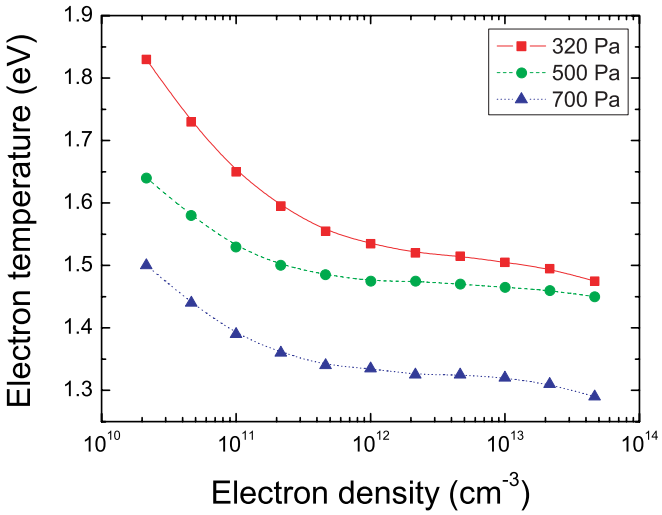

Figure 10. Variation of the determined electron temperature for the spectra measured at the axial position of 1 cm with the change of electron density entered into the model. In the range 10^{12}–10^{13} cm^{-3}, the electron density does not substantially influence the resulting electron temperature.

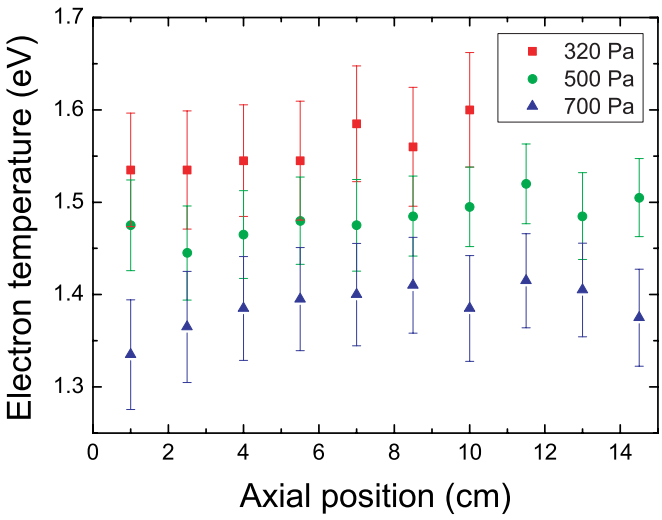

Figure 11. Axial dependence of the electron temperature at different pressures. The error bars denote the standard uncertainty determined from the fit. The length of the plasma column differed with pressure: 12 cm for pressure 320 Pa and 17 cm for 500 Pa and 700 Pa, respectively.

the densities of both metastable states were simultaneously varied and the result of the model with respect to the electron temperature or the reduced electric field was monitored. The electron density was kept fixed at 10^{12} cm^{-3}. Within two orders of metastable density change, the electron temperature depended logarithmically on the metastable density, increasing 0.3 eV per one order increase in the metastable density. The reduced electric field dependence was also approximately logarithmical, increasing 2 Td per one order increase in the metastable density.

5.2.2. Axial dependence. The axial dependences of the electron temperature and the reduced electric field strength are shown in figures 11 and 12, respectively. Whilst the axial profile of electron temperature was found to be relatively flat along the plasma column, the reduced electric field strength decreased with the axial position due to gas cooling. The decrease in the gas temperature along the column was approximated in the calculations with the axial N_2 rotational temperature dependence (see figure 6). Since ω/N then decreases along the column, the electron heating is more efficient and lower E/N is needed to maintain the plasma. The calculated E/N would be constant along the column with a constant gas temperature, as expected from invariable mean power for electron–ion pair maintenance [9, 48]. This proves the importance of the proper account of the gas temperature in SWDs at pressures above 1 Torr, as pointed out in [13].

Since the electron temperature governing the value of excitation rate coefficients does not change along the tube, the strong intensity decrease of the 3p → 3s transitions ($2p_i \rightarrow 1s_i$ in Paschen notation) along the tube, shown for the spectral line 633 nm and several axial positions in figure 5, can be explained mainly by the decrease in electron density along the plasma column. Such a decrease is well known in

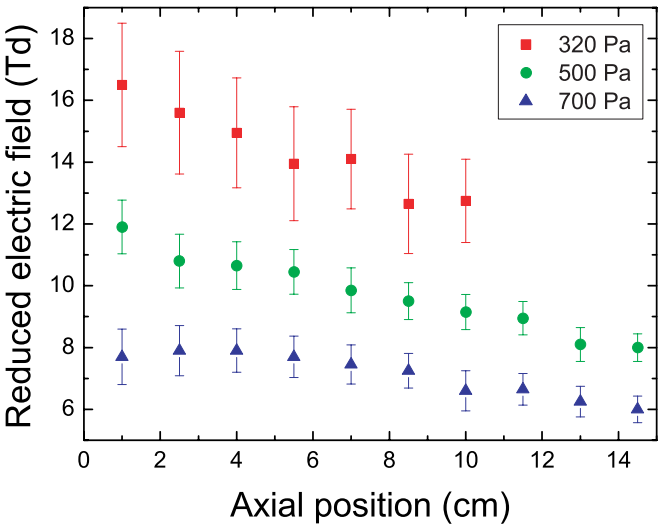

Figure 12. Axial dependence of the reduced electric field strength at different pressures. The error bars denote the standard uncertainty determined from the fit. The value of the electric field strength has a meaning of amplitude.

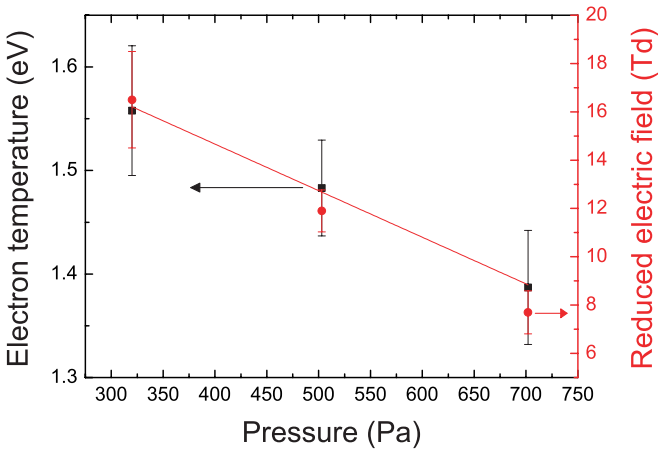

Figure 13. Pressure dependence of the electron temperature and the reduced electric field strength. The electron temperature is averaged over all measured axial positions in figure 11, the reduced field is plotted for the axial position 1 cm. The error bars denote the standard uncertainty determined from the fit.

SWDs [15]. However, using the present method the electron density could not be obtained from the relative intensities of spectral lines. The decrease in the density of $2p_i$ states towards the column end has been observed both theoretically and experimentally in argon [18]. The populations of the lower $1s_i$ states can behave variously depending on the discharge conditions [13].

5.2.3. Pressure dependence. The values of the electron temperature and the reduced electric field strength from figures 11 and 12 are shown in dependence on gas pressure in figure 13. Whilst the electron temperature is averaged over all measured axial positions, the reduced field is plotted for one axial position of 1 cm. Both curves decrease with pressure. The derived electric field, corrected for gas cooling, is within the experimental error constant of 8 V cm^{-1}. On the other hand, a decrease in the electric field with pressure in a larger pressure range is observed [13, 48].

Using the Maxwellian EDF, the electron temperature decreases with increasing pressure, but only in a range comparable to the statistical uncertainty. The decrease in the Maxwellian temperature is somewhat stronger than that of the mean electron energy, calculated with the EDF from the Boltzmann kinetic equation. The mean electron energy varies around 3.5 eV only a little with the pressure, since the number of electrons, which can excite atoms directly into the 3p states and for which the EDF is mainly optimized, is small (see EDFs in figure 8). In this case, the use of Maxwellian EDF in the calculations provides a slightly different picture of the plasma behaviour.

6. Conclusion

This work was concerned with the optical diagnostics of a low-pressure surface-wave-sustained microwave discharge in neon. The self-absorption method was used to determine the density of the neon metastable states $1s_3$ and $1s_5$ from the partially self-absorbed spectra in the axial direction. The obtained values were in the range (0.12–0.53) $\times$ 10^{16} m^{-3} and (3.4–4.1) $\times$ 10^{16} m^{-3} for $1s_3$ and $1s_5$ states, respectively. The pressure affected the densities only slightly, comparatively to the measurement error.

The determined metastable densities and the estimation of the electron density were introduced into the collisional–radiative model for the neon discharge. Two EDF types were used for the calculation of the rate coefficients of elementary processes—the Maxwellian EDF and the solution of the electron Boltzmann kinetic equation. By fitting the neon spectra measured in the azimuthal direction with the calculation of the CR model, the electron temperature and the reduced electric field strength were determined. Whilst the axial profile of the electron temperature was found approximately constant, the reduced electric field strength decreased along the column in the range 16.5–6.0 Td. A large influence of the gas temperature variation along the column on the determined reduced electric fields was observed. Both reduced electric field strength and electron temperature decreased with pressure. In the range of the expected electron densities, the results only weakly depended on the chosen value of the electron density.

A drawback of this work is its reliance upon the axially averaged metastable densities. A proper account of the absorption coefficient and of the gas temperature along the plasma column is needed to improve the model predictions about axial variations of plasma parameters. Also, the effect of incorporation of e–e collisions on the EDF shape and on the CR model results has to be studied. A further investigation in this field is therefore necessary.

Acknowledgments

This work has been supported by the project R&D center for low-cost plasma and nanotechnology surface modifications CZ.1.05/2.1.00/03.0086 funding by the European Regional

Development Fund and by Grant Nos 104/09/H080 and P205/10/1374 of the Czech Science Foundation.

References

[1] Ferreira C M and Moisan M (ed) 1993 *NATO ASI Series* B vol 302 (New York: Plenum)
[2] Moreau S, Moisan M, Tabrizian M, Barbeau J, Pelletier J, Ricard A and Yahia L 2000 *J. Appl. Phys.* **88** 1166–74
[3] Kabouzi Y, Moisan M, Rostaing J, Trassy C, Guerin D, Keroack D and Zakrzewski Z 2003 *J. Appl. Phys.* **93** 9483–96
[4] Ilias S, Campillo C, Borges C and Moisan M 2000 *Diamond Relat. Mater.* **9** 1120–4
[5] Sera B, Stranak V, Sery M, Tichy M and Spatenka P 2008 *Plasma Sci. Technol.* **10** 506–11
[6] Hnilica J, Kudrle V and Potocnakova L 2012 *IEEE Trans. Plasma Sci.* **40** 2925–30
[7] Schlüter H and Shivarova A 2007 *Phys. Rep.* **443** 121
[8] Glaude V M M, Moisan M, Pantel R, Leprince P and Marec J 1980 *J. Appl. Phys.* **51** 5693–8
[9] Ferreira C 1983 *J. Phys. D: Appl. Phys.* **16** 1673–85
[10] Kortshagen U, Schluter H and Shivarova A 1991 *J. Phys. D: Appl. Phys.* **24** 1571–84
[11] Aliev Y, Grosse S, Schluter H and Shivarova A 1996 *Phys. Plasmas.* **3** 3162–75
[12] Benova E, Petrova T, Blagoev A and Zhelyazkov I 1998 *J. Appl. Phys.* **84** 147–53
[13] Petrova T, Benova E, Petrov G and Zhelyazkov I 1999 *Phys. Rev.* E **60** 875–86
[14] Nowakowska H, Zakrzewski Z, Moisan M and Lubanski M 1998 *J. Phys. D: Appl. Phys.* **31** 1422–32
[15] Moisan M and Zakrzewski Z 1991 *J. Phys. D: Appl. Phys.* **24** 1025
[16] Calzada M, Moisan M, Gamero A and Sola A 1996 *J. Appl. Phys.* **80** 46–55
[17] Calzada M D, Saez M and Garcia M C 2000 *J. Appl. Phys.* **88** 34–9
[18] Lao C, Gamero A, Sola A, Petrova T, Benova E, Petrov G and Zhelyazkov I 2000 *J. Appl. Phys.* **87** 7652–9
[19] Cardoso R P, Belmonte T, Noël C, Kosior F and Henrion G 2009 *J. Appl. Phys.* **105** 093306
[20] Hnilica J, Kudrle V, Vasina P, Schaefer J and Aubrecht V 2012 *J. Phys. D: Appl. Phys.* **45** 055201
[21] Abed S, Bouvier A, Bouvier A, Charlet B and Leprince P 1982 *J. Phys. D: Appl. Phys.* **15** 595–604
[22] Moutoulas C, Moisan M, Bertrand L, Hubert J, Lachambre J and Ricard A 1985 *Appl. Phys. Lett.* **46** 323–5
[23] Czylkowski D, Jasinski M, Mizeraczyk J and Zakrzewski Z 2006 *Czech. J. Phys.* **56** B684–9
[24] Rolin M N, Shabunya S I, Rostaing J C and Perrin J M 2007 *Plasma Sources Sci. Technol.* **16** 480–91
[25] Sáinz A and García M 2008 *Spectrochim. Acta* B **63** 948–56
[26] Kabouzi Y, Calzada M, Moisan M, Tran K and Trassy C 2002 *J. Appl. Phys.* **91** 1008–19
[27] Rauchle E 1998 *J. Phys. IV* **8** 99–108
[28] Gritsinin S, Kossyi I, Malykh N, Misakyan M, Temchin S and Bark Y 1999 *Preprint* No 1 (Moscow: General Physics Unit RAS)
[29] Neichev Z, Benova E, Gamero A and Sola A 2006 *J. Phys.: Conf. Ser.* **44** 133
[30] Bogdanov T and Benova E 2010 *J. Phys.: Conf. Ser.* **207** 012031
[31] Donnelly V M 2004 *J. Phys. D: Appl. Phys.* **37** R217
[32] Yanguas-Gil A, Cotrino J and Gonzalez-Elipe A 2004 *Phys. Plasmas.* **11** 5497–506
[33] Zhu X M, Chen W C, Li J and Pu Y K 2009 *J. Phys. D: Appl. Phys.* **42** 025203
[34] Boffard J B, Jung R O, Lin C C and Wendt A E 2010 *Plasma Sources Sci. Technol.* **19** 065001
[35] Zhu X M, Pu Y K, Celik Y, Siepa S, Schuengel E, Luggenhoelscher D and Czarnetzki U 2012 *Plasma Sources Sci. Technol.* **21** 024003
[36] van der Sijde B, van der Mullen J J A M and Schram D C 1984 *Beitr. Plasma Phys.* **24** 447–73
[37] Navrátil Z, Dvořák P, Brzobohatý O and Trunec D 2010 *J. Phys. D: Appl. Phys.* **43** 505203
[38] Jolly J and Touzeau M 1975 *J. Quant. Spectrosc. Radiat. Transf.* **15** 863–72
[39] Wamsley R C, Mitsuhashi K and Lawler J E 1993 *Rev. Sci. Instrum.* **64** 45–8
[40] Navrátil Z, Trunec D, Hrachová V and Kaňka A 2007 *J. Phys. D: Appl. Phys.* **40** 1037
[41] Chang R S F and Setser D W 1980 *J. Chem. Phys.* **72** 4099–110
[42] Holstein T 1946 *Phys. Rev.* **70** 367–84
[43] Hagelaar G J M and Pitchford L C 2005 *Plasma Sources Sci. Technol.* **14** 722–33
[44] Thorne A, Litzén U and Johansson S 1999 *Spectrophysics: principles and applications* (Berlin: Springer)
[45] Laux C O 2002 *Physico-Chemical Modeling of High Enthalpy and Plasma Flows* (*von Karman Institute Lecture Series 2002–07*) ed D Fletcher *et al* (Rhode-Saint-Genese, Belgium)
[46] Chelouah A, Marode E, Hartmann G and Achat S 1994 *J. Phys. D: Appl. Phys.* **27** 940–5
[47] Lao C, Cotrino J, Palmero A, Gamero A and Gonzalez-Elipe A 2001 *Eur. Phys. J. D* **14** 361–6
[48] Boisse-Laporte C, Granier A, Dervisevic E, Leprince P and Marec J 1987 *J. Phys. D: Appl. Phys.* **20** 197–203

IOP Publishing Plasma Sources Science and Technology

Plasma Sources Sci. Technol. **24** (2015) 065022 (13pp) doi:10.1088/0963-0252/24/6/065022

Determination of titanium atom and ion densities in sputter deposition plasmas by optical emission spectroscopy

P Vašina, M Fekete, J Hnilica, P Klein, L Dosoudilová, P Dvořák and Z Navrátil

Department of Physical Electronics, Masaryk University, Kotlářská 2, CZ-61137 Brno, Czech Republic

E-mail: vasina@physics.muni.cz and zdenek@physics.muni.cz

Received 26 May 2015, revised 25 September 2015
Accepted for publication 22 October 2015
Published 25 November 2015

Abstract

The thorough characterizations of deposition plasma lead to important achievements in the fundamental understanding of the deposition process, with a clear impact on the development of technology. Measurement of the spatial and, in the case of pulse excited plasma, also temporal evolution, of the concentrations of sputtered atoms and ions is a primary task in the diagnostics of any sputter deposition plasma. However, it is difficult to estimate absolute number densities of the sputtered species (atoms and ions) in ground states directly from optical emission spectroscopy, because the species in the ground levels do not produce any optical signal. A method using effective branching fractions enables us to determine the density of non-radiating species from the intensities of self-absorbed spectral lines. The branching fractions method described in the first part of this paper was applied to determine the ground state densities of the sputtered titanium atoms and ions. The method is based on fitting the theoretically calculated branching fractions to experimentally measured ratios of the relative intensities of carefully selected resonant titanium atomic and ionic lines. The sputtered species density is determined in our experimental setup with a relative uncertainty of less than 5% for the dc driven magnetron and typically 15% for time-resolved measurements of high-power impulse magnetron sputtering (HiPIMS) discharge. In the second part of the paper, the method was applied to determine the evolution of titanium atom and ion densities in three typical cases ranging from the dc driven sputter process to HiPIMS.

Keywords: sputter species density, magnetron, HIPIMS, plasma diagnostics, titanium

(Some figures may appear in colour only in the online journal)

1. Introduction

The sputtering technique first reported by Grove in 1852 [1] has developed rapidly over recent decades to the point where it has become established as the process of choice for the deposition of a wide range of industrially important coatings, as it enables the deposition of high quality metals, alloys, ceramics and polymer thin films onto a wide range of substrate materials [2–6]. Magnetron sputtering belongs to the group of physical vapor deposition (PVD) techniques which generally involve the condensation of vapor created from a solid state source, often in the presence of a glow discharge or plasma. In many cases, magnetron sputtered films now outperform films deposited by other PVD processes, and can offer the same functionality as much thicker films produced by other coating techniques. Thin films deposited by magnetron sputtering find application in numerous technological domains including hard, wear-resistant, optical, corrosion-resistant coatings or coatings for microelectronics, etc [2–6].

In magnetron sputtering, film-forming species are sputtered by the plasma discharge from the magnetron target. In the sputtering process, atoms or small clusters of atoms [4] are physically ejected from the target surface and, as such, they have a significantly high kinetic energy of several eV,

on average, corresponding to a significantly high velocity of several km s^{-1}, on average [3, 7, 8]. Before being deposited onto the samples, the film-forming species should follow a certain pathway. On their pathway these particles may be ionized, neutralized, or they can chemically react with other particles in the gas phase. During their transport, it is also very likely that they exhibit gas-phase collisions with background gas atoms. In these collisions, significant kinetic energy can be shared with the gas atom, resulting in both cooling of the sputtered species and heating of the background gas [9, 10]. The film-forming species (sputtered species, ionized sputtered species, etc) are characterized through the spatial evolution of the physical parameters like their corresponding number density, ionization degree, energy or velocity distribution function, flux, etc.

The recently developed pulsed magnetron sputtering process (PMS) overcomes many of the problems encountered when operating in the reactive sputtering mode. It has been found that pulsing the magnetron discharge in the medium frequency range (tens to hundreds of kHz), when depositing insulating films, can significantly reduce the formation of arcs and consequently reduce the number of defects in the deposited film [11, 12]. In the mid 1990s [13, 14] pulsed sputtering techniques were modified to HiPIMS (high-power impulse magnetron sputtering) by using high power pulsed-dc plasma excitation [13, 14]. Due to the very low duty cycle (typically 1%), a very high pulse power density (several kW cm^{-2}) is delivered to the cathode during the active part of the period, resulting in a highly ionized fraction of the sputtered species and enhancement of the density and energy of the ions bombarding the growing film occurs [15–18]. In PMS and HiPIMS, the physical parameters describing the film-forming species are time dependent [15, 16, 18].

The establishment of the sputtering techniques, including reactive sputtering, PMS and HiPIMS, as a technology in high demand for many industrial applications, was possible because of the detailed characterization of the deposition plasma followed by a fundamental understanding of plasma physics. Several techniques that are suitable to follow the temporal and spatial evolution of sputtered species densities have been developed. Resonant optical absorption spectroscopy (ROAS) is based on measuring the absorption of the light emitted by a reference source (lamp or diode laser) in a medium containing the studied species [19–21]. The method was developed to measure the spatial and temporal evolution of the densities of sputtered atoms and ions [22–25]. ROAS is a typical line-of-sight method enabling us to derive averaged densities of the sputtered species. Laser induced fluorescence (LIF) based on resonant absorption of a photon followed by a fluorescence [26–28] provides a good spatial and temporal distribution of the studied species densities, velocities and fluxes [29–33].

Since the sputtered species in ground or metastable levels do not produce any optical signal directly, it is difficult to obtain information about the number densities of the species in these levels from optical emission spectroscopy (OES). However, recently a variety of indirect methods based on self-absorption have been developed to obtain number densities, particularly of the rare gases' atoms in metastable levels [34–36]. In this paper, we applied the method based on effective branching fractions [35] to be able to determine the number densities of the sputtered atoms and ions in ground levels in PVD experiments. The method is based on fitting theoretically calculated branching fractions to measured ratios of the relative intensities of carefully selected lines of the measured species. The proposed method belongs to the group of line-of-sight methods like ROAS. The method does not require any reference source (lamp or diode laser) and the densities are determined directly from optical emission spectroscopy signals. The OES measurement is simple and also enables us to implement the proposed method for sputtering experiments with very limited access. Only a window or a vacuum feed-through for an optical fiber, together with a spectrometer with sufficient resolution, is needed to perform the measurement. The theoretical background of the proposed method, as well as the fitting procedure, will be presented in the paper together with several examples of the application of the proposed method, including the determination of the steady-state titanium atom density in a dc sputtering experiment and temporal evolution of titanium atom and ion densities in a HiPIMS experiment.

2. Experimental setup

The measurements were carried out on the magnetron sputtering system Alcatel SCM 650. The sputtering system was equipped with a Ti target (99.95% purity) of 20 cm in diameter and balanced magnetic field configuration. The discharge was powered by a Melec SIPP 2000 HiPIMS generator operated in both dc and HiPIMS mode. The supplied power varied from 0.1 to 2.0 kW in dc mode. In HiPIMS mode, the voltage was set to 500 V and 400 V for short (200 μs) and long pulse (1200 μs), respectively, and the repetition rate was 20 Hz for both pulses.

The deposition chamber was evacuated by a turbo-molecular pump backed with a Roots pump down to a pressure of 10^{-4} Pa. The buffer gas was argon (99.999%) and the gas inlet was located at a distance of 20 mm above the target. The working pressure was varied from 0.3 Pa to 5.4 Pa by the gas flow meter (1–140 sccm) and measured by a MKS Baratron.

The Melec generator was equipped with a current and voltage probe for electric measurements. The optical emission spectroscopy (OES) was carried out using a Jobin–Yvon Horiba FHR1000 spectrometer (Czerny–Turner configuration) with 1 m focal length and 2400 grooves mm^{-1} grating. Both CCD and an intensified CCD camera (Andor IStar 720) at the exit ports of the monochromator served as the detectors. The specified spectral resolution is 8 pm, whereas when using ICCD the time resolution is up to 3 ns. The total integration time was set to achieve sufficient line intensities. The optical fiber was placed on a movable holder to collect the light from two different spaces above the target (7.5 mm and 23 mm) and it was directed along the tangent line of the racetrack, parallel with the target, to achieve the longest optical depth.

3. Effective branching fractions method

3.1. Theory

The effective branching fractions method (EBF method) was originally developed to measure the metastable and resonant state densities of argon atoms from self-absorbed optical emission spectra [35, 36]. In contrast to absorption methods measuring the attenuation of light passing through the plasma from an external light source, self-absorption methods consider the studied plasma as both a light emitting and a light absorbing medium. When the optical depth of a transition is $kL \gtrsim 1$ (k is the absorption coefficient and L is the plasma depth in the direction of observation), photons emitted in the discharge may be significantly re-absorbed by atoms in the lower state of the transition before escaping the plasma. Unlike classical self-absorption methods comparing intensities of transitions with the same lower level [34], the EBF method compares intensities of transitions from a common upper level i by means of branching fractions

$$\Gamma_{ij} = \frac{\Phi_{ij}}{\sum_l \Phi_{il}}, \tag{1}$$

where Φ_{ij} is the photon emission rate of transition $i \rightarrow j$ and the summing is performed over all possible lower states l. In the absence of absorption, the photon emission rates are simply proportional to the product of the Einstein coefficient for spontaneous emission A_{ij} and the number of atoms in the excited states and the branching fractions are equal to

$$\Gamma_{ij}^{\text{free}} = \frac{A_{ij}}{\sum_l A_{il}}. \tag{2}$$

The branching fractions for absorption-free plasma are therefore simply determined by the Einstein coefficients.

When self-absorption of radiation occurs in plasma, apparent branching fractions of escaping radiation may be altered, since the light of different transitions is absorbed to a different extent. The self-absorption in plasma is often estimated using the concept of escape factors developed by Holstein [37]. The effective branching fraction of a spectral line in the presence of self-absorption is calculated as

$$\Gamma_{ij}^{\text{eff}} = \frac{g(k_{ij}^0 L) A_{ij}}{\sum_l g(k_{il}^0 L) A_{il}}, \tag{3}$$

where g is the (radiation) escape factor depending on the absorption coefficient k_{il}^0 evaluated at the spectral line center and L is a sensed plasma depth. The accurate evaluation of self-absorption in a magnetron sputtering system is a non-trivial problem. In order to keep the method simple, we adopted the commonly-used approximative formula of Mewe [38]

$$g(k_{ij}^0 L) = \frac{2 - \mathrm{e}^{-k_{ij}^0 L/1000}}{1 + k_{ij}^0 L}. \tag{4}$$

The formula assumes a uniform spatial distribution of atoms in both upper and lower states of transition. In our case, the distributions of atoms in the chamber are inhomogeneous, with most of the atoms located just above the racetrack. When the optical fiber is directed along the tangent line of the racetrack (and parallel with the target), the fiber senses a region of enhanced density of a depth $L \approx 10$ cm. This value is taken into account in the calculations as the absorption path; however, the uncertainty of the determination of this absorption path can contribute significantly to the measurement error. Since Doppler broadening is the dominant broadening mechanism at a pressure of ≈1 Pa, the absorption coefficient k_{ij}^0 at the line center is calculated as

$$k_{ij}^0 = \frac{\lambda_{ij}^3}{8\pi^{3/2}} \sqrt{\frac{m_0}{2k_\mathrm{b}T}} \frac{g_i}{g_j} A_{ij} n_j, \tag{5}$$

in which m_0 is atomic mass, λ_{ij} is the wavelength of the transition in the line center, T is kinetic temperature of atoms and g_i and g_j are the statistical weights of the upper and lower levels, respectively. In this paper, $T = 500$ K was assumed. The density of the lower state n_j is the unknown quantity. In order to determine the density of a specific atomic state, the intensities of spectral lines of spontaneous transitions ending in the studied state and of their competitive transitions from the same upper level must be measured. Since such transitions will end on several lower states, several densities n_j are typically simultaneously determined. It is recommended [36] to measure more spectral lines and fit the effective branching fractions (3) using the least squares method to the measured values

$$\Gamma_{ij}^{\text{exp}} = \frac{I_{ij}/h\nu_{ij}}{\sum_l I_{il}/h\nu_{il}}. \tag{6}$$

where $h\nu_{ij}$ are photon energies. The measured intensities I_{ij} should be corrected for spectrometer spectral sensitivity and integrated over the spectral profiles.

For ease of use the *EBF fit* software was developed [39], enabling the calculation of branching fractions from measured line intensities and their fit by the least squares method. The software enables us to determine the titanium atom and ion ground state density from optical emission spectra. A database of spectral lines with wavelengths, Einstein coefficients, statistical weights etc needed for the calculation of branching fractions of the titanium atom and ion is included in the software.

3.2. Application to ground state Ti atoms

The ground state of a titanium neutral atom, originating from electron configuration $1s^2 2s^2 2p^6 3s^2 3p^6 3d^2 4s^2$, is a $^3\mathrm{F}_2$. Letter 'a' ('b', 'c', ... or 'z', 'y', ...) appearing in front of the term symbol, distinguishes the same terms of even or odd parity, respectively, but of a different configuration, ordering them according to increasing energy [41]. In other levels a $^3\mathrm{F}_3$ and a $^3\mathrm{F}_4$ of the triplet term lie 0.021 and 0.048 eV above the ground state, respectively.

The optical spectrum of titanium in the UV-VIS range is plentiful. The spectral lines sorted according to their upper state, fulfilling the condition of one transition going to the ground state, are summarized in table 1. The lines

Table 1. Einstein coefficients of spontaneous emission and branching fractions for transitions of isolated titanium atom [40].

Transition	λ (nm)		A_{ij} (10^7 s^{-1})	Γ_{ij}
$3d^2(^3\mathrm{F})4s4p(^3\mathrm{P}^\circ)$ z $^5\mathrm{D}^\circ_3 \rightarrow 3d^24s^2$ a $^3\mathrm{F}_3$	542.624 80		0.003 68	0.724
$3d^2(^3\mathrm{F})4s4p(^3\mathrm{P}^\circ)$ z $^5\mathrm{D}^\circ_3 \rightarrow 3d^24s^2$ a $^3\mathrm{F}_4$	549.084 80		0.001 40	0.276
$3d^2(^3\mathrm{F})4s4p(^3\mathrm{P}^\circ)$ z $^3\mathrm{F}^\circ_2 \rightarrow 3d^24s^2$ a $^3\mathrm{F}_2$	517.374 00		0.423 00	0.940
$3d^2(^3\mathrm{F})4s4p(^3\mathrm{P}^\circ)$ z $^3\mathrm{F}^\circ_2 \rightarrow 3d^24s^2$ a $^3\mathrm{F}_3$	521.969 90		0.027 10	0.060
$3d^2(^3\mathrm{F})4s4p(^3\mathrm{P}^\circ)$ z $^3\mathrm{F}^\circ_3 \rightarrow 3d^24s^2$ a $^3\mathrm{F}_2$	514.747 70		0.048 50	0.103
$3d^2(^3\mathrm{F})4s4p(^3\mathrm{P}^\circ)$ z $^3\mathrm{F}^\circ_3 \rightarrow 3d^24s^2$ a $^3\mathrm{F}_3$	519.296 90		0.386 00	0.865
$3d^2(^3\mathrm{F})4s4p(^3\mathrm{P}^\circ)$ z $^3\mathrm{F}^\circ_3 \rightarrow 3d^24s^2$ a $^3\mathrm{F}_4$	525.209 90		0.014 20	0.032
$3d^2(^3\mathrm{F})4s4p(^3\mathrm{P}^\circ)$ z $^3\mathrm{F}^\circ_4 \rightarrow 3d^24s^2$ a $^3\mathrm{F}_3$	515.218 40		0.035 10	0.083
$3d^2(^3\mathrm{F})4s4p(^3\mathrm{P}^\circ)$ z $^3\mathrm{F}^\circ_4 \rightarrow 3d^24s^2$ a $^3\mathrm{F}_4$	521.038 40		0.389 00	0.917
$3d^2(^3\mathrm{F})4s4p(^3\mathrm{P}^\circ)$ z $^3\mathrm{D}^\circ_2 \rightarrow 3d^24s^2$ a $^3\mathrm{F}_4$	499.709 30		0.046 90	0.095
$3d^2(^3\mathrm{F})4s4p(^3\mathrm{P}^\circ)$ z $^3\mathrm{D}^\circ_2 \rightarrow 3d^24s^2$ a $^3\mathrm{F}_3$	503.995 50		0.449 00	0.905
$3d^2(^3\mathrm{F})4s4p(^3\mathrm{P}^\circ)$ z $^3\mathrm{D}^\circ_3 \rightarrow 3d^24s^2$ a $^3\mathrm{F}_3$	500.964 50		0.024 10	0.052
$3d^2(^3\mathrm{F})4s4p(^3\mathrm{P}^\circ)$ z $^3\mathrm{D}^\circ_3 \rightarrow 3d^24s^2$ a $^3\mathrm{F}_4$	506.465 20		0.437 00	0.948
$3d^2(^3\mathrm{F})4s4p(^3\mathrm{P}^\circ)$ z $^3\mathrm{G}^\circ_3 \rightarrow 3d^24s^2$ a $^3\mathrm{F}_2$	465.646 80		0.229 00	0.964
$3d^2(^3\mathrm{F})4s4p(^3\mathrm{P}^\circ)$ z $^3\mathrm{G}^\circ_3 \rightarrow 3d^24s^2$ a $^3\mathrm{F}_3$	469.366 40		0.008 50	0.036
$3d^2(^3\mathrm{F})4s4p(^3\mathrm{P}^\circ)$ z $^3\mathrm{G}^\circ_4 \rightarrow 3d^24s^2$ a $^3\mathrm{F}_3$	466.758 40		0.251 00	0.973
$3d^2(^3\mathrm{F})4s4p(^3\mathrm{P}^\circ)$ z $^3\mathrm{G}^\circ_4 \rightarrow 3d^24s^2$ a $^3\mathrm{F}_4$	471.529 90		0.006 90	0.027
$3d^2(^3\mathrm{F})4s4p(^3\mathrm{P}^\circ)$ z $^1\mathrm{F}^\circ_3 \rightarrow 3d^24s^2$ a $^3\mathrm{F}_2$	446.208 80		0.004 28	0.280
$3d^2(^3\mathrm{F})4s4p(^3\mathrm{P}^\circ)$ z $^1\mathrm{F}^\circ_3 \rightarrow 3d^24s^2$ a $^3\mathrm{F}_3$	449.623 40		0.011 00	0.720
$3d^2(^3\mathrm{P})4s4p(^3\mathrm{P}^\circ)$ z $^5\mathrm{S}^\circ_2 \rightarrow 3d^24s^2$ a $^3\mathrm{F}_2$	398.248 06	✓	0.450 00	0.764
$3d^2(^3\mathrm{P})4s4p(^3\mathrm{P}^\circ)$ z $^5\mathrm{S}^\circ_2 \rightarrow 3d^24s^2$ a $^3\mathrm{F}_3$	400.965 65	✓	0.139 00	0.236
$3d^2(^3\mathrm{F})4s4p(^1\mathrm{P}^\circ)$ y $^3\mathrm{F}^\circ_2 \rightarrow 3d^24s^2$ a $^3\mathrm{F}_2$	398.176 16	✓	4.420 00	0.846
$3d^2(^3\mathrm{F})4s4p(^1\mathrm{P}^\circ)$ y $^3\mathrm{F}^\circ_2 \rightarrow 3d^24s^2$ a $^3\mathrm{F}_3$	400.892 73	✓	0.807 00	0.154
$3d^2(^3\mathrm{F})4s4p(^1\mathrm{P}^\circ)$ y $^3\mathrm{F}^\circ_3 \rightarrow 3d^24s^2$ a $^3\mathrm{F}_2$	396.285 08	✓	0.471 00	0.083
$3d^2(^3\mathrm{F})4s4p(^1\mathrm{P}^\circ)$ y $^3\mathrm{F}^\circ_3 \rightarrow 3d^24s^2$ a $^3\mathrm{F}_3$	398.975 86	✓	4.480 00	0.794
$3d^2(^3\mathrm{F})4s4p(^1\mathrm{P}^\circ)$ y $^3\mathrm{F}^\circ_3 \rightarrow 3d^24s^2$ a $^3\mathrm{F}_4$	402.457 09	✓	0.691 00	0.122
$3d^2(^3\mathrm{F})4s4p(^1\mathrm{P}^\circ)$ y $^3\mathrm{F}^\circ_4 \rightarrow 3d^24s^2$ a $^3\mathrm{F}_3$	396.426 94	✓	0.364 00	0.070
$3d^2(^3\mathrm{F})4s4p(^1\mathrm{P}^\circ)$ y $^3\mathrm{F}^\circ_4 \rightarrow 3d^24s^2$ a $^3\mathrm{F}_4$	399.863 66	✓	4.810 00	0.930
$3d^3(^4\mathrm{F})4p$ y $^3\mathrm{D}^\circ_2 \rightarrow 3d^24s^2$ a $^3\mathrm{F}_2$	392.987 40	✓	0.851 00	0.197
$3d^3(^4\mathrm{F})4p$ y $^3\mathrm{D}^\circ_2 \rightarrow 3d^24s^2$ a $^3\mathrm{F}_3$	395.633 43	✓	3.460 00	0.803
$3d^3(^4\mathrm{F})4p$ y $^3\mathrm{D}^\circ_3 \rightarrow 3d^24s^2$ a $^3\mathrm{F}_2$	389.848 86		0.037 70	0.007
$3d^3(^4\mathrm{F})4p$ y $^3\mathrm{D}^\circ_3 \rightarrow 3d^24s^2$ a $^3\mathrm{F}_3$	392.452 68	✓	0.810 00	0.141
$3d^3(^4\mathrm{F})4p$ y $^3\mathrm{D}^\circ_3 \rightarrow 3d^24s^2$ a $^3\mathrm{F}_4$	395.820 16	✓	4.880 00	0.852
$3d^2(^1\mathrm{D})4s4p(^3\mathrm{P}^\circ)$ $^3\mathrm{P}^\circ_2 \rightarrow 3d^24s^2$ a $^3\mathrm{F}_2$	392.142 25		0.248 00	0.205
$3d^2(^1\mathrm{D})4s4p(^3\mathrm{P}^\circ)$ $^3\mathrm{P}^\circ_2 \rightarrow 3d^24s^2$ a $^3\mathrm{F}_3$	394.776 86		0.960 00	0.795
$3d^2(^3\mathrm{P})4s4p(^3\mathrm{P}^\circ)$ $^5\mathrm{D}^\circ_3 \rightarrow 3d^24s^2$ a $^3\mathrm{F}_3$	390.095 94		0.147 00	0.766
$3d^2(^3\mathrm{P})4s4p(^3\mathrm{P}^\circ)$ $^5\mathrm{D}^\circ_3 \rightarrow 3d^24s^2$ a $^3\mathrm{F}_4$	393.423 36		0.045 00	0.234
$3d^2(^3\mathrm{P})4s4p(^3\mathrm{P}^\circ)$ $^5\mathrm{D}^\circ_4 \rightarrow 3d^24s^2$ a $^3\mathrm{F}_3$	388.139 55		0.030 00	0.115
$3d^2(^3\mathrm{P})4s4p(^3\mathrm{P}^\circ)$ $^5\mathrm{D}^\circ_4 \rightarrow 3d^24s^2$ a $^3\mathrm{F}_4$	391.433 47		0.230 00	0.885
$3d^2(^1\mathrm{D})4s4p(^3\mathrm{P}^\circ)$ x $^3\mathrm{F}^\circ_2 \rightarrow 3d^24s^2$ a $^3\mathrm{F}_2$	372.980 65		4.930 00	0.857
$3d^2(^1\mathrm{D})4s4p(^3\mathrm{P}^\circ)$ x $^3\mathrm{F}^\circ_2 \rightarrow 3d^24s^2$ a $^3\mathrm{F}_3$	375.363 32		0.820 00	0.143
$3d^2(^1\mathrm{D})4s4p(^3\mathrm{P}^\circ)$ x $^3\mathrm{F}^\circ_3 \rightarrow 3d^24s^2$ a $^3\mathrm{F}_2$	371.739 16		0.430 00	0.072
$3d^2(^1\mathrm{D})4s4p(^3\mathrm{P}^\circ)$ x $^3\mathrm{F}^\circ_3 \rightarrow 3d^24s^2$ a $^3\mathrm{F}_3$	374.105 97		4.810 00	0.810
$3d^2(^1\mathrm{D})4s4p(^3\mathrm{P}^\circ)$ x $^3\mathrm{F}^\circ_3 \rightarrow 3d^24s^2$ a $^3\mathrm{F}_4$	377.165 11		0.695 00	0.117
$3d^2(^1\mathrm{D})4s4p(^3\mathrm{P}^\circ)$ x $^3\mathrm{F}^\circ_4 \rightarrow 3d^24s^2$ a $^3\mathrm{F}_3$	372.257 03		0.340 00	0.055
$3d^2(^1\mathrm{D})4s4p(^3\mathrm{P}^\circ)$ x $^3\mathrm{F}^\circ_4 \rightarrow 3d^24s^2$ a $^3\mathrm{F}_4$	375.285 88		5.810 00	0.945
$3d^2(^1\mathrm{D})4s4p(^3\mathrm{P}^\circ)$ x $^3\mathrm{D}^\circ_2 \rightarrow 3d^24s^2$ a $^3\mathrm{F}_2$	364.619 60		0.260 00	0.325
$3d^2(^1\mathrm{D})4s4p(^3\mathrm{P}^\circ)$ x $^3\mathrm{D}^\circ_2 \rightarrow 3d^24s^2$ a $^3\mathrm{F}_3$	366.896 34		0.540 00	0.675

(*Continued*)

Table 1. (*Continued*)

Transition	λ (nm)	A_{ij} (10^7 s^{-1})	Γ_{ij}
$3d^2(^1\mathrm{D})4s4p(^3\mathrm{P}^\circ)$ x $^3\mathrm{D}^\circ_3 \rightarrow 3d^24s^2$ a $^3\mathrm{F}_2$	363.796 50	0.093 00	0.116
$3d^2(^1\mathrm{D})4s4p(^3\mathrm{P}^\circ)$ x $^3\mathrm{D}^\circ_3 \rightarrow 3d^24s^2$ a $^3\mathrm{F}_3$	366.062 92	0.300 00	0.375
$3d^2(^1\mathrm{D})4s4p(^3\mathrm{P}^\circ)$ x $^3\mathrm{D}^\circ_3 \rightarrow 3d^24s^2$ a $^3\mathrm{F}_4$	368.991 42	0.407 00	0.509
$3d^2(^3\mathrm{F})4s4p(^1\mathrm{P}^\circ)$ y $^3\mathrm{G}^\circ_3 \rightarrow 3d^24s^2$ a $^3\mathrm{F}_2$	363.546 25	9.090 00	0.931
$3d^2(^3\mathrm{F})4s4p(^1\mathrm{P}^\circ)$ y $^3\mathrm{G}^\circ_3 \rightarrow 3d^24s^2$ a $^3\mathrm{F}_3$	365.809 52	0.642 00	0.066
$3d^2(^3\mathrm{F})4s4p(^1\mathrm{P}^\circ)$ y $^3\mathrm{G}^\circ_3 \rightarrow 3d^24s^2$ a $^3\mathrm{F}_4$	368.733 96	0.036 80	0.004
$3d^2(^3\mathrm{F})4s4p(^1\mathrm{P}^\circ)$ y $^3\mathrm{G}^\circ_4 \rightarrow 3d^24s^2$ a $^3\mathrm{F}_3$	364.267 39	8.950 00	0.946
$3d^2(^3\mathrm{F})4s4p(^1\mathrm{P}^\circ)$ y $^3\mathrm{G}^\circ_4 \rightarrow 3d^24s^2$ a $^3\mathrm{F}_4$	367.167 11	0.506 00	0.054
$3d^2(^3\mathrm{F})4s4p(^1\mathrm{P}^\circ)$ w $^3\mathrm{D}^\circ_2 \rightarrow 3d^24s^2$ a $^3\mathrm{F}_2$	335.827 11	0.760 00	0.099
$3d^2(^3\mathrm{F})4s4p(^1\mathrm{P}^\circ)$ w $^3\mathrm{D}^\circ_2 \rightarrow 3d^24s^2$ a $^3\mathrm{F}_3$	337.757 52	6.900 00	0.901
$3d^2(^1\mathrm{G})4s4p(^3\mathrm{P}^\circ)$ x $^3\mathrm{G}^\circ_3 \rightarrow 3d^24s^2$ a $^3\mathrm{F}_2$	334.187 40	6.500 00	0.926
$3d^2(^1\mathrm{G})4s4p(^3\mathrm{P}^\circ)$ x $^3\mathrm{G}^\circ_3 \rightarrow 3d^24s^2$ a $^3\mathrm{F}_4$	338.566 06	0.520 00	0.074
$3d^2(^1\mathrm{G})4s4p(^3\mathrm{P}^\circ)$ x $^3\mathrm{G}^\circ_4 \rightarrow 3d^24s^2$ a $^3\mathrm{F}_3$	335.463 36	6.900 00	0.918
$3d^2(^1\mathrm{G})4s4p(^3\mathrm{P}^\circ)$ x $^3\mathrm{G}^\circ_4 \rightarrow 3d^24s^2$ a $^3\mathrm{F}_4$	337.921 11	0.620 00	0.082
$3d^3(^4\mathrm{F})4p$ w $^3\mathrm{G}^\circ_3 \rightarrow 3d^24s^2$ a $^3\mathrm{F}_2$	318.645 10	8.000 00	0.917
$3d^3(^4\mathrm{F})4p$ w $^3\mathrm{G}^\circ_3 \rightarrow 3d^24s^2$ a $^3\mathrm{F}_3$	320.382 54	0.720 00	0.083
$3d^3(^4\mathrm{F})4p$ w $^3\mathrm{G}^\circ_4 \rightarrow 3d^24s^2$ a $^3\mathrm{F}_3$	319.199 31	8.500 00	0.929
$3d^3(^4\mathrm{F})4p$ w $^3\mathrm{G}^\circ_4 \rightarrow 3d^24s^2$ a $^3\mathrm{F}_4$	321.423 73	0.650 00	0.071
$3d^3(^4\mathrm{F})4p$ w $^3\mathrm{F}^\circ_4 \rightarrow 3d^24s^2$ a $^3\mathrm{F}_3$	298.147 30	0.073 00	0.057
$3d^3(^4\mathrm{F})4p$ w $^3\mathrm{F}^\circ_4 \rightarrow 3d^24s^2$ a $^3\mathrm{F}_4$	300.086 50	1.200 00	0.943
$3d^2(^1\mathrm{G})4s4p(^3\mathrm{P}^\circ)$ v $^3\mathrm{F}^\circ_2 \rightarrow 3d^24s^2$ a $^3\mathrm{F}_2$	294.199 50	0.073 00	0.847
$3d^2(^1\mathrm{G})4s4p(^3\mathrm{P}^\circ)$ v $^3\mathrm{F}^\circ_2 \rightarrow 3d^24s^2$ a $^3\mathrm{F}_3$	295.678 20	1.800 00	0.153
$3d^2(^1\mathrm{G})4s4p(^3\mathrm{P}^\circ)$ v $^3\mathrm{F}^\circ_3 \rightarrow 3d^24s^2$ a $^3\mathrm{F}_2$	293.352 80	0.960 00	0.085
$3d^2(^1\mathrm{G})4s4p(^3\mathrm{P}^\circ)$ v $^3\mathrm{F}^\circ_3 \rightarrow 3d^24s^2$ a $^3\mathrm{F}_3$	294.824 20	9.300 00	0.819
$3d^2(^1\mathrm{G})4s4p(^3\mathrm{P}^\circ)$ v $^3\mathrm{F}^\circ_3 \rightarrow 3d^24s^2$ a $^3\mathrm{F}_4$	296.722 50	1.100 00	0.097
$3d^2(^1\mathrm{G})4s4p(^3\mathrm{P}^\circ)$ v $^3\mathrm{F}^\circ_4 \rightarrow 3d^24s^2$ a $^3\mathrm{F}_3$	293.730 40	0.770 00	0.074
$3d^2(^1\mathrm{G})4s4p(^3\mathrm{P}^\circ)$ v $^3\mathrm{F}^\circ_4 \rightarrow 3d^24s^2$ a $^3\mathrm{F}_4$	295.612 30	9.700 00	0.926

Note: Lines are divided into groups with a common upper level.

taken for measurement are marked with a checkmark. The utilizable lines have to meet several requirements: high transition probability (Einstein coefficient), no overlapping with surrounding spectral features in the measured spectra, ease of measurement and instrument calibration etc. A number of transitions cannot be used. For example, the lowest excited state with stronger transition down to ground state is z $^3\mathrm{F}^\circ_2$, with line 517.3740 nm ($A = 4.2 \times 10^6$ s^{-1}). However, other lines with the same upper state are weak—521.9699 nm ($A = 2.7 \times 10^5$ s^{-1}) or in the infrared region, e.g. 1283.1432 nm ($A = 3.3 \times 10^5$ s^{-1}). Therefore, this line cannot be used in our measurement. The line with the highest transition probability going down to the ground state is 264.108 70 nm line ($A = 1.8 \times 10^8$ s^{-1}, upper state u $^3\mathrm{D}^\circ_1$). Since there is no other transition out of the u $^3\mathrm{D}^\circ_1$ level, the line cannot be used in the EBF method. On the other hand, all three lines 396.285 08, 398.975 86 and 402.457 09 nm coming from the y $^3\mathrm{F}^\circ_3$ level can be used. Ending in different levels of the ground state term a ^{3}F, they have sufficiently high Einstein coefficients and intensities in spectra, and the Einstein coefficient ratio is up to 9.5. Close wavelengths provide a low impact of varying instrument sensitivity on the measured intensity values.

The selected transitions of the neutral Ti atom with their upper and lower levels are shown in a diagram in figure 1(a). In order to calculate the effective branching fractions from formula (3), the densities of all three a ^{3}F levels must be taken into account. Since the energy splitting of the levels is low, the levels are assumed to be in local thermodynamic equilibrium with the densities following the Boltzmann law

$$n_j = n_0 \frac{g_j}{g_0} \mathrm{e}^{-\frac{E_j - E_0}{k_\mathrm{b} T_\mathrm{exc}}},$$

where T_exc is the excitation temperature of the a ^{3}F triplet state and n_0 is the density of the a $^3\mathrm{F}_2$ level. By fitting 13 branching fractions of selected transitions (see table 1), n_0 and T_exc quantities are determined. Since the populations of a $^3\mathrm{F}_3$ and a $^3\mathrm{F}_4$ levels are not negligible, the sum of the densities of all three levels is taken as the resulting density of titanium atoms [Ti].

3.3. Application to ground state Ti ions

The ground state of singly ionized titanium, originating from electron configuration $1s^22s^22p^63s^23p^63d^24s$, is a $^4\mathrm{F}_{3/2}$. Other

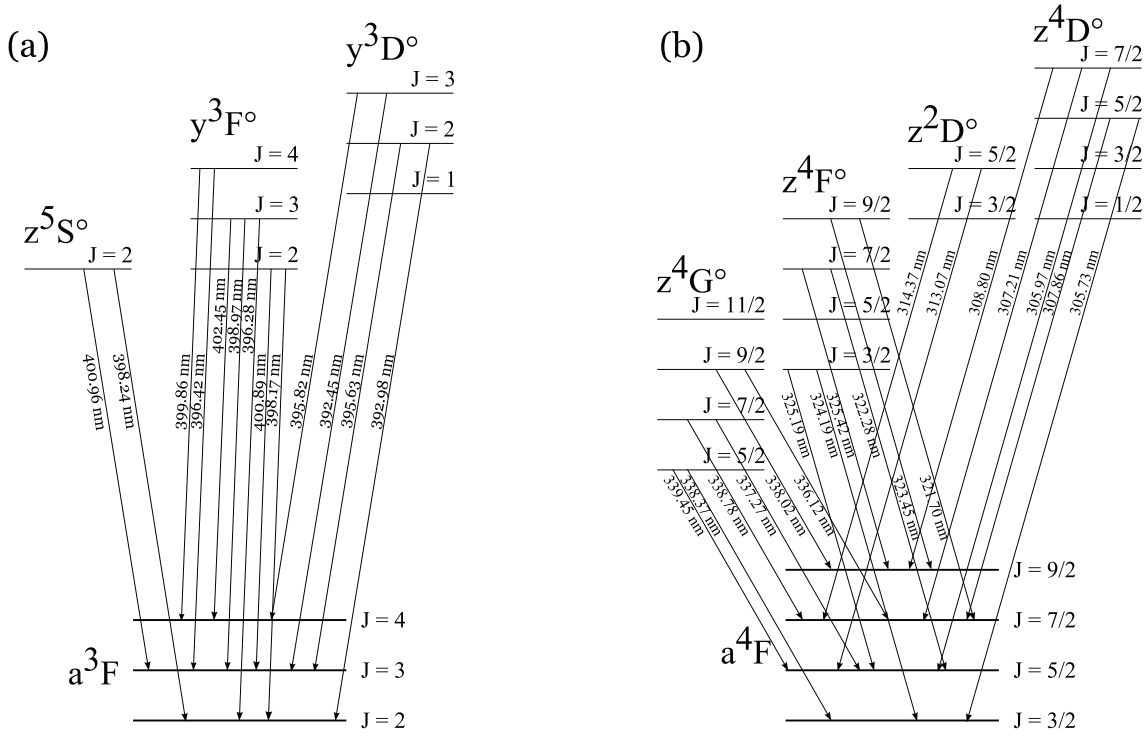

Figure 1. Energy levels and selected transitions for density measurement of (a) Ti neutral atom and (b) Ti ion.

levels, a $^4F_{5/2}$, a $^4F_{7/2}$ and a $^4F_{9/2}$, of the quartet term lie 0.012, 0.028 and 0.049 eV above the ground state, respectively, [41].

The spectral lines of the Ti ion sorted according to their upper state, fulfilling the condition of one transition going to the ground state, are summarized in table 2; 19 selected transitions with their upper and lower levels are shown in a diagram in figure 1(b). In order to calculate the effective branching fractions, the densities of all a ^4F levels must be evaluated. As in the case of neutral titanium, Boltzmann's law is taken to decrease the number of fitted parameters. The sum of densities of all four levels is taken as the resulting density of titanium ions $[Ti^+]$.

4. Examples

In the forthcoming section the developed method to determine the number density of the titanium atoms and ions in the ground state based on the effective branching fractions will be applied to several demonstrative examples. We would like to compare the results based on the developed methods with another independent method like ROAS or LIF, as well, but our experimental setup does not allow this direct comparison because of the lack of properly oriented observation windows. Therefore, we present the results of several case studies, where the results can be either directly compared to data from the literature obtained by other techniques under similar experimental conditions, or where the results can be well predicted on the basis of the experience. The following three case studies were selected: an evolution of the Ti atom density with dc power and argon pressure, an evolution of the Ti atom and ion density for a constant average power and a pulse length but a different duty cycle, and as the third example, a time evolution of the Ti atom and ion density in a HiPIMS pulse. In the selected case studies the spectra in the appropriate spectral range were measured and the data were processed as described in the previous chapter. The purpose of this section is not to present completely new and original findings, but to demonstrate on a few selected examples the application of the EBF method for determining the density of sputtered particles from optical emission spectra and to compare the obtained results with data from the literature and expectations based on the state-of-the-art.

4.1. Power and pressure dependence of Ti atom density in dc mode

As the first case study, the dependency of the density of titanium atoms sputtered in the dc mode on argon pressure and power supplied to the discharge was measured. The Ti ion lines were not strong enough to acquire good data for the calculation of titanium ion density in the dc driven magnetron discharge. The spectra were recorded using a CCD detector with the integration time adjusted to achieve good data quality in the spectral range corresponding to selected Ti lines (see table 1). The optical fiber with a collimator was placed to collect the light from the area located 23 mm above the target surface.

Two examples of the fit of effective branching fractions for the applied powers of 100 W and 2000 W are shown in figures 2(a) and (b), respectively. The branching fractions obtained from the measured line intensities are represented by colored vertical lines, the branching fractions for the absorption-free case by black horizontal abscissae, and the fitted branching fractions are represented by blue crosses. Lines of the same upper state are visualized with the same

Table 2. Einstein coefficients of spontaneous emission and branching fractions for transitions of titanium ion [40].

Transition	λ (nm)		A_{ij} (10^7 s^{-1})	Γ_{ij}
$3d^2(^3\mathrm{F})4p$ z $^4\mathrm{G}^\circ_{5/2} \rightarrow 3d^2(^3\mathrm{F})4s$ a $^4\mathrm{F}_{3/2}$	338.375 84	✓	13.900 00	0.833
$3d^2(^3\mathrm{F})4p$ z $^4\mathrm{G}^\circ_{5/2} \rightarrow 3d^2(^3\mathrm{F})4s$ a $^4\mathrm{F}_{5/2}$	339.457 21	✓	2.690 00	0.161
$3d^2(^3\mathrm{F})4p$ z $^4\mathrm{G}^\circ_{5/2} \rightarrow 3d^2(^3\mathrm{F})4s$ a $^4\mathrm{F}_{7/2}$	340.980 84		0.099 60	0.006
$3d^2(^3\mathrm{F})4p$ z $^4\mathrm{G}^\circ_{7/2} \rightarrow 3d^2(^3\mathrm{F})4s$ a $^4\mathrm{F}_{5/2}$	337.279 27	✓	14.100 00	0.830
$3d^2(^3\mathrm{F})4p$ z $^4\mathrm{G}^\circ_{7/2} \rightarrow 3d^2(^3\mathrm{F})4s$ a $^4\mathrm{F}_{7/2}$	338.783 34	✓	2.810 00	0.165
$3d^2(^3\mathrm{F})4p$ z $^4\mathrm{G}^\circ_{7/2} \rightarrow 3d^2(^3\mathrm{F})4s$ a $^4\mathrm{F}_{9/2}$	340.720 22		0.071 50	0.004
$3d^2(^3\mathrm{F})4p$ z $^4\mathrm{G}^\circ_{9/2} \rightarrow 3d^2(^3\mathrm{F})4s$ a $^4\mathrm{F}_{7/2}$	336.121 21	✓	15.800 00	0.920
$3d^2(^3\mathrm{F})4p$ z $^4\mathrm{G}^\circ_{9/2} \rightarrow 3d^2(^3\mathrm{F})4s$ a $^4\mathrm{F}_{9/2}$	338.027 66	✓	1.370 00	0.080
$3d^2(^3\mathrm{F})4p$ z $^4\mathrm{F}^\circ_{3/2} \rightarrow 3d^2(^3\mathrm{F})4s$ a $^4\mathrm{F}_{3/2}$	324.198 25	✓	14.700 00	0.782
$3d^2(^3\mathrm{F})4p$ z $^4\mathrm{F}^\circ_{3/2} \rightarrow 3d^2(^3\mathrm{F})4s$ a $^4\mathrm{F}_{5/2}$	325.190 78	✓	4.090 00	0.218
$3d^2(^3\mathrm{F})4p$ z $^4\mathrm{F}^\circ_{5/2} \rightarrow 3d^2(^3\mathrm{F})4s$ a $^4\mathrm{F}_{3/2}$	322.918 95		2.930 00	0.154
$3d^2(^3\mathrm{F})4p$ z $^4\mathrm{F}^\circ_{5/2} \rightarrow 3d^2(^3\mathrm{F})4s$ a $^4\mathrm{F}_{5/2}$	323.903 66		12.600 00	0.664
$3d^2(^3\mathrm{F})4p$ z $^4\mathrm{F}^\circ_{5/2} \rightarrow 3d^2(^3\mathrm{F})4s$ a $^4\mathrm{F}_{7/2}$	325.290 57		3.440 00	0.181
$3d^2(^3\mathrm{F})4p$ z $^4\mathrm{F}^\circ_{7/2} \rightarrow 3d^2(^3\mathrm{F})4s$ a $^4\mathrm{F}_{5/2}$	322.284 13	✓	3.070 00	0.162
$3d^2(^3\mathrm{F})4p$ z $^4\mathrm{F}^\circ_{7/2} \rightarrow 3d^2(^3\mathrm{F})4s$ a $^4\mathrm{F}_{7/2}$	323.657 20		13.700 00	0.723
$3d^2(^3\mathrm{F})4p$ z $^4\mathrm{F}^\circ_{7/2} \rightarrow 3d^2(^3\mathrm{F})4s$ a $^4\mathrm{F}_{9/2}$	325.424 53	✓	2.170 00	0.115
$3d^2(^3\mathrm{F})4p$ z $^4\mathrm{F}^\circ_{9/2} \rightarrow 3d^2(^3\mathrm{F})4s$ a $^4\mathrm{F}_{7/2}$	321.705 43	✓	2.090 00	0.109
$3d^2(^3\mathrm{F})4p$ z $^4\mathrm{F}^\circ_{9/2} \rightarrow 3d^2(^3\mathrm{F})4s$ a $^4\mathrm{F}_{9/2}$	323.451 46	✓	17.100 00	0.891
$3d^2(^3\mathrm{F})4p$ z $^2\mathrm{F}^\circ_{5/2} \rightarrow 3d^2(^3\mathrm{F})4s$ a $^4\mathrm{F}_{3/2}$	320.343 13		0.161 00	0.395
$3d^2(^3\mathrm{F})4p$ z $^2\mathrm{F}^\circ_{5/2} \rightarrow 3d^2(^3\mathrm{F})4s$ a $^4\mathrm{F}_{5/2}$	321.312 14		0.091 80	0.225
$3d^2(^3\mathrm{F})4p$ z $^2\mathrm{F}^\circ_{5/2} \rightarrow 3d^2(^3\mathrm{F})4s$ a $^4\mathrm{F}_{7/2}$	322.676 90		0.155 00	0.380
$3d^2(^3\mathrm{F})4p$ z $^2\mathrm{F}^\circ_{7/2} \rightarrow 3d^2(^3\mathrm{F})4s$ a $^4\mathrm{F}_{5/2}$	318.411 69		0.046 00	0.095
$3d^2(^3\mathrm{F})4p$ z $^2\mathrm{F}^\circ_{7/2} \rightarrow 3d^2(^3\mathrm{F})4s$ a $^4\mathrm{F}_{7/2}$	319.751 86		0.110 00	0.226
$3d^2(^3\mathrm{F})4p$ z $^2\mathrm{F}^\circ_{7/2} \rightarrow 3d^2(^3\mathrm{F})4s$ a $^4\mathrm{F}_{9/2}$	321.476 70		0.330 00	0.679
$3d^2(^3\mathrm{F})4p$ z $^2\mathrm{D}^\circ_{3/2} \rightarrow 3d^2(^3\mathrm{F})4s$ a $^4\mathrm{F}_{3/2}$	314.803 61		1.100 00	0.902
$3d^2(^3\mathrm{F})4p$ z $^2\mathrm{D}^\circ_{3/2} \rightarrow 3d^2(^3\mathrm{F})4s$ a $^4\mathrm{F}_{5/2}$	315.739 34		0.120 00	0.098
$3d^2(^3\mathrm{F})4p$ z $^2\mathrm{D}^\circ_{5/2} \rightarrow 3d^2(^3\mathrm{F})4s$ a $^4\mathrm{F}_{3/2}$	312.159 79		0.059 00	0.039
$3d^2(^3\mathrm{F})4p$ z $^2\mathrm{D}^\circ_{5/2} \rightarrow 3d^2(^3\mathrm{F})4s$ a $^4\mathrm{F}_{5/2}$	313.079 85	✓	0.820 00	0.547
$3d^2(^3\mathrm{F})4p$ z $^2\mathrm{D}^\circ_{5/2} \rightarrow 3d^2(^3\mathrm{F})4s$ a $^4\mathrm{F}_{7/2}$	314.375 46	✓	0.620 00	0.414
$3d^2(^3\mathrm{F})4p$ z $^4\mathrm{D}^\circ_{3/2} \rightarrow 3d^2(^3\mathrm{F})4s$ a $^4\mathrm{F}_{3/2}$	306.634 63		3.470 00	0.206
$3d^2(^3\mathrm{F})4p$ z $^4\mathrm{D}^\circ_{3/2} \rightarrow 3d^2(^3\mathrm{F})4s$ a $^4\mathrm{F}_{5/2}$	307.522 39		13.400 00	0.794
$3d^2(^3\mathrm{F})4p$ z $^4\mathrm{D}^\circ_{5/2} \rightarrow 3d^2(^3\mathrm{F})4s$ a $^4\mathrm{F}_{3/2}$	305.739 29	✓	0.198 00	0.012
$3d^2(^3\mathrm{F})4p$ z $^4\mathrm{D}^\circ_{5/2} \rightarrow 3d^2(^3\mathrm{F})4s$ a $^4\mathrm{F}_{5/2}$	306.621 82		3.010 00	0.181
$3d^2(^3\mathrm{F})4p$ z $^4\mathrm{D}^\circ_{5/2} \rightarrow 3d^2(^3\mathrm{F})4s$ a $^4\mathrm{F}_{7/2}$	307.864 42	✓	13.400 00	0.807
$3d^2(^3\mathrm{F})4p$ z $^4\mathrm{D}^\circ_{7/2} \rightarrow 3d^2(^3\mathrm{F})4s$ a $^4\mathrm{F}_{5/2}$	305.973 53	✓	0.240 00	0.014
$3d^2(^3\mathrm{F})4p$ z $^4\mathrm{D}^\circ_{7/2} \rightarrow 3d^2(^3\mathrm{F})4s$ a $^4\mathrm{F}_{7/2}$	307.210 71	✓	2.130 00	0.123
$3d^2(^3\mathrm{F})4p$ z $^4\mathrm{D}^\circ_{7/2} \rightarrow 3d^2(^3\mathrm{F})4s$ a $^4\mathrm{F}_{9/2}$	308.802 56	✓	15.000 00	0.864

Note: Lines are divided into groups with a common upper level.

color. For the low applied power of 100 W, the self-absorption is weak and the measured branching fractions are close to the absorption-free values (see figure 2(a)). This proves the validity of the line intensity measurement. For the applied power of 2000 W, the self-absorption is more pronounced and the measured branching fractions depart from the absorption-free values (see figure 2(b)). By fitting them with the formula (3), an excellent agreement between the measured and the fitted values is obtained. The absolute densities of titanium atoms determined from the fit were 7.2×10^{16} m^{-3} and 2.7×10^{17} m^{-3} for the applied power of 100 W and 2000 W, respectively.

The density of Ti atoms as a function of the dc power and two different pressures of 2 and 5.4 Pa is shown in figure 3. The Ti atom density increases with the input power nonlinearly at both studied pressures. For the lower pressure, the Ti atom density increases with increasing power up to 400 W. Increasing the power further, the Ti atom density is saturated at 7.6×10^{16} m^{-3}. For higher working pressure (5.4 Pa), the Ti atom density is for the same input power always higher compared to the lower pressure (2 Pa) case. For low applied power, the Ti atom density increases at the argon pressure of 5.4 Pa with increasing input power, too. However, as the applied power increases over approx. 400 W, the increase in Ti atom density is slowed down and the evolution also shows a trend towards saturation. For the applied power of 2000 W corresponding to the power density of 6.6 W cm^{-2}, the Ti atom density of 2.7×10^{17} m^{-3} is achieved. The statistical uncertainties are roughly the same (4%) for measurements performed at both pressures studied.

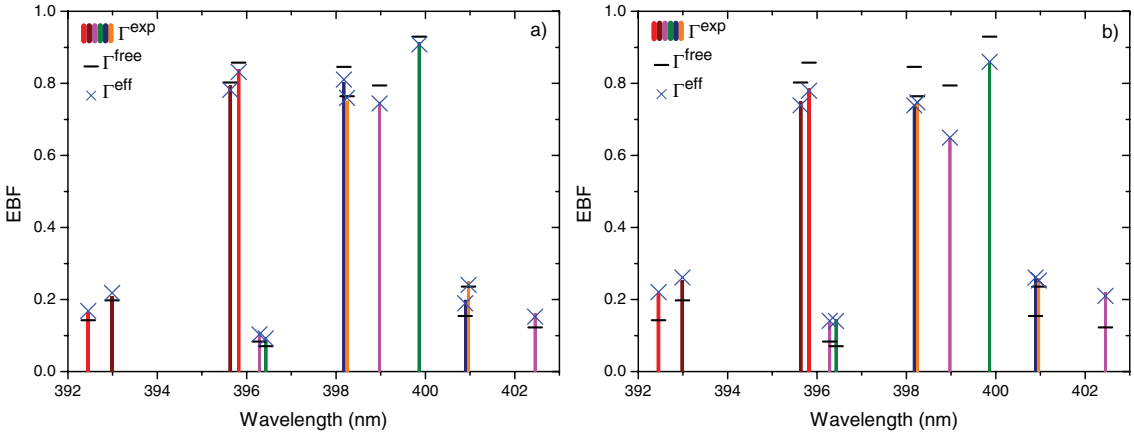

Figure 2. Example of the branching fraction fit used to determine Ti atom density. The measured branching fractions are represented by colored lines, the absorption-free case by black horizontal abscissae, and the fitted branching fractions by blue crosses. The pressure was set to 5.4 Pa, the applied power was (a) 100 W and (b) 2000 W and the optical fiber was placed at 23 mm above the target surface.

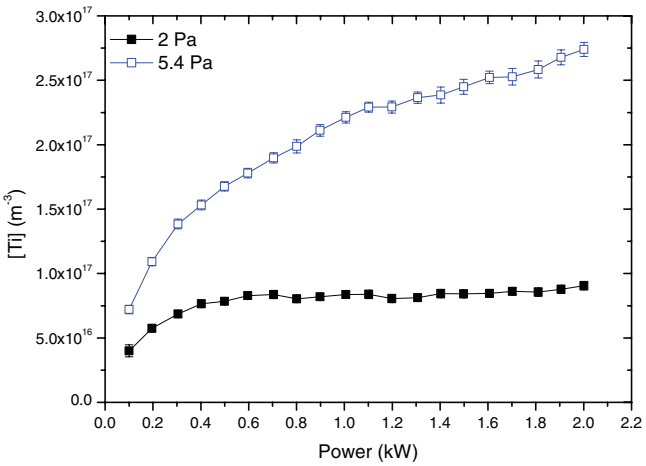

Figure 3. Power dependence of Ti atom density for 2 and 5.4 Pa. The dc generator was used and the optical fiber was placed 23 mm above the target surface in this experiment.

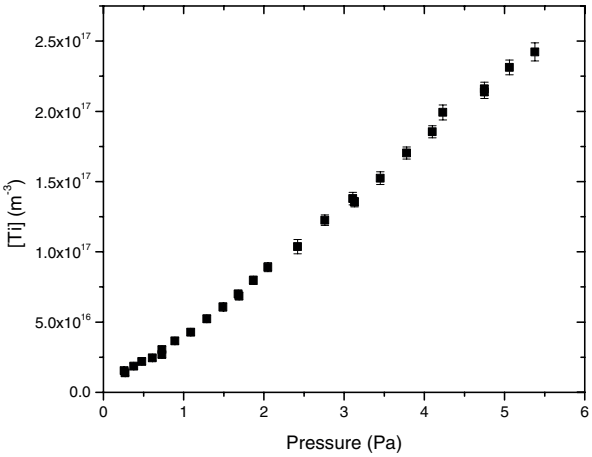

Figure 4. Pressure dependence of Ti atom density for 2 kW input power. The dc generator was used and the optical fiber was placed 23 mm above the target surface in this experiment.

Evolution of the Ti atom density was measured previously by Vašina [42] as a function of the magnetron current ranging from 0.1 to 2.0 A at the distance of 20 mm from the rectangular titanium magnetron target of the surface area of 190 cm^2 for argon pressure 4 Pa, using resonant optical absorption spectroscopy (ROAS). The Ti atom density increased nonlinearly with the applied power, too. For magnetron currents higher than 1 A (applied power higher than 300 W) the increase in the titanium atom density was progressively slowed down giving a density of around 3×10^{17} m^{-3} at the maximum studied discharge current of 2.0 A, corresponding to a power density of 3 W cm^{-2}. In our experimental setup, for the pressure of 5.4 Pa and the applied power of 900 W, corresponding to the same power density of 3 W cm^{-2}, a similar Ti atom density of 2.0×10^{17} m^{-3} was attained.

Galliard *et al* [43] measured by the ROAS technique the absolute density of the titanium atoms in the ground state at the distance of 40 mm from the titanium magnetron target at an argon pressure of 4 Pa. In this research a much smaller cylindrical magnetron target, with a surface area of only 20 cm^2, was used. For the power density of 5.5 W cm^{-2}, the higher Ti atom density of 5×10^{17} m^{-3} was detected, which was comparable to the 2.7×10^{17} m^{-3} attained at 6.6 W cm^{-2} in our case. The saturation trend was observed, too; however, in Galliards experiments the saturation shows up at much higher power densities of approx. 8 W cm^{-2}. The difference in the compared absolute values of the density is not significant and can be easily attributed to the difference in size of the magnetron targets in these two compared experiments, especially considering that, in our case, saturation has almost been reached. However, saturation has not yet been reached in the case of Galliard *et al*.

Britun *et al* [44] utilized laser induced fluorescence (LIF) to determine the densities of Ti atoms and ions in a dc magnetron discharge for different discharge conditions. For low discharge currents, the density of Ti atoms increases and becomes saturated at high current. Britun measurements performed at the distance of 40 mm from the magnetron target (3.5×10^{16} m^{-3} for 2.5 mA cm^{-2}) result in much lower values of titanium atom density compared to our result (1.1×10^{17} m^{-3} for 2.6 mA cm^{-2}) measured at the distance of 23 mm from the magnetron target at the same discharge current densities. This

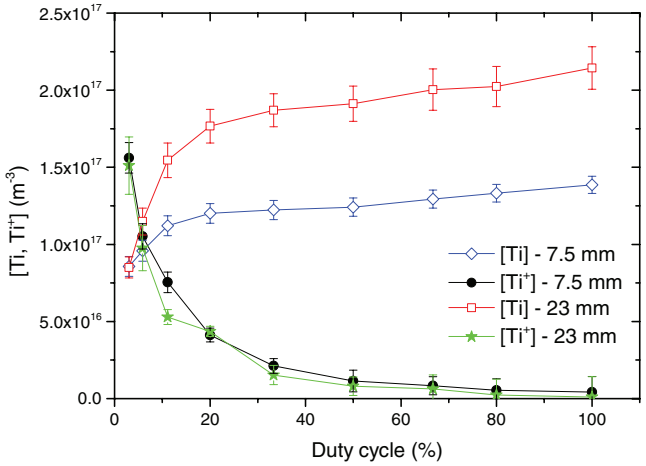

Figure 5. Density of Ti atoms and ions for different duty cycles and for two positions of the optical fiber above the target surface, 7.5 mm and 23 mm, respectively. The operation pressure was set to 5 Pa, the input power to 1.5 kW, the on-time of the pulse to 200 μs.

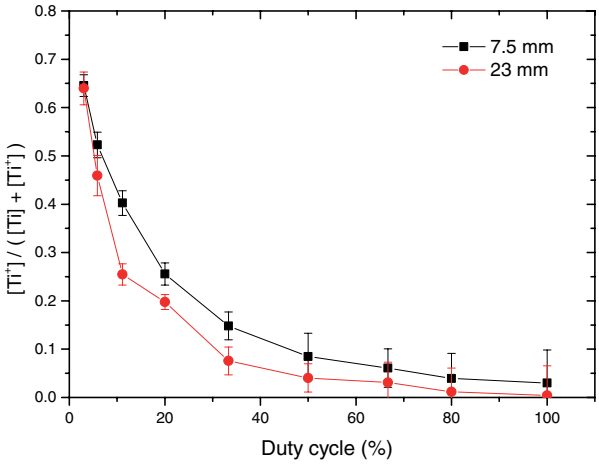

Figure 6. Ionization fraction of titanium sputtered species for different duty cycles and for two positions of the optical fiber above the target surface, 7.5 mm and 23 mm, respectively.

is understandable because the absolute density of sputtered particles decreases rapidly with the distance from the magnetron target (see i.e. [22, 44, 45]).

An attempt to measure the Ti ion density was performed for dc driven magnetron at the higher pressure of 5.4 Pa. Despite all the effort, only insignificant self-absorption on the Ti ion resonant lines was measured. For example, for the maximal discharge power of 2 kW, a Ti ion density of 6×10^{15} m^{-3} with a very high error of 5×10^{15} m^{-3} was determined from the measured spectra. Because of the very high error, the determined value is so uncertain that, practically, it is not possible to determine the absolute density of Ti ions in the dc case in our experimental setup.

The pressure dependence of titanium ground state atom density, measured at the distance of 23 mm from the magnetron target for the dc power of 2 kW (6.6 W cm^{-2}), is plotted in figure 4. The pressure was set by the variable flow of argon gas and the pumping speed was kept constant during the measurement. The Ti atom density increases with increasing pressure from 1.4×10^{16} m^{-3} for the lowest studied pressure of 0.3 Pa up to 2.4×10^{17} m^{-3} for the highest studied pressure of 5.4 Pa.

Konstantinidis *et al* [46] also observed an increase in the titanium ground state atom density with increasing pressure from 0.7 Pa to 6.5 Pa using the ROAS method. The measurement in [46] was performed at the distance of 50 mm from the titanium cathode for the dc power of 500 W (6.4 W cm^{-2}). The Ti atom density increased from 5×10^{15} m^{-3} for 0.7 Pa up to 4.75×10^{16} m^{-3} for 6.5 Pa. Since in the experiment by Konstantinidis *et al* the measurement was carried out for the same power density, however, at twice the distance from the magnetron target compared to our experiment, their measured absolute values of the titanium ground state density are smaller.

Britun *et al* [44] used LIF for the determination of the pressure dependency of the titanium atom ground state density, too. In the range 0.2–0.5 Pa the density of Ti atoms increased from 2×10^{16} m^{-3} up to 1×10^{17} m^{-3}. For higher pressures, the Ti atom density saturated and decreased, which is contrary to our results and those of Konstantinidis *et al* [46]. Britun's measurements were performed at the distance of 40 mm from the target surface.

In conclusion, the saturation trend of Ti atom density with the applied power and pressure dependency of Ti atom density measured by two independent methods—ROAS and LIF—are observed also with the presented OES method based on effective branching fractions. The same trends were observed and described in paper [44], where complete discussion is also available, supported by measured data of the velocity distribution function of the sputtered species. The absolute values of the titanium atom densities are generally in agreement in all methods.

4.2. Ti atom and ion densities for transition from dc to HiPIMS mode

The second case study was dedicated to the determination of the evolution of the density of the titanium atoms and ions for the transition from conventional dc to the HiPIMS regime of operation. In this experiment, the pressure, the mean input power and the on-time of the pulse were set to 5 Pa, 1.5 kW and 200 μs, respectively, and the duty cycle varied from 100% to 3%. Decreasing the duty cycle, the same average power was concentrated into fewer pulses with a higher on-time power value. The intensities of the selected Ti atom lines (see table 1) and Ti ion lines (see table 2) were integrated during both the on-time of the pulse and the whole afterglow using a CCD detector with the integration time adjusted to achieve good data quality. The optical fiber with the collimator was placed to collect the light from two areas located 7.5 mm and 23 mm above the target surface. The densities of Ti atoms and ions as a function of the duty cycle, determined for these two distances from the magnetron target, are plotted in figure 5. Although the densities of the Ti atoms and ions were calculated from the spectra time-averaged over the entire pulse and its afterglow, it would be misleading to interpret this density as the mean density time-average over the entire pulse or over the entire pulse and

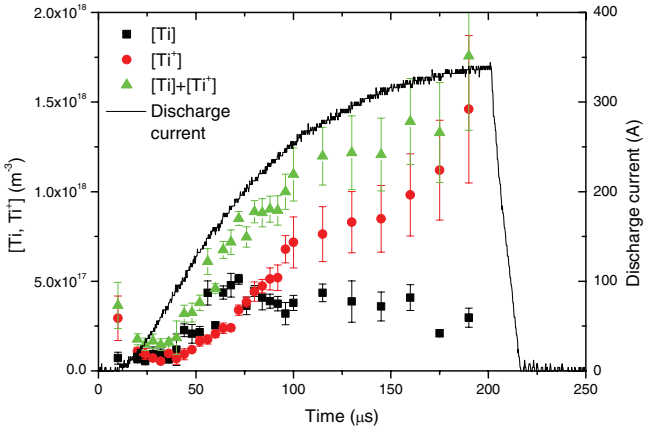

Figure 7. Measurements of the Ti atom and ion density for 200 μs pulse in HiPIMS mode. The pressure was set to 5 Pa, the repetition rate to 20 Hz and the optical fiber was placed 23 mm above the target surface. The total density of the sputtered species is added too.

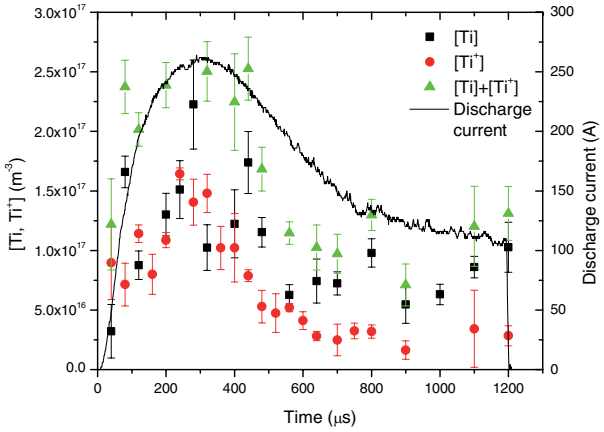

Figure 8. Measurements of the Ti atom and ion density for 1200 μs pulse in HiPIMS mode. The pressure was set to 5 Pa, the repetition rate to 20 Hz and the optical fiber was placed 23 mm above the target surface. The total density of the sputtered species is added too.

its afterglow. Given that the intensity of the spectral lines reaches its maximum at the end of the pulse in which we find the maximal discharge current, the plotted density reflects rather the Ti atom and ion densities attained at the end of the pulse, where the spectral lines are the strongest.

As shown in figure 5, for position 7.5 mm the Ti atom density slightly decreases from 1.4×10^{17} m^{-3} for 100% duty cycle (dc mode) to 1.2×10^{17} m^{-3} for 20% of the duty cycle. For position 23 mm the Ti atom density decreases from 2.1×10^{17} m^{-3} for 100% duty cycle to 1.8×10^{17} m^{-3} for 20% of the duty cycle. For the lower optical fiber position (7.5 mm), the Ti atom density is always lower compared to the higher optical fiber position (23 mm) for the same duty cycle. Lowering the duty cycle to below 20%, the Ti atoms density drops rapidly for both positions of the optical fiber to the same value of 8.5×10^{16} m^{-3} attained at 3% of the duty cycle.

The opposite behavior is observed for the density of titanium ions. With the initial decrease in the duty cycle the Ti ion density rises very slowly up to 20% of the duty cycle, when the Ti ion density reaches 4.1×10^{16} m^{-3} for the position 7.5 mm above the target surface and 4.4×10^{16} m^{-3} for position 23 mm above the target surface. Since Ti ion lines were very weak for the duty cycles in the range 100–33%, Ti ion densities calculated for these conditions are very inaccurate and statistical uncertainties are of the same order as the estimated values. Further decreasing of the duty cycle leads to rapid growth of the Ti ions density up to 1.6×10^{17} m^{-3} for the position 7.5 mm above the target surface and 1.5×10^{17} m^{-3} for the position 23 mm above the target surface, respectively, for 3% of the duty cycle.

The ionization fraction of the titanium sputtered species was determined directly from the titanium atoms and ion densities in figure 5 and it is shown as a function of duty cycle in figure 6. The ionization fraction is higher at a distance of 7.5 mm than at a distance of 23 mm from the target for the duty cycle from 100% to 6%. At 3% of the duty cycle the ionization fraction measured at both studied positions merges. The increase of the ionization fraction of the titanium sputtered species for transition from dc to HiPIMS mode is expected. The ionization fraction for the dc case (100% duty cycle) is less than 1% and corresponds well to the results measured using OES and ROAS [47–49]. The ionization fraction in HiPIMS discharge, measured by OES and ROAS, ranges from 50% to 90% [50, 51]. This broad range can be caused by various magnetron configurations and/or different applied power densities. The highest value of the ionization fraction of the titanium sputtered species of 65% is attained, in our case, for 3% of the duty cycle and fits well into the range 50–90% available in the literature.

4.3. Time-resolved Ti atom and ion densities for short and long pulse in HiPIMS mode

The third case study deals with the determination of the temporal evolution of the titanium atom and ion density during short (200 μs) and long (1200 μs) HiPIMS pulses. The repetition rate of 20 Hz and the working pressure of 5 Pa were set to be constant during this experiment. The applied voltage was set to 500 V and 400 V for the short and long pulses, respectively. The intensities of the selected Ti atom lines (see table 1) and the Ti ion lines (see table 2) were measured with a time step in the range of 4–40 μs during the on-time of the pulse using a ICCD detector with the integration time adjusted to achieve good data quality. The optical fiber with a collimator was placed to collect the light from the area 23 mm above the target surface.

The time evolution of the titanium atom and ion density during the 200 μs HiPIMS pulse is shown in figure 7. At the applied voltage of 500 V the discharge current steadily increases over the whole pulse and reaches the maximum value of 340 A at the end of the pulse. The average power during the 200 μs HiPIMS pulse was 400 W. The titanium atom density reaches its maximum of 5×10^{17} m^{-3} at the time of 70 μs followed by a slow decrease. The Ti ion density increases over the whole pulse and it attains 1.4×10^{18} m^{-3} at the end of the pulse. It corresponds to the ionization fraction of the sputtered species of 84%. The ionization fraction of the sputtered species of 50% is reached already at the time of 80 μs.

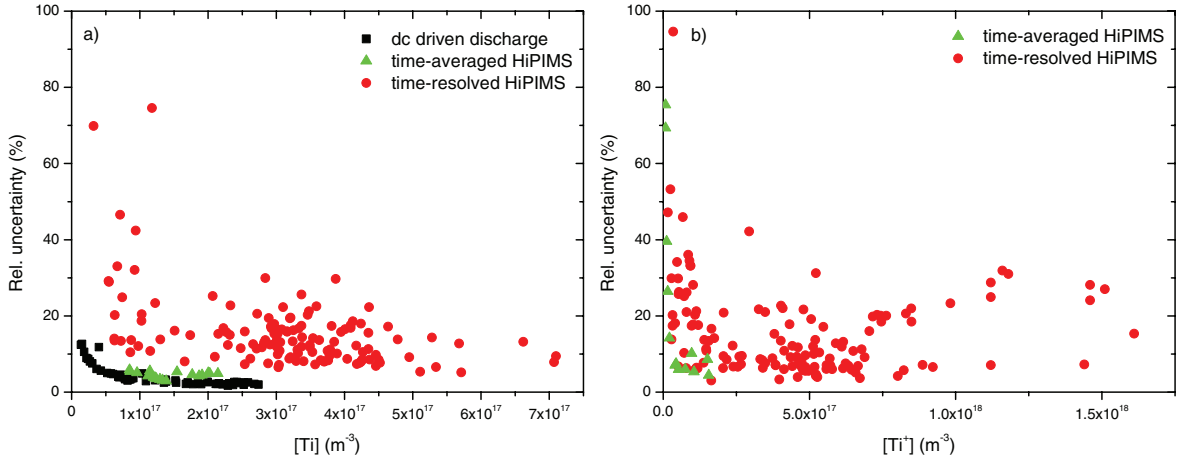

Figure 9. Evolution of relative uncertainty of absolute (a) Ti atom and (b) Ti ion density. Data shown are collected from previous sections, i.e. obtained under various pressures, powers, duty cycles, from different pulses and distances from the target.

The ionization fraction determined in our experiment corresponds well with previously reported data on the ionization fraction measured using OES and ROAS [50, 51].

Assuming that the multiply charged sputtered particle density is low compared to the density of Ti ions, the evolution of the total density of the sputtered species can be calculated as the sum of Ti atom density and Ti ion density. The evolution of the total density of the sputtered species plotted in figure 7 follows the evolution of the discharge current. Increasing the discharge current, the flux of the sputtered species from the target, and consequently the total density of the sputtered species, is increased. The slow decrease in Ti atom density observed after 70 μs results from two competitive processes. Increasing the discharge current increases the flux of sputtered atoms from the target and forces the Ti atom density to increase. Simultaneously increasing the discharge current enhances the probability of a sputtered atom being ionized, which forces the Ti atom density to decrease and the Ti ion density to increase.

The time evolution of the titanium atom and ion density during the 1200 μs HiPIMS pulse is shown in figure 8 for the applied voltage of 400 V. Under these conditions, the evolution of the discharge current shows a peak of 260 A at a time of 300 μs, followed by a decrease to the current plateau phase characterized by a relatively low current of 100 A. The average power during the 1200 μs HiPIMS pulse was 1400 W. Anders *et al* [52] showed that by increasing the applied voltage, the drop in the discharge current can be suppressed. The time evolution of the titanium atom and ion density reproduces well the temporal evolution of the discharge current. The maximum density of the Ti atom and ion of 2.2×10^{17} m^{-3} and 1.6×10^{17} m^{-3}, respectively, is attained at the time of 300 μs when the ionization fraction of the sputtered species is maximal and reaches almost 60%. As the discharge current decreases, the densities of the Ti atoms and ions also decrease. The ionization fraction of the sputtered species drops to 27% at the current plateau phase.

The temporal evolution of titanium atom and ion densities in HiPIMS was measured by tunable diode laser absorption spectroscopy (TDLAS), ROAS and LIF techniques, mainly to understand the transport mechanisms of sputtered species [45, 53–56]. Because most authors [45, 53, 55, 56] used much shorter pulses (10–20 μs), the comparison with our data obtained for longer pulses is not possible. Sushkov *et al* [54] measured by TDLAS the temporal evolution of titanium atom density during a 200 μs HiPIMS pulse and its afterglow at 4 Pa of the argon pressure, current density of 0.4 A cm^{-2} and at a distance of 70 mm from the target of 5 cm in diameter. Sushkov's Ti atom density was 2.3×10^{16} m^{-3} at the end of the pulse compared to our value of 3×10^{17} m^{-3}, which is one order of magnitude higher. Although our measurement was carried out for the same pulse length and similar working pressure, our current density at the end of the pulse was higher (1.1 A cm^{-2}) and the distance from the magnetron target was lower (23 mm) compared to the experiment by Sushkov *et al*. Therefore the presented absolute values of titanium ground state density are higher.

We have demonstrated the possibility of determining simultaneously the time evolution of the titanium atom and ion density during the short and long HiPIMS pulse. The measured ionization fractions of the sputtered species match well with data from the literature, however, the direct comparison of temporal evolution of the Ti atom and ion density is not possible, due to a lack of comparable measurements. Positioning of the optical fiber with the collimator at different distances above the magnetron target can provide the spatial-temporal evolutions of the Ti atom and ion densities.

5. Typical uncertainty of Ti atom and Ti ion densities estimation

The aim of this section is to provide an insight into the accuracy of the proposed method of determining the absolute density of sputtered species. All the error bars shown in the previous sections are the standard uncertainties, determined statistically by the fitting procedure from the residual sums of squares. The sources of measurement error as the plasma depth accuracy, assumption of the gas kinetic temperature

used in the Doppler spectral profile etc were not taken into account in the uncertainty calculation.

The overview of the obtained uncertainties of the measured densities of Ti atoms and Ti ions in our experimental setup is presented in figures 9(a) and (b), respectively. The figures show the relative uncertainty of the determined absolute density of sputtered species as a function of this density, i.e. the *x*-axis coordinate represents the absolute density of sputtered particles and the *y*-axis coordinate represents the relative uncertainty of the determined density.

Concerning the titanium atom density, the relative uncertainty first decreases as the determined density of the Ti atoms increases and then stays practically constant in a broad range of densities. For the dc driven discharge measured with the CCD detector, the relative uncertainty is less than 5% for a Ti atom density that is higher than 5×10^{16} m^{-3} in our experimental setup. Even the lowest measured density of 1×10^{16} m^{-3} is still estimated with the acceptable uncertainty of 12%. A slightly higher uncertainty of 6% was obtained in the experiment where the HiPIMS discharge was studied using a CCD detector and the density was calculated from time-averaged spectra. However, the time-resolved measurements using the ICCD detector show significantly higher relative uncertainty of around 15% for a Ti atom density that is higher than 1×10^{17} m^{-3}. Since the densities of Ti atoms that are lower than 1×10^{17} m^{-3} have even higher relative uncertainties, it can be concluded that titanium atom densities lower than 1×10^{17} m^{-3} cannot be reliably measured with time resolution in our experimental setup. The higher relative uncertainties of time-resolved measurement are caused by the difficulties in time-resolved measurement and the ICCD camera used. Spectra recorded using the CCD detector had a lower background and a higher signal to noise ratio compared to those recorded by the ICCD detector. The typical integration time of time-averaged measurements was less than 2 s, in contrast to the tens of seconds in time-resolved measurements.

Concerning the titanium ion density, the density was too low to be measured in the dc driven magnetron; the figure 9(b) shows the data from the HiPIMS experiments. The relative uncertainty also firstly decreases as the determined density of the Ti ions increases. Then the relative uncertainty stays practically constant in a broad range of Ti ion densities. The uncertainty of the density of Ti ion lower than 10% is typical for time-averaged CCD measurements of HiPIMS discharge. Densities of Ti ions that are lower than 4×10^{16} m^{-3} show significantly higher relative uncertainties. Thus, a Ti ion density lower than 4×10^{16} m^{-3} cannot be reliably estimated for time-averaged measurements in our experimental setup. Time-resolved HiPIMS measurements using the ICCD detector show a relative uncertainty of around 15% for Ti ion density higher than 1×10^{17} m^{-3}. Uncertainties of Ti ion densities that are lower than 1×10^{17} m^{-3} are significantly higher. Thus, a Ti ion density lower than 1×10^{17} m^{-3} cannot be reliably estimated for time-resolved measurements in our experimental setup.

It should be noted that arranging the experiment with a longer plasma depth or improved sensitivity of the ICCD detector can considerably decrease the minimal absolute density of the sputtered species detectable with the EBF self-absorption method and reduce the relative uncertainty of the density determination.

6. Conclusions

In this paper, the OES method of effective branching fractions, originally developed to measure the metastable densities of argon atoms, was adopted to measure the ground state titanium atom and ion densities in a PVD and ionized PVD process. The EBF method is based on fitting theoretically calculated branching fractions to measured ratios of the relative intensities in optical emission spectra. The measured Ti atom and ion lines were carefully selected to have high transition probability (Einstein coefficient), to be measured easily and to show no overlapping with surrounding spectral features. The density of Ti atoms and ions can be determined from the intensities of these lines using the developed software *EBF fit*.

The presented EBF method was applied to several case studies including the determination of the titanium atom density in a dc sputtering experiment, of titanium atom and ion densities for transition from dc to HiPIMS mode, and of the temporal evolution of titanium atom and ion densities during the HiPIMS pulse. It was demonstrated that the developed method is easy to implement, is robust and provides data comparable with those available in the literature. The typical relative uncertainty of Ti atom density determination is less than 5% for measurements with a CCD detector and around 15% for time-resolved HiPIMS measurements using an ICCD detector in our experimental setup. The typical relative uncertainty of Ti ion density determination for time-resolved HiPIMS measurements using an ICCD detector is around 15%.

Acknowledgments

This research has been partially financially supported by the Czech Science Foundation in frame of the project 15-00863S by the project CZ.1.05/2.1.00/03.0086 funded by European Regional Development Fund and the project LO1411 (NPU I) funded by Ministry of Education Youth and Sports of Czech Republic.

References

[1] Grove W R 1852 *Phil. Trans.* **142** 87
[2] Vossen J L and Cuomo J J 1978 *Thin Films Processes* (New York: Academic)
[3] Rossnagel S M 1995 *Sputter Deposition* (Switzerland: Technomic.)
[4] Powell R A and Rossnagel S M 1999 *PVD for Microelectronics: Sputter Desposition to Semiconductor Manufacturing* (New York: Academic)
[5] Kelly P J and Arnell R D 2000 *Vacuum* **56** 159–72
[6] Schneider J M, Rohde S, Sproul W D and Matthews A 2000 *J. Phys. D: Appl. Phys.* **33** R173
[7] Vlček J, Kudláček P, Burcalová K and Musil J 2007 *Europhys. Lett.* **77** 45002
[8] Vašina P, Meško M, de Poucques L, Bretagne J, Boisse-Laporte C and Touzeau M 2008 *Plasma Sources Sci. Technol.* **17** 035007

[9] Hoffman D W 1985 *J. Vac. Sci. Technol.* A **3** 561
[10] Rossnagel S M 1988 *J. Vac. Sci. Technol.* A **6** 19
[11] Scherer M, Schmitt J, Latz R and Schanz M 1992 *J. Vac. Sci. Technol.* A **10** 1772
[12] Schiller S, Goedicke K, Reschke J, Kirchhoff V, Schneider S and Milde F 1993 *Surf. Coat. Technol.* **61** 331–7
[13] Mozgrin D V, Fetisov I K and Khodachenko G V 1995 *Plasma Phys. Rep.* **21** 400
[14] Kouznetsov V, Macak K, Schneider J M, Helmersson U and Petrov I 1999 *Surf. Coat. Technol.* **122** 290–3
[15] Helmersson U, Lattemann M, Böhlmark J, Ehiasarian A P and Gudmundsson J T 2006 *Thin Solid Films* **513** 1–24
[16] Sarakinos K, Alami J and Konstantinidis S 2010 *Surf. Coat. Technol.* **204** 1661–84
[17] Anders A 2014 *Surf. Coat. Technol.* **257** 308
[18] Britun N, Minea T, Konstantinidis S and Snyders R 2014 *J. Phys. D: Appl. Phys.* **47** 224001
[19] Lochte-Holtgreven W 1968 *Plasma Diagnostics* (Amsterdam: North-Holland)
[20] Mitchell A C and Zemansky M W 1971 *Resonance Radiation and Excited Atoms* (Cambridge: Cambridge University Press)
[21] de Poucques L, Imbert J-C, Vasina P, Boisse-Laporte C, Teule-Gay L, Bretagne J and Touzeau M 2005 *Surf. Coat. Technol.* **200** 800–3
[22] Leroy O, de Poucques L, Boisse-Laporte C, Ganciu M, Teule-Gay L and Touzeau M 2004 *J. Vac. Sci. Technol.* A **22** 192–200
[23] Konstantinidis S, Dauchot J P, Ganciu M and Hecq M 2006 *Appl. Phys. Lett.* **88** 021501
[24] de Poucques L, Imbert J C, Boisse-Laporte C, Bretagne J, Ganciu M, Teulé-Gay L, Vasina P and Touzeau M 2007 *Plasma Process. Polym.* **4** S424–9
[25] Britun N, Ershov S, El Mel A A, Konstantinidis S, Ricard A and Snyders R 2013 *J. Phys. D: Appl. Phys.* **46** 175202
[26] Kirkbright G F and Sargent M 1974 *Atomic Absorption and Fluorescence Spectroscopy* (London: Academic)
[27] Amorim J, Baravian G and Jolly J 2000 *J. Phys. D: Appl. Phys.* **33** R51
[28] Döbele H F, Mosbach T, Niemi K and Schulz-von der Gathen V 2005 *Plasma Sources Sci. Technol.* **14** S31–S41
[29] Nafarizal N, Takada N, Shibagaki K, Nakamura K, Sago Y and Sasaki K 2005 *Jpn. J. Appl. Phys.* **44** L737
[30] Vitelaru C, Aniculaesei C, de Poucques L, Minea T M, Boisse-Laporte C, Bretagne J and Popa G 2010 *J. Phys. D: Appl. Phys.* **43** 124013
[31] Vitelaru C, de Poucques L, Minea T M and Popa G 2011 *Plasma Sources Sci. Technol.* **20** 045020
[32] Palmucci M, Britun N, Konstantinidis S and Snyders R 2013 *J. Appl. Phys.* **114** 113302
[33] Desecures M, de Poucques L and Bougdira J 2015 *Plasma Sources Sci. Technol.* **24** 015012
[34] Jolly J and Touzeau M 1975 *J. Quant. Spectrosc. Radiat. Transfer.* **15** 863
[35] Schulze M, Yanguas-Gil A, von Keudell A and Awakowicz P 2008 *J. Phys. D: Appl. Phys.* **41** 065206
[36] Boffard J B, Jung R O, Lin C C and Wendt A E 2009 *Plasma Sources Sci. Technol.* **18** 035017
[37] Holstein T 1947 *Phys. Rev.* **72** 1212
[38] Mewe R 1967 *Br. J. Appl. Phys.* **18** 107
[39] Software EBF fit 2015 http://physics.muni.cz/~zdenek/ebffit/
[40] Kramida A, Ralchenko Yu, Reader J and NIST ASD Team 2014 *NIST Atomic Spectra Database (version 5.2)* [Online] http://physics.nist.gov/asd
[41] Saloman E B 2012 *J. Phys. Chem. Ref. Data* **41** 013101
[42] Vašina P 2005 Plasma diagnostics focused on new magnetron sputtering devices for this film deposition *PhD Thesis* Université Paris-Sud, Orsay, France
[43] Gaillard M, Britun N, Kim Y M and Han J G 2007 *J. Phys. D: Appl. Phys.* **40** 809–17
[44] Britun N, Gaillard M and Han J G 2008 *J. Phys. D: Appl. Phys.* **41** 185201
[45] de Poucques L, Imbert J-C, Boisse-Laporte C, Bretagne J, Ganciu M, Teule-Gay L and Touzeau M 2006 *Plasma Sources Sci. Technol.* **15** 661–9
[46] Konstantinidis S, Ricard A, Snyders R, Vandeparre H, Dauchot J P and Hecq M 2005 *Surf. Coat. Technol.* **200** 841–5
[47] Christou C and Barber Z H 2000 *J. Vac. Sci. Technol.* A **18** 2897
[48] Ricard A, Nouvellon C, Konstantinidis S, Dauchot J P, Wautelet M and Hecq M 2002 *J. Vac. Sci. Technol.* A **20** 1488
[49] Konstantinidis S, Ricard A, Ganciu M, Dauchot J P, Ranea M and Hecq M 2004 *J. Appl. Phys.* **95** 2900
[50] Bohlmark J, Alami J, Christou C, Ehiasarian A P and Helmersson U 2005 *J. Vac. Sci. Technol.* A **23** 18
[51] Konstantinidis S, Dauchot J P, Ganciu M and Hecq M 2006 *J. Appl. Phys.* **99** 013307
[52] Anders A, Andersson J and Ehiasarian A 2007 *J. Appl. Phys.* **102** 113303
[53] Britun N, Palmucci M, Konstantinidis S and Snyders R 2012 *IOP Conf. Ser.: Mater. Sci. Eng.* **39** 012013
[54] Sushkov V, Do H T, Cada M, Hubicka Z and Hippler R 2013 *Plasma Sources Sci. Technol.* **22** 015002
[55] Britun N, Palmucci M, Konstantinidis S and Snyders R 2015 *J. Appl. Phys.* **117** 163302
[56] Britun N, Palmucci M, Konstantinidis S and Snyders R 2015 *J. Appl. Phys.* **117** 163303

INSTITUTE OF PHYSICS PUBLISHING JOURNAL OF PHYSICS D: APPLIED PHYSICS

J. Phys. D: Appl. Phys. **37** (2004) 2112–2120 PII: S0022-3727(04)74672-0

Deposition of thin organosilicon polymer films in atmospheric pressure glow discharge

D Trunec, Z Navrátil, P Šťahel, L Zajíčková, V Buršíková and J Čech

Department of Physical Electronics, Faculty of Science, Masaryk University, Kotlářská 2, 611 37 Brno, Czech Republic

E-mail: trunec@physics.muni.cz

Received 12 January 2004
Published 14 July 2004
Online at stacks.iop.org/JPhysD/37/2112
doi:10.1088/0022-3727/37/15/010

Abstract

The atmospheric pressure glow discharge burning in nitrogen with small admixture of organosilicon compounds such as hexamethyldisilazane or hexamethyldisiloxane was used for the deposition of thin organosilicon polymer films. The properties of the discharge were studied by means of optical emission spectroscopy and electrical measurements. The deposited films were characterized by atomic force microscopy, x-ray photoelectron spectroscopy, infrared transmission measurements, ellipsometry, depth sensing indentation technique and contact angle measurements. The films were polymer-like, transparent in the visible range, with uniform thickness and without pinholes. The film hardness varied from 0.3 to 0.6 GPa depending on deposition conditions, the elastic modulus was in the range 15–28 GPa and the surface free energy was in the range 26–45 mJ m^{-2}. The studied films exhibited good adhesion to the substrate.

1. Introduction

Dielectric barrier discharges (DBDs) are widely used for industrial purposes such as modification of polymer surface properties, e.g. wettability or adhesion, owing to the possibility of atmospheric pressure processing and on-line treatment. Although this method is very useful, the main disadvantage of DBDs is the lack of uniformity. This is due to the fact that at atmospheric pressure the discharge is normally a filamentary discharge. Because of this drawback, an effort to homogenize DBDs has been made and it was found that under certain conditions homogeneous DBD can be obtained. Such homogeneous discharge is called atmospheric pressure glow discharge (APG discharge, APGD). The uniformity of the plasma favours this discharge type for thin film deposition techniques such as plasma enhanced chemical vapour deposition (PECVD) as well. PECVD methods enable the preparation of coatings with a wide range of properties, e.g. wetting and sticking behaviour, mechanical, optical or electrical properties. The disadvantage of the low pressure PECVD techniques is their demand of expensive vacuum pumping systems. Moreover, the difficulties in arranging the deposition system for large area depositions have to be overcome. Recently, plasma deposition at atmospheric pressure has become a promising technology due to its economical and ecological advantages. Sawada *et al* [1] reported the organosilicon thin films deposition in APGD in helium with the admixture of tetraethoxysilane (TEOS) or hexamethyldisiloxane (HMDSO) and oxygen. Prat *et al* [2] reported the fluoro-polymer film deposition in helium APGD with admixture of hexafluoropropylene or tetrafluoroethylene. Gherardi *et al* [3] used N_2–SiH_4–N_2O APGD for SiO_2 deposition. Foest *et al* [4] used APGD in helium with admixture of HMDSO for organosilicon thin film deposition.

The APG discharges can be easily generated in various pure gases [5–8]. However, in nitrogen, which is the most suitable gas from the technological point of view, the small admixture of impurities such as oxygen can lead to the generation of filamentary DBD instead of APGD [8]. Therefore, it is important to study the influence of monomer

admixture and its concentration on the character of the barrier discharge. In this paper we have studied the APG discharges in nitrogen with small admixture of two different organosilicon compounds, hexamethyldisilazane ($C_6H_{19}Si_2N$, HMDSN) and hexamethyldisiloxane ($C_6H_{18}Si_2O$, HMDSO), which can be used for the deposition of thin films with desired surface energy, permeability, optical and mechanical properties [9–11].

2. Experimental

The experiments were carried out in a Plexiglas discharge reactor with the dimensions 180 mm × 115 mm × 310 mm. The discharge burned between two plane metal electrodes, both covered with Simax glass, 2 mm thick. The diameter of the bottom electrode was 150 mm and the diameter of the top electrode was 80 mm. The bottom electrode was movable in one direction in the horizontal plane by a stepping motor. The space between the electrodes was set to 1 mm. The working gas with monomers was fetched through an inlet in one upper corner of the discharge reactor and it was pumped off in the corner on the other end of the body diagonal with regard to the gas inlet. Before starting the experiments the discharge chamber was pumped down to 1 kPa and then filled with nitrogen to a pressure of 101 kPa. A nitrogen flow of 6 slm was then added and the atmospheric pressure was maintained by slight pumping. High voltage with the frequency 6 kHz was used for discharge generation. The type of discharge as concern a filamentary or a glow mode was determined from the current–voltage measurements. The power density 10 W cm^{-3} was kept constant in all experiments presented in this paper. The discharge current and voltage were recorded by digital oscilloscope HP 54820A Infinium (500 MHz, 2 GS s^{-1}). The discharge was also studied by means of the optical emission spectroscopy. The spectra emitted by the discharge were recorded with the Jobin-Yvon TRIAX 550 spectrometer with a CCD detector.

The films were deposited from HMDSO or from 94% HMDSN/6% HMDSO mixture mixed with nitrogen. The mixture of 94% HMDSN with 6% HMDSO is hereafter referred to as HMDSN. The pure nitrogen flow was mixed with nitrogen driven through the glass bottle containing the liquid monomer. The flow rate of the nitrogen through the monomer was in the range from 0.2 to 1.4 slm. The monomer flow rate was determined by the weighing of monomer before and after the deposition, the concentration of the monomers in the nitrogen ranged from 890 to 8660 ppm. Thin polymer-like layers were deposited on the thin glass substrate of 25 mm × 60 mm × 0.3 mm size, for ellipsometry and infrared transmission analysis on the silicon wafer of 10 cm in diameter. The bottom electrode with the substrate was moving in the discharge with the speed 10 cm min^{-1} in order to achieve better homogeneity of deposited films. The total processing time was 30 min in all cases, the total deposition time was then only 10 min due to the movement of the substrate from and back to the discharge.

The morphology of the deposited films was studied by atomic force microscopy (AFM) using Topometrix Accurex II.L. microscope. The chemical structure of the films was studied by Fourier transform infrared (FTIR) spectroscopy using NICOLET Impact 400 spectrometer. The bare silicon substrate was taken as a reference. The resolution of the spectrometer was set as 0.96 cm^{-1}. The surface composition of the deposited films was studied by x-ray photoelectron spectroscopy (XPS) by means of an ADES 400 VG scientific photoelectron spectrometer using Mg K_α (1253.6 eV) photon beams at the normal emission angle.

The total surface free energy of the films was determined from measurements of contact angles between testing liquids and the film surfaces using a sessile drop technique. The system developed in our lab enables the observation of a solid–liquid meniscus directly by a CCD camera and the contact angles are determined from the CCD snapshots. For the determination of the total surface free energy, the so-called 'acid–base' theory [12], described in detail in the next section, was used.

In the ultraviolet–visible (UV–VIS) range, the optical properties of the films on the silicon substrates were investigated by ellipsometry. The UVISEL Jobin Yvon ellipsometer was used to measure the ellipsometric parameters at five angles of incidence (55–75°) in the spectral range 240–830 nm.

The mechanical properties were studied by means of the depth sensing indentation technique using a Fischerscope H100 tester.

3. Results and discussion

The first part of this section is devoted to the diagnostics of the discharge itself. This is particularly important in order to observe the transition between the filamentary and glow modes of DBD and to understand the chemistry in the discharge. The second part of this section describes the properties of the deposited films which are important from the application point of view.

3.1. Discharge diagnostics

The characteristic course of the discharge voltage and current in APGD and filamentary discharge is presented in figure 1.

Whereas the applied voltage is sinusoidal, the discharge current consists of two parts. The sinusoidal current course corresponds to the capacitive current, the small broad peak represents the current of the APGD and the narrow pulses represent the current of filamentary discharge. In pure nitrogen or at low monomer concentration APGD was observed, but at high concentration of monomer the nature of the discharge changed to the filamentary discharge (see figure 1). The change from APG to filamentary discharge was observed at the flow rate 0.27 g min^{-1} of HMDSN (total nitrogen flow 7.6 litre min^{-1}) and at the flow rate 0.72 g min^{-1} of HMDSO (total nitrogen flow 8.4 litre min^{-1}). At the deposition of thin films individual filamentary microdischarges can start from the edges of the substrate even at lower monomer flow rate.

The typical emission spectra of the APG discharge in nitrogen containing organosilicon vapours are shown in figure 2.

The spectra were recorded in the range of 300–800 nm but above 450 nm only the second spectral order was registered. Spectra of the discharges containing HMDSO or HMDSN are very similar. Spectra consist of the molecular bands of the

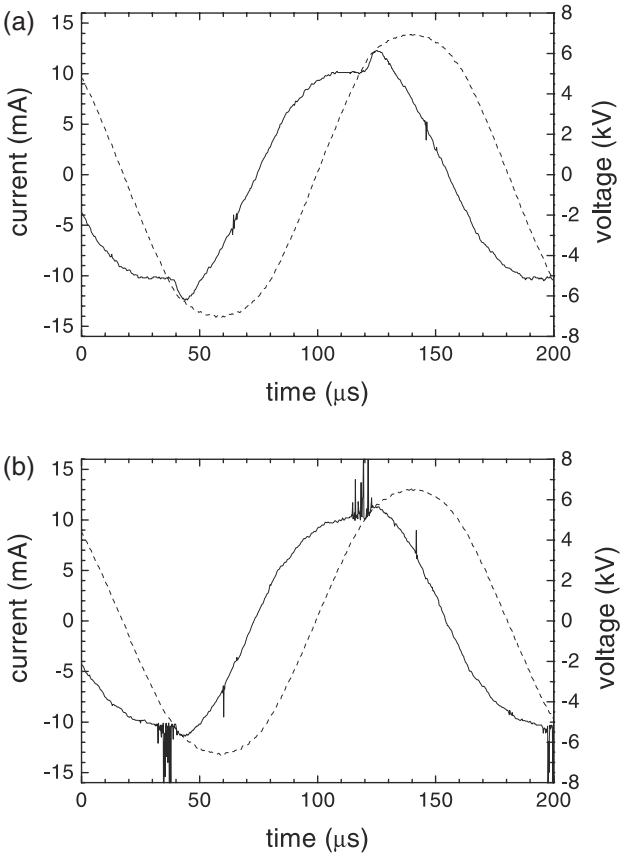

Figure 1. The time variation of the current and applied voltage. (*a*) APG discharge, pure nitrogen; (*b*) filamentary discharge, nitrogen +0.72 g min^{-1} HMDSO. ——, current; - - - -, voltage.

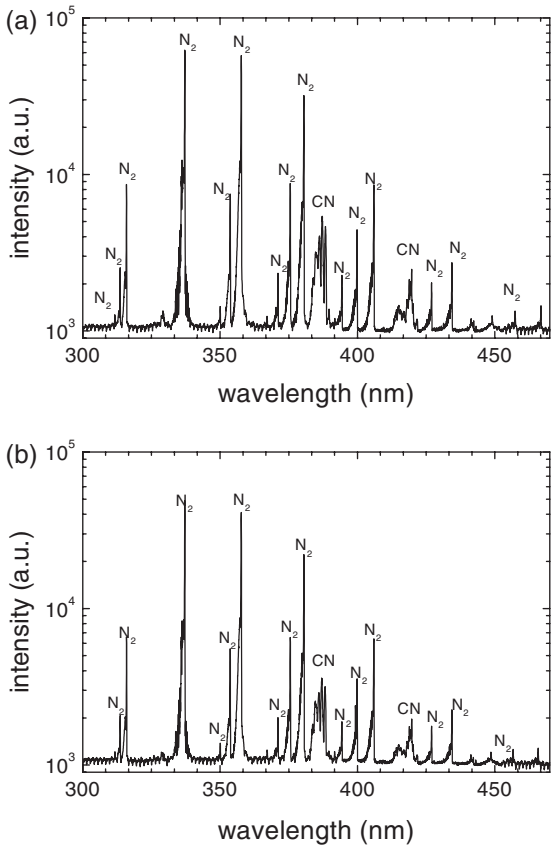

Figure 2. Emission spectra of APGD in nitrogen with organosilicon. (*a*) HMDSO, 0.259 g min^{-1}; (*b*) HMDSN, 0.10 g min^{-1}. The total nitrogen flow rate was 6.8 slm in both cases.

second positive system of nitrogen ($C\,^3\Pi_u \rightarrow B\,^3\Pi_g$). In the case of the monomer admixture to nitrogen two intensive bands of CN violet system ($B\,^2\Sigma^+ \rightarrow X\,^2\Sigma^+$) appear at 388 and 422 nm. In figure 3, the structure and intensity variation of CN band for different concentrations of organosilicon are plotted.

Since not only the intensity of CN band but also the intensity of N_2 system depends on the flow rate of the organosilicon, the ratio of the integrated intensities of CN band and N_2 system was calculated. For CN, only the band at 388 nm was integrated, the second CN band was neglected owing to its low intensity. For N_2 all important bands were integrated. The CN/N_2 ratio of integrated intensities increases with increasing concentration of HMDSO or HMDSN and reaches a constant value at higher monomer flow rate (see figure 4).

The bands of the second positive system of nitrogen N_2 0–2, N_2 1–3 and N_2 2–4 were used to calculate the vibrational temperature. The vibrational temperature determined is at about 1710 ± 20 K in case of HMDSO, 1760 ± 30 K in case of HMDSN and does not change with the variation of the flow rate of organosilicon. The same values of vibrational temperature were also measured in pure nitrogen APGD.

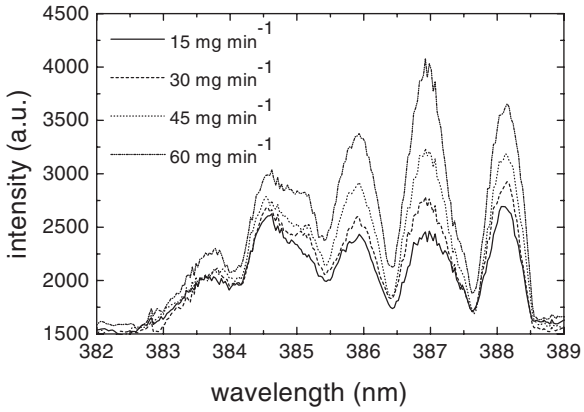

Figure 3. Structure and intensity variation of the CN band at 388 nm with the flow rate of HMDSN.

3.2. Film characterization

In this section we summarize the results on the film characterization with AFM, FTIR spectroscopy, XPS, contact angle and ellipsometric measurements. The films were deposited from pure HMDSO (labelled O_i) and from HMDSN (labelled Z_i) with different monomer flow rates. The monomer and nitrogen flow rates and corresponding labelling of the samples are given in table 1. The films marked with 'Si' were deposited on the silicon substrates. The thicknesses of the films were in the range from 200 to 1000 nm which corresponded to the deposition rates from 20 to 100 nm min^{-1}.

3.2.1. AFM. The AFM micrographs of two films deposited in homogeneous APGD and filamentary DBD are shown in figures 5 and 6, respectively. We observed, especially on the

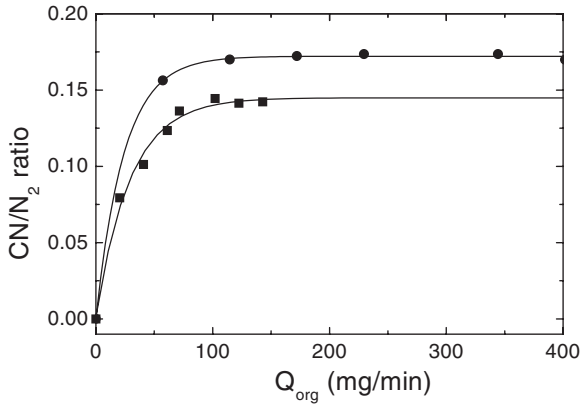

Figure 4. Ratio of integrated intensities of CN 388.3 nm band and N_2 system versus flow rate of organosilicon. ●, HMDSO; ■, HMDSN.

Table 1. Film deposition conditions together with the film surface composition found by XPS. The films were deposited from pure HMDSO (labelled O_i) and from HMDSN (labelled Z_i) on the silicon (labelled Si) or glass substrates. The monomer and total nitrogen flow rates are Q_{org} and Q_{N_2}, respectively. Remarks: fil., individual filamentary microdischarges burned from the edges of the substrate; XPS N/A, XPS analysis is not available for this sample.

Sample	Q_{org} (g min^{-1})	Q_{N_2} (slm)	C (%)	O (%)	Si (%)	N (%)	Na (%)	Remark
Z_1	0.037	6.2	39.1	29.4	11.1	16.7	3.6	
Z_{1Si}	0.037	6.2	36.2	27.2	11.3	25.2	0	
Z_2	0.058	6.4	37.6	28.6	11.8	19.5	2.6	
Z_3	0.078	6.6	36.6	29.8	11.7	21.0	0.8	
Z_4	0.120	7.0	43.1	29.0	12.8	13.8	1.3	
Z_5	0.160	7.4	42.4	24.7	12.9	19.3	0.6	fil.
O_1	0.087	6.2	41.3	26.0	14.6	17.0	1.1	
O_2	0.144	6.4	46.0	30.3	14.3	<0.5	9.3	
O_{2Si}	0.144	6.4	40.8	25.7	12.3	21.3	0	
O_3	0.259	6.8	—	—	—	—	—	XPS N/A
O_4	0.431	7.4	44.0	26.3	20.5	9.2	0	fil.

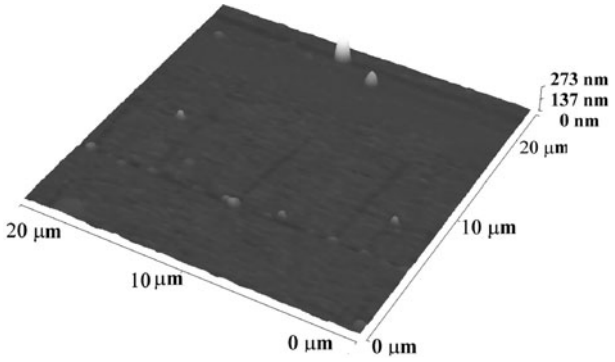

Figure 5. AFM micrograph of the film deposited in APGD—sample Z_1.

surface of the films deposited in filamentary DBD, very sharp objects. Their average height is about 150 nm. However, their shape is not visualized correctly by AFM. Due to their sharpness the pictures represent more the shape of the AFM tip. The density of these objects is very high in case of filamentary DBD and they occur seldom also on the surface of the films deposited in APGD.

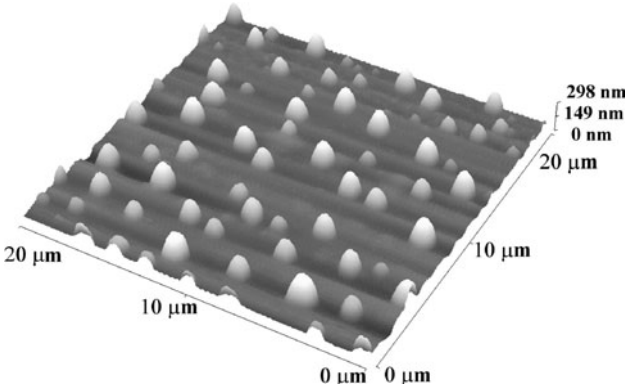

Figure 6. AFM micrograph of the film deposited in filamentary DBD—sample Z_5.

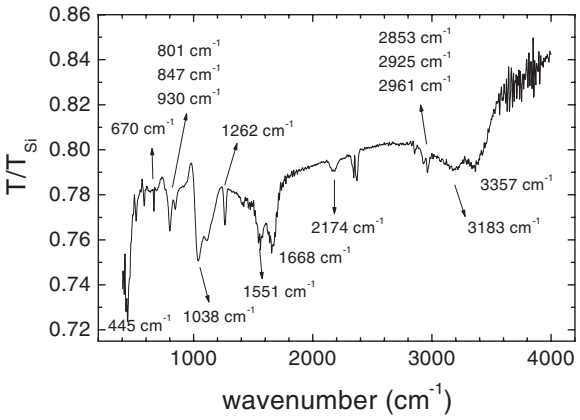

Figure 7. Infrared spectra of the O_{2Si} film deposited from $HMDSO/N_2$ gas feed. The deposition conditions are given in table 1.

The films deposited in APGD are relatively smooth and free from pinholes. Excluding the two highest objects from the calculation the roughness of the film surface shown in figure 5 expressed as RMS is 7.9 nm.

3.2.2. FTIR spectroscopy. The infrared spectra of the film O_{2Si} deposited from pure HMDSO and the spectra of the film Z_{1Si} deposited from HMDSN are shown in figures 7 and 8, respectively. The deposition conditions of these films are given in table 1. The assignment of particular absorption bands in the system containing five elements, namely carbon, hydrogen, oxygen, nitrogen and silicon, is a very complicated task that need not result in a unique solution. According to the structure of both monomers we can expect abundance of hydrocarbon groups bonded namely to silicon. The region from 2855 to 2960 cm^{-1} is characteristic for asymmetric and symmetric stretching of CH_3 (2960 cm^{-1} and 2870 cm^{-1}, respectively) and CH_2 (2925 cm^{-1} and 2855 cm^{-1}, respectively) groups with carbon in sp^3 hybridization [13]. In both types of the films, the most intensive absorption band in this region is observed at ≈2960 cm^{-1} which indicates the presence of CH_3 groups (denoted further as R). The IR spectrum of the film O_{2Si} also contains bands at 2927 cm^{-1} and 2854 cm^{-1} assigned to asymmetric and symmetric stretching of CH_2 groups, respectively. The narrow and relative intensive peak

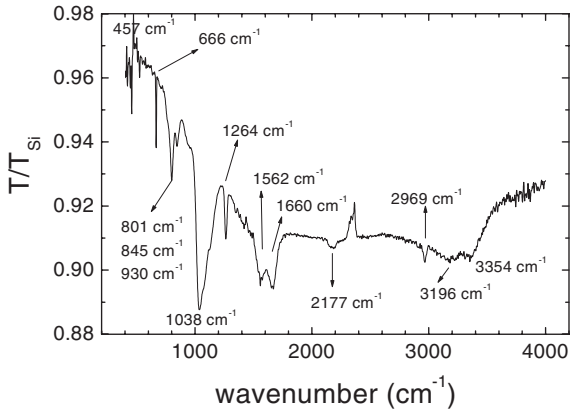

Figure 8. Infrared spectra of the Z_{1Si} film deposited from HMDSN/N_2 gas feed. The deposition conditions are given in table 1.

assigned to Si–$R_{x=1,2,3}$ is found at 1263 cm^{-1}. However, its higher wavenumber as compared to 1250 cm^{-1} in both the monomers [14] suggests that less than three methyl groups are bonded to silicon [15]. Accordingly, the narrow peak at 667 cm^{-1} can be assigned to the symmetric stretching of SiC_2 in R_2Si groups. Asymmetric stretching of SiC_2 and rocking of CH_3 groups in R_2Si and RSi is referred at higher wavenumbers and they may be a part of the two broad bands centred at 801 and 845 cm^{-1}. Moreover, the peak at 801 cm^{-1} can be assigned to Si–O–Si bending observed in silicon dioxides at 810 cm^{-1}. Other two absorption bands characteristic for silicon dioxides are observed at 1100 cm^{-1} (Si–O–Si asymmetric stretching) and 460 cm^{-1} (Si–O–Si rocking) [16]. The most intensive band at 1100 cm^{-1} is, however, overlapped with vibration of other compounds containing either carbon (1020–1100 cm^{-1} Si–O–C, Si–CH_2–Si [17, 18]) or nitrogen (1100 cm^{-1} C–N [17] and 1184 cm^{-1} Si–NH–Si [19]). We observed, in the region discussed, two distinguished broad bands centred at 1038 and 1112 cm^{-1} in the O_{2Si} film and one broad band at 1038 cm^{-1} with two weak side peaks at 1074 and 1125 cm^{-1} in the Z_{1Si} film. Detailed analyses of these broad bands is beyond the scope of this paper.

The band at ≈450 cm^{-1} can be associated with Si–O–Si rocking [20] and/or Si_3N stretching [17]. The broad weak peak centred at ≈930 cm^{-1} can be assigned to Si–N–Si asymmetric stretching [17, 19] and Si–OH bending [21, 22]. Two broad absorption bands centred at 3180 and 3360 cm^{-1} are observed in the range 3000–3600 cm^{-1}. They consist of several peaks belonging to NH_2, NH and OH groups [23, 24]. Additionally, we need to assign three broad bands at about 1555, 1655 and 2175 cm^{-1}. The presence of carbon double bonded to nitrogen is revealed by the first two bands [25]. The last one can be associated with Si–H stretching and its position suggests that silicon is surrounded by some organic environment rather than incorporated in a silicon oxide network [22, 26]. The results of the band assignment are summarized in table 2.

3.2.3. XPS analysis. The results on the atomic composition obtained by XPS are summarized in table 1. It reflects the composition of the film surface modified by post-discharge chemical reactions, e.g. oxidation, because the measurement depth of XPS is only 6–8 nm and the XPS analyses were

Table 2. Assignment of IR absorption bands for the films O_{2Si} and Z_{1Si}. For deposition conditions see table 1. Methyl groups are denoted as R.

Wavenumber (cm^{-1})	Film	Comments	Vibration
445, 457	O_{2Si}, Z_{1Si}	Narrow	$\rho(Si_2O)$, $\nu(Si_3N)$
667	O_{2Si}, Z_{1Si}	Narrow	$\nu_s(SiC_2)$ in R_2Si
801	O_{2Si}, Z_{1Si}	Broad	$\nu(SiC_x)$, $\rho(CH_3)$ in R_xSi, $\delta(Si_2O)$
845	O_{2Si}, Z_{1Si}	Broad	$\nu(SiC_x)$, $\rho(CH_3)$ in R_xSi
930	O_{2Si}, Z_{1Si}	Broad	$\nu(SiN)$, $\nu_{as}(Si_2N)$, Si–OH
980–1230	O_{2Si}, Z_{1Si}	Broad bands	Si–O–Si, Si–O–C, C–N, Si–NH–Si
1263	O_{2Si}, Z_{1Si}	Narrow	$\delta_s(CH_3)$ in R_xSi
1550, 1560	O_{2Si}, Z_{1Si}	Broad	C=N
1668, 1660	O_{2Si}, Z_{1Si}	Broad	C=N
2170–2180	O_{2Si}, Z_{1Si}	Broad	ν(SiH)
2962, 2967	O_{2Si}, Z_{1Si}	Narrow	$\nu_s(CH_3)$
2927	O_{2Si}	Narrow	$\nu_{as}(CH_2)$
2854	O_{2Si}	Narrow	$\nu_s(CH_2)$
3000–3600	O_{2Si}, Z_{1Si}	Two broad bands	$\nu(NH_2)$, ν(NH) and ν(OH)

performed after several months of storage. Besides carbon, oxygen, nitrogen and silicon present in the gas feed, a small amount of sodium was found on the surface. It originated from the glass substrate material. It is interesting to notice that the films deposited on silicon substrates, Z_{1Si} and O_{2Si}, contain much more nitrogen than their counterparts, Z_1 and O_2, on glass. The most striking difference among the samples is the shape of the C 1s atomic signal (see figure 9). The carbon signal of the samples Z_1–Z_5, Z_{1Si}, O_1 and O_{2Si} exhibits very high asymmetry towards higher binding energies (BEs) spreading the signal over 7–8 eV. This evidences a presence of carbon in many different chemical binding states related namely to oxygen and nitrogen moieties. The samples O_2 and O_4 have quite symmetrical C 1s signals. Relatively good fits can be obtained with only one Gaussian of 1.65 eV and 1.78 eV FWHM, respectively. Comparing the oxygen and nitrogen concentrations for all of the samples we can see that the only significant difference between them is the nitrogen concentration (see table 1). The oxygen concentration varies in the range 25–30% without any clear dependence. The nitrogen concentration is below 9% for O_2 and O_4 films and in the range 14–25% for the rest of them. Therefore, we expect that broadening and high asymmetry of the carbon peak is caused mainly by CN functionalities. This is also in agreement with the fact that the narrowest carbon peak is obtained on the film O_2 which has the lowest nitrogen concentration.

The position of all atomic signals is influenced by a charging of the insulating films. At first we tested the correction on charging for sample O_2 with very low amount of nitrogen. We corrected the position of the C 1s to the BE in siloxanes, i.e. 284.4 eV [27, 28]. The position of O 1s after the same correction, 532.0 eV, corresponds very well with siloxanes [29]. For Si $2p_{3/2}$, we get 102.5 eV, which is a little bit higher than the expected value of 102.15 ± 0.36 eV [29]. Anyway, the energy of silica, 103.4–103.5 eV [28–30], is not reached and we conclude that the hydrocarbon groups are bonded in the siloxane network. Since the proposed correction

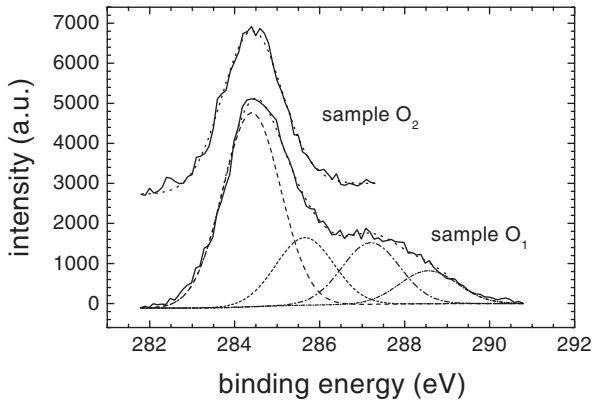

Figure 9. XPS spectra of C 1s for two pp-HMDSO films deposited at different monomer flow rate and their deconvolution. For the discussion see text.

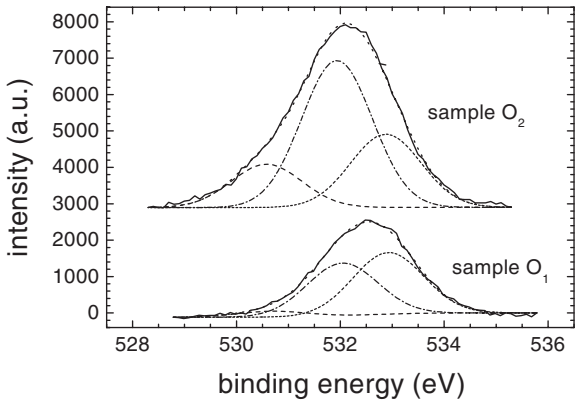

Figure 10. XPS spectra of O 1s for pp-HMDSO films deposited at different monomer flow rates and their deconvolution. For the discussion see text.

on charging gave reasonable results, we decided to correct all the spectra in following discussion by positioning the main carbon peak at 284.4 eV.

The deconvolution of the C 1s signal was performed using four Gaussian profiles with the fixed FWHM of 1.6 eV. An example of this fit is shown in figure 9. Except the samples O_2 and O_4 with low amount of nitrogen, the C 1s signal was composed of the siloxane peak at 284.4 eV (dash profile in figure 9) and three additional peaks at 285.5–286.1, 287.2–287.5 and 288.6–289.1 eV. According to the literature on CN_x films, the most widely accepted approach in assignment of nitrogen-bonded carbon species attributes the carbon peaks at 285.1–286.2 eV and 287.3–287.8 eV (short dash and dash dot profiles in figure 9) to sp^2 and sp^3 hybridized carbon bonded to nitrogen (sp^2C–N, sp^3C–N), respectively [31–33]. This assignment is further supported by the FTIR analyses discussed above where the presence of C=N bonds was observed at 1555, 1655 cm^{-1} and the C–N bonds could be a part of the broad intensive peak centred at $\approx$1040 cm^{-1}. Although we think that the major contribution of the higher BE peaks is related to nitrogen-bonded carbon, the presence of the small peak at 288.6–289.1 eV (short dash dot profile in figure 9) revealed oxygen-bonded carbon and some oxygen related species can contribute to the other two peaks too [27, 29].

The Si 2p signal was symmetrical, but the relatively large FWHM of the Gaussian fits, 2.0–2.3 eV, suggested that it is composed of different binding states. Indeed, the narrowest peak was observed for samples O_2 and O_4. The position of Si $2p_{3/2}$ ranged from 102.0 to 102.7 eV. The broadening at the side of higher BEs can be attributed to silicon surrounded by more oxygen atoms. The position 103.4–103.5 eV found for silica (–O–SiO_2–O–) [28, 29] is a high energy limit in this case. The broadening at the side of the lower energies is caused by silazane groups (101.2–101.3 eV [29]). However, the plasma polymerized (pp) HMDSN films Z_1–Z_5 reacted with air humidity replacing silazane groups by siloxanes and therefore the Si 2p peak for all the samples corresponds to the position expected for siloxane compounds. As regards the O 1s atomic signal, the samples Z_1, Z_2, Z_3 and O_2 show clear asymmetry to lower BEs. When fitted by one Gaussian profile, the FWHM is in the range 2.0–2.2 eV and the position, 532.0–532.6 eV, agrees with that for siloxanes. The asymmetry at the lower BEs is caused by oxygen bonded to sodium which position for ONa_x compounds was found at 530.8–530.9 eV [34]. Therefore, we deconvoluted the oxygen signal into three Gaussian profiles with the FWHM fixed at 1.6 eV. The comparison of the results for two samples, O_1 and O_2, differing in the concentration of sodium is shown in figure 10. The low energy peak at $\approx$530.6 eV (dash profile in figure 10) is assigned to sodium-bonded oxygen, whereas the peak at $\approx$532.3 eV (dash dot profile in figure 10) corresponds to siloxanes and the high energy peak at 532.9–533.8 eV (short dash profile in figure 10) can be ascribed to O–H bonds (H_2O, Si–O–H) referred for silicate glasses at 533.3 eV [35]. This assignment is further supported by the presence of bands of silanol groups in the FTIR spectra. The position of the relatively symmetrical nitrogen signal for samples Z_1–Z_5 increases from 399.2 to 400.5 eV. For O_1, O_{2Si} and O_4 the position ranged from 398 to 400 eV. The FHWMs are larger than 2.5 eV. The observed shift to the higher energies can be explained by a decreased contribution of silicon-bonded nitrogen (398 eV [29,36]), presence of N–C–O groups (400 eV [29]) and carbon-bonded nitrogen species with sp^3 and sp^2 hybridized C, 399.1–400.2 eV [31, 37, 38] and 400.4–401.7 eV [31, 37, 38], respectively.

3.2.4. Surface free energy. The so-called 'acid–base' theory is very often used for the surface free energy calculation. This theory enables to determine the polar and apolar (dispersion) parts of the total surface free energy γ and the electron-donor and electron-acceptor components of the polar part of the surface free energy

$$\gamma = \gamma^{LW} + \gamma^{AB}. \tag{1}$$

The superscript LW indicates the total apolar (dispersive) Lifshitz–van der Walls interaction and AB refers to the acid–base or electron-acceptor/electron-donor interaction according to Lewis

$$\gamma^{AB} = 2\sqrt{\gamma^{+}\gamma^{-}}, \tag{2}$$

where γ^+ is the electron-donor and γ^- the electron-acceptor component of the acid–base part of surface free energy. The surface free energy can be calculated according to the Young–Dupré equation expressed by terms as electron-donor γ^+ and

Table 3. List of testing liquids. γ_{tot} is the total surface tension of the liquid, γ^{LW} is its apolar and γ^{AB} is its polar component. γ^+ is the electron-donor and γ^- is the electron-acceptor parameter.

Testing liquid	γ_{tot} (mJ m^{-2})	γ^{LW} (mJ m^{-2})	γ^{AB} (mJ m^{-2})	γ^+ (mJ m^{-2})	γ^- (mJ m^{-2})
Distilled water	72.8	21.8	51.0	25.5	25.5
Glycerol	64.0	34.0	30.0	3.9	57.4
Ethylene glycol	48.0	29.0	19.0	3.0	30.1
CH_2I_2	50.8	50.8	—	—	—

Table 4. The results of the surface energy calculation. γ_{tot} is the total surface energy, γ^{LW} is its apolar and γ^{AB} is its polar component. γ^+ is the electron-acceptor and γ^- is the electron-donor parameter. Due to large error in γ^{AB} the value of γ^+ and γ^- were not calculated for the samples Z_1 and Z_2.

Sample	γ_{tot} (mJ m^{-2})	γ^{LW} (mJ m^{-2})	γ^{AB} (mJ m^{-2})	γ^+ (mJ m^{-2})	γ^- (mJ m^{-2})
Z_1	28.2 ± 0.5	28.1 ± 0.3	0.1 ± 0.1	—	—
Z_2	26.0 ± 0.5	25.8 ± 0.3	0.2 ± 0.1	—	—
Z_3	36.0 ± 0.7	29.6 ± 0.4	6.4 ± 0.2	0.3 ± 0.2	35 ± 5
Z_4	30.0 ± 0.5	26.9 ± 0.3	2.8 ± 0.2	0.1 ± 0.2	16 ± 3
Z_5	28.0 ± 0.5	26.4 ± 0.3	1.6 ± 0.2	0.4 ± 0.2	1 ± 2
O_1	37.8 ± 0.7	24.3 ± 0.4	13.5 ± 0.3	1.5 ± 0.3	30 ± 5
O_2	44.7 ± 0.9	24.8 ± 0.4	19.9 ± 0.4	7.3 ± 0.4	14 ± 4
O_3	29.1 ± 0.6	23.3 ± 0.4	5.8 ± 0.4	0.4 ± 0.2	19 ± 5
O_4	28.2 ± 0.4	25.6 ± 0.3	2.6 ± 0.3	0.3 ± 0.2	6 ± 3

electron-acceptor γ^- components

$$(1 + \cos\theta_i)\gamma_i = 2\left(\sqrt{\gamma_i^{LW}\gamma_j^{LW}} + \sqrt{\gamma_i^+\gamma_j^-} + \sqrt{\gamma_i^-\gamma_j^+}\right). \qquad (3)$$

Here j refers to the studied material and i refers to the testing liquid. The values can be determined from contact angle measurements with three liquids of which two must have polar component. The liquids and their characteristic parameters used for contact angle measurements are listed in table 3.

In table 4, the surface free energy and its above-mentioned components calculated according to (3) characterizing the surface of the prepared pp-HMDSN and pp-HMDSO coatings are given. The results of the surface free energy calculation are in good agreement with the results of XPS analysis. The base part of the surface energy has similar dependence on the deposition conditions as the amount of nitrogen in the surface region of the coating which is known to be responsible for the base character of the surface.

In case of the films deposited from HMDSO the apolar part does not change with the concentration of monomer, but the polar part decreases with increasing concentration. Total surface free energy of the films deposited from HMDSN and its polar and apolar parts depend only slightly on the concentration of HMDSN.

3.2.5. Optical properties. The films were only slightly absorbing in the UV–VIS and the ellipsometric measurements could be fitted using a simple Cauchy formula for film refractive index n and an exponential form for the film extinction coefficient k (λ is the wavelength)

$$n = a + \frac{b}{\lambda^2} + \frac{c}{\lambda^4}, \qquad k = \alpha \exp(-\beta\lambda), \qquad (4)$$

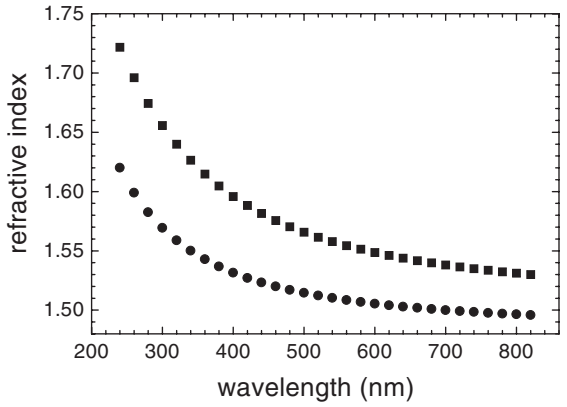

Figure 11. Refractive index of the films deposited from HMDSO/N_2 (●), sample O_{2Si} and HMDSN/N_2 (■), sample Z_{1Si}.

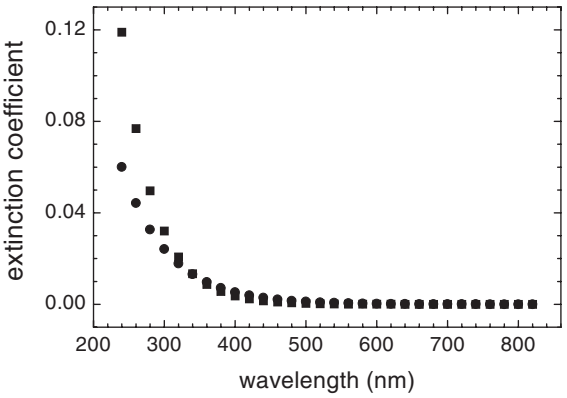

Figure 12. Extinction coefficient of the films deposited from HMDSO/N_2 (●), sample O_{2Si} and HMDSN/N_2 (■), sample Z_{1Si}.

where a, b, c, α and β are the dispersion parameters. The optical properties, refractive index and extinction coefficient in the UV–VIS for films deposited from both monomers are given in figures 11 and 12.

The refractive indices are higher than for silicon oxides but lower than for silicon nitrides. Although both mentioned materials are fully transparent, the deposited polymers exhibit absorption especially in UV.

3.2.6. Mechanical properties. The Fischerscope H100 depth sensing indentation tester equipped with Vickers indenter was used to study the mechanical properties of the coating–substrate system. On the basis of the load–penetration dependences, we studied the universal hardness, the elastic deformation work, the irreversibly dissipated indentation work, the plastic hardness and elastic modulus of the pp-HMDSO and pp-HMDSN films deposited on glass substrate. The applied load ranged from 0.4 mN to 1 N. In the following definition A_c is the contact area between the indenter and the material studied under load L

$$\mathrm{HU} = \frac{L}{A_c} = \frac{L}{26.43h^2}. \qquad (5)$$

Here HU is the so-called universal hardness and 26.43 is a factor, which characterizes the Vickers indenter geometry. The universal hardness gives information about the resistance of the

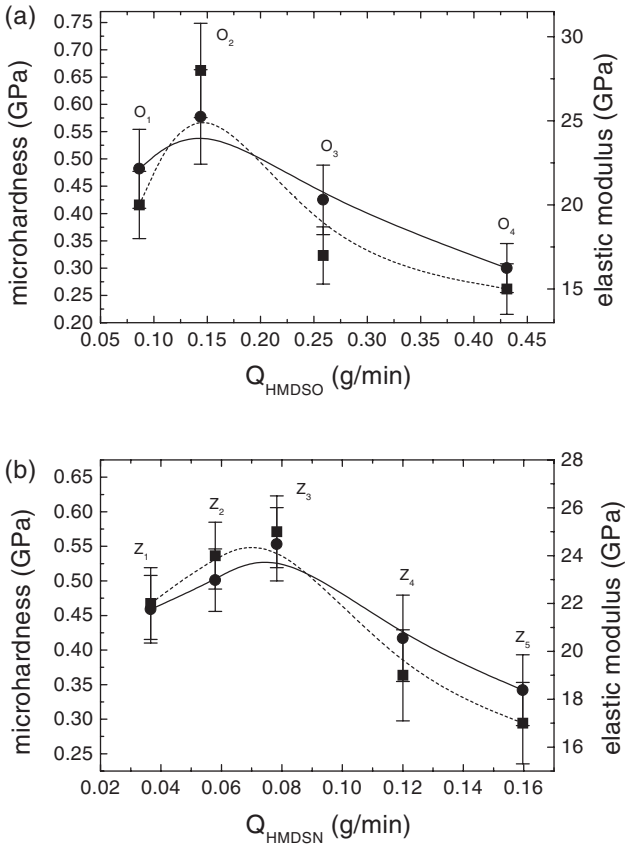

Figure 13. The film microhardness and elastic modulus. (*a*) pp-HMDSO films, (*b*) pp-HMDSN films. ●, microhardness; ■, elastic modulus.

material to either elastic or plastic deformation. On the basis of the load–penetration curves it is possible to determine also the material resistance against plastic deformation (so-called plastic hardness or microhardness) H_{pl}

$$H_{pl} = \frac{L_{max}}{26.43 h_r^2}, \tag{6}$$

where h_r is the depth of the remaining indentation print.

The coatings exhibited good abrasion resistance and the microhardness of the films deposited from organosilicon/nitrogen mixtures (measured on films deposited on thin glass plates) was about 0.3–0.7 GPa. The elastic modulus Y ($Y = E/(1-\nu^2)$, where E is the Young's modulus and ν is the Poisson's ratio) ranged from 15 to 28 GPa. The film microhardness and elastic modulus dependences on the monomer flow rate are depicted in figure 13. In order to illustrate the reproducibility of the mechanical tests, several load–penetration curves obtained at different places on the coating Z_1 are depicted in figure 14. The coatings exhibited polymer-like visco-plastic behaviour. We also studied the creep (time dependent plastic deformation at constant applied load) behaviour of the deposited film Z_1. In figure 15 the time dependence of the creep strain is illustrated for the coating prepared from mixture of HMDSN and nitrogen. The creep strain is expressed as the percentage of the maximum depth achieved under the testing load at the beginning of the creep test.

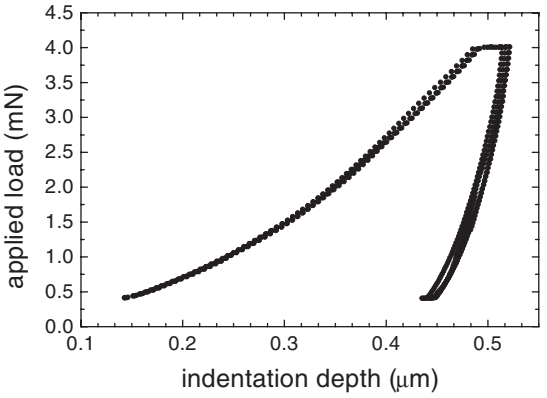

Figure 14. The load–penetration curves for the coating deposited on glass substrate from a mixture of HMDSN and nitrogen (sample Z_1). The universal hardness was (0.45 ± 0.07) GPa, the plastic hardness was (0.46 ± 0.07) GPa, the elastic modulus was (22 ± 2) GPa. The indentation tests exhibited good reproducibility, as can be seen from this figure for several load–penetration curves.

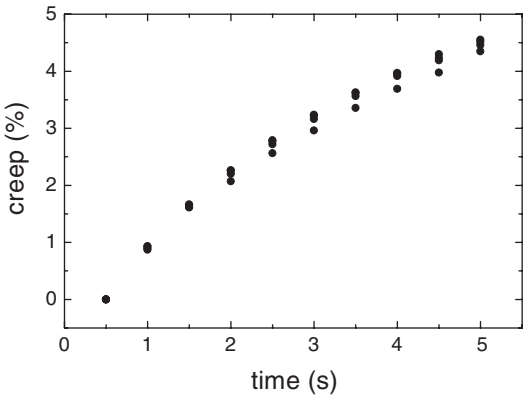

Figure 15. Creep curves measured at constant load of 4 mN for coating deposited on glass substrate from mixture of HMDSN and nitrogen (sample Z_1).

4. Conclusion

A new deposition technique based on atmospheric pressure glow discharge was studied. The layers were deposited from mixtures of organosilicon monomers (HMDSO, HMDSN) with nitrogen. The discharge was homogeneous (APGD) at low monomer flow rate and filamentary at higher flow rate. The optical emission spectra of the discharges containing HMDSO or HMDSN were very similar. The spectra consisted of the molecular bands of the second positive system of nitrogen ($C\,^3\Pi_u \rightarrow B\,^3\Pi_g$) and in case of the monomer addition two intensive bands of CN violet system ($B\,^2\Sigma^+ \rightarrow X\,^2\Sigma^+$) appeared at 388 and 422 nm. The CN/N_2 ratio of integrated intensities increased with increasing concentration of HMDSO or HMDSN and reached constant value at higher monomer flow rates. The films deposited in APGD were homogeneous with uniform thickness, whereas the films deposited in filamentary discharge were full of sharp objects. The films were polymer-like and transparent in visible range. The film hardness varied from 0.3 to 0.6 GPa depending on deposition conditions, the elastic modulus was in the range 15–28 GPa. The free surface energy of deposited coatings was in the range of 30–45 mJ m^{-2} (pp-HMDSO) and 26–40 mJ m^{-2} (pp-HMDSN) depending on

the conditions of the deposition. The FTIR spectra showed organic structure of the films, the presence of $(CH_3)_x$–Si–O– groups, C–N and C=N bonds and also C–O and O–H bonds. The XPS analysis confirmed the presence of above-mentioned bonds. The basic character of the film surface determined by the surface energy measurement is in good agreement with the nitrogen content in the films.

Acknowledgments

The present work was supported by the Grant Agency of the Czech Republic, contract Nos 202/02/0880 and 202/02/D097 and by the Ministry of Education of the Czech Republic, contracts MSM143100003, COST 527.20 and ME489.

References

[1] Sawada Y, Ogawa S and Kogoma M 1995 *J. Phys. D: Appl. Phys.* **28** 1661
[2] Prat R, Koh Y J, Babukutty Y, Kogoma M, Okazaki S and Kodama M 2000 *Polymer* **41** 7355
[3] Gherardi N, Martin S and Massines F 2000 *J. Phys. D: Appl. Phys.* **33** L104
[4] Foest R, Adler F, Sigeneger F and Schmidt M 2003 *Surf. Coat. Technol.* **163–164** 323
[5] Kanazawa S, Kogoma M, Moriwaki T and Okazaki S 1988 *J. Phys. D: Appl. Phys.* **21** 838
[6] Gherardi N, Gouda G, Gat E, Ricard A and Massines F 2000 *Plasma Sources Sci. Technol.* **9** 340
[7] Trunec D, Brablec A and Buchta J 2001 *J. Phys. D: Appl. Phys.* **34** 1697
[8] Brandenburg R, Kozlov K V, Massines F, Michel P and Wagner H-E 2000 *Proc. HAKONE VII (Greifswald)*
[9] Wrobel A M and Wertheimer M R 1990 *Plasma Deposition, Treatment and Etching of Polymers* ed R d'Agostino (New York: Academic)
[10] Zajíčková L, Buršíková V, Peřina V, Macková A, Subedi D, Janča J and Smirnov S 2001 *Surf. Coat. Technol.* **142–144** 449
[11] Sonnenfeld A, Tun T M, Zajíčková L, Kozlov K V, Wagner H-E, Behnke J F and Hippler R 2001 *Plasma Polym.* **6** 266
[12] Good R J 1993 *Contact Angle, Wettability and Adhesion* ed K L Mittal (Utrecht: VSP BV)
[13] Dischler B, Bubenzer A and Koidl P 1983 *Solid State Commun.* **48** 105
[14] *NIST Chemistry WebBook* http://webbook.nist.gov
[15] Ball D F, Carter T, McKean D C and Woodward L A 1964 *Spektrochim. Acta* **20** 1721
[16] Martinet C and Devine R A B 1995 *J. Appl. Phys.* **77** 4343
[17] Bürger H 1968 *Organometal. Chem. Rev.* A **3** 425
[18] Kim M T 1997 *Thin Solid Films* **311** 157
[19] Smith A L 1983 *Analysis of Silicones* (New York: Wiley)
[20] Kim M T and Lee J 1997 *Thin Solid Films* **303** 173
[21] Lamendola R, D'Agostino R and Fracasi F 1997 *Plasmas Polym.* **2** 147
[22] Pecheur A, Autran J L, Lazarri J P and Pinard P 1999 *J. Non-Cryst. Solids* **245** 20
[23] Mutsukura N and Akita K 1999 *Thin Solid Films* **349** 115
[24] Ungureanu A, Trong On D, Dumitriu E and Kaliaguine S 2003 *Appl. Catalysis A: General* **254** 203
[25] Thärigen T *et al* 1999 *Thin Solid Films* **348** 103
[26] Aumaille K, Vallée C, Granier A, Goullet A, Gaboriau F and Turban G 2000 *Thin Solid Films* **359** 188
[27] Beamson G and Briggs D 1992 *High Resolution XPS of Organic Polymers* (Chichester: Wiley)
[28] Alexander M R, Short R D, Jones F R, Stollenwerk M, Zabold J and Michaeli W 1996 *J. Mater. Sci.* **31** 1879
[29] Gengenbach T R and Griesser H J 1999 *Polymer* **40** 5079
[30] Fourches N, Turban G and Grolleau B 1993 *Appl. Surf. Sci.* **68** 149
[31] Sánchez López J C, Donnet C and Le Mogne T 2002 *Vacuum* **64** 198
[32] Bell J, Chen Z and Olofinjana A 2001 *Diamond Relat. Mater.* **10** 2184
[33] Riedo E, Comin F, Chevrier J and Bonnot A M 2000 *J. Appl. Phys.* **88** 4365
[34] Ji S, Xiao T, Li S, Chou L, Zhang B, Xu Ch, Hou R, York A P E and Green M L H 2003 *J. Catalysis* **220** 47
[35] Schultz-Münzenberg C, Meisel W and Gütlich P 1998 *J. Non-Cryst. Solids* **238** 83
[36] Inakagi N, Kondo S, Hirata M and Urushibata H 1985 *J. Appl. Polym. Sci.* **30** 3385
[37] Lai S H, Chen Y L, Chan L H, Pan Y M and Shih H C 2003 *Thin Solid Films* **444** 38
[38] Hammer P and Alvarez F 2001 *Thin Solid Films* **398–399** 166

Plasma Sources Sci. Technol. **15** (2006) 8–17 doi:10.1088/0963-0252/15/1/002

Comparative study of diffuse barrier discharges in neon and helium

Z Navrátil[1,2], R Brandenburg[3,4], D Trunec[1], A Brablec[1], P St'ahel[1], H-E Wagner[3] and Z Kopecký[5]

[1] Department of Physical Electronics, Faculty of Science, Masaryk University in Brno, Kotlářská 2, CZ-611 37 Brno, Czech Republic
[2] Department of General Physics, Faculty of Science, Masaryk University in Brno, Kotlářská 2, CZ-611 37 Brno, Czech Republic
[3] Institute of Physics, Ernst-Moritz-Arndt University of Greifswald, Domstrasse 10a, D-17489 Greifswald, Germany
[4] Institute of Low Temperature Plasma Physics, F.-L.-Jahn-Strasse 19, D-17489 Greifswald, Germany
[5] Department of Theoretical Physics and Astrophysics, Faculty of Science, Masaryk University in Brno, Kotlářská 2, CZ-611 37 Brno, Czech Republic

E-mail: zdenek@physics.muni.cz

Received 10 February 2005
Published 18 November 2005
Online at stacks.iop.org/PSST/15/8

Abstract

Diffuse dielectric barrier discharges in neon and helium at atmospheric pressure were studied. The discharges were generated between two metal electrodes, both covered by an alumina layer and driven by ac voltage of frequency 10 kHz. The discharge gap was 2.2 mm and 5 mm, respectively.

The discharges were investigated by electrical measurements and by temporally and spatially resolved optical emission spectroscopy. The experimental results revealed similar discharge behaviour in both gases being considered. Although the discharges were ignited at slightly different electric field strengths, their evolutions were found to be similar. At maximum discharge current the spatial light intensity distribution was characterized by the formation of a cathode fall. A difference was observed in the magnitudes of the current density only.

In addition to the regime with a single discharge pulse per voltage half period $T/2$, a discharge mode with two and more subsequent current pulses per $T/2$ (also referred to as the pseudoglow discharge regime in the literature) was obtained due to an increase in the voltage amplitude or an admixture of nitrogen.

(Some figures in this article are in colour only in the electronic version)

1. Introduction

Dielectric barrier discharges (DBDs) are convenient plasma sources for the generation of non-thermal plasmas at atmospheric pressure. Usually the DBD plasma consists of many tiny microdischarges (or filaments) of nanosecond or microsecond duration. The properties of these so-called filamentary discharges and the actual microdischarges have been studied elsewhere (see e.g. Eliasson and Kogelschatz(1991), Gibalov and Pietsch(2000), Kozlov *et al* (2001)).

Under special operation conditions, particularly in certain gases or gas mixtures, so-called diffuse DBDs can be obtained in a DBD configuration. These discharges are also referred to as homogeneous DBDs or atmospheric pressure glow discharges (APGDs). So far, diffuse DBD has been revealed and investigated in helium, neon, nitrogen and argon with admixtures of acetone (see e.g. Massines *et al* (1998), Gherardi *et al* (2000), Trunec *et al* (2001)). The homogeneity of the diffuse DBD is very desirable for industrial applications, especially for surface treatment processes.

Diffuse discharges in helium, at conditions similar to those being considered in this paper, have been studied by means of electrical measurements and short time exposure photography (e.g. Massines *et al* (1998), Radu *et al* (2004)), by temporally resolved optical emission spectroscopy(Ricard *et al* 1999) and by numerical modelling (e.g.Golubovskii *et al* (2003)). It was found that the diffuse DBD in helium is a transient glow discharge, since the formation of a cathode fall and a positive column were observed. According to Massines *et al* (1998) electrons and ions are trapped in the positive column from one discharge cycle to the following one. This process leads to a pre-ionization of the gas below the ignition voltage and is manifested in the so-called 'residual current peak', a small increase of the discharge current about 2 μs after the inversion of the voltage polarity. Furthermore Massines *et al* (1998) as well as Müller and Zahn(1996), Golubovskii *et al* (2003) and Radu *et al* (2004) pointed out the important role of indirect ionization processes, e.g. Penning ionization of N_2 molecules originating from dilute gas impurities by helium metastable states.

Trunec *et al* (2001) demonstrated that a diffuse DBD can be generated in neon as well. But the character of the discharge remains unknown at this point of time. As demonstrated by different teams (e.g. Gherardi *et al* (2000), Kozlov *et al* (2005)) in nitrogen a different kind of diffuse DBD is generated. This discharge reveals the structure of a Townsend discharge. No significant space charges are formed; the maximum of excited species was found in front of the anode.

The distinction between the diffuse and filamentary regimes is mostly monitored with the use of electrical measurements. However, the distinction between the different discharge structures (as concerning Townsend or glow discharge) and the study of a discharge development can be performed by means of optical methods with a temporal and spatial resolution as short time exposure photography or temporally and spatially resolved optical emission spectroscopy.

In this work spatially and spectrally resolved time-correlated single photon counting (TC-SPC) was used for the comparative study of the diffuse DBDs in neon and helium. A description of our experimental set-up is given in section 2. The results are presented in section 3. While section 3.1 is concerned with the electrical measurements, in section 3.2 overview spectra and the spatio-temporally resolved discharge development are discussed.

2. Experimental set-up

The experimental set-up is schematically shown in figure 1. It is basically the same set-up as described by Kozlov *et al* (2001) and Kozlov *et al* (2005), and it was originally equipped for cross-correlation spectroscopy (CCS) on DBD-microdischarges. The discharge was generated in a parallel plane discharge cell consisting of two metal electrodes (1) both covered by a 0.7 mm thick alumina (Al_2O_3) layer (2) with a relative permittivity of $\epsilon_r = 9.4 \pm 0.3$. The electrode area was 20 mm × 20 mm and the area of the covering dielectric plates was 30 mm × 36 mm. The electrodes were fixed by two space holders made of organic glass (3) ensuring a constant discharge gap. Two discharge cells, with discharge gaps of 2.2 mm and 5.0 mm respectively, were used.

The discharge cell was placed in a stainless steel vacuum chamber connected to a rotary vacuum pump (ILMVAC PK 4D rotary pump) and to a gas supply, with a flow control unit. The chamber was evacuated down to 10 Pa first and then filled with neon or helium gas (purity 99.999 vol%) slightly above atmospheric pressure. After that, the gas outlet was opened to the atmosphere, sustaining the discharge in the gas flowing regime. Using a sealing ring with a nozzle on the gas entrance and a pipe (4) the gas was directly injected into the discharge volume. A small admixture of a second gas (e.g. nitrogen) could be added to the working gas. The pressure in the chamber was controlled by ILMVAC Piza 2000 manometer. The total gas flow rate was 450 sccm, kept by MKS 1259 CC gas flow controllers.

The discharge was driven by an ac voltage of frequency 10 kHz. The sinusoidal voltage signal from a Voltcraft MXG-9802 function generator was amplified using a Conrad Skyline-Storm amplifier (400 W) and transformed to a high voltage signal with amplitude $U_{a0} = 0.5$–2 kV. The applied voltage U_a and the discharge current I were measured by Tektronics TDS 380 (400 MHz bandwidth, 2 GSamples/s) digital oscilloscope. The applied voltage U_a was measured via a 1000 : 1 voltage divider; the current I was monitored by measuring the voltage across a 100 Ω resistor, connected in series with the discharge cell. The gap voltage U_g and the memory voltage U_m were calculated from the applied voltage U_a and the current I using equations (1) and (2) as described by Massines *et al* (1998):

$$U_a(t) = U_g(t) + U_m(t), \tag{1}$$

$$U_m(t) = U_m(t_0) + \frac{1}{C_d}\int_{t_0}^{t} I(t')\,dt', \tag{2}$$

where $C_d \approx 24$ pF is the dielectric capacitance of the dielectric barriers, and $U_m(t_0)$ is the initial memory voltage across the dielectrics, which was adjusted in order to obtain the symmetrical evolution of the gap voltage (i.e. $\langle U_g \rangle = 0$).

The chamber was equipped with two quartz windows for discharge diagnostics. The window (5) served for direct observations, the other (6) was used for spatially and temporally resolved optical emission spectroscopy measurements. The lens (7) was placed at a distance of double focal length $2f_L$ from the discharge cell centre, imaging the discharge $1:(-1)$ onto an optical slit (8). This optical slit, 0.3 mm wide, was moved in the image and collected the light from a narrow discharge area, providing a one-dimensional spatial resolution along the discharge gap. Thus the slit was placed together with a lens (9) and the end of an optical fibre on an optical table, which was vertically adjustable by a computer controlled stepper motor. The lens (9) was used to project the slit onto the fibre entrance.

The optical fibre led to a Jobin Yvon TRIAX 320 spectrometer. The overview spectra were taken with a standard R 928 Hamamatsu photomultiplier (not shown in figure 1). For temporally resolved measurements the light was detected by water cooled highly sensitive PMH-100-4 photomultiplier (Hamamatsu) and analysed by means of TC-SPC module (SPC-530, Becker and Hickl). The SPC module was originally

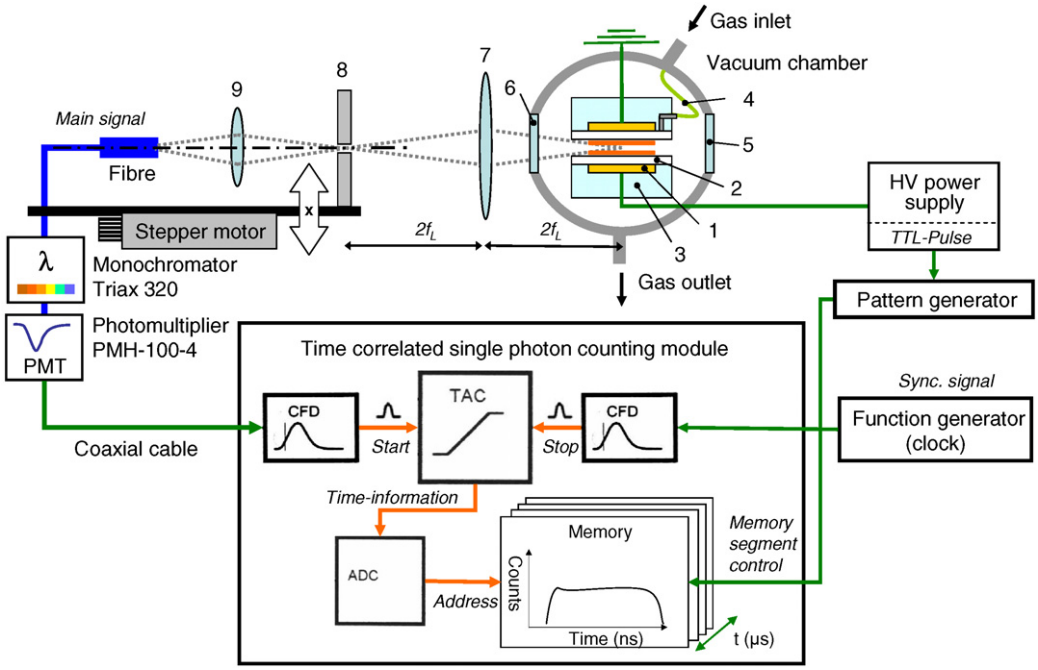

Figure 1. Scheme of the experimental set-up. (1) Metal electrode, (2) dielectric layer, (3) block of organic glass, (4) pipe, (5) and (6) quartz windows, (7) and (9) quartz lenses and (8) slit.

designed for the CCS method, and it had to be modified to investigate the diffuse DBD (Kozlov *et al* 2005). The diffuse DBDs produce periodical light pulses with a duration of typically several microseconds. Since the CCS apparatus was designed for optical triggering using statistically occurring light pulses with a duration in the nanosecond-range, the synchronization signal was missing. Therefore, an external independent function generator was used to provide the synchronization signal. The time-resolution of the photon counting procedure was realized by the pattern generator, which controlled the memory segment allocation of the SPC device. Since the discharge was periodical, the pattern generator was triggered directly by the power supply. A maximum time-resolution of 0.4 μs could be achieved with the apparatus.

3. Results and discussion

3.1. Electrical characteristics

Typical current and voltage oscillograms of diffuse DBDs burning in 5 mm discharge cell in pure neon and helium are shown in figure 2. The applied voltage was sinusoidal in both cases, except the voltage drop during the current pulse. This voltage drop was due to the limitations of the power supply. The breakdown voltage was evidently different with regard to both neon and helium. Before the current peak starts to rise, the applied voltage reached values of 0.3 kV and 0.7 kV in neon and helium, respectively. The gap voltage thus reached values of 0.7 kV and 1.3 kV in neon and helium, respectively. This difference is to be expected when comparing the energy dependences of neon and helium ionization cross sections (see figure 3). The ionization cross section of neon has a lower threshold energy than that of helium, and it is also higher above the threshold. Thus at comparable low electric field strength the ionization rate in neon can be expected to be higher than that of helium.

If the value of the applied voltage is close to the breakdown voltage, a single current peak per voltage half period is observed; the discharge operates in the so-called single peak mode (SPM). When comparing figures the current peaks of neon and helium discharge appear very similar. First a fast current increase (lasting about 4 μs) is observed in both cases, followed by a decay of about 20 μs. This current discharges and charges the dielectrics (see the slope of the memory voltage). The change of the memory voltage and the drop of the applied voltage (due to the limitations of the power supply) results in the drop of the gap voltage and the current decrease.

As observed by Mangolini *et al* (2002) as well as by Radu *et al* (2003), a higher applied voltage or a small admixture of nitrogen in the range of 100–800 ppm produced additional current peaks within the same half period. Up to four current peaks per $T/2$ could be investigated using our set-up. The electrical characteristics of this so-called double peak mode (DPM), also referred to as pseudoglow discharge regime and first reported by Bartnikas(1968) (see Radu *et al* (2003)), are displayed in figure 4. When the current decays at the end of the preceding peak, the applied and the gap voltage increase again, and a second breakdown can take place.

If nitrogen is admixed, electrons and N_2^+ ions are created by Penning effect (equations (3) and (4) and similarly for helium), which is the dominating ionization process in the time of current pulse decay (Radu *et al* 2003, Mangolini *et al* 2004):

$$\mathrm{Ne}(3s'[1/2]_0, 3s[3/2]_2) + \mathrm{N_2} \rightarrow \mathrm{N_2^+} + \mathrm{Ne} + \mathrm{e^-}, \quad (3)$$

$$\mathrm{Ne_2^*} + \mathrm{N_2} \rightarrow \mathrm{N_2^+} + 2\mathrm{Ne} + \mathrm{e^-}. \quad (4)$$

The generation of free electrons by this additional process results in a decrease of the voltage required for the breakdown.

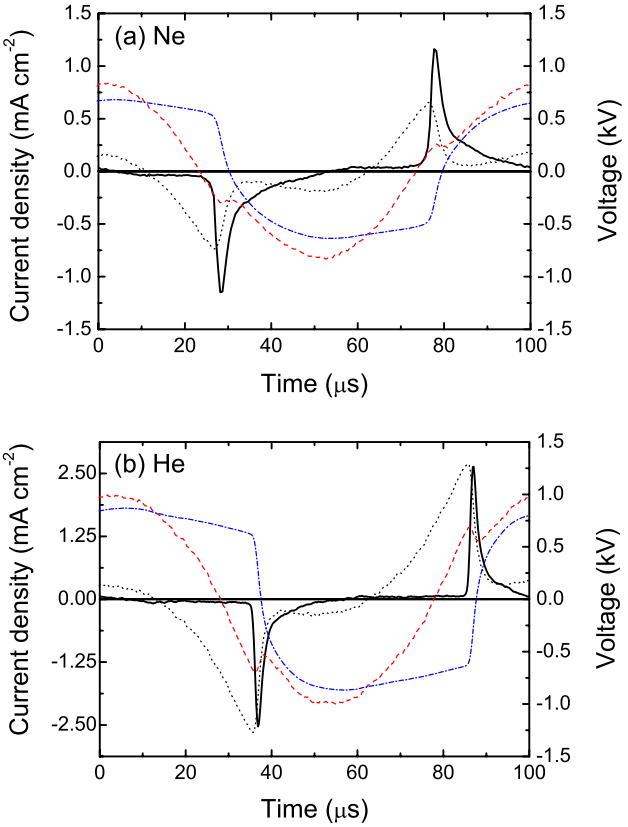

Figure 2. The current (——), applied voltage (- - - -), gap voltage (· · · · · ·) and memory voltage (— · —) evolution of the diffuse discharge in neon (*a*) and helium (*b*) in SPM.

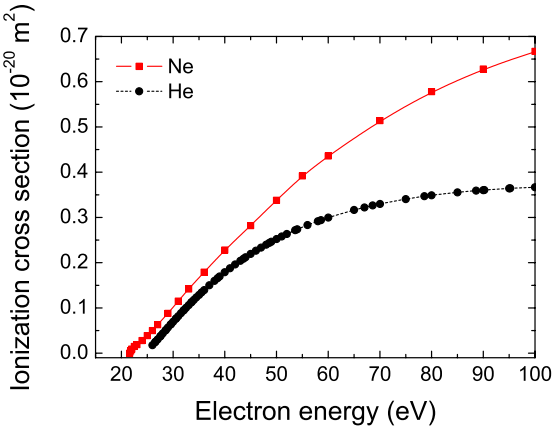

Figure 3. Total ionization cross sections of neon (Wetzel *et al* 1987) and helium (Kim and Rudd1994). The ionization energy is 21.6 eV and 24.6 eV, respectively.

Consequently, the second discharge is ignited at lower gap voltage than at the first breakdown (see figure 4). This explanation is in agreement with the discussion of Radu *et al* (2003) as well as of Mangolini *et al* (2002). The former discussed in great detail the influence of impurities, voltage amplitude and frequency in discharge cells with a gap of 0.5 mm.

In figure 5 an enlarged view of the current oscillogram is shown. A small 'residual current peak' was registered in our

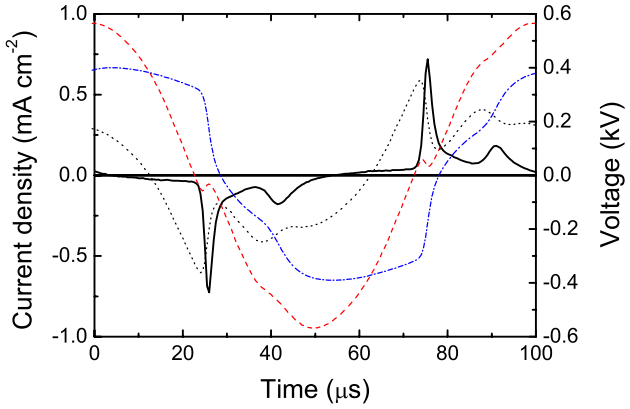

Figure 4. The current (——), applied voltage (- - - -), gap voltage (· · · · · ·) and memory voltage (— · —) evolution of the diffuse neon discharge in DPM.

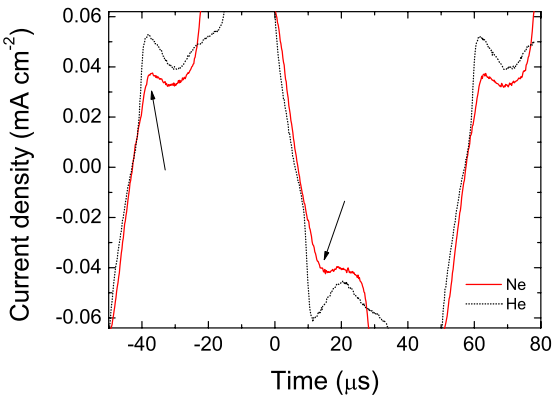

Figure 5. Enlarged view of the current oscillograms, showing the 'residual current peak' in diffuse DBDs in neon and helium. The helium current oscillogram is shifted in time for better comparison.

experiments in neon and helium with a similar magnitude as described by Massines *et al* (1998) (see the arrows in figure 5). However, the high luminosity of neon lines allowed us to assign the occurrence of such a current peak to a small spurious discharge burning on the edge of the dielectric layer, which appeared only at a narrow band of voltage frequencies approximately at 10 kHz. Furthermore, in the discharge cell with a gap of 2.2 mm a diffuse DBD was generated, but no residual current peak was observed. From our results, we suggest that free electrons from the previous discharge cannot remain in the area of the positive column of the transient glow discharge. Furthermore, we consider the indirect ionization involving long-lived species such as metastables and excimers to be fundamental for the generation of a diffuse DBD in helium and neon. Similarly Mangolini *et al* (2004) modelling the helium diffuse discharge came to the conclusion that most electrons leave the discharge gap after the current pulse, and up to the formation of the next breakdown the Penning ionization of nitrogen is by far the dominant source of electrons.

3.2. Optical emission spectroscopy

3.2.1. Overview spectra. Overview spectra of the light emitted by the SPM discharge in pure neon and helium are shown in figures 6(*a*) and (*b*), respectively. In both cases

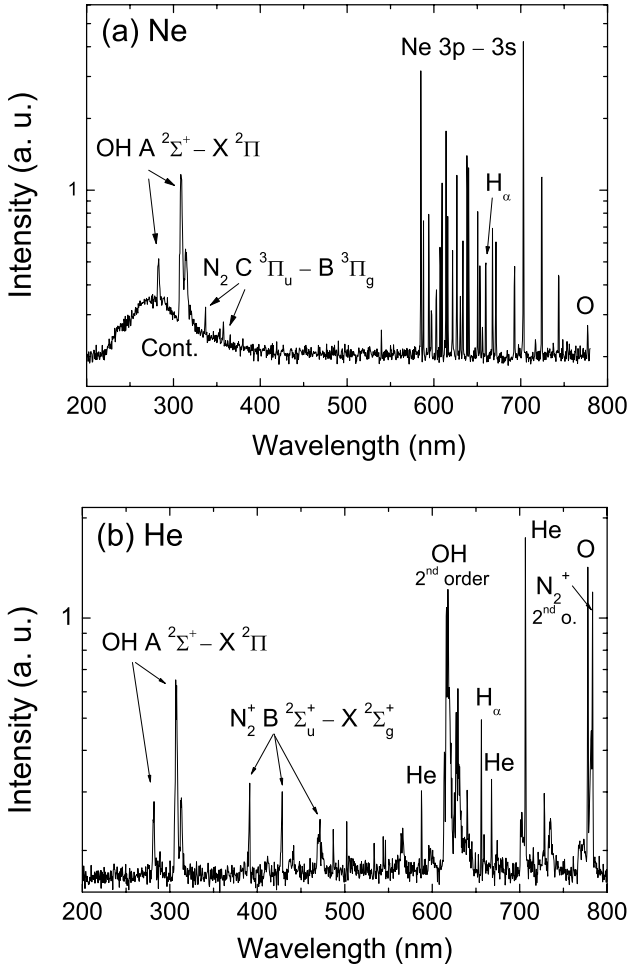

Figure 6. The typical overview spectra of diffuse DBDs in SPM (*a*) in neon and (*b*) in helium.

the spectra consisted of atomic lines of the working gas (neon, helium) as well as of atomic lines and molecular bands originating from inevitable gas impurities (nitrogen, hydrogen, oxygen and hydroxyl-radical). The impurities can be present in the working gas as well as be desorbed from the chamber walls and the dielectrics. In the case of neon, the atomic spectral lines of the transitions between the states $2p^5\,3p \rightarrow 2p^5\,3s$ of neon ($2p_i \rightarrow 1s_j$ in Paschen notation) were the most intensive. Although our diagnostic tool was optimized for the measurements in the near UV-region, no lines in the range 335–370 nm, originating from $2p^5\,4p$ states, were registered. Since some cross sections for electron impact excitation from the ground state to the levels $2p^5\,3p$ ($E_{\rm exc} \approx 18.7$ eV) and $2p^5\,4p$ ($E_{\rm exc} \approx 20.3$ eV) are similar above the threshold (Meneses *et al* 2002), a strong decay of the electron energy distribution function to higher energies is indicated by our experimental findings. Apart from neon lines, hydrogen atomic lines H_α and H_β at 656.3 nm and 486.1 nm, respectively, oxygen triplet line at 777 nm ($3p\,^5P \rightarrow 3s\,^5S^\circ$), N_2 second positive system ($C\,^3\Pi_u \rightarrow B\,^3\Pi_g$) and OH molecular system ($A\,^2\Sigma^+ \rightarrow X\,^2\Pi$) were observed. When the amount of the impurities was low (i.e. nitrogen bands were weak), a continuum in the wavelength range 220–450 nm was registered. The origin of this continuum is unclear, but its shape is quite similar to bremsstrahlung continuum of electrons impacting on neutral atoms observed by Lissovski and Treshchalov(2003) and Rutscher and Pfau(1976). However, numerical simulations with the corresponding plasma parameters (not presented here) and the time development of the continuum did not validate this explanation (see the discussion in section 3.2.3). According to Bojčenko *et al* (1993), a very similar continuum is produced by radiative transitions out of highly excited Rydberg Ne_2 molecules, or by transition between states correlating with Ne^{+*}+Ne and Ne^++Ne^*. To clarify the origin of this continuum further investigation is needed.

In the case of helium, several helium lines were intensive: at 706.5 nm ($3s\,^3S_1 \rightarrow 2p\,^3P$), 587.6 nm ($3d\,^3D \rightarrow 2p\,^3P$) and 667.8 nm ($3d\,^1D_2 \rightarrow 2p\,^1P_1$). As in neon the lines of oxygen and hydrogen as well as OH bands were present, but the N_2^+ first negative system ($B\,^2\Sigma_u^+ \rightarrow X\,^2\Sigma_g^+$) was the dominant nitrogen system due to the effective Penning ionization of nitrogen molecules by helium metastables. Comparable to the results in neon, when the degree of gas impurity was low, a weak continuum was observed in the range 250–800 nm (not seen in the figure).

3.2.2. Temporally resolved spectra. The intensive lines and bands in the overview spectra were further investigated by means of temporally and spatially resolved optical emission spectroscopy. The temporal intensity development of investigated lines was always measured at 24 positions along the whole discharge gap. These spatio-temporally resolved data are presented in section 3.2.3. In order to obtain the temporal intensity development only, the individual temporal intensity evolutions measured at different positions have been summarized. The intensities were normalized to their maximum values in order to compare the temporal dependences of various spectral lines. The results of this procedure are displayed in figure 7.

The temporally resolved intensity development of the spectral lines can be used to estimate the excitation mechanism of radiative states (in comparison with the temporal development of the discharge current). Whereas the direct excitation by energetic electrons occurs primarily at high electric field and electron concentration during the current pulse, indirect excitation processes involving e.g. metastables (excitation transfer, Penning ionization, recombination etc) will excite species even after the current pulse. In the case of neon (figure 7(*a*)), the temporally resolved intensities of two different lines originating from different upper states are shown. Their development is approximately the same and promptly follows the current first, but their decay is even faster (in comparison with the current). Therefore their upper states must be primarily populated by electron impact. The intensity evolution of the N_2 second positive system shows the best agreement with the current pulse. Initially it quickly reaches the maximum as the neon lines, but it decreases comparatively slowly. However, the slower decrease can be caused by the increase of the intensity of continuum (compare these two curves), which forms the background for the nitrogen system. Therefore the temporal evolution of nitrogen emission can also have a sharp maximum, and it can be excited mainly by electron impact as well. Oxygen and hydrogen and OH emissions are

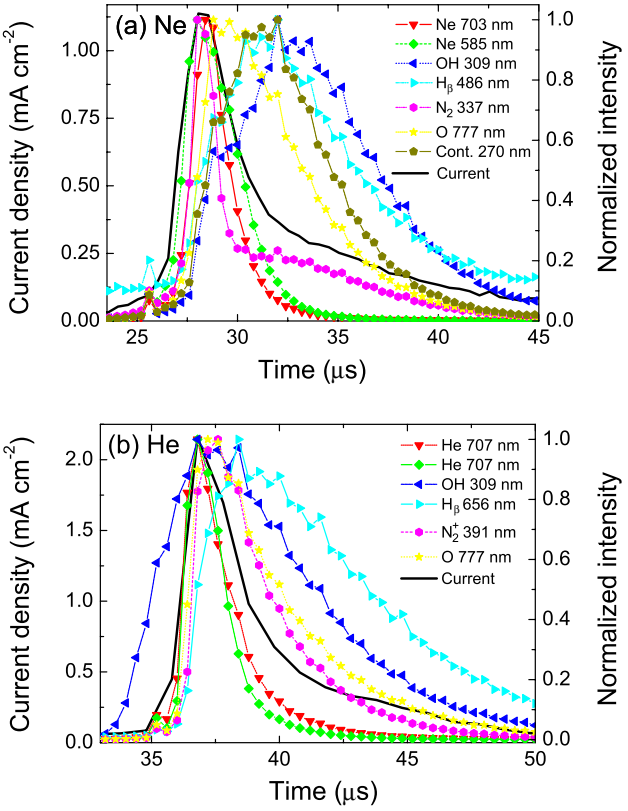

Figure 7. The temporal intensity development of various emissions of (*a*) neon discharge and (*b*) helium discharge in comparison with the discharge current (——).

clearly delayed in respect of the current pulse. This is due to the necessary preceding dissociation and ionization of the impurity species and due to the participation of metastables in these processes. The excitation mechanism of OH, which is the most delayed emission, is further discussed in section 3.2.3. The delay of the continuum intensity maximum probably excludes the possibility of being a bremsstrahlung radiation on neutrals, since electrons with energy of several electronvolts are needed in such a process (which are not expected to be present in the discharge after the current pulse).

In the case of helium (figure 7(*b*)), the same helium line at 707 nm was measured twice, at the beginning as the first measured line and then later after the measurement of other emissions (N_2^+, OH and H), in order to test the discharge stability and the reproducibility of the presented results. As can be seen in the figure, these two temporal dependences differ only slightly, and their maxima are as sharp as those of the neon lines. Consequently, helium is excited by the electron impact. The intensity dependences of impurity emissions denote the role of metastables as in the case of the neon discharge. Quite peculiar is the development of OH, the intensity of which increases faster than the discharge current.

3.2.3. Temporally and spatially resolved spectra. The temporally and spatially resolved intensity distributions of 5 mm SPM diffuse discharge in neon and helium are displayed in figures 8 and 9, respectively. These figures show the normalized intensity of various lines and bands in a logarithmic scale within almost the whole voltage period ($T = 100\,\mu$s) and resolved along the discharge gap. In the case of neon, the intensity distributions of the neon line at 703.2 nm, the N_2 second positive system at 337.1 nm, OH system at 309.0 nm, continuum at 270.0 nm, H_β at 486.1 nm and O triplet line at 777 nm are shown (figure 8). Wavelength 270 nm, at which the continuum was measured, was chosen in order to avoid an overlapping of the intensity of the OH system. In the case of helium, the intensity distributions of the helium line at 706.5 nm, N_2^+ first negative system at 391.4 nm, OH system at 309.0 nm and H_α at 656.3 nm are shown (figure 9).

The common discharge characteristic is that two intensity maxima appear within one voltage period. They can be clearly assigned to the two current pulses in the period, as they occur approximately at the same time (with an eventual small shift depending on the radiating specie). Since the voltage commutes between the current peaks, the positions of the electrodes exchange in the figures. In all figures, which display the whole period, the cathode is at the bottom of the figure first and the anode at the top (for $t < 62\,\mu$s), and vice versa. As the magnitudes of the positive and negative current peaks were nearly the same, the electrode system was symmetrical, and the optical system was carefully adjusted; no substantial difference was registered between both polarities—the intensity maxima appear similarly as mirrored by the plane passing through the gap centre.

The intensity distributions of neon and helium lines appear to be very similar. In both figures a cathode directed wave of increasing luminosity starts in the middle of the discharge gap and propagates to the cathode within 2 μs. Roughly 2.5 μs after its arrival at the cathode a second maximum of emission is registered at the anode, but with lower intensity than at the cathode. This result resembles the structure of a dc glow discharge with an intensive cathode light and a less intensive positive column. A small area of lower intensity, located between the cathode light and the positive column, which can be clearly seen in particular in neon (and in the case of the oxygen line of the neon discharge, too), evokes the Faraday dark space. The intensity is not zero, probably due to reflections. Cathode glow and negative glow cannot be resolved, since these regions are very close to each other at atmospheric pressure (Raizer1991, Massines *et al* 1998). The observed development is in agreement with the Townsend mechanism of the discharge breakdown, which presumes the discharge sustenance by secondary electrons being created by ion bombardment of the cathode and by photoionization. These findings are also in agreement with observations and numerical modelling carried out by Massines *et al* (1998) and Golubovskii *et al* (2003). In particular, the diagram of ionization rate in the breakdown phase in Golubovskii *et al* (2003) (see figure 8 of this reference) is very similar to the measured intensity distribution, although it was calculated for slightly different parameters.

The narrow (i.e. short in time) intensity maxima of both neon and helium line reflect the direct excitation of the atoms by electron collisions. The most important difference between the evolution of the neon and helium lines is the time of intensity onset as the breakdown in helium occurs later at a higher electric field.

The intensity maxima of most of the impurities (OH, O, H) are broader and shifted in time. This is due to the necessary

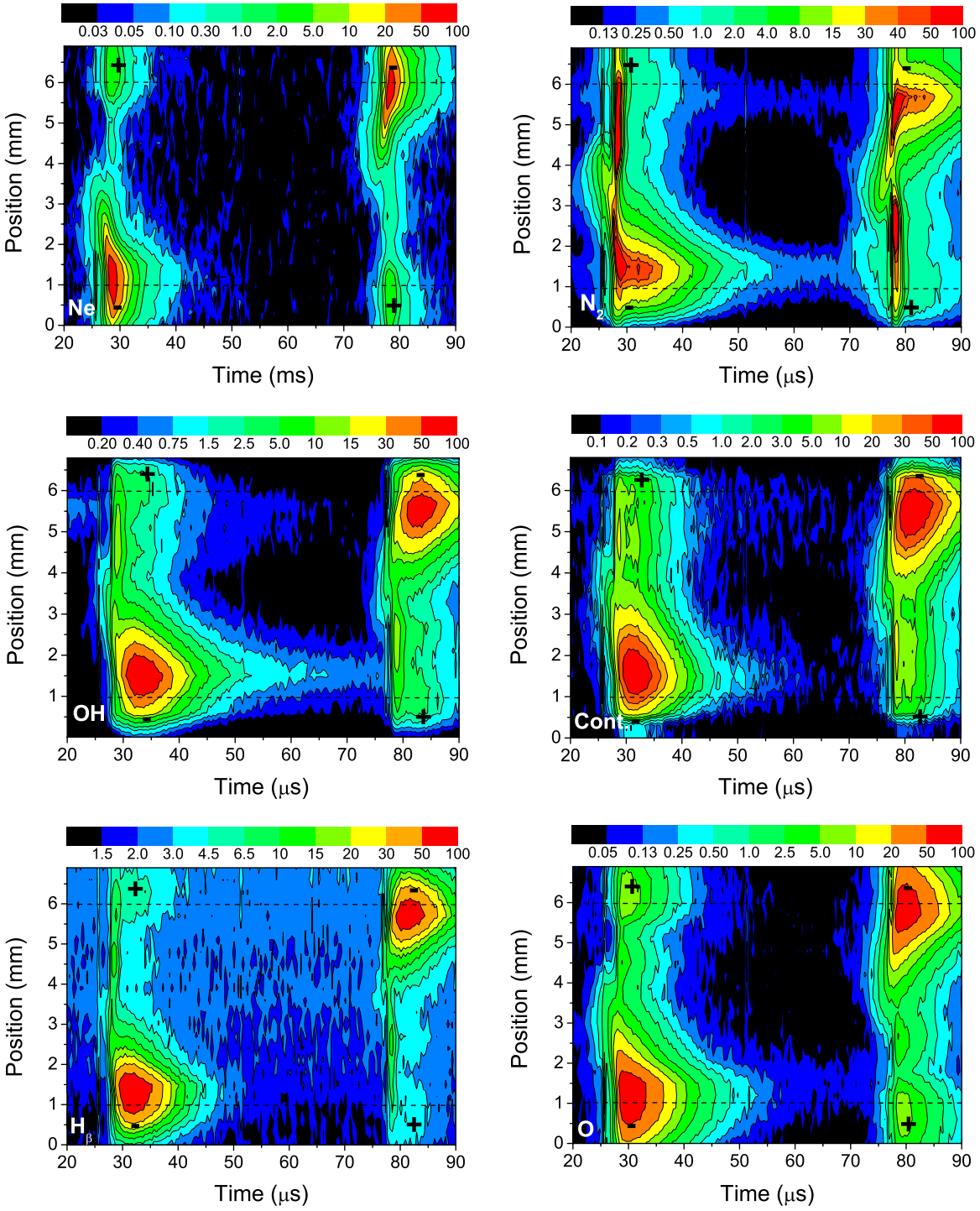

Figure 8. Spatially and temporally resolved intensity distributions of neon SPM diffuse discharge in a 5 mm cell. The relative intensity of the neon line at 703.2 nm, the N_2 second positive system at 337.1 nm, OH system at 309.0 nm, continuum at 270.0 nm, H_β at 486.1 nm and O triplet line at 777 nm are plotted in a logarithmic scale versus the time and the position across the discharge gap. The cathode is located at the bottom first, then at the top. The positions of the electrodes (i.e. of the dielectric layers) are marked out by the dashed lines.

dissociation and ionization of the impurities to form H and OH radicals and due to the participation of metastables in these processes. However, the intensity distribution of the light emitted by impurities basically follows the structure of the neon or helium line with intensive cathode directed light and less intensive anode light. The only exception is the emission of the N_2 second positive system of the neon discharge. Here the maximum value of the anode light intensity is comparable to that at the cathode and further persists (together with the emission at the cathode) throughout the whole period. The strong intensity maximum near the anode resembles the intensity development of the space charge free Townsend discharge in pure nitrogen (Brandenburg *et al* 2002). This similarity is moreover increased by the fact that the displayed

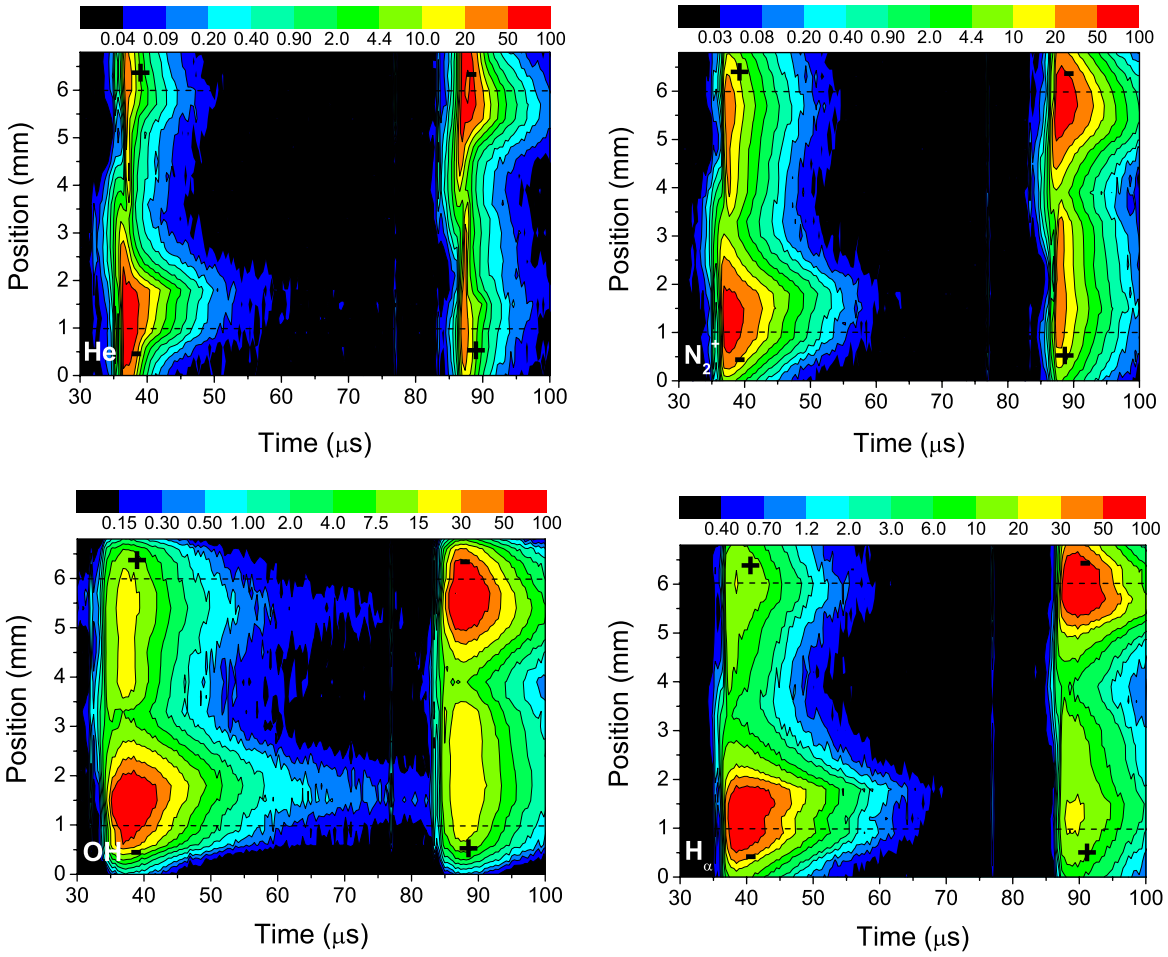

Figure 9. Spatially and temporally resolved intensity distributions of helium SPM diffuse discharge in a 5 mm cell. The relative intensity of helium line at 706.5 nm, N_2^+ first negative system at 391.4 nm, OH system at 309.0 nm and H_α at 656.3 nm are plotted in a logarithmic scale versus the time and the position across the discharge gap. The cathode is located at the bottom first, then at the top. The positions of the electrodes are marked out by the dashed lines.

intensity of N_2 partially belongs to the continuum, being—especially in the area of the cathode maximum—a relatively intensive background.

Besides N_2 emission of the second positive system, OH emission is observed throughout the voltage period in both neon and helium discharges. This is again in close agreement with Massines *et al* (1998), where the whole period of lasting light emission of helium diffuse discharge operating at similar conditions was reported. The radiation of OH in the afterglow (9) is explained in helium (Ricard *et al* 1999) considering the production of radiative states OH(A) by the recombination of H_2O^+ ions—reaction (8), which are created by metastable helium atoms in reactions as in (5) or by metastable helium dimers $He_2(a)$—reaction (7). Helium excimers are produced in three-body collisions of the helium metastable atom with two helium atoms in the ground state—reaction (6).

$$He(2s\,^3S) + H_2O \rightarrow He + H_2O^+(X, A, B) + e^-, \quad (5)$$

$$He(2s\,^3S) + 2He \rightarrow He_2(a) + He, \quad (6)$$

$$He_2(a) + H_2O \rightarrow 2He + H_2O^+(X, A, B) + e^-, \quad (7)$$

$$H_2O^+(A) + e^- \rightarrow OH(A) + H, \quad (8)$$

$$OH(A) \rightarrow OH(X) + h\nu. \quad (9)$$

In neon, similar processes can be expected. Since the production of the metastables is spatially inhomogeneous and has a higher maximum at the cathode and a lower maximum at the anode (see Mangolini *et al* (2004), figure 6 of the reference in particular), two spatially limited light traces of OH emission of different intensities appear between the main intensity maxima. Taking into account the excitation mechanism discussed above, the evolution of the OH emission can be explained by the relative long radiatively lifetime of $H_2O^+(A)$ ions (about 10 μs, see Ricard *et al* (1999)) and the existence of thermalized electrons and $H_2O^+(A)$ ions in front of the anode after the change of polarity. However, these species do not trigger the following discharge pulse. As can be seen clearly in figures 8–10 the development of the cathode directed luminosity wave begins in the middle of the discharge gap and not at the anode.

A very short intensity maximum crossing the gap at the time of 77 μs can be located in some plots in figures 8 and 9. At first this maximum was considered to be a product of the previously mentioned residual current peak. However, since the intensity dependence was always measured during four periods of the voltage signal and the temporal position of this maximum changes in respect of the main maxima,

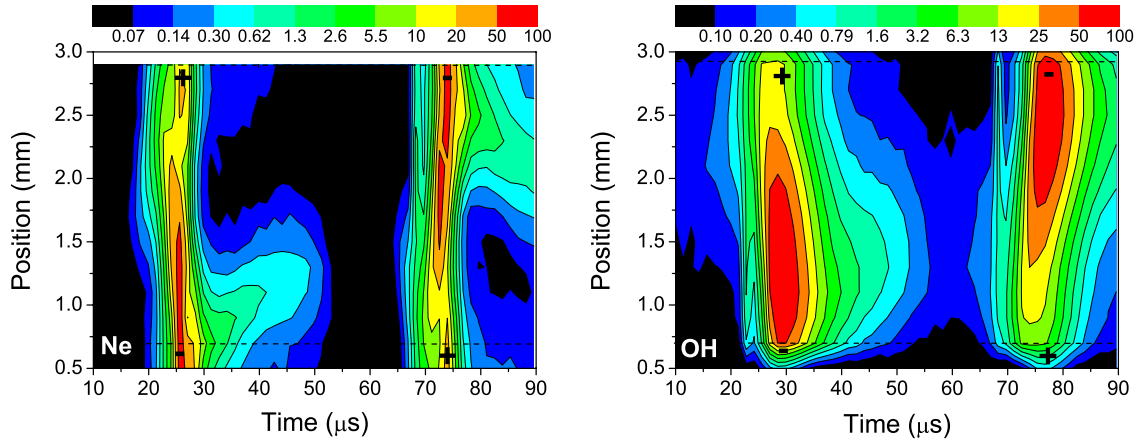

Figure 10. Spatially and temporally resolved intensity distributions of neon SPM diffuse discharge in a 2.2 mm cell. The relative intensity of the neon line at 703.2 nm and the OH system at 309.0 nm are plotted in a logarithmic scale versus the time and the position across the discharge gap. The cathode is located at the bottom first, then at the top. The positions of the electrodes (of the dielectric layers, exactly) are marked out by the dashed lines.

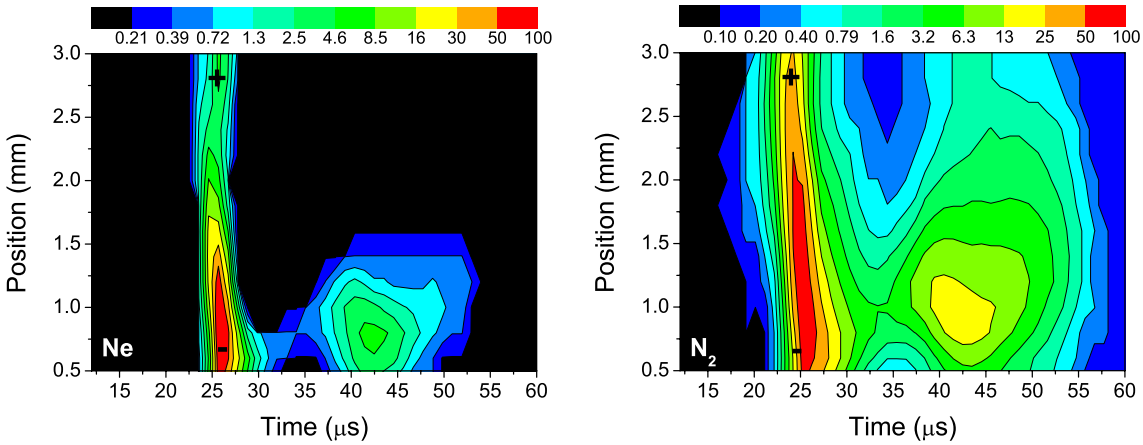

Figure 11. Spatially and temporally resolved intensity distributions of neon DPM diffuse discharge in a 2.2 mm cell. The relative intensity of the neon line at 703.2 nm and the N_2 second positive system at 337.1 nm are plotted in a logarithmic scale versus the time and the position across the discharge gap. The time range covers only the first voltage half period, i.e. only one polarity is shown. The cathode is located at the bottom.

this short maximum could have been produced by a device error.

The diffuse discharge in neon was also studied in the discharge cell with a discharge gap of 2.2 mm. In figure 10 spatially and temporally resolved intensities of the neon line at 703.2 nm and the OH system at 309.0 nm of neon SPM discharge are shown. The temporal resolution was 1.4 μs in this experiment, so the discharge structure is less resolved as in figures 8 and 9. However, the discharge development was investigated to be almost the same as in the 5 mm discharge gap, namely, with a bright cathode light and a less intensive anode region. Solely, the intensity maxima at the cathode were broader. This is probably due to a slight transition from SPM to DPM. A small spatial intensity maximum also appeared near the anode. However, in contrast to the discharge structure in the 5 mm discharge gap (figure 8) no positive column was formed. Thus, it is suggested again that the free electrons cannot be stored in the positive column, and this electron/ion-trapping mechanism fails to explain the mechanism of generating a diffuse DBD in neon. The emission of OH persisted throughout the entire period as in the 5 mm discharge cell. Its spatial distribution clearly determined the discharge gap area.

It is interesting that in argon a filamentary DBD is investigated at the conditions being considered. A comparison of the energetic levels of the metastable states of helium, neon and argon and the ionization energy of N_2 supports the important role of indirect ionization processes, e.g. Penning ionization of N_2 molecules (equations (3) and (4)) as pointed out by different authors (e.g. Massines *et al* (1998), Golubovskii *et al* (2003)). Helium and neon metastables (with excitation energy of 20 eV and 16.6 eV, respectively) and excimers have enough energy to ionize nitrogen directly (ionization energy, 15.6 eV), but argon metastables do not (11.6 eV). Thus, in neon and helium the indirect ionization may produce a preionization level, which is sufficient for an overlapping and a coalescence of electron avalanches, as first proposed by Palmer(1974) and by Levatter and Lin(1980). This avalanche coalescence leads to a suppression of the microdischarges and to the generation of the diffuse regime of the DBD.

The intensity distributions of the neon line at 703.2 nm and the N_2 second positive system at 337.1 nm of neon 2.2 mm DPM diffuse discharge are shown in figure 11. In contrast to the previous figures, figure 11 shows, only, the development within one voltage half period. In this half period the cathode was located at the bottom of the figure. Two intensity maxima with maximum value at the cathode were investigated. These maxima correspond to the two subsequent current peaks of the DPM (compare with figure 4). Both discharge events have a similar structure as the discharge in the SPM, namely, the formation of the cathode light. Between the first and the second discharge the intensity did not decrease to zero. The maximum value of intensity in the second pulse was due to the lower current being generally lower than in the first pulse. However, the ratios of the maximum intensity in the second pulse to the maximum intensity in the first pulse were found to differ for the various emissions. The highest ratio was found for the N_2 second positive system, followed by oxygen emission (not shown here) and neon radiation. These experimental results are in agreement with the spectrally integrated but temporally and radially resolved discharge recordings of Mangolini *et al* (2002) as well as with the results presented by Radu *et al* (2003). The recordings of the former authors revealed that the subsequent discharge pulses are generated due to inhomogeneous charge accumulation on the dielectric in different regions of the discharge volume. This radial discharge development cannot be verified, since our investigation was only one-dimensional.

4. Conclusion

Diffuse DBDs in neon and helium were investigated by electrical measurements and temporally and spatially resolved optical emission spectroscopy. The experiments revealed similar behaviour of the diffuse discharges in neon and helium. Although the breakdown takes place at different electric field strengths, the discharge current development is almost the same for both gases, differing only in the magnitudes of the current density. Furthermore, the measured spatio-temporally resolved intensity evolutions revealed the same structure of the discharges in neon and helium. In agreement with other authors the structure of a transient subnormal glow discharge consisting of a cathode fall, a positive column and an anode fall was observed (glow-like discharge) in helium as well as in neon. The spatial distributions in the 2.2 mm gap were quite similar, but no positive column was observed. Since in argon the filamentary discharge is observed at the same conditions, indirect ionization processes between long-lived excited states (metastables and excimers) and N_2 molecules (Penning ionization) are assumed to be important for the existence of the diffuse DBD in helium and neon. These processes can provide the gas preionization, which is needed for the overlapping of the avalanches leading to the suppression of the microdischarge development and to the generation of the diffuse discharge.

Different discharge regimes were investigated in both gases. The standard regime was named SPM, since a single discharge pulse per voltage half period was registered. However, two or more current peaks per half period (DPM, etc) can be obtained by the voltage increase, or by nitrogen admixture in the range of 100–800 ppm. Our results confirm the findings of various authors, which are, namely, the generation of subsequent discharges due to a re-rise of the gap voltage in combination with a decrease of the breakdown voltage due to the presence of long-lived excited species remaining from the first discharge event.

Acknowledgments

This work was supported by research project MSM0021622411 and grants No 202/05/0777, 202/02/D097 of Czech Science Foundation, Deutsche Forschungsgemeinschaft, SFB 198, 'Kinetics of partially ionized plasmas'. The work of Z Navrátil in Greifswald was supported by Deutscher Akademischer Austausch Dienst (DAAD).

References

Bartnikas R 1968 *Br. J. Appl. Phys.* **1** 659–61
Bojčenko A M, Tarasenko V F, Fomin E A and Jakovlenko S I 1993 *Kvant. Elektron.* **20** 7–30
Brandenburg R, Kozlov K V, Gherardi N, Michel P, Khampan C, Wagner H-E and Massines F 2002 *Hakone VIII Contributed Papers (Tartu, Pühajärve, Estonia)* p 28
Eliasson B and Kogelschatz U 1991 *IEEE Trans. Plasma Sci.* **19** 309–23
Gibalov V I and Pietsch G J 2000 *J. Phys. D: Appl. Phys.* **33** 2618–36
Gherardi N, Gouda G, Gat E, Ricard A and Massines F 2000 *Plasma Sources Sci. Technol.* **9** 340–6
Golubovskii Y B, Maiorov V A, Behnke J and Behnke J F 2003 *J. Phys. D: Appl. Phys.* **36** 39–49
Kim Y and Rudd M E 1994 *Phys. Rev.* A **50** 3954–67
Kozlov K V, Wagner H-E, Brandenburg R and Michel P 2001 *J. Phys. D: Appl. Phys.* **34** 3164–76
Kozlov K V, Brandenburg R, Morozov A M, Wagner H-E and Michel P 2005 *J. Phys. D: Appl. Phys.* **38** 518–29
Levatter J and Lin S-C 1980 *J. Appl. Phys.* **51** 210–22
Lissovski A and Treshchalov A 2003 *ICPIG: Proc. 26th Int. Conf. on Phenomena of Ionized Gases (Greifswald)* p 247
Mangolini L, Orlov K, Kortshagen U, Heberlein J and Kogelschatz U 2002 *Appl. Phys. Lett.* **80** 1722–4
Mangolini L, Anderson C, Heberlein J and Kortshagen U 2004 *J. Phys. D: Appl. Phys.* **37** 1021–30
Massines F, Rabehi A, Décomps P, Ben Gadri R, Séguer P and Mayoux C 1998 *J. Appl. Phys.* **83** 2950–7
Meneses G D, Clark R E H, Abdallah J Jr and Csanak G 2002 *J. Phys. B: At. Mol. Opt. Phys.* **35** 3119–36
Müller S and Zahn R-J 1996 *Contrib. Plasma Phys.* **36** 697–709
Palmer A J 1974 *Appl. Phys. Lett.* **25** 138–40
Radu I, Bartnikas R and Wertheimer M R 2003 *IEEE Trans. Plasma Sci.* **31** 1363–78
Radu I, Bartnikas R and Wertheimer M R 2004 *J. Phys. D: Appl. Phys.* **37** 449–62
Raizer Y P 1991 *Gas Discharge Physics* (Berlin: Springer) p 169
Ricard A, Décomps P and Massines F 1999 *Surf. Coat. Technol.* **112** 1–4
Rutscher A and Pfau S 1976 *Physica* C **81** 395–402
Trunec D, Brablec A and Buchta J 2001 *J. Phys. D: Appl. Phys.* **34** 1697–9
Wetzel R C, Baiocchi F A, Hayes T R and Freund R S 1987 *Phys. Rev.* A **35** 559–77

IOP PUBLISHING JOURNAL OF PHYSICS D: APPLIED PHYSICS

J. Phys. D: Appl. Phys. **42** (2009) 085208 (10pp) doi:10.1088/0022-3727/42/8/085208

The transition between different modes of barrier discharges at atmospheric pressure

R Brandenburg[1], Z Navrátil[2], J Jánský[2], P St'ahel[2], D Trunec[2] and H-E Wagner[3]

[1] INP Greifswald e.V. (Leibniz-Institute for Plasma Science and Technology), F.-Hausdorff-Str. 2, 17489 Greifwald, Germany

[2] Department of Physical Electronics, Faculty of Science, Masaryk University, Kotlářská 2, 611 37 Brno, Czech Republic

[3] Institute of Physics, University of Greifswald, F.-Hausdorff-Str. 6, 17489 Greifswald, Germany

E-mail: brandenburg@inp-greifswald.de

Received 2 December 2008, in final form 25 February 2009
Published 2 April 2009
Online at stacks.iop.org/JPhysD/42/085208

Abstract

Barrier discharges (BDs) can be operated in so-called diffuse modes. In contrast to the usual filamentary regime, which is characterized by a large number of individual microdischarges, the plasma of a diffuse BD covers the entire electrode area uniformly. Depending on the operation conditions (gas composition, amplitude and frequency of applied voltage), different diffuse modes can be investigated, namely, the atmospheric pressure Townsend discharge (APTD) and the atmospheric pressure glow discharge (APGD). The subject of the paper is the study of the transition between APTD and APGD as well as between diffuse and filamentary BD modes. Therefore, BDs were studied in the gas mixtures N_2/H_2, N_2/He, N_2/Ne and N_2/Ar. It is shown that APGD in the noble gases helium and neon is formed due to high ionization rate at a comparatively low electric field, assisted by indirect ionization mechanisms involving metastable states of inert gases and nitrogen impurities, while the existence of APTD is coupled to the existence of metastable states of molecular nitrogen. Furthermore, a similar memory effect of residual surface charges on the dielectric barriers as described for filamentary BDs was observed in diffuse BDs.

(Some figures in this article are in colour only in the electronic version)

1. Introduction

Barrier discharges (BDs) at atmospheric pressure usually operate in the filamentary mode, i.e. the plasma consists of a large number of individual microdischarges (observable as filaments) with short durations and sub-millimetre size [1–3]. But under selected conditions (concerning gas mixture, discharge configuration, frequency of the applied voltage, properties of external electrical circuit and power supply) uniform plasmas, the so-called diffuse BDs can be generated [4–10]. Diffuse BDs are of great interest for various applications, in particular surface treatment and thin film coating since they ensure a homogeneous treatment of the sample with a lower local energy density than filamentary BDs.

As shown in figure 1, different regimes of diffuse BDs do exist. In pure nitrogen a Townsend discharge is investigated (so-called atmospheric pressure townsend discharge, APTD) [11, 12], while in helium and neon the discharge can be described as a subnormal glow-discharge (so-called atmospheric pressure glow discharge, APGD) [13–15]. The plots in figure 1 compare the active current I_{act} (i.e. the measured current without the sinusoidal capacitive current of the BD electrode arrangement) and the applied voltage U_{appl} oscillograms with the spatio-temporally resolved evolution of the most intensive emission of the plasma (i.e. the molecular band of the second positive system of N_2 at 337 nm for APTD; He I line at 707 nm ($3s^3S_1$–$2p^3P$) for APGD).

In the APTD the electron density increases towards the anode, while the local electric field is not significantly distorted by space charges. Thus, the light emission intensity grows towards the anode. In contrast, in the APGD the cathode-directed light wave can be regarded as the development of

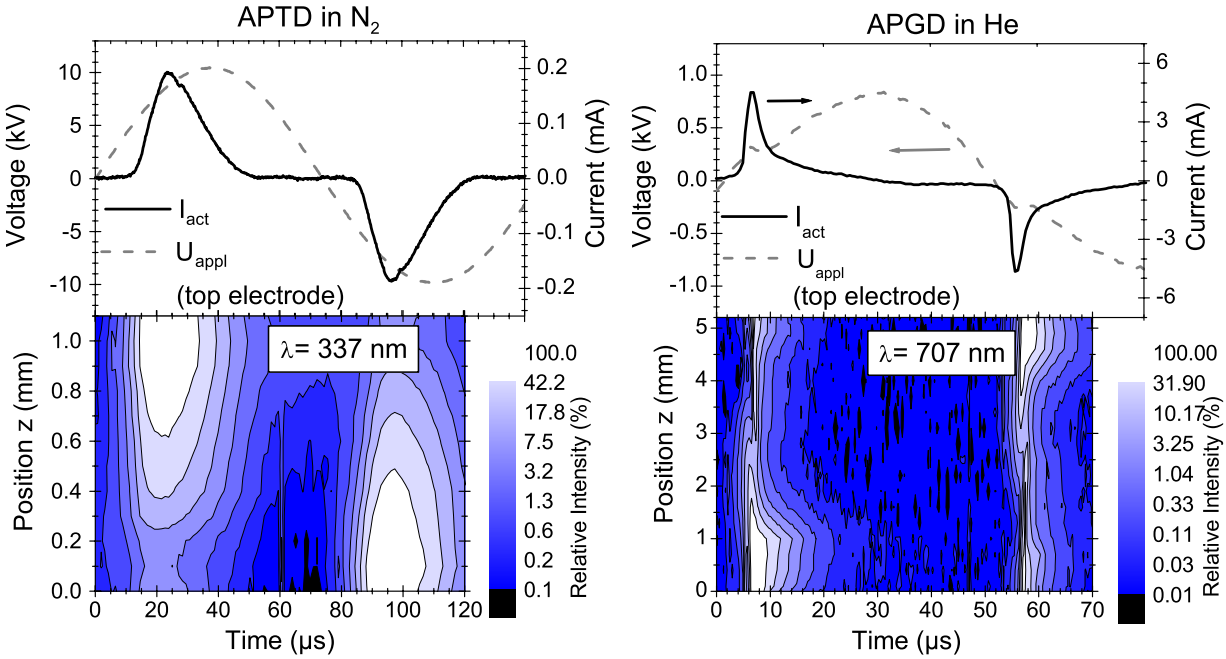

Figure 1. Modes of diffuse barrier discharges: APTD (gas: nitrogen, discharge gap 1.1 mm [16]) and APGD (helium, discharge gap 5 mm [15]). Top figures show oscillograms of active discharge current I_{act} and applied voltage U_{appl}. Voltage is applied to the top electrode in the bottom pictures showing the spatio-temporally resolved evolution of the most intensive emission band or line (see text).

the corresponding negative glow within a period of several microseconds. The formation of the cathode fall is followed by a zone with reduced emission intensity (Faraday dark space), a positive column as well as an anode glow and thus the discharge contains all features of a subnormal glow discharge (the positive column is not observed in shorter discharge gaps).

The generation of a diffuse BD can be understood as a uniform Townsend breakdown at atmospheric pressure. However, at atmospheric pressure a streamer breakdown is more probable due to the high collision frequency of electrons leading to rapid space charge build-up. And furthermore, the radial diffusion length of electrons is much smaller than the discharge gap [8, 17]. But the generation of a uniform breakdown at atmospheric pressure can be achieved if (i) the electron avalanches grow with small density increase (low ionization rate), (ii) the electron density at the beginning of each half cycle is high enough or (iii) the emission of secondary electrons at the cathode is sufficient [18]. Interactions between the plasma and the power supply have been found to influence the discharge uniformity. Instabilities during the APTD formation can be caused when the load on the power supply changes from the total capacitance (gas gap and dielectric barriers in series) to the capacity of the barriers alone [9, 20]. A uniform BD can be generated and stabilized by an electronic feedback, too [10, 22]. But to a great extent, the breakdown and the plasma properties are determined by the elementary process in the gas bulk and at the surfaces [4, 7, 8, 17, 19]. Within the last years an increasing number of applications of diffuse BDs was demonstrated [24–28]. The stability of diffuse BDs was found to be very sensitive to gas impurities or admixtures, e.g. to precursor gases. Therefore, a profound knowledge on the discharge processes and the effect of gas admixtures is needed in order to use diffuse BDs industrially. This contribution contains collected experimental material investigating the transition of diffuse BD, either to the filamentary regime or between different diffuse modes, with the aim (i) to carry out the conditions for the generation of diffuse BDs and (ii) to discuss the discharge formation processes of diffuse BDs on the background of the influence of different operation parameters. The used experimental set-ups will be described briefly in section 2. Section 3 will present and discuss the experimental results concerning general findings on discharge behaviour (ignition and sustainment of discharges). Results describing the transition between APGD and filamentary BDs are presented in section 4. Section 5 deals with the transition between APTD and filamentary BDs in N_2–H_2 gas mixtures, including results of a numerical model. Finally, the investigation of the transition between the two different diffuse modes APTD and APGD in nitrogen–noble gas mixtures is presented in section 6.

2. Experimental set-up

Two experimental set-ups were used for the studies. The first one (at Greifswald University/Germany) was originally built for diagnostics on microdischarges [29]. It is schematically shown in figure 2.

The discharges were generated in a stainless-steel vacuum chamber. Several electrode arrangements (the so-called discharge cells), presented in table 1 could be placed in the vacuum chamber. In all cases a 'two-sided' symmetric volume BD was driven, i.e. both electrodes were covered by a barrier with the same thickness d_{diel} and dielectric constant ε_r. The discharge gap d_g of the cells 1–3 was fixed, while cell 4 with semi-spherical electrodes (originally designed for the

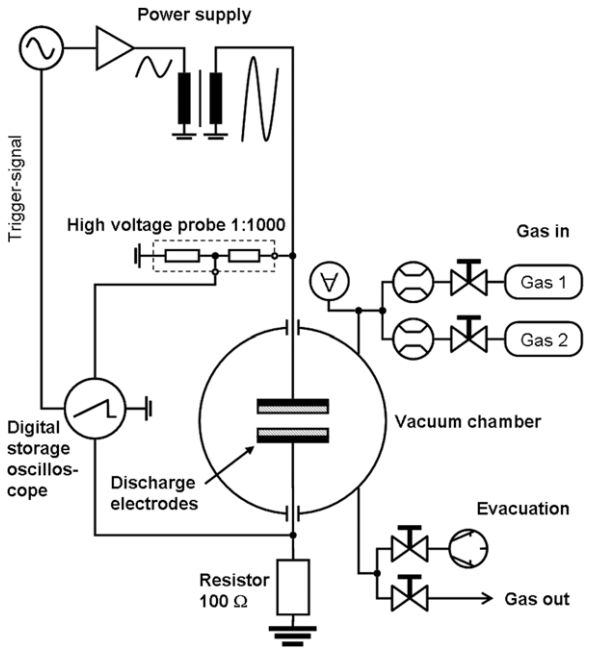

Figure 2. Experimental set-up for the generation of BDs and electrical diagnostics.

Table 1. Discharge cells used in the investigations.

No	Discharge cell geometry	Dielectric material	Dielectric constant ε_r	Dielectric thickness d_{diel}	Discharge gap d_g
1	Plane parallel (area 4 cm^2)	Glass (Duran)	4.6	2.1 mm	1.1 mm
2	Plane parallel (area 4 cm^2)	Ceramics (Al_2O_3)	9.4	0.7 mm	5.0 mm
3	Plane parallel (area 4 cm^2)	Ceramics (Al_2O_3)	9.4	0.7 mm	2.2 mm
4	Semi-spherical (radius 7.5 mm)	Glass (Duran)	4.6	1.5 mm	Variable
5	Plane parallel (area 50 cm^2)	Glass (Simax)	4.6	2 mm	1.0 mm

stabilization of microdischarges; see, e.g. [12, 29]) was used for since it enables the variation of the discharge gap d_g.

The vacuum chamber was evacuated down to 10 Pa by a rotary pump and then filled with working gas. By means of a gas flow controlling system different gases of defined purity (99.999 vol%) could be mixed systematically. After filling the chamber above atmospheric pressure, the gas outlet was opened to the atmosphere and the discharge was sustained in flowing regime (total gas flow rate was usually 500 sccm), in order to avoid the accumulation of plasma-chemical products, which may affect the discharge behaviour.

The discharges were driven by sinusoidal voltage of several kilohertz frequency. Therefore, the signal from a function generator was amplified and transformed to high voltage by a coil. A maximum signal amplitude of about 28 kV_{pp} (peak-to-peak voltage) could be reached if the discharge was driven at the resonance frequency (usually $f = 6.9$ kHz) of the system consisting of the power supply and the discharge cell. For the electrical discharge diagnostics the applied voltage U_{appl} and the discharge current I_{tot} were recorded with a digital storage oscilloscope (400 MHz bandwidth, 2 GSamples s^{-1}). The applied voltage U_{appl} was measured via a 1000 : 1 high voltage divider. The current I_{tot} was recorded as a voltage on a 100 Ω resistor in series to the discharge cell.

The set-up described above enables the investigation of gas discharges under very defined conditions, but it is not suitable to study the application of diffuse BD for surface treatment. Some of the results presented in this contribution were observed with a reactor developed for this purpose (located at the Brno University/Czech Republic) [25]. It consists of an acrylic glass chamber with two circular and planar metal electrodes (referred to as discharge cell no 5 in table 1; bottom electrode 150 mm diameter; top electrode 80 mm diameter). Thus, the active area is about 12 times larger than in the discharge cells arrangements 1–3. The sample can be mounted on the bottom electrode, which was movable in one direction in the horizontal plane by a stepping motor. The space between the electrodes was set to 1 mm. In the same manner as described above, the applied voltage and the current were measured. To reduce impurities the same procedure as described above was used (evacuation and flushing of the discharge chamber). The working gases (nitrogen, hydrogen) were supplied with a total gas flow rate of up to 6 slm. The discharge was driven at a frequency of 10 kHz.

3. Discharge operation

3.1. Diffuse discharges in planar and semi-spherical discharge geometries

Diffuse BDs were observed in the gases nitrogen (APTD), helium and neon (both APGD). In the plane-parallel discharge arrangement similar current and voltage oscillograms as observed by a number of authors were investigated. As shown in figure 1, the discharge mode characterization can be done by means of the current–voltage oscillogramms. Despite several efforts, in pure argon it was not possible to generate a diffuse BD. In argon a filamentary discharge with microdischarges with a duration in the microsecond-range is investigated in all discharge cells. The semi-spherical electrode arrangement of discharge cell no 4 did not prevent the generation of diffuse BDs. In this case the BDs visually looked like two round luminous uniform spots on the tips of both dielectric electrodes. If the discharge was sustained with a low feeding voltage amplitude only the central part of the glass electrodes was covered by plasma. A moderate rise of the feeding voltage amplitude caused a visible broadening of the plasma spots on the electrodes. In this situation the discharge current pulse increased in amplitude and duration. Due to the non-uniform discharge gap the current pulse shape was slightly deformed.

3.2. Ignition-, burning- and re-ignition voltage

It is well known from filamentary BDs that a higher (over-)voltage (so-called ignition voltage U_{ign}) is needed for the first discharge ignition than for the sustainment of the once ignited discharge [2, 30, 31]. An electric field with a polarity inverse to the applied field is generated due to residual charges

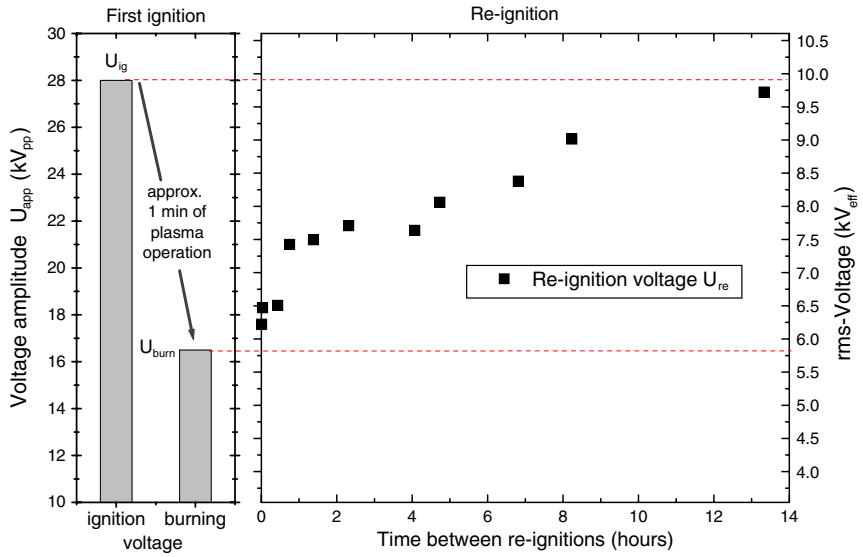

Figure 3. The difference of ignition U_{ign} and burning voltage U_{bur} in an APTD in nitrogen (left). Development of the re-ignition voltage amplitude U_{re} as a function of the time between re-ignitions after one minute of discharge operation (right).

on the barriers leading to the extinction of the plasma. After the reversal of the feeding voltage the surface charge field enhances the applied field and thus a lower feeding voltage amplitude is needed to sustain the discharge. The lower threshold value is called the burning voltage U_{bur}. As shown here, the same effect can be observed for diffuse BDs. The results in figure 3 were obtained in pure nitrogen with the discharge cell no 4 (see table 1, $d_{\mathrm{g}} = 1.2\,\mathrm{mm}$, $f = 6.7\,\mathrm{kHz}$).

In the left diagram of figure 3 the difference between U_{ign} and U_{bur} is demonstrated. To ignite the discharge for the very first time (after more than one day without plasma operation) an overvoltage of about $28\,\mathrm{kV_{pp}}$ is necessary. This value varies strongly (at least 20%), since the first ignition is a statistical phenomenon. As a rule of thumb, the lower the overvoltage, the longer is the time lag for ignition. Once ignited and after 1 min of plasma operation the feeding voltage amplitude could be decreased to about $16.5\,\mathrm{kV_{pp}}$ without causing the discharge extinction. The development of the so-called re-ignition voltage amplitude is shown in the right diagram of figure 3. To measure the re-ignition voltage U_{re} the discharge was switched off after 1 min of operation and after waiting a certain time (up to 14 h) the feeding voltage amplitude was increased slowly, so that the corresponding value of U_{re} could be registered. As shown in the diagram, after some minutes of break the discharge re-ignites at a voltage amplitude only slightly higher than U_{bur}. This value increases slowly with time between re-ignitions. It takes about 14 h for the residual surface charges on the barriers to recombine.

4. The transition between APGD and filamentary BD by gas impurities

4.1. Experimental results, transition voltage

In the studies described here the transition from diffuse to filamentary BD is caused (i) by the increase in the applied voltage amplitude, (ii) the change in the gas mixture and

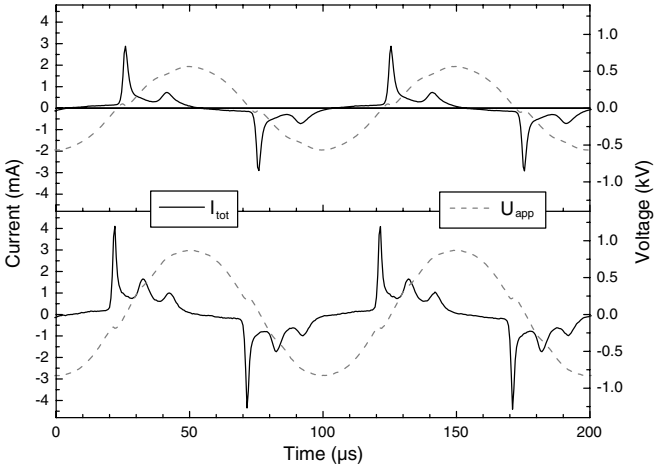

Figure 4. Voltage and current ($I_{\mathrm{tot}} \simeq I_{\mathrm{act}}$) oscillograms of transient APGDs in neon with 400 ppm of nitrogen, showing two (top) and three (bottom) discharge current pulses per half-period. Measured with discharge cell 2 ($d_{\mathrm{g}} = 5\,\mathrm{mm}$, $U = 1.4\,\mathrm{kV_{pp}}$, $f = 10\,\mathrm{kHz}$).

(iii) a combination of (i) and (ii). The lowest voltage, at which the diffuse discharge gets unstable or is superimposed by microdischarges is called the transition voltage U_{tra}.

For the APGD in helium and neon the transition starts with the generation of more than one pulse per half-period $T/2$ as shown in figure 4. If the inert gas is slightly impure (300–800 ppm of N_2/air or 0.05–0.25 vol% of Ar) up to four current pulses per $T/2$ can be observed by increasing the applied voltage amplitude. This mode is also referred to as a 'pseudoglow' discharge [32] and has already been observed by several teams [14, 15, 21, 33–35].

4.2. Discussion

In helium and neon the ionization rate is high at a low reduced electric field strength E/N compared with nitrogen, air or other molecular gases. Furthermore, a plasma in helium or

neon is sustained at comparable low E/N [36] and the first derivative of the first ionization coefficient α over E/N is relatively small, i.e. the ionization rate is not rapidly changing with the local electric field. Thus, a reasonable ionization rate can be achieved at comparatively low electric field strength and ion multiplication in the gas bulk is not rapidly growing [4, 15, 17, 21, 23]. Under these conditions the electrons have enough time to diffuse radially [17]. The avalanches can coalesce with each other and there are no large local electric field gradients build-up by space charges.

Metastables created during one discharge will be active during the next discharge cycle if the driving voltage frequency is large enough to fit with the inverse of the effective lifetime τ_{eff} of the metastable species (i.e. 100 kHz range). In this case indirect ionization processes such as Penning ionization with nitrogen molecules from ever-present residual air, stepwise ionization or chemoionization are generating a low current and continuous diffuse mode as observed in BDs in Ne and Ne/N_2 gas mixtures [6]. For the conditions being considered here (maximum driving frequency of 10 kHz) indirect ionization processes including metastable states and excimers are more likely to support the suppression of rapid growing avalanches and space charges during the breakdown as described above [7, 13, 19, 33, 34, 37].

At very small admixtures of nitrogen or argon (up to some hundreds ppm) into helium or neon the indirect ionization processes may support the APGD state due to enhanced indirect ionization. Thus during the first discharge pulse a sufficient density of metastables is generated, inducing the subsequent discharge event as observed in the 'pseudoglow' regime [33, 35]. Spectroscopic measurements presented in a previous publication [15] suggest that metastable species from the previous discharge pulse decrease the voltage level for the subsequent discharge event. However, an air admixture higher than 800 ppm leads to an increase in the breakdown voltage and to the decrease in the first ionization coefficient α of the gas mixture conversely, which cannot be balanced by indirect ionization processes. Thus, the formation of microdischarges is favoured.

Depending on the overvoltage level, the increase in the applied voltage leads to the 'pseudoglow' regime or to microdischarges [14, 15, 21, 33] due to higher direct ionization rates by the increased electric field strength.

5. The transition between APTD and filamentary BDs in N_2–H_2 gas mixtures

5.1. Experimental results

In an APTD in nitrogen the admixture of oxygen of 800 ppm and higher resulted in the generation of microdischarges [12, 16]. Another example of the transition between APTD and filamentary BD is described here, namely, in nitrogen–hydrogen gas mixtures. When 0.5 vol% of H_2 is admixed into N_2 (APTD), a regular oscillation on the active discharge current is observed, as shown in figure 5. The oscillation gets more distinct at a hydrogen admixture of 1 vol% and a higher applied voltage amplitude. The frequency of the oscillation is about

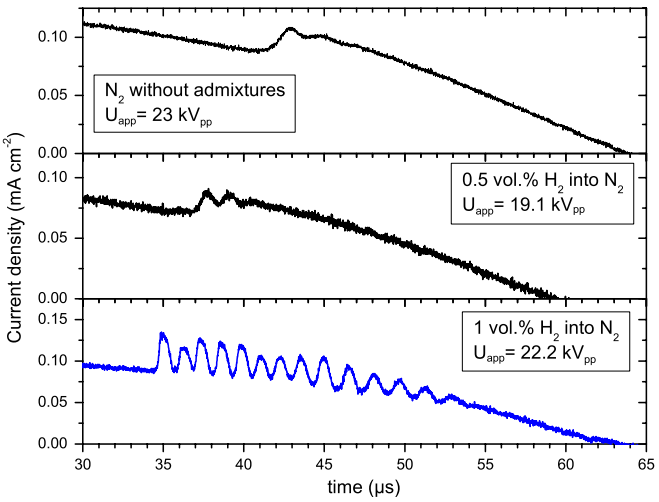

Figure 5. Current profile (enlargement of the measured current showing the active part) of transient APTD in nitrogen without and with admixtures of hydrogen measured at discharge cell no 1 for $f = 5.18$ kHz (time scales are relative).

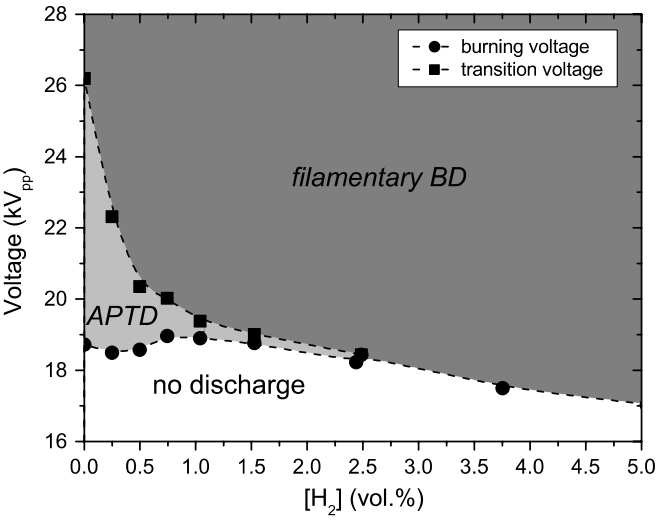

Figure 6. The dependence of burning and transition voltages of APTD in nitrogen on hydrogen admixture.

1 MHz. A similar result was observed in N_2/O_2 gas mixtures, but for lower absolute impurities (about 480 ppm of O_2 into N_2 cause oscillative mode [16]).

Figure 6 shows the measured dependence of burning and transition voltages of BDs in nitrogen with hydrogen admixture. Between the curves area of the discharge modes (APTD, filamentary) can be identified. For hydrogen content more than 2.5 vol% no diffuse discharge is observed. For an (gas mixture dependent) overvoltage of several kilovolts above the burning voltage the discharge still shows the behaviour of an APTD.

5.2. Numerical model

To interpret the experimental results a numerical model based on the one-dimensional continuity equations for electrons and ions and the Poisson equation has been developed. The basic

equations state as follows:

$$\frac{\partial n_i}{\partial t} + \frac{\partial j_i}{\partial x} = S_i, \tag{1}$$

$$\frac{\partial^2 \phi}{\partial x^2} = -\frac{\rho}{\varepsilon_0}, \tag{2}$$

where n_i, j_i, S_i are the density, the particle flux and the source term for the particles of the ith type. ϕ is the potential of electric field, ρ is the charge density and ε_0 is the permittivity of vacuum. The particle flux is calculated from the momentum equation as

$$j_i = -D_i \frac{\partial n_i}{\partial x} + \mu_i E n_i, \tag{3}$$

where D_i, μ_i are the diffusion coefficient and the mobility for the particles of the ith type and E is the electric field strength.

Equations (1) for electrons, N_4^+ ions, $N_2(A\,^3\Sigma_u^+)$, $N_2(a = a'\,^1\Sigma_u^-, a^1\Pi_g, w^1\Delta_u)$ and H atoms were solved by modified TVD method [38]. This splitting method allowed separate solving of each part of equation (3). The boundary condition for the diffusion part is a zero particle volume density at the electrodes. The advection part is solved by means of boundary conditions for electron flux $j_{e,surf}$ and ion flux $j_{i,surf}$ at the dielectric surfaces

$$j_{e,surf} = -n_e \mu_e E + \gamma_m D_m \frac{\partial n_m}{\partial x} + \frac{k_{ph} n_0}{2} \int_{d_{diel}}^{d_{diel}+d_g} k_{ion} n_e \mathrm{d}x, \tag{4}$$

$$j_{i,surf} = n_i \mu_i E. \tag{5}$$

where γ_m, k_{ph}, k_{ion}, d_{el} are secondary electron emission coefficient due to nitrogen $N_2(A\,^3\Sigma_u^+)$ and $N_2(a)$ metastables, photoemission coefficient, ionization coefficient and the distance between the electrodes ($d_{el} = d_g + 2d_{diel}$). n_0 is the neutral gas density. Index m refers to nitrogen metastables.

The electron emission from dielectrics by the diffusion flux of metastables and photoemission are taken as the source of electrons from dielectrics. The secondary emission due to ions is not considered, since for our purposes it has similar influence as photoemission. The photoemission is considered linear to ionization with coefficient k_{ph}, as a product of the emission coefficient γ_{ph} and the emission-ionization ratio, which is approximated by the value 0.1. If the drift velocity is directed away from the electrodes, the drift term is not taken into account. The surface densities of electrons σ_e and ions σ_i at both dielectric barriers are described by the following equations:

$$\frac{\mathrm{d}\sigma_e}{\mathrm{d}t} = j_{e,surf} - \alpha_{rw} \sigma_e \sigma_i, \tag{6}$$

$$\frac{\mathrm{d}\sigma_i}{\mathrm{d}t} = j_{i,surf} - \alpha_{rw} \sigma_e \sigma_i, \tag{7}$$

where $\alpha_{rw} = 1.0 \times 10^{-11}\ \mathrm{m^2\,s^{-1}}$ is the surface recombination coefficient of the dielectric material [19].

The potential on electrodes is set

$$\phi(x = 0) = U \tag{8}$$

and

$$\phi(x = d_{el}) = 0, \tag{9}$$

where U is the applied voltage. Electrode at $x = d_{el}$ is grounded. On both electrodes are dielectrics of thickness d_{diel}. The conditions for electric field on the dielectric-volume boundary are

$$\left(\frac{\partial \phi}{\partial x}\right)^+_{x=d_{diel}} = \varepsilon_r \left(\frac{\partial \phi}{\partial x}\right)^-_{x=d_{diel}} + \frac{\sigma_a}{\varepsilon_0}, \tag{10}$$

$$\left(\frac{\partial \phi}{\partial x}\right)^-_{x=d_{el}-d_{diel}} = \varepsilon_r \left(\frac{\partial \phi}{\partial x}\right)^+_{x=d_{el}-d_{diel}} - \frac{\sigma_c}{\varepsilon_0}, \tag{11}$$

where σ_a, resp. σ_c are the surface charge densities of dielectrics at the anode, resp. the cathode and ε_r is the relative permittivity of dielectrics.

The source terms S_e, S_i, S_A, S_a, S_H for electrons, ions, nitrogen metastables $N_2(A\,^3\Sigma_u^+)$, $N(a)$ and hydrogen atoms are

$$S_e = \alpha_t j_e + k_{Aa} n_A n_a + K_{aa} n_a n_a - k_{rec_N} n_e n_i, \tag{12}$$

$$S_i = \alpha_t j_e + k_{Aa} n_A n_a + K_{aa} n_a n_a - k_{rec_N} n_e n_i, \tag{13}$$

$$S_A = \alpha_{exca} n_e - k_{Aa} n_A n_a - 2k_{radAA} n_A n_A - k_{AH} n_A n_H - k_{AH_2} n_A n_{H_2}, \tag{14}$$

$$S_a = \alpha_{excA} n_e - k_{Aa} n_A n_a - 2k_{aa} n_a n_a - k_{aH_2} n_a n_{H_2} - k_{aX} n_a n_N, \tag{15}$$

$$S_H = 2k_{AH_2} n_A n_{H_2} + 2k_{aH_2} n_a n_{H_2} - k_{rec_H} n_H n_H, \tag{16}$$

where all kinetic coefficients are presented in table 2. The conversion of N_2^+ ion to N_4^+ ion is very efficient at atmospheric pressure (reaction (R11)). Therefore, all ions are considered as N_4^+ ions.

The calculation was done for discharge cell no 1, but with the dielectric constant $\varepsilon_r = 4$. The drift velocity and the diffusion coefficient dependence on electric field strength for electrons were taken from [39] and were supposed to not change with small hydrogen admixture. Still, the exact secondary emission coefficients or photoemission coefficient have not been determined for given experimental settings. Thus, consensus of generally used data in modelling of BDs were adopted in the simulation, namely, $\gamma_{ph} = 0.02$, $\gamma_m = 0.3$. The influence of hydrogen was introduced through the reactions of quenching of the main metastable $N_2(A\,^3\Sigma_u^+)$ by hydrogen molecule and hydrogen atoms. Other hydrogen reactions were not considered in the model due to the exponentially rising complexity of the problem.

5.3. Comparison of experiment and model, discussion

At first the burning voltage was calculated. The calculated burning voltage in pure nitrogen was 20 $\mathrm{kV_{pp}}$, which is in good agreement with 19 $\mathrm{kV_{pp}}$ measured burning voltage. The calculated voltage does not depend on the hydrogen content till 2.5%, which is also in good agreement with experiment, too (see figure 6). For an overvoltage of several kilovolts above the burning voltage the discharge shows the character of an APTD, i.e. the electric field is not disturbed by space charges and the maximum of electron density is at the anode.

Table 2. Reactions used in the numerical model.

	Reaction	Rate coefficient	References
R1	$N_2 + e^- \rightarrow N_2^+ + 2e^-$	$\alpha_t = f(E/N)$	[39]
R2	$N_2 + e^- \rightarrow N_2(A) + 2e^-$	$\alpha_{excA} = f(E/N)$	[39]
R3	$N_2 + e^- \rightarrow N_2(a) + 2e^-$	$\alpha_{exca} = f(E/N)$	[39]
R4	$N_4^+ + e^- \rightarrow N_2 + N_2$	$k_{rec_N} = 6.0 \times 10^{-15}\ m^3\ s^{-1}$	[19]
R5	$N_2(A) + N_2(a) \rightarrow N_4^+ + e^-$	$k_{Aa} = 5.0 \times 10^{-17}\ m^3\ s^{-1}$	[19]
R6	$N_2(a) + N_2(a) \rightarrow N_4^+ + e^-$	$k_{aa} = 2.0 \times 10^{-16}\ m^3\ s^{-1}$	[19]
R7	$N_2(a) + N_2 \rightarrow N_2(B, A, X) + N_2$	$k_{aX} = 2.0 \times 10^{-19}\ m^3\ s^{-1}$	[19]
R8	$N_2(A) + N_2(A) \rightarrow N_2(B, a, C) + N_2(X)$	$k_{radAA} = 4.0 \times 10^{-17}\ m^3\ s^{-1}$	[19]
R9	$N_2(A) + H_2 \rightarrow N_2(X) + 2H$	$k_{aa} = 2.5 \times 10^{-21}\ m^3\ s^{-1}$	[40]
R10	$N_2(A) + H \rightarrow N_2(X) + H$	$k_{aa} = 2.5 \times 10^{-16}\ m^3\ s^{-1}$	[40]
R11	$N_2^+ + N_2 + N_2 \rightarrow N_4^+ + N_2$	$k_{tr} = 5.0 \times 10^{-41}\ m^6\ s^{-1}$	[19]

The calculated discharge currents for different applied voltages and hydrogen contents are shown in figure 7. The current profiles change with the increase in the hydrogen admixture and with the increase in the applied voltages, as observed in the experiment. However, much higher voltages must be set for the simulation of APTD changes. This is the feature of the 1D model and its simplifications. In reality, the electric field near the edges of the dielectric is higher than in the middle of the discharge cell, and therefore the changes can be observed in the experiment at lower applied voltages. For a voltage amplitude of 50 kV_{pp} applied to pure nitrogen gas small damped oscillations (figure 7, top) are observed, while for 2 vol% hydrogen admixture oscillations with a much higher amplitude appear (figure 7, bottom). The oscillative mode is caused by the quenching of nitrogen metastables by hydrogen and the prevailing role of photoemission. Generally one-peak structure is caused by electron emission by metastables or by electron desorption, multi-peak structure is caused by photoemission and secondary electron emission by ions (see, e.g. [19]). Since the latter both depend on ionization in the gap, they cause similar current oscillations.

In the case of pure nitrogen the secondary electron emission flux by metastables is one order of magnitude higher than photoemission flux while for hydrogen admixture the photoemission flux is of the same order (figure 7). Similar current profiles were measured (see figure 5). The calculated discharge current profile (figure 7, top) shows small secondary peak as can be seen in the measured current profile (figure 5). The calculated current profile for discharge with hydrogen admixture and for higher voltages (figure 7, bottom) is similar to measured current profile (figure 5). The results strongly support the general idea that the presence of metastable states is important for APTD generation. Secondary electron emission by metastables is a possible mechanism to produce free electrons at low electric field [7, 16]. As the calculations show, the admixture of a molecular gas such as hydrogen leads to a considerable quenching of the metastable states and thus discharge instability.

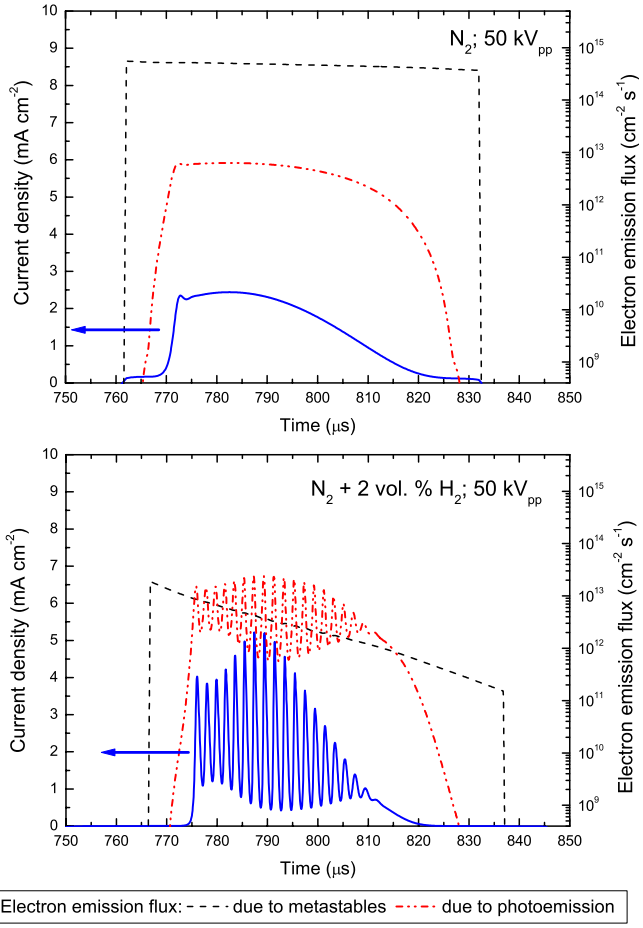

Figure 7. The simulated current profile and electron of BDs in pure nitrogen (top) and in nitrogen with 2 vol% hydrogen admixture (bottom). Applied voltage $U = 50\,kV_{pp}$; electron emission fluxes from cathode dielectric due to metastables and photoemission shown on the right axis.

6. The transition between APTD and APGD

6.1. Experimental results

To investigate the transition between APTD and APGD, BDs in different gas mixtures of nitrogen with noble gases helium, neon and argon, respectively, were studied. The experiments described below were carried out in the discharge cell no 4. A discharge gap of $d_g = 1.4$ mm was chosen since it enables the generation of both diffuse modes, APTD and APGD. The discharge behaviour in the He/N_2 mixtures is shown in figure 8. The burning voltage and the transition voltage are shown as functions of the gas composition. The different BD modes (APGD, APTD or transient/filamentary

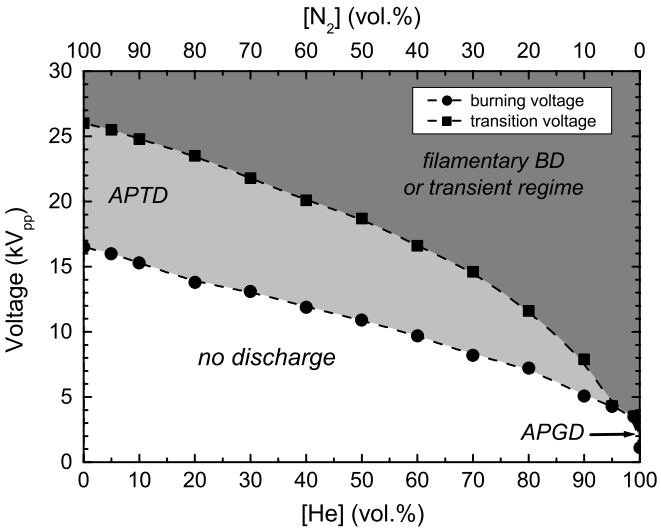

Figure 8. Burning and transition voltage measured in N_2/He gas mixtures and indicated BD modes (semi-spherical glass electrodes, discharge gap 1.4 mm, frequency 6.95 kHz).

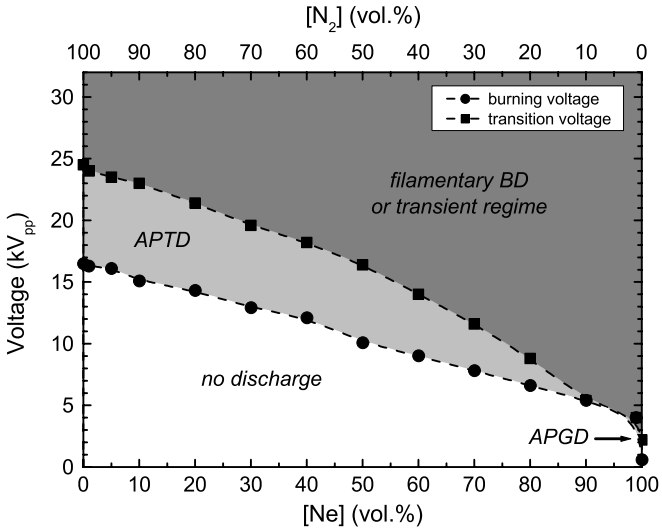

Figure 9. Burning and transition voltage measured in N_2/Ne gas mixtures and indicated BD modes (same set-up as in figure 8).

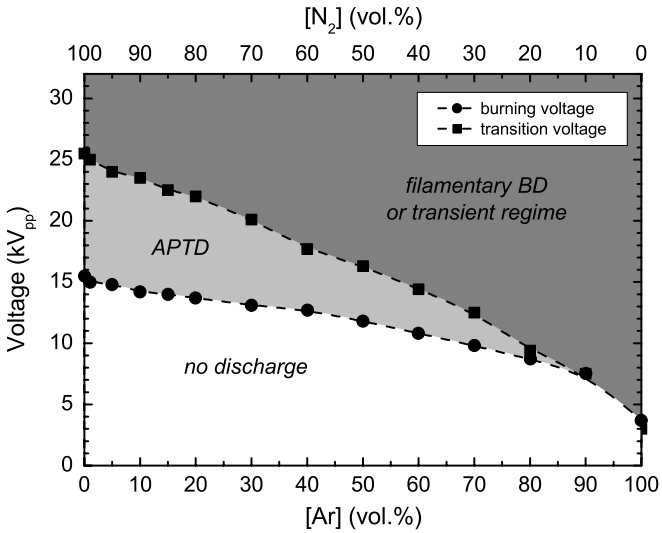

Figure 10. Burning and transition voltage measured in N_2/Ar gas mixtures and indicated BD modes (same set-up as in figure 8).

BD) are distinguished by means of current oscillograms, as demonstrated in the previous sections.

Surprisingly, considerable amounts of the noble gas (more than 90 vol%) can be added to nitrogen without destroying the APTD mode of the BD, as long as the applied voltage amplitude is below U_{tra}. Both threshold voltages U_{bur} and U_{tra} depend on gas composition and decrease with increasing noble gas content. Consequently, the voltage range of APTD decreases. Similar behaviour of the BDs was observed for the binary gas mixtures N_2/Ne and N_2/Ar as shown in figures 9 and 10. The only exception is pure argon, in which a filamentary BD is always generated instead of the APGD. Between 10 and 0.1 vol% of N_2 in the noble gases Ne and He the discharge is quite unstable and not clearly diffuse or pseudoglow-like.

6.2. Discussion

In nitrogen the derivative of α over E/N is comparatively high for the E/N values corresponding to the breakdown voltage. Thus electron multiplication in nitrogen is very rapid, which favours a filamentary discharge. The effective quenching of the metastable states by oxygen or hydrogen molecules explains the transition from the diffuse to the filamentary BD due to molecular gas admixture ([12, 16], section 5). At a certain level of gas admixture the direct ionization will become the main mechanism of electron production. This fast process is strongly effected by the local electric field.

In the case of argon, the energy of atomic metastables Ar^m ($E_{Ar} = 11.6$ eV) is not high enough to ionize N_2 ($E_{ion} = 15.5$ eV). The missing of Penning-ionization process could be one reason for the filamentary character of a BD in pure argon. If another component with an ionization energy of about 11.6 eV or less (e.g. NH_3) is admixed to argon, an APGD can be generated [7, 41].

The collisional quenching of nitrogen metastables is less effective by noble gas atoms than by oxygen or hydrogen molecules, since the lowest energetic levels of argon, helium and neon are at least 5 eV higher than the metastable levels of nitrogen ($N_2(A, a)$). Thus, the admixture of noble gases does not lead to a dramatic decrease in the density of metastable species in contrast to the admixture of the molecular gases. Metastable states, dimers and molecular ions of the noble gases (e.g. He^m, He_2, He_2^+) can act similarly as $N_2(A, a)$ states or they can even produce nitrogen metastables by excitation transfer [13, 19, 37]. Penning ionization and charge transfer are known to be very effective in He/N_2 non-thermal plasma at atmospheric pressure [13, 19, 42]. Secondary emission of electrons from the dielectrics caused by some noble gas excited states may be possible, too. Due to the higher first ionization coefficient α in noble gases, the electron multiplication increases with the noble gas content. In a similar manner, an increase in the mean electron energy with noble gas admixture at the same reduced electric field strength E/N has to be considered [43]. This leads to the decrease in the burning voltage. If direct ionization is dominant, localized

space charges causing microdischarges can be formed much faster. As a consequence the transition voltage decreases with noble gas admixture.

7. Conclusions

BDs in various gases and gas mixtures were investigated and characterized by electrical measurements. Diffuse BDs can exist in different modes, namely, APTD and APGD. The APTD can be investigated in nitrogen, while APGDs can be operated in the noble gases helium and neon. In diffuse BDs the same memory effect by residual surface charges on the dielectric barriers as for filamentary BDs is investigated. Thus, the feeding voltage amplitude needed to sustain the discharge is much lower than for the very first ignition. The intrinsic neutralization of the residual charges on the dielectric electrodes can last several hours.

The behaviour of the diffuse BDs in the different gas mixtures is quite heterogeneous. By molecular gas admixtures in the hundred-ppm range the diffuse discharges are unstable and tend to the filamentary regime. For an APTD in nitrogen with small admixtures of hydrogen quite similar results are investigated as for an oxygen admixture. The simulation results based on an appropriate fluid model give a qualitative explanation for the transition between an APTD and a filamentary BD. In contrast, more than 80 vol% of an inert gas (helium, argon or neon) can be admixed to nitrogen APTD without affecting the stability, despite the fact that the burning voltage is decreased.

The results are found to be consistent with the following explanations for a uniform Townsend breakdown in a BD at atmospheric pressure. The APTD is formed due to processes induced by metastable nitrogen molecules, i.e. secondary electron emission from the dielectric barriers. The formation of the APGD is due to efficient ionization rate at a comparatively low electric field strength and the breakdown retardation by indirect ionization processes involving metastable states of inert gases or compounds of air impurities.

Acknowledgments

The work was supported by Deutsche Forschungsgemeinschaft, SFB 198, 'Kinetics of partially ionised plasmas' as well as the research project from the Ministry of Education of the Czech Republic under contract MSM0021622411 and by the Czech Science Foundation under contract 202/06/1473 and project 'Nanotechnologie pro společnost' by the Academy of Science of the Czech Republic (No KAN 101630651). The authors are grateful to K V Kozlov (Department of Chemistry, Moscow State University) for fruitful discussions and helpful remarks.

References

[1] Becker K H, Kogelschatz U, Schönbach K H and Barker R J 2005 *Series in Plasma Physics: Non-Equilibrium Air Plasmas at Atmospheric Pressure* (Bristol: Institute of Physics Publishing)
[2] Samoilovich V G, Gibalov V I and Kozlov K V 1997 *Physical Chemistry of the Barrier Discharge* 2 (Düsseldorf: DVS)
[3] Fridmann A, Chirokov A and Gutsol A 2005 *J. Phys. D: Appl. Phys.* **38** R1–R24
[4] Kogelschatz U 2002 *IEEE Trans. Plasma Sci.* **30** 1400–8
[5] Okazaki S, Kogoma M, Uehara M and Kimura Y 1993 *J. Phys. D: Appl. Phys.* **26** 889–92
[6] Müller S and Zahn R-J *Contrib. Plasma Phys.* **36** 697–709
[7] Massines F, Gherardi N, Naude N and Segur P 2005 *Plasma Phys. Control. Fusion* **47** B577–88
[8] Kunhardt E E 2000 *IEEE Trans. Plasma Sci.* **28** 189–200
[9] Naude N, Cambronne J-P, Gherardi N and Massines F 2005 *J. Phys. D: Appl. Phys.* **38** 530–8
[10] Aldea E, Peeters P, de Vries H and van de Sanden M C M 2005 *Surf. Coat. Technol.* **200** 46–50
[11] Gherardi N, Gouda G, Gat E, Ricard A and Massines F 2000 *Plasma Sources Sci. Technol.* **9** 340–6
[12] Kozlov K V, Brandenburg R, Wagner H-E, Morozov A M and Michel P 2005 *J. Phys. D: Appl. Phys.* **38** 518–29
[13] Massines F, Rabehi A, Decomps P, Gadri R B, Segur P and Mayoux C 1998 *J. Appl. Phys.* **83** 2950–7
[14] Mangolini L, Orlov K, Kortshagen U, Heberlein J and Kogelschatz U 2002 *Appl. Phys. Lett.* **80** 1722–4
[15] Navrátil Z, Brandenburg R, Trunec D, Brablec A, Šťahel P, Wagner H-E and Kopecky Z 2006 *Plasma Sources Sci. Technol.* **15** 8–17
[16] Brandenburg R, Maiorov V A, Golubovskii Yu B, Wagner H-E, Behnke J and Behnke J F 2005 *J. Phys. D: Appl. Phys.* **38** 2187–97
[17] Boeuf J P, Pitchford L C and Callegari Th 2004 *Proc. 17th Europhysics Conf. on Atomic and Molecular Physics of Ionized Gases (ESCAMPIG) (Constanta, Romania, 1–5 September 2004)*
[18] Ishihara O, Candler G, Laux Ch O, Napartovich A P, Pitchford L C, Boeuf J P and Verboncoeur J 2005 Modeling *Series in Plasma Physics: Non-Equilibrium Air Plasmas at Atmospheric Pressure* (Bristol: Institute of Physics Publishing) ed K H Becker *et al* 183pp, chapter 5
[19] Golubovskii Yu B, Maiorov V A, Behnke J and Behnke J F 2002 *J. Phys. D: Appl. Phys.* **35** 751–61
[20] Maiorov V A and Golubovskii Yu B 2007 *Plasma Sources Sci. Technol.* **16** S67–S75
[21] Radu I, Bartnikas R, Czeremuszkin G and Wertheimer M R 2003 *IEEE Trans. Plasma Sci.* **31** 411–21
[22] Bouwstra J B, Aldea E, van de Sanden M C M and de Vries H W *Patent EP* 1548795
[23] Brenning N, Axnäs I, Nilsson O and Eninger J E 1997 *IEEE Trans. Plasma Sci.* **25** 83–8
[24] Massines F, Gouda G, Gherardi N, Duran M and Croquesel E 2001 *Plasmas Polym.* **6** 35–49
[25] Trunec D, Navrátil Z, Šťahel P, Zajíčková L, Buršíková V and Čech J 2004 *J. Phys. D.: Appl. Phys.* **37** 2112–20
[26] Martin S, Massines F, Gherardi N and Jimenez C 2004 *Surf. Coat. Technol.* **177–178** 693–8
[27] Šíra M, Trunec D, Šťahel P, Buršíková V, Navrátil Z and Buršík J 2005 *J. Phys. D.: Appl. Phys.* **38** 621–7
[28] Massines F, Gherardi N, Fornelli A and Martin S 2005 *Surf. Coat. Technol.* **20** 1855–61
[29] Kozlov K V, Wagner H-E, Brandenburg R and Michel P 2001 *J. Phys. D: Appl. Phys.* **34** 3164–76
[30] Kogelschatz U 2003 *Plasma Chem. Process.* **23** 1–45
[31] Kogelschatz U, Eliasson B and Egli W 1997 *J. Physique IV* C **4** 47–66
[32] Bartnikas R 1968 *Br. J. Appl. Phys. Ser. 2* **1** 65961
[33] Radu I, Bartnikas R and Wertheimer M R 2003 *IEEE Trans. Plasma Sci.* **31** 1363–78

[34] Sublet A, Ding C, Dorier J-L, Hollenstein Ch, Fayet P and Coursimault F 2006 *Plasma Sources Sci. Technol.* **15** 627–34
[35] Shin J and Raja L L 2003 *J. Appl. Phys.* **94** 7408–15
[36] Tochikubo F, Chiba T and Watanabe T 1999 *Japan. J. Appl. Phys.* **38** 5244–50
[37] Zhang P and Kortshagen U 2006 *J. Phys. D.: Appl. Phys.* **39** 153–63
[38] Bobrov Y K and Yurghelenas Y V 1998 *Comput. Math. Math. Phys.* **38** 1652
[39] Phelps A V and Pitchford L C 1985 *JILA Information Center Report* #26, JILA, University of Colorado
[40] Gordiets B, Ferreira C M, Pinheiro M J and Rocard A 1998 *Plasma Sources Sci. Technol.* **7** 363
[41] Tochikubo F, Chiba T and Watanabe T *Proc. 10th Int. Symp. on High Pressure Low Temperature Plasma Chemistry (HAKONE X) (Saga, Japan, 4–8 September 2006)*
[42] Bibinov N K, Fateev A A and Wiesemann K 2002 *Selected Research Papers on Spectroscopy of Nonequilibrium Plasma at Elevated Pressures Proc. SPIE* **4460** 251
[43] Tas M A, van Veldhuizen E M and Rutgers W R 1997 *J. Phys. D: Appl. Phys.* **30** 1636–45

IOP PUBLISHING JOURNAL OF PHYSICS D: APPLIED PHYSICS

J. Phys. D: Appl. Phys. **43** (2010) 345205 (10pp) doi:10.1088/0022-3727/43/34/345205

An investigation of dielectric barrier discharge in Ar and Ar/NH_3 mixture using cross-correlation spectroscopy

P Kloc[1], H-E Wagner[2], D Trunec[1], Z Navrátil[1] and G Fedoseev[3]

[1] Department of Physical Electronics, Faculty of Science, Masaryk University, Kotlářská 2, 611 37 Brno, Czech Republic
[2] Institute of Physics, University of Greifswald, F.-Hausdorff-Str 6., 17489 Greifswald, Germany
[3] Department of Material Science, Moscow State University of Design and Technology, Sadovnicheskaya str. 33, 117997 Moscow, Russia

E-mail: kloc@physics.muni.cz

Received 20 May 2010, in final form 13 July 2010
Published 12 August 2010
Online at stacks.iop.org/JPhysD/43/345205

Abstract

Dielectric barrier discharges (BDs) are known to operate in two distinctive modes. The filamentary mode of BD is characterized by a large number of short lasting spatially bounded microdischarges. This type of discharge is typical for most cases of BDs at atmospheric pressure. Under some specific conditions another form of BD may arise. In this mode plasma uniformly covers the whole electrode area. This mode is usually referred to as the diffuse or homogeneous mode of BD.

This work presents studies of the filamentary mode of BD in argon and its transition to the diffuse mode by ammonia addition. The discharges were investigated by means of cross-correlation spectroscopy. Particularly, the influence of electrode shape, discharge gap and the influence of ammonia admixture on discharge development were studied. The measurement offers results with high temporal and spatial resolution which are useful for comparison with results of numerical models.

The obtained results include the electrical current measurement of discharge in several ammonia admixtures to argon. The diffuse discharge appeared at ammonia admixture above 3 vol%. The observed propagation of streamer in discharge in pure argon for two different electrode configurations is presented. When compared with discharge in pure argon the streamer velocity is decreased for 0.1 vol% ammonia admixture. With increasing ammonia concentration the streamer velocity increases again. The behaviour of presented impurities was observed and the results are included in this report. The basic model of the discharge kinetic is included. For reduced electric field below 10 Td the electron drift is much higher in argon–ammonia mixture than in pure argon.

(Some figures in this article are in colour only in the electronic version)

1. Introduction

The plasma in dielectric barrier discharge (BD) is a non-thermal low temperature plasma. Usually BDs appear in the form of many microdischarges of nanoseconds to microseconds durations [1]. The properties of one filament (microdicharge) are determined mainly by the used gas, but they can be also influenced by the electrodes as is shown later in this paper. The typical filament in synthetic air at atmospheric pressure has diameters of roughly 0.1 mm at the middle of the discharge gap. This diameter stretches close to electrodes where the covered area diameter can be an order of magnitude larger. The duration of microdischarge is in the order of nanoseconds.

The development of one microdischarge is driven by the streamer mechanism due to the formation of a high

concentration of charged particles. The microdischarge is formed when both electrodes are connected by streamer. The buildup of charge on the surface of dielectrics effectively reduces the electric field in the filament area, thus effectively terminating the microdicharge. The charge transported by one microdischarge is small, just in the order of nanocoulombs [2]. Due to the short duration of the microdischarge, the heating up of surrounding area is negligible and the temperature of neutral particles is close to room temperature.

At some specific conditions (electrode configuration, applied voltage, gas) another form of BD may appear. This type of discharge does not form filaments but uniformly covers the whole electrode area. Since the appearance of this discharge type is more diffused, it is often referred to as diffuse BD or homogeneous BD. More mechanisms leading to transition from filamentary to diffuse BD exist. Recent progress in understanding the diffuse discharges was summarized in [3].

The BD was investigated in many different gases. The study of diffuse BD in nitrogen and its transition to the filamentary mode after oxygen admixture was presented in [4, 5] . The diffuse barrier discharge in neon and helium was investigated e.g. in [6–8].

A method of cross-correlation spectroscopy (CCS) is suitable for the micodischarge investigation. This technique provides temporal and spatial resolution of light emission at a selected wavelength. The time resolution of CCS is in the order of tenths of nanoseconds. The spatial resolution is determined by the quality of optical system and it is usually in the order of micrometres. Such good temporal resolution can hardly be achieved by any other method. We decided to use this technique for our measurements because filamentary discharges have generally very short duration.

The comparison of discharge in neon and argon using CCS was presented in [9]. The difference in discharge characteristics was clearly visible. While discharges in pure neon and helium can burn in diffuse form, no such behaviour was observed in the case of pure argon. However, it was reported in [10] that an admixture of ammonia to argon can also lead to diffuse mode. This diffuse discharge in the mixture of argon and ammonia could be used for thin film deposition, especially for deposition of Si_3N_4 films from suitable monomer [11].

In this paper we focused on a thorough investigation of the discharge in pure argon and in argon with an admixture of ammonia. The results reported by Kozlov *et al* in [9] had low resolution, so it was not possible to observe the beginning phase of the discharge in detail. The measurement was also done with only one set of electrodes. In this work we studied the influence of different electrode shapes on discharge in argon. The influence of the discharge gap was also studied. In our investigation we mainly used the CCS technique but other diagnostic methods were also used. The second goal of our study was to evaluate the influence of ammonia on the development of discharge in argon/ammonia mixtures.

2. Experimental setup

The experimental setup is consistent with the setup used for CCS described in [12]. The schema of the setup is shown in figure 1. The discharge was generated between two electrodes covered with dielectric layer. Three different electrode configurations were used during experiments. A cross section of the electrodes is shown in figure 2. Electrode characteristics are summarized in table 1. The metal parts of the electrodes were made of steel in all cases. The first electrode configuration was a planar configuration. The metal electrodes with area 20 mm × 20 mm were fastened inside an organic glass holder. The metal electrodes were covered with a 2.1 mm thick glass ($\epsilon_r \doteq 4$). Discharge gap width was fixed at 1.1 mm with two organic glass holders. This electrode configuration could not be used for CCS since the microdischarges were not spatially stable. It could, however, provide information on the type of discharge.

The second electrode configuration consisted of a metal rod covered with 1 mm alumina oxide layer ($\epsilon_r \doteq 9$). The tip of both electrode and rod had a spherical shape. This configuration ensures spatially stable microdischage. The disadvantage of this electrode configuration was the occurrence of long surface discharges running along the electrode. This phenomenon was not observed in the case of planar electrode configuration.

The last electrode configuration was cylindrical with a total diameter of 1.5 cm. These electrodes were made of 1 mm diameter metal rod covered with ceramics called MACOR ($\epsilon_r \doteq 6$). The metal rod ended 1 mm below the surface of the electrode. This configuration of electrodes ensures spatially stable filamentary discharge which is needed for the CCS technique. The discharge gap was varied from 1 to 3 mm.

The electrodes were placed in a stainless steel vacuum chamber. The system was evacuated by a rotary vacuum pump to approximately 1 mbar. After several minutes the pump was switched to a membrane pump and the chamber was filled either with argon (purity 99.999 vol%) or a mixture of argon and ammonia. The gas flow was kept at 100 sccm and it was controlled by a MKS 647C Multigas Controller equipped with a MKS 1259CC-01000RV gas flow controller. The pressure was kept slightly above atmospheric pressure and measured by a Balzers APG 011 pressure probe.

The sinusoidal voltage at 5.2 kHz for discharge operation was supplied by Voltcraft MXG-9802 function generator which also provided TTL pulses for synchronization. The sinusoidal voltage was then amplified by a Trek PM04015A High-Voltage AC/DC Generator operated in amplifier mode. The applied high voltage was measured by a Tektronix TDS3034B digital oscilloscope (300 MHz, 2.5 G Samples s^{-1}) via a Tektronix P6015A 1000 : 1 high-voltage probe. Electrical current through the discharge was measured as the voltage on a 461 Ω resistor connected in series with a discharge cell. For this purpose a Tektronix P6114B 1 : 10 probe was used.

The discharge chamber was equipped with two quartz windows used for CCS measurements. One window was used for MAIN signal, the second one for obtaining SYNC signal

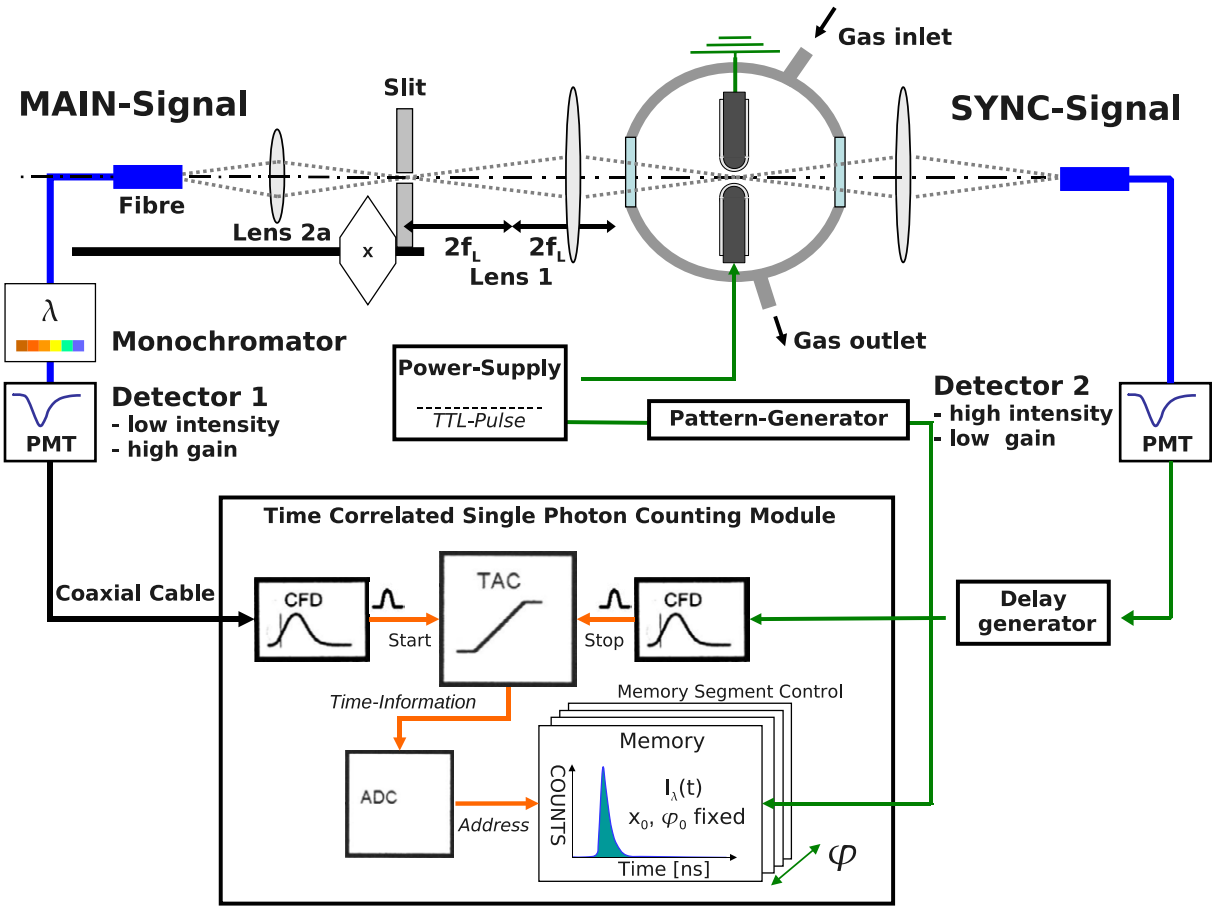

Figure 1. Experimental setup schema.

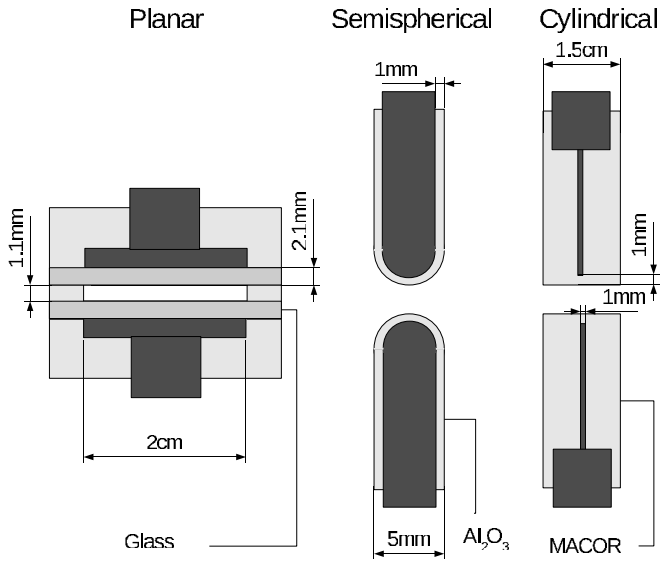

Figure 2. Electrode configuration used in experiments.

(see figure 1). In the MAIN signal path the image of the discharge image was projected onto a 0.1 mm wide movable slit which ensured spatial resolution of the measurement. The signal was then guided with optical fibre to the input of a Jobin Yvon Triax 320 monochromator equipped with a fast PMH-100-4 photomultiplier. The signal obtained from the photomultiplier was then measured by an SPC-530 module. In the case of temporally unresolved overview spectra measurement the PMH-100-4 photomultiplier was replaced by a Jobin Yvon DPM-HV photomultiplier. The SYNC signal (see figure 1) was sensed with the PMH-100-4 for pure argon. The sensitivity of this photomultiplier was insufficient for the argon/ammonia mixture so a PMH-100-6 photomultiplier was used instead. A Stanford Research System Inc. DG645 delay generator was inserted between the photomultiplier and the SPC module in order to delay the SYNC signal.

Table 1. Summary of electrode parameters.

Electrode shape	Gap width (mm)	Dielectric material	ϵ_r
Planar	1.1	Glass	4
Semispherical	1.0	Alumina oxide	9
Cylindrical	2.0	MACOR	6

3. Experimental results and discussion

3.1. Breakdown voltage in planar configuration

The influence of ammonia on argon discharge was investigated in the planar electrode configuration. Under various conditions more than one type of discharge can occur. After discharge ignition the diffuse mode can be established but after further voltage increase the discharge changes to filamentary mode. In this case the voltage at which the transition occurred is referred

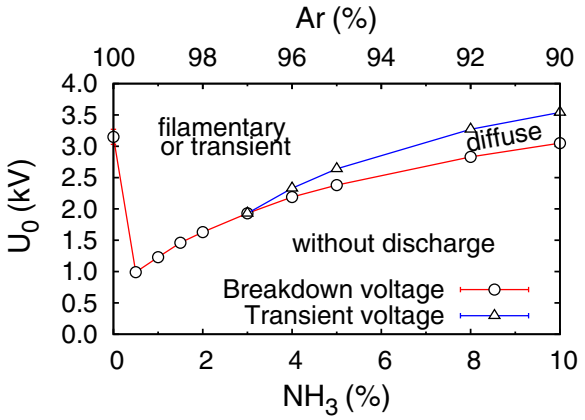

Figure 3. Breakdown voltage and transient voltage dependence on ammonia admixture. U_0 denotes amplitude of the sinusoidal applied voltage.

to as transient voltage. Since breakdown voltage is highly dependent on time since last discharge [13], the following technique was used. The applied voltage was increased until discharge appeared. The voltage was kept at this value for 1 min. Then it was raised to check the existence of transient voltage. If such a discharge type transition occurred, the corresponding voltage was recorded. The applied voltage was then decreased until the discharge extinguished. The discharge gap was then kept for 1 min without discharge. The whole cycle was repeated ten times to obtain more precise results.

The influence of ammonia admixtures on breakdown voltage and transient voltage was studied for several concentrations of ammonia admixtures to argon. The obtained results, shown in figure 3, exhibit a strong influence of ammonia on breakdown voltage. Mainly small admixtures very drastically reduce the voltage required for the discharge ignition. This can be explained by the Penning ionization of ammonia molecules by argon metastables. For the reaction scheme of argon–ammonia mixture see [10]. The diffuse discharge appears at ammonia admixture above 3 vol%, which is different from the observation reported in [10] where homogeneous glow was observed even for concentrations below 1 vol%. The diffuse mode existence was mainly confirmed by the shape of the discharge current peak as shown in figure 4. The overall light emission decreases rapidly with increasing ammonia concentration thus it was difficult to confirm the diffuse mode by naked eye observation.

The dependence of discharge current shape on the applied voltage as well as on the ammonia concentration is shown in figure 4. In the case of pure argon and small admixtures of ammonia the current oscillograms are of filamentary mode. Higher applied voltage leads to the production of a higher number of filaments per halfperiod. This behaviour is consistent with standard behaviour of BD as described in [2]. With ammonia admixture higher than 3 vol% the response to voltage increase changes. The broad small peak representing diffuse discharge is distorted by oscillations at higher applied voltage. This behaviour is similar to that which was observed in neon or nitrogen [13]. Also the appearance of some filaments can be observed. The filaments were not observed directly due to weak overall light intensity from the discharge.

3.2. Streamer development in semispherical configuration

The semispherical electrode configuration was chosen for the study of discharge in pure argon because it provides a spatially stable microdischarge required for CCS measurement. A 1 mm gap was chosen in order to reduce the length of surface discharges which were running along the dielectric surface. The length of surface discharges can exceed the discharge gap width by an order of magnitude.

The presence of impurities was checked by optical emission spectroscopy. A typical spectrum is presented in figure 5. It shows a typical line structure of an argon discharge. Spectral bands belonging to nitrogen (337.1 nm) and OH (309.5 nm) were observed as well. These impurities were present due to the high ultimate pressure of the oil rotary pump. Since their intensity distributions can serve as indicators of discharge kinetics, they were included for CCS measurements.

The results obtained from CCS measurements are presented in figure 6. It can be seen that both investigated light emissions of argon atoms exhibit the very similar pattern. The streamer appears first close to the anode and it propagates towards the cathode. After the streamer hits the cathode the discharge starts to develop. The most intensive light emission is observed close to the anode. The discharge is shortly afterwards terminated by charge buildup on the dielectric surfaces. The long afterglow is then observed. There are also visible surface discharges which start to run from the discharge gap on both electrode surfaces. At a time corresponding to the start of these surface discharges a second intensity maximum is observed in the middle of the discharge gap.

A completely different distribution of light emission was observed for impurities. Neither nitrogen nor OH emission shows streamer-like pattern at the beginning of the discharge. Their intensities are low at the time when the streamer develops. The light emission from these impurities then starts to grow close to both electrodes with higher light intensity closer to the anode. Their emissions reach maximum intensity, 100 ns for nitrogen and 300 ns for OH, after appearance of the discharge. This behaviour indicates that impurity molecules are not excited in direct electron collisions. The excitation of impurities can thus be attributed to excitation energy transfer from excited argon atoms.

3.3. Ammonia influence in cylindrical configuration

When attempting to perform CCS measurement in the semispherical electrode configuration we found out that the light emission was too weak in the discharge in the mixture of argon with ammonia to trigger the measurement. To overcome this drawback a new pair of electrodes was designed. The new electrodes have the shape of a dielectric cylinder with a metal rod placed in the center (see figure 2). In this configuration the surface discharges did not leave the area which was observed by SYNC fibre so they could be used for measurement synchronization. Another effect was the reduction in the length of the surface discharges.

This new configuration was first tested in pure argon. The discharge gap was 2 mm in this experiment. The comparison of results from semispherical configuration and cylindrical

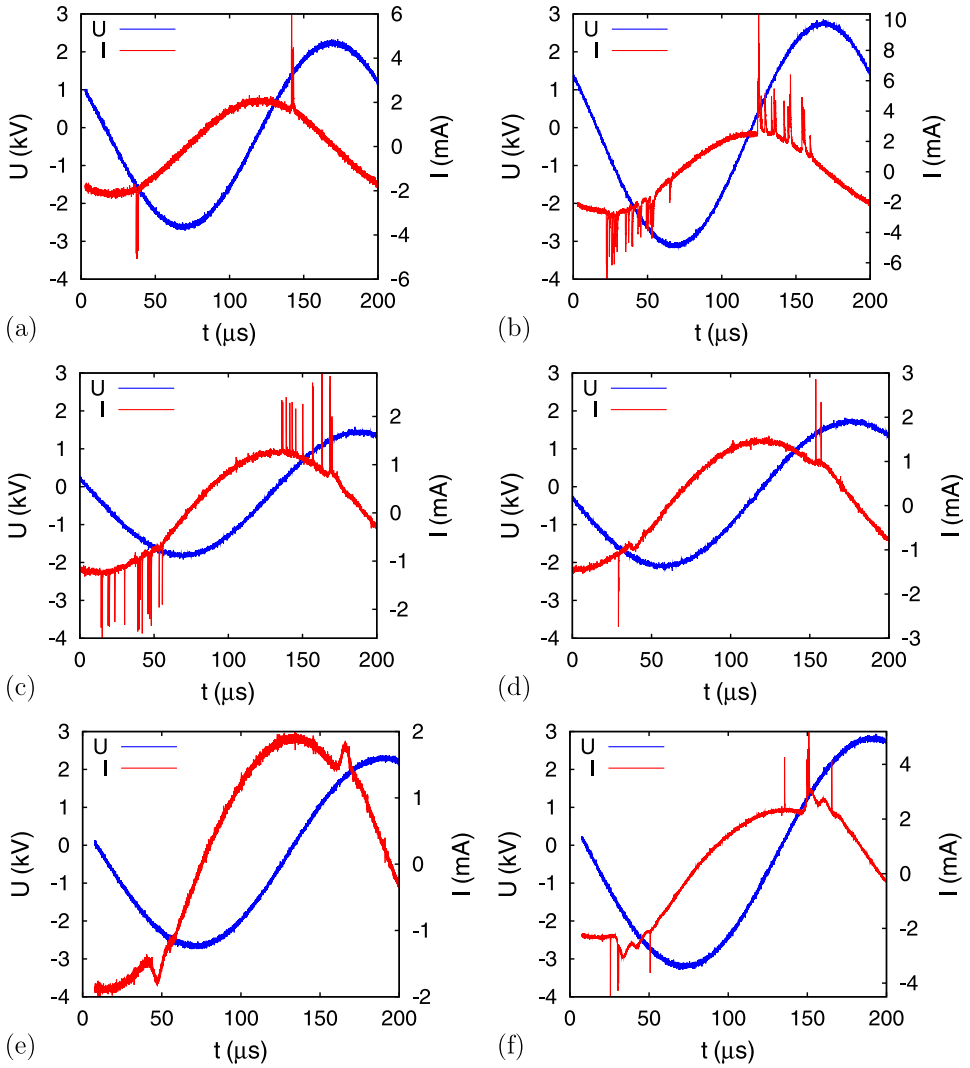

Figure 4. Electrical characteristics of discharge in pure argon and argon with small admixture of ammonia. (*a*) Pure argon, applied voltage slightly above breakdown voltage, (*b*) pure argon, voltage raised to higher value than in case (*a*), (*c*) 2 vol% admixture of ammonia into argon, voltage slightly above breakdown voltage, (*d*) 3 vol% admixture of ammonia to argon, applied voltage slightly above breakdown voltage, (*e*) 5 vol% admixture of ammonia to argon, applied voltage slightly above breakdown voltage, (*f*) 5 vol% admixture of ammonia to argon, voltage raised to higher values than in case (*e*).

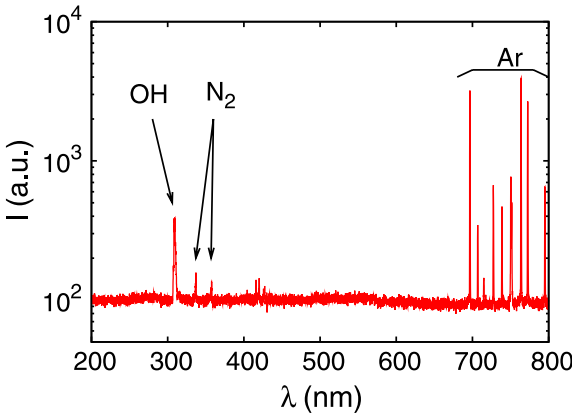

Figure 5. Spectrum of discharge in pure argon (semispherical electrodes).

configuration is shown in figure 7. While the light emissions of impurities are unaffected by electrode change, the duration of argon light emission is reduced and no second intensity maximum in the middle of the discharge gap is observed. The difference can be attributed to the reduction in surface discharges and it does not affect initial phase and streamer propagation. This is also confirmed by comparison of the streamer velocity as shown in figure 8. The streamer velocity was measured by analysing the intensity development of two different argon lines for both electrode configurations. The velocity was measured using the following technique. The position of maximum light emission from discharge was determined at different times. The obtained temporal dependence of position was fitted with analytical function. The sum of exponential and linear function fitted the measured data best. From the fitted analytical function the velocity was calculated. In all cases the streamer starts to propagate with the same velocity of approximately 4000 m s^{-1} and

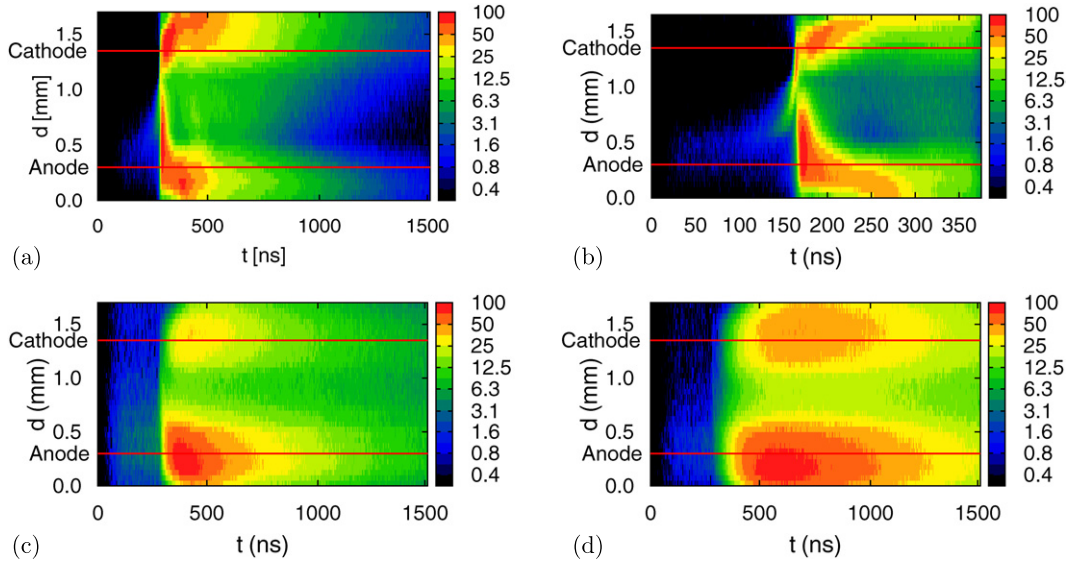

Figure 6. Results of CCS of discharge in pure argon. (*a*) Argon line 763.5 nm; (*b*) Argon line 750.5 nm with higher temporal resolution. (*c*) Nitrogen emission at 337.1 nm. (*d*) OH emission at 309.5 nm.

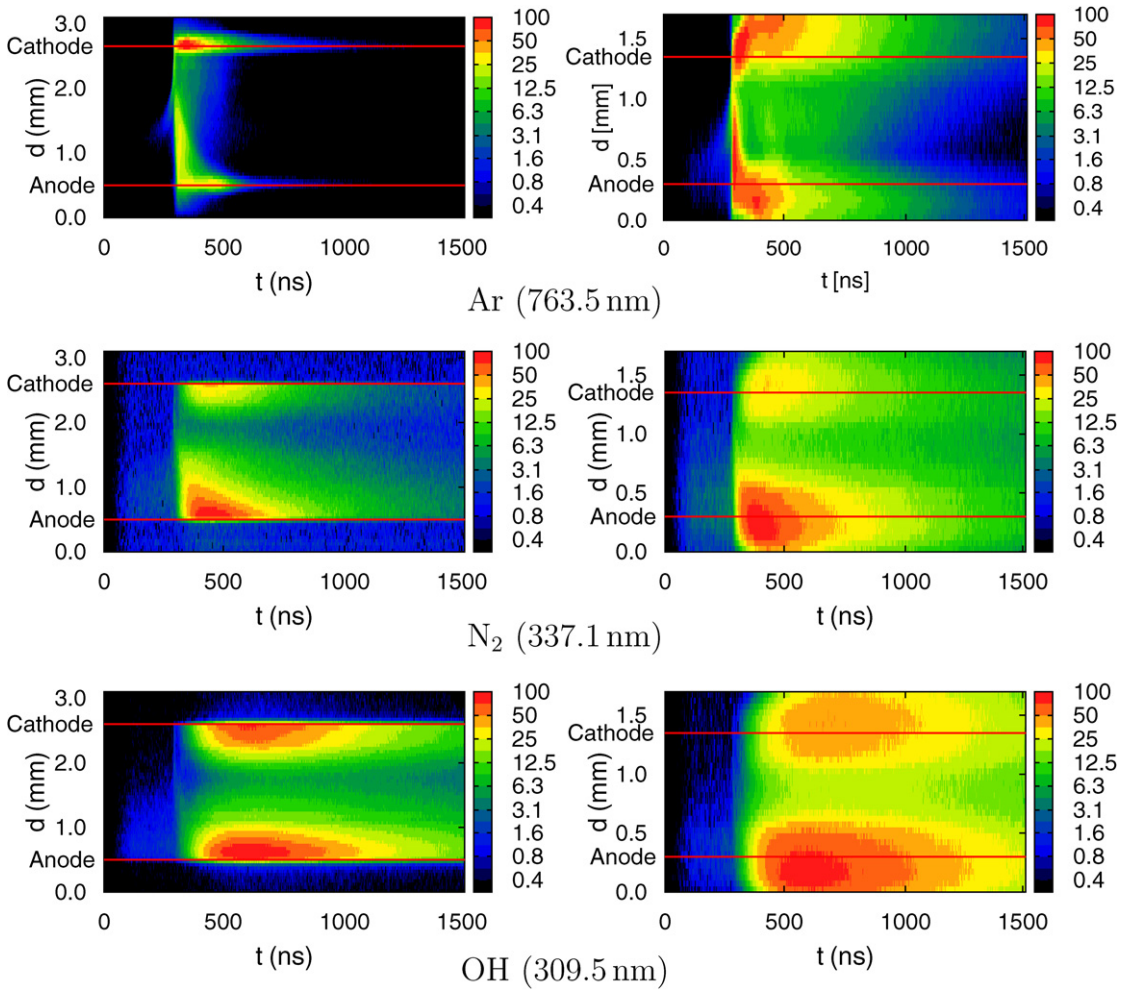

Figure 7. The comparison of the discharge in pure argon in semispherical and cylindrical configuration. Left column—cylindrical configuration. Right column—semispherical configuration.

then accelerates as it approaches the cathode. The final streamer velocity at the cathode surface is the same for both configurations.

Since a wider discharge gap was used for the cylindrical configuration, the influence of discharge gap on discharge characteristics was also investigated. Only argon lines were studied in this experiment, since development of molecular emissions remained the same (see figure 7). Obtained results are shown in figure 9. The streamer ignites in all cases at approximately the same distance from the cathode. Also, the region of light emission close to the anode is affected only slightly. The gap width mainly influences the duration and intensity of surface discharges. The maximum of light emission shifts from the inside of the gap to the anode surface with increasing gap width.

The ammonia influence on argon discharge was studied by optical emission spectroscopy. The observed changes were similar to [10]—appearance of NH bands, disappearance of OH band and decrease in argon line intensity by nearly one hundred times, thus highly reducing overall light intensity of the discharge. The intensity of both argon lines and NH bands decreased with increasing concentration of ammonia.

The influence of ammonia on discharge current for selected ammonia concentrations is shown in figure 10. The current peak of discharge in pure argon is identical to peaks observed in the semispherical configuration. Only in the case of the 1 mm discharge gap and the semispherical electrode configuration does the discharge current peak exhibit a second small peak at the decreasing part of current.

The CCS measurements were carried out for concentrations of ammonia of 0.1%, 1.0% and 5.0%. Obtained results for the argon line at 763.5 nm are shown in figure 11. When compared with discharge in pure argon the streamer velocity is highly decreased for 0.1% ammonia admixture. Such a huge decrease in the streamer velocity can be explained by the change in the ionization mechanism—the direct electron ionization is replaced by the Penning ionization. This behaviour also manifests itself in the deep decrease in breakdown voltage (see figure 3). With increasing ammonia concentration the streamer velocity increases again. The strong light emission close to the anode after streamer hits cathode almost disappears after ammonia addition. Also the surface discharges are completely eliminated in the mixture. Light emission of NH bands exhibits the same temporal and spatial distribution as emission of argon lines.

Contrary to the measurement in the planar configuration, the discharge in the cylindrical configuration did not exhibit the diffuse behaviour. Although the discharge channel seemed to be wider compared with discharge in pure argon, the electric current measurement did not exhibit a small broad discharge peak. This behaviour can probably be attributed to the electric field inhomogeneity. The electric field in the cylindrical configuration is localized in the electrode axis, dropping with

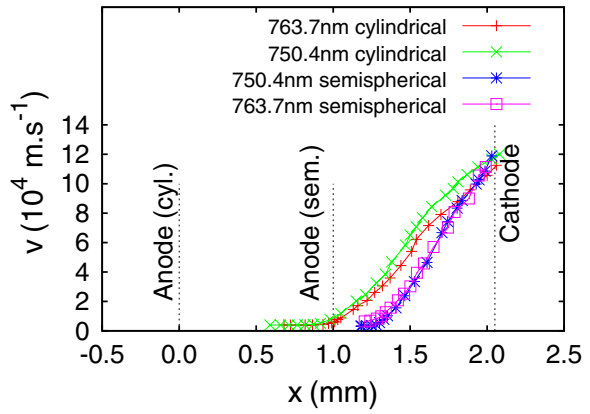

Figure 8. The dependence of the streamer velocity on distance from anode for the discharge in pure argon. The horizontal dashed lines indicate the positions of electrode surfaces.

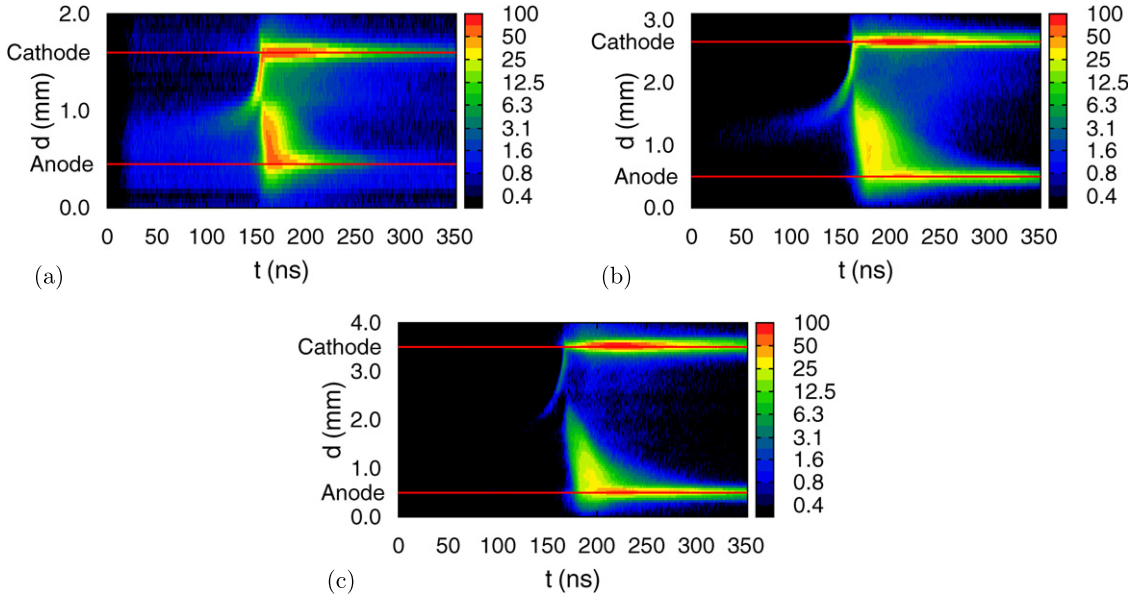

Figure 9. Influence of discharge gap on discharge in pure argon (argon line 750.5 nm). (*a*) 1 mm gap; (*b*) 2 mm gap; (*c*) 3 mm gap measured in cylindrical configuration.

distance from the axis. This may prevent the discharge from spreading radially.

3.4. Theoretical model

To explain the behaviour of discharge in the mixture of argon with ammonia, the fully selfconsistent model is required. Some of the issues can, however, be addressed by simpler methods based on discharge kinetics analysis.

We solved Boltzmann equation (BE) using the method described in [14] for electrons. The considered elementary processes are described in table 2. The input cross section data for argon were obtained from [15–21] and for ammonia from [22]. Because of the low frequency of applied voltage the steady-state approximation was assumed.

To evaluate the validity of our solution of BE, we calculated drift electron velocities in pure argon and pure ammonia and compared them with experimental data. This comparison is shown in figure 12. The experimental data were obtained from [23] for argon and from [22] for ammonia. The calculated drift velocity for argon fits very well the experimental data. In the case of ammonia the curve does not fit well in the range 10–45 Td. This is probably due to inaccuracy of the input cross sections. Since we investigated only small admixtures of ammonia to argon, we decided to continue even with this inaccuracy.

The electron drift velocities calculated for several admixtures of ammonia to argon are presented in figure 13. Here the effect of ammonia can be clearly seen. The largest influence of ammonia is observed for reduced electric field below 10 Td. In this region the electron drift is much higher in the argon–ammonia admixture than in pure argon. At the reduced electric field values above 10 Td, the values of electron drift velocity converge to the values of argon drift velocity with increasing reduced electric field.

In CCS measurements we observed the propagation of the ionization wave in the direction from anode to cathode. This convinced us that in argon and in the mixture of argon with ammonia the discharge mechanism is driven by streamer formation. There is a strong electric field at the frontal region of the streamer. But in the subsequent area the electric field is reduced by the charged particles created in frontal wave.

The ratio of diffusion coefficient and mobility is given by Einstein–Smoluchowsky relation $D/\mu = k_b T/e$. Due to higher electron mobility in the area behind the streamer front in the mixture of ammonia (see figure 13), the electrons also retain a higher diffusion coefficient assuming the average electron temperature remains the same. This can lead to a higher spread of electrons between the discharges and preionization in a larger area. However, this effect has to be confirmed by numerical simulation.

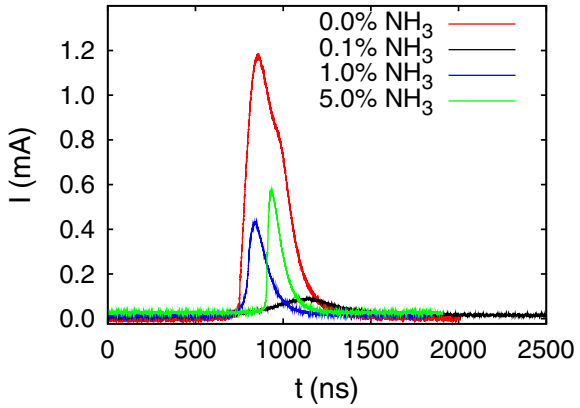

Figure 10. The comparison of discharge current peaks for different concentrations of ammonia admixture (cylindrical electrode configuration, 2 mm gap). The peaks are slightly shifted in time due to different trigger levels.

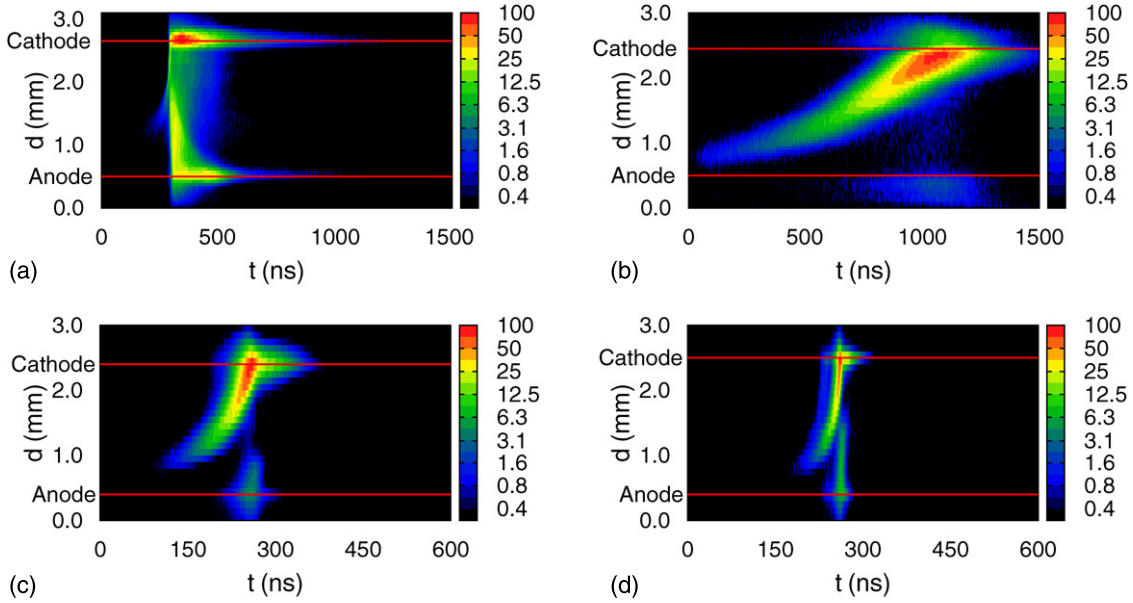

Figure 11. Influence of ammonia admixture on discharge light emission characteristics measured in cylindrical configuration. All four figures shows line at 763.5 nm belonging to argon. (*a*) Pure argon; (*b*) 0.1% ammonia admixture; (*c*) 1.0% ammonia admixture; (*d*) 5.0% ammonia admixture. Note the different time scale of figures (*a*), (*b*) and (*c*), (*d*).

Table 2. List of elementary processes considered in BE solving.

Elastic collision	$Ar + e^- \rightarrow Ar + e^-$
Inelastic collisions (36 states)	$Ar + e^- \rightarrow Ar^* + e^-$
Impact ionization	$Ar + e^- \rightarrow Ar^+ + 2e^-$
Elastic collision	$NH_3 + e^- \rightarrow NH_3 + e^-$
Inelastic collisions (3 rotational, 4 vibrational)	$NH_3 + e^- \rightarrow NH_3^* + e^-$
Dissociative excitation	$NH_3 + e^- \rightarrow NH + H_2 + e^-$
Dissociative excitation	$NH_3 + e^- \rightarrow NH_2 + H + e^-$
Dissociative excitation	$NH_3 + e^- \rightarrow NH + 2H + e^-$
Impact ionization	$NH_3 + e^- \rightarrow NH_3^+ + 2e^-$
Electron attachment	$NH_3 + e^- \rightarrow NH_2^- + H$

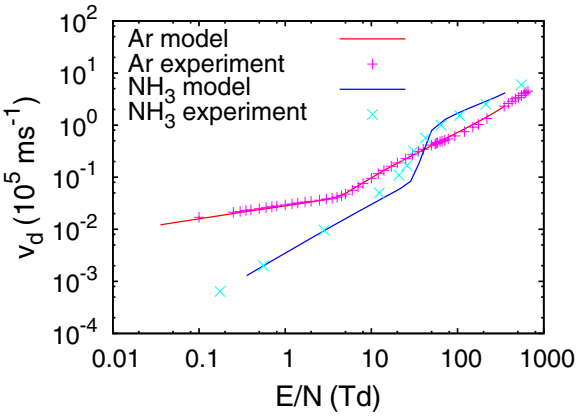

Figure 12. Comparison of calculated electron drift velocity with the experimental data. The experimental data for comparison were obtained from [23] for argon and [22] for ammonia.

Ammonia is a molecular gas with large rotation cross sections for low energy. This causes a shift of the electron energy distribution function maximum to the lower energy. This expected effect was observed in our calculations. However, our calculation did not include super elastic collisions. We therefore cannot qualify the full effect of ammonia on the electron distribution function.

The diffuse discharge could not be produced in the cylindrical electrode configuration. Even though the discharge was visibly more diffuse, no substantial change was observed in the discharge current peak. The electric field in this electrode configuration is highly localized close to the axis, thus creation of a large area diffuse mode is not possible.

4. Conclusion

We obtained high temporally and spatially resolved spectroscopic data from discharge argon and in argon with an ammonia admixture. The influence of electrode configuration on discharge in pure argon was investigated. We concluded that the influence of electrode shape is negligible in time of propagation of the streamer. The argon discharge then spreads over a large surface area of electrodes. The length of this surface discharge depends on the electrode configuration and it has an important effect on the discharge dissipation.

The influence of ammonia admixture on discharge properties was investigated. The decrease in overall light intensity from discharge was observed. The light emission

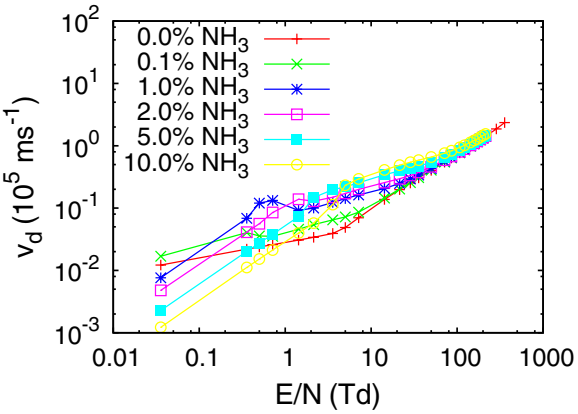

Figure 13. Electron drift velocity calculated for several concentrations of ammonia.

characteristics of discharge change after even a small addition of ammonia. The transition to diffuse mode was observed in the case of planar electrode configuration and ammonia concentration above 3%. No transition was observed in the case of cylindrical electrode configuration probably due to electric field localization.

BE for electrons in a mixture of argon with ammonia was solved. For high reduced electric field strength the drift velocity of electrons in mixture converges to that of pure argon. It was shown that for low reduced electric field strength the electrons in mixture have higher mobility and diffusion coefficient than in the case of pure argon. This can positively influence the generation of the diffuse mode in the argon–ammonia mixture.

Acknowledgments

This work was supported by the Czech Science Foundation under contract 104/09/H080 and Deutscher Akademischer Austausch Dienst (DAAD). The authors are grateful to K V Kozlov (Moscow State University, Department of Chemistry), T Hoder and R Brandenburg (Leibnitz-Institut fuer Plasmaforschung und Technologie) for their insight and opinions on covered topic.

References

[1] Kogelschatz U 2002 *IEEE Trans. Plasma Sci.* **30** 1400–8
[2] Kogelschatz U, Eliasson B and Egli W 1997 *Proc. Phenomena Ionized in Gases ICPIG (Toulose, France)*
[3] Massines F, Gherardi N, Naude N and Segur P 2009 *Eur. Phys. J.—Appl. Phys.* **47** 22805
[4] Brandenburg R, Maiorov V A, Golubovskii Yu B, Wagner H-E, Behnke J and Behnke J F 2005 *J. Phys. D: Appl. Phys.* **38** 2187–97
[5] Kozlov K V, Brandenburg R, Wagner H-E, Morozov A M and Michel P 2005 *J. Phys. D: Appl. Phys.* **38** 518–29
[6] Trunec D, Brablec A and Buchta J 2001 *J. Phys. D: Appl. Phys.* **34** 1697–99
[7] Massines F, Rabehi A, Decomps P, Gadri R B, Segur P and Mayoux C 1998 *J. Appl. Phys.* **83** 2950–7
[8] Navratil Z, Brandenburg R, Trunec D, Brablec A, Stahel P, Wagner H-E and Kopecky Z 2006 *Plasma Sources Sci. Technol.* **15** 8–17

[9] Kozlov K V and Wagner H-E 2007 *Contrib. Plasma Phys.* **47** 26–33
[10] Fateev A, Leipold F, Kusano Y, Stenum B, Tsakadze E and Bindslev H 2005 *Plasma Process. Polym.* **2** 193-200
[11] Lieberman M A and Lichtenberg A J 1994 *Principles of Plasma Discharges and Material Processing* (New York: Wiley)
[12] Kozlov K V, Wagner H-E, Brandenburg R and Michel P 2001 *J. Phys. D: Appl. Phys.* **34** 3164–76
[13] Brandenburg R, Navratil Z, Jansky J, Stahel P, Trunec D and Wagner H-E 2009 *J. Phys. D: Appl. Phys.* **42** 085208
[14] Hagelaar G J M and Pitchford L C 2005 *Plasma Sources Sci. Technol.* **14** 722–33
[15] Yamabe C, Buckman S J and Phelps A V 1983 *Phys. Rev.* A **27** 1345–52
[16] Khakoo M A *et al* 2004 *J. Phys. B: At. Mol. Phys.* **37** 247–81
[17] Chiltin J E, Boffard J B, Schappe R S and Lin C C 1998 *Phys. Rev.* A **57** 267–77
[18] Hayashi M 2003 *Bibliography of Electron and Photon Cross-Sections with Atoms and Molecules Published in the 20th Century—Argon* (Tokyo: National Institute for Fusion Science)
[19] Weber T, Boffaed J B and Lin C C 2003 *Phys. Rev.* A **68** 32719–30
[20] Drawin H W 1967 *Report EUR-CEA-FC-383* Association Euroatom-CEA
[21] Rapp D and Englander-Golden P 1965 *J. Chem. Phys.* **43** 1464–79
[22] Yousfi M and Benabdessadok M D 1996 *J. Appl. Phys.* **80** 6619–30
[23] Ellis H W, Pai R Y, McDaniel E W, Mason E A and Viehland L A 1976 *At. Data Mol. Data Tables* **17** 177

IOP Publishing Journal of Physics D: Applied Physics

J. Phys. D: Appl. Phys. **48** (2015) 355204 (10pp) doi:10.1088/0022-3727/48/35/355204

Investigation of helium barrier discharges with small admixtures of oxygen

L Dosoudilová[1], R Tschiersch[2], M Bogaczyk[2,3], Z Navrátil[1], H-E Wagner[2] and D Trunec[1]

[1] Department of Physical Electronics, Faculty of Science, Masaryk University, Kotlářská 2, 611 37 Brno, Czech Republic
[2] Institute of Physics, University of Greifswald, Felix-Hausdorff-Str. 6, 17489 Greifswald, Germany
[3] INP Greifswald, Felix-Hausdorff-Str. 2, 17489 Greifswald, Germany

E-mail: ldosoudi@mail.muni.cz

Received 16 April 2015, revised 18 June 2015
Accepted for publication 3 July 2015
Published 10 August 2015

Abstract

Barrier discharges in helium and in helium with small admixtures of oxygen were investigated by electrical measurements, the spatiotemporally resolved optical emission spectroscopy and surface charge diagnostics via the electro-optic Pockels effect. As already known, in pure helium a diffuse discharge is typically formed because of the significant role of the metastable species. However, even a very small oxygen admixture (0.025 vol.%) causes the transition to a filamentary mode as a result of the effective quenching of helium metastables by oxygen molecules. This effect was indicated by a significant decrease of N_2^+ the first negative system emission. The transition region was characterized by several Townsend-like discharge breakdowns becoming more and more unstable with an increasing O_2 admixture. The formation of the atmospheric pressure Townsend-like discharge was confirmed by the spatiotemporally resolved emission. The development of the surface charges agrees qualitatively and quantitatively well with the transported charge during the discharge breakdown calculated from the discharge current.

Keywords: barrier discharge, helium/oxygen mixture, surface charge

(Some figures may appear in colour only in the online journal)

1. Introduction

Barrier discharges (BDs) are widely used in many technological applications, e.g. ozone generation, material processing, light sources, destruction of pollutants, sterilization and other biomedical applications [1–3]. One crucial advantage of BDs is the possibility to generate the reactive species at atmospheric pressure. It is well-known that different discharge modes, namely a filamentary and a diffuse mode, can occur depending on the working gas, the frequency, the amplitude and the shape of the feeding voltage, the discharge gap width, the material of the dielectric barriers, and the geometry of the electrodes [1, 4]. The filaments are statistically distributed breakdown channels of several tens of nanoseconds duration. The filamentary mode is commonly observed e.g. in air, oxygen [1] and argon [5].

The homogeneously distributed diffuse discharge mode is classified as the so called atmospheric pressure glow-like discharge (APGD) and atmospheric pressure Townsend-like discharge (APTD) [6–8]. The characteristics of the APGD are narrow current pulses of a high current density in comparison to the APTD and a spatial structure similar to the low pressure glow discharge [6]. These properties are typical for the barrier discharge operated in helium [6] and neon [9]. The APTD is characterized by a relatively long current pulse duration with a small current density. The electric field is weakly disturbed by a small space charge formation [10]. The APTD is typical for a diffuse discharge operated in pure nitrogen [8].

The discharges operated in pure oxygen or in oxygen mixed with other gases play a crucial role especially in plasma chemistry and biomedicine. They are effective sources of radicals as oxygen atoms and ozone. However, it is quite inefficient to

generate a discharge in pure oxygen due to the higher power requirements in comparison e.g. to atomic gases. The influence of adding oxygen into the discharge was already studied e.g. for nitrogen [11, 12], neon [5] and argon [13]. The transition from the diffuse mode to the filamentary mode was observed in nitrogen and neon discharges. The transition to the filamentary mode in the case of the nitrogen discharge (1.1 mm discharge gap) occurs in the range of 0.05–0.1 vol.% O_2 admixture [12]. The microdischarge channel of about 1 mm in diameter has been formed between the electrodes (1 mm discharge gap) at 1 vol.% O_2 admixture in neon gas [5]. The transition from the diffuse mode to the filamentary mode is caused by the quenching of long-lived metastable states of parent gases by oxygen molecules [14, 15]. For various technical applications the detailed understanding of an influence of oxygen on the BDs modes and plasma characteristics is very important due to the determination of the optimal oxygen admixture to the parent gas.

The discharge operated in He/N_2 mixtures was investigated in [16–18]. Helium as a buffer gas maintains the gas temperature close to the room temperature due to its high thermal conductivity [19]. This is well suited for applications dealing with temperature-sensitive materials such as biological samples [20]. Both the APTD and the APGD can be achieved in any He/N_2 mixture at adequate discharge cell geometry and gap voltages [18]. The filamentary mode in He/N_2 mixture can be established by overvoltage. The surface charge measurement in the filamentary mode of barrier discharge generated in helium with 10 vol.% admixture of nitrogen was performed in [17]. It was shown that the microdischarges prefer a re-ignition on locations of surface charges accumulated during previous discharge breakdowns.

In this work, the barrier discharge in helium with small admixtures of oxygen (from 0.01 vol.% up to 1 vol.% of O_2) was investigated by means of electrical measurements in order to distinguish the discharge modes. Additionally, the spatiotemporally and spectrally resolved discharge emission was recorded in the diffuse discharge modes in order to compare the important processes ongoing in the discharge development in dependence of the oxygen admixture to helium. The phase resolved surface charge measurements can provide the insight into the surface processes and their influence on the discharge behaviour.

The paper is organized as follows: the experimental apparatus and used diagnostic techniques are described in section 2. The results and the discussions are presented in section 3. The conclusions are given in section 4.

2. Experimental set-up and diagnostic techniques

2.1. Discharge cell configuration and operating conditions

The used discharge cell is already well established [17, 18]. It consists of two parallel plane electrodes each covered with a different dielectric materials (see figure 1(b)). The grounded electrode is a polished aluminium mirror. Here, an undoped electro-optic $Bi_{12}SiO_{20}$ (BSO) crystal is mounted on the mirrors top side showing the Pockels effect which is applied for surface charge measurements. The driven electrode is a thin, transparent and electrically conductive ITO layer on the top side of a glass plate. The area A of the electrode, where the discharge operates, is 1.77 cm^2. The gap distance of 1 mm between the dielectrics is realised by gap spacers made of PEEK polymer. Two sidewise oppositely located orifices enable the optical diagnostics. Perpendicular to both orifices a third one is used for the gas flow controlled by a multi gas flow controller (MKS 647c). The working gases are pure helium (<10 ppm nitrogen impurities) and helium with small oxygen admixture (up to 1 vol.% of O_2). The discharge is operated at a gas pressure of 500 mbar and is sustained in a flowing regime (flow up to 100 sccm) in order to ensure a constant helium/oxygen mixture during the experiment.

2.2. Power supply and electrical measurements

The driven electrode is connected to a high voltage power amplifier (Trek 615-10) which amplifies the signal of the function generator (SRS DS345) by a factor of 1000 (see figure 1(b)). The frequency of an applied sine wave voltage is $f = 2$ kHz. Depending on the gas mixture, the applied voltage amplitude is varied from 0.3 kV to 2.7 kV measured by a 1000:1 high voltage probe (Tektronix P6105A). The total current is measured with a resistor ($R = 100\ \Omega$). A switch allows to use a capacitor of $C = 1$ nF instead of the resistor to measure the transported charge during the discharge breakdown. All electrical signals are recorded by an digital oscilloscope (Tektronix TDS3034B).

2.3. Surface charge measurements

The experimental set-up for the measurement of surface charges via the electro-optic Pockels effect [21] is shown in figure 1(a). The BSO crystal is homogeneously illuminated by the combination of a LED light source ($\lambda = 634$ nm), a Koehler illumination system consisting of lens 1 and 2 and two apertures, and a telescopic system (lens 3 and 4). A polarization filter placed in between the Koehler illumination changes the polarization state of the LED light from unpolarized to linearly polarized. After passing through the Koehler illumination system, the LED light beam is reflected by a beam splitter into the direction of the discharge cell. Passing the $\lambda/8$ wave plate the light becomes elliptically polarized. Since the crystal is birefringent in the presence of an electrical field (caused by the applied voltage as well as deposited surface charges), the ellipticity of the LED light changes after passing through the crystal. Due to the reflection on the aluminium mirror, the light beam passes the crystal twice. The reflected light passes again the optical elements before being detected by a CCD high speed camera. In front of the camera, a linear polarization filter and coloured filter are placed. The polarization filter, orientated perpendicular to the filter in the Koehler illumination system, is necessary to measure changes of the ellipticity caused by an electric field. The coloured filter (transparent from 620 to 640 nm) is used to exclude the light emission from the discharge. The spatial resolved surface charge density is determined by analysing the measured light intensity taken

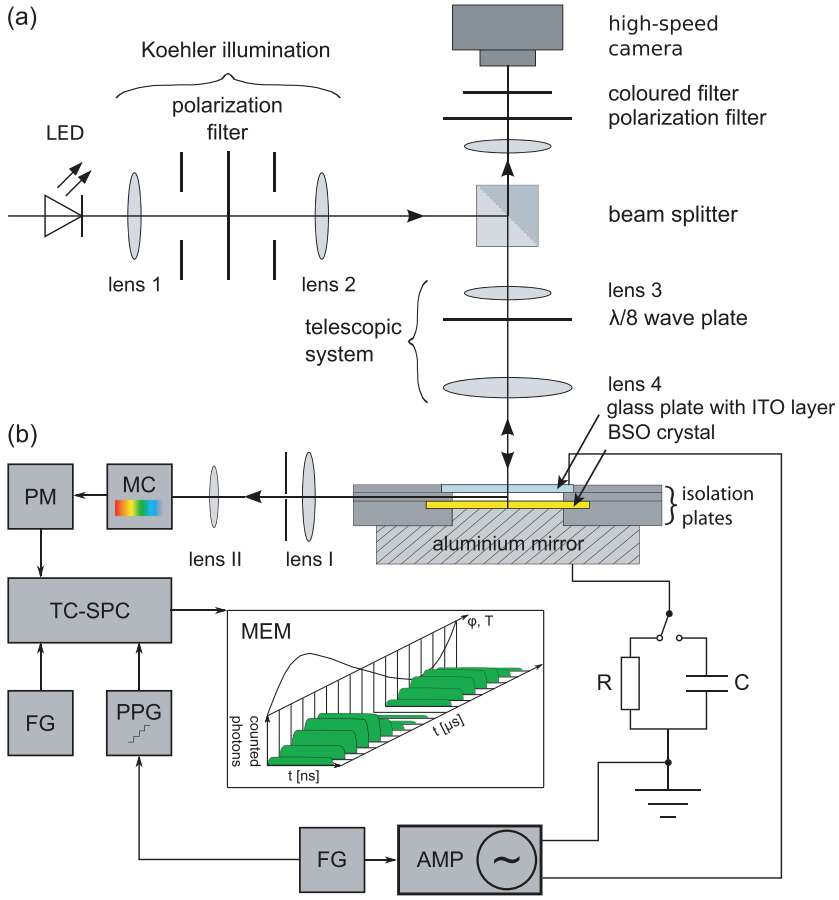

Figure 1. Scheme of the experimental setup: (a) the surface charge diagnostics, and (b) the spatiotemporally resolved optical emission spectroscopy in combination with electrical measurements performed at one discharge cell configuration. Abbreviations: AMP—amplifier, FG—function generator, MC—monochromator, MEM—memory, PM—photomultiplier, PPG—pulse pattern generator, TC-SPC—time-correlated single photon counting.

with deposited surface charges and as the reference *without* any surface charges. This is necessary to cancel out the contribution of the applied voltage. The latter is recorded when only the external voltage is applied and no discharge has been ignited. For further details see e.g. [17, 18, 22].

2.4. Spectroscopic measurements

The radiation emission from the diffuse barrier discharge is investigated by the spatiotemporally resolved optical emission spectroscopy (OES). The optical radiation from the discharge volume is focused by the lens I (see figure 1(b)) onto a vertically movable 0.1 mm slit which enables the spatial resolved investigation of the whole discharge gap; the spatial step of the measurement was 0.05 mm. The lens II focuses the slit image onto an optical fibre connected to a monochromator (spectral resolution 0.1 nm). The optical emission signal is converted by a photomultiplier tube (PM) into an electrical signal which is processed by a time-correlated single photon counting (TC-SPC) module. A pulse pattern generator (PPG), which controls the memory segment allocation of the SPC device, is triggered by a function generator defining also the sinusoidal voltage feeding the discharge (see figure 1(b)). Thereby, the photon counting is synchronized with the phase of the applied voltage. The temporal resolution of 1.4 μs is defined by the temporal window of one channel (in total 64 or 128 channels) for the photon counting by the TC-SPC. The result is a spatiotemporally resolved development of the discharge light emission. For further details see [17, 22].

3. Results and discussion

3.1. Discharge operation

Different operating modes of the BD can be generated in pure helium and helium with small admixtures of oxygen depending on the amplitude of the sinusoidal feeding voltage (see figure 2). The minimal voltage amplitude to sustain the discharge rises with an increasing oxygen admixture. This is due to the effective consumption of the bulk electron energy in excitation of oxygen vibrational-rotational molecular states and in dissociation processes not directly contributing to the gas ionization [23]. Additionally, the electron energy distribution function is changed by electron attachment processes generating negative oxygen ions. For the gap width of 1 mm, the APTD is formed in pure helium [22]. Also, this discharge mode occurs in both half periods of the applied voltage with a very small admixture of oxygen (up to 0.025 vol.%). Admixtures of more oxygen cause a transition from the APTD to the filamentary mode only in the positive half period. Most likely, this is

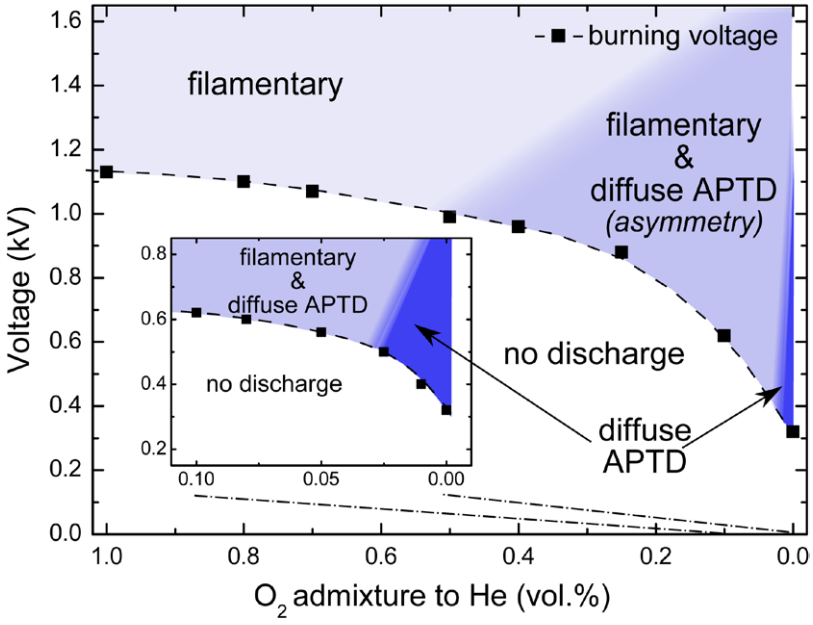

Figure 2. Existence diagram for the filamentary and diffuse barrier discharges depending on the oxygen admixture to helium.

due to the different dielectrics with different secondary emission coefficients γ [18]. The transition to the filamentary mode is attributed to an effective quenching of long-lived metastable helium species by oxygen [14]. The metastable species play an important role in generating the seed electrons by stepwise ionization and chemoionization [24]. Also, the strong dependence of $\alpha(E/N) - \beta(E/N)$ on reduced field strength E/N for oxygen, where α is the Townsend ionization coefficient and β the second Townsend coefficient describing the attachment probability, is important for the formation of the filamentary mode. Only a small overvoltage can lead to a large increase in the number of charge carrier avalanches [5]. About 0.5 vol.% oxygen admixture to helium results in a filamentary discharge in both half periods. The electrons are no more available before the discharge ignition due to a high electron attachment and it is more difficult to ignite and maintain the discharge. The influence of the electron attachment reactions generating negative ions becomes important with a further increasing admixture of oxygen [25].

The temporal development of the net current over one discharge cycle was recorded for the indication of the different discharge modes. The minimal applied voltage amplitude for a discharge operated in pure helium is 330 V. In this case, only one current pulse of diffuse mode is observed. The number of current pulses rises with an increasing voltage amplitude for pure helium as well as with increasing oxygen admixture (see figure 3). In each case, the applied voltage amplitude amounts to 940 V. Several current pulses per half-cycle were interpreted as current oscillation [10, 11, 26, 27]. The current oscillations can be caused by a lag between the ion production nearby the anode and the subsequent ion-electron emission on the cathode [10]. The magnitude of subsequent current pulses decreases and the duration of pulses increases. Finally, the filamentary mode occurs when adding at least 0.05 vol.% of oxygen to helium. This is indicated by a considerable increase in the net current amplitude of the first breakdown in the positive half period of the applied voltage (see e.g. figure 3(c)).

Figure 4 shows in detail the temporal evolution of the net current in the negative half period. Here, the cathode is covered by the BSO crystal whose surface has a significantly lower secondary electron emission coefficient γ compared with the glass plate [28]. The diffuse discharge mode is therefore more stable in the negative half period for a higher oxygen admixture then in the positive one. The first breakdown occurs just before the inversion of the applied voltage polarity and it is not the strongest one. The maximum current density is reached later in the half period, when the voltage (the absolute value) is increasing up to the maximum. The duration of the current pulses, described as the full width at half-maximum (FWHM) value, decreases with an increasing amount of oxygen (see figure 5).

3.2. Optical emission spectra

The spectra of the optical emission originating from the diffuse discharge in pure helium (with <10 ppm impurities of nitrogen) and helium with an admixture of 0.1 vol.% oxygen are shown in figures 6 and 7. Both spectra are identically scaled. The highest measured intensity for the pure helium discharge corresponds to the 0–0 transition of nitrogen molecular ion N_2^+ of the first negative system (FNS, $N_2^+(B\ ^2\Sigma_u^+)_{v'=0} \rightarrow N_2^+(X\ ^2\Sigma_g^+)_{v''=0}$) at 391 nm. In the helium discharge with nitrogen impurities, the FNS is mainly induced by Penning ionization of nitrogen by helium metastable atoms

$$N_2(X) + He^m \longrightarrow N_2^+(B\ ^2\Sigma_u^+) + e + He(1\ ^1S). \qquad (1)$$

The second positive system of nitrogen (SPS) at 337 nm ($N_2(C\ ^3\Pi_u)_{v'=0} \rightarrow N_2(B\ ^3\Pi_g)_{v''=0}$) is present in the spectrum, too. The SPS upper state $N_2(C\ ^3\Pi_u)$ is mainly populated by direct excitation via electron impact [29]

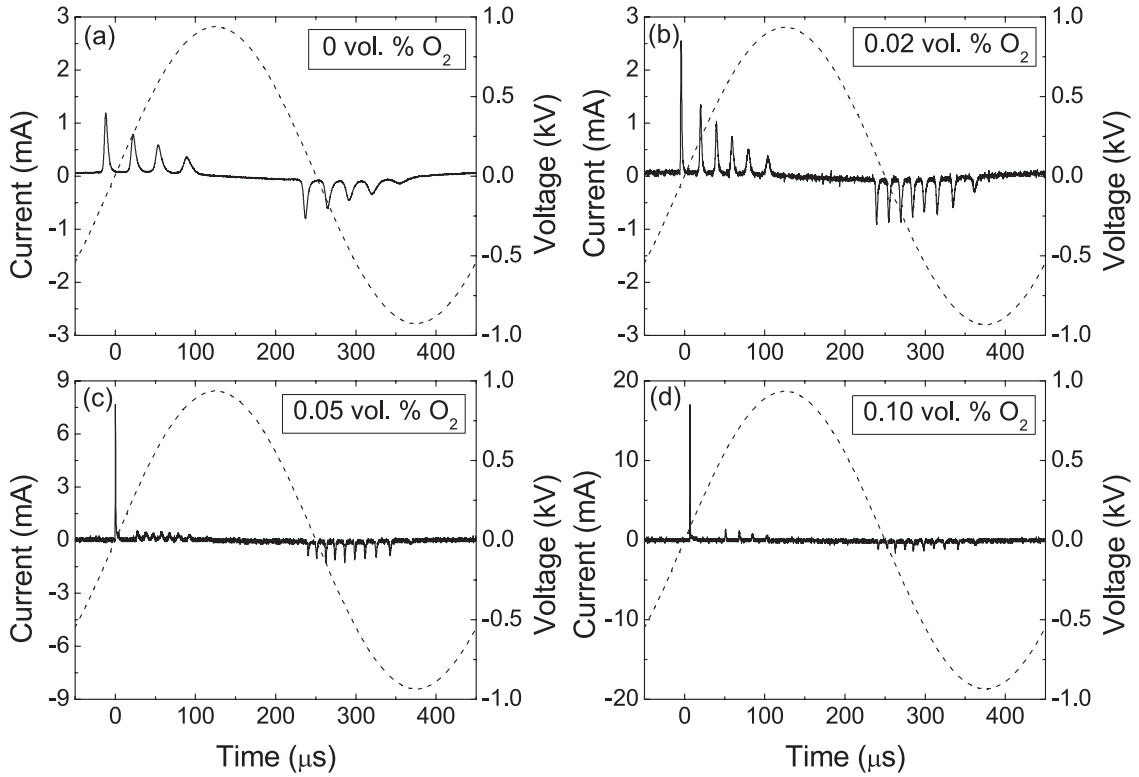

Figure 3. Applied voltage and discharge net current for helium barrier discharge with (a) no oxygen admixture, (b) 0.02 vol.%, (c) 0.05 vol.%, and (d) 0.10 vol.% O_2 admixture to helium. The applied voltage amplitude is 940 V.

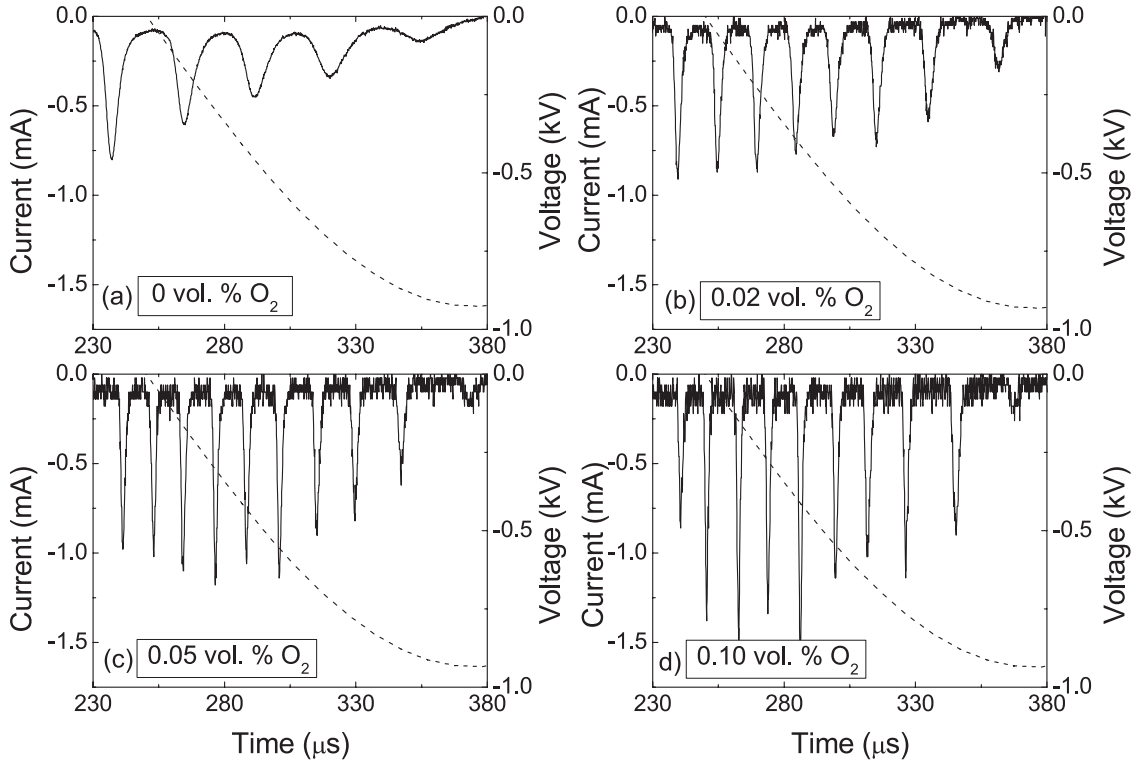

Figure 4. Temporal evolution of the net current in the negative half period (diffuse discharge mode) with (a) no oxygen admixture, (b) 0.02 vol.%, (c) 0.05 vol.%, and (d) 0.10 vol.% O_2 admixture to helium. The applied voltage amplitude is 940 V.

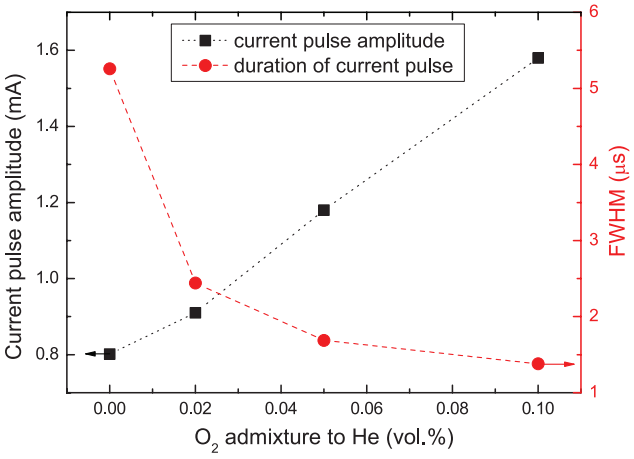

Figure 5. Amplitude and duration (FWHM) of the most intensive discharge current pulse for the diffuse discharge in the negative half period of the applied voltage depending on the oxygen admixture to helium.

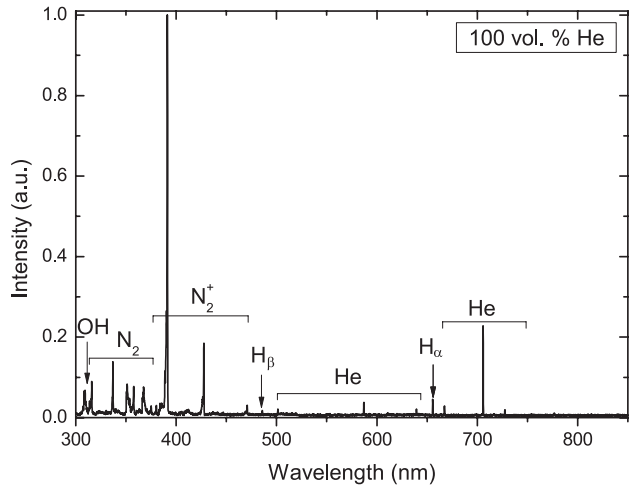

Figure 6. Overview spectrum of the barrier discharge in pure helium. Intensities are normalized on the FNS of singly ionized nitrogen at 391 nm.

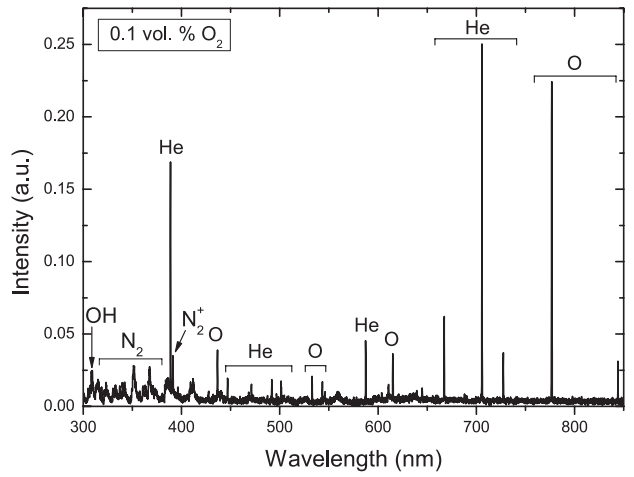

Figure 7. Overview spectrum of the barrier discharge operated in 99.9 vol.% helium and 0.1 vol.% oxygen (in the scale of figure 6, notice the different maximum intensity).

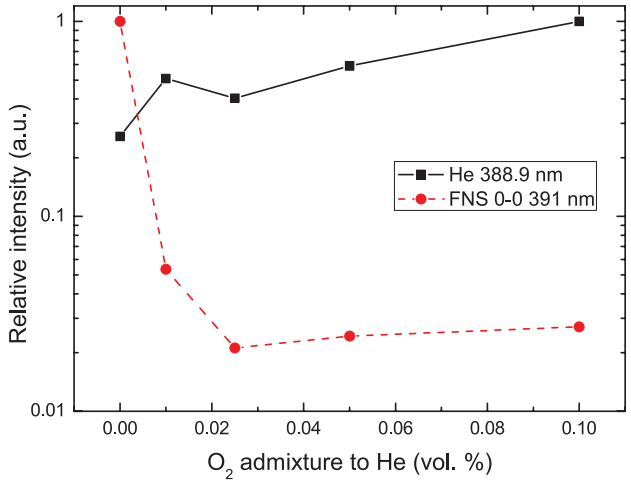

Figure 8. Maximum intensities of the FNS of nitrogen at 391 nm and helium 388.9 nm line in dependence on the oxygen admixture.

$$N_2(X) + e \longrightarrow N_2(C\ ^3\Pi_u) + e. \quad (2)$$

The OH band $(A\ ^2\Sigma^+)_{v'=0} \rightarrow (X\ ^2\Pi)_{v''=0}$ at 311 nm and H_α, H_β lines are also detected. The atomic lines of helium are not so intensive, except line $3\ ^3S \rightarrow 2\ ^3P$ at 706.5 nm.

The spectrum of the diffuse discharge with 0.1 vol.% oxygen admixture to helium is very different in comparison to the pure helium discharge (see figure 7). Only a small admixture of oxygen changes dramatically the plasma chemistry. The radiation of the impurities (OH, H, N_2) is almost completely suppressed, only the FNS of nitrogen is still detectable. The intensities of several atomic helium lines are increased with an increasing oxygen content probably due to the elimination of the quenching of the helium excited states by nitrogen species (see further). The most rapid increase is observed for 388.9 nm line ($3\ ^3P \rightarrow 2\ ^3S$, the ^3S state being metastable). The enhancement of this line in the helium/oxygen discharge spectrum was also observed in [30] for a BD operated in He + 1 vol.% O_2 gas mixture at 33 mbar. Additionally, the lines of atomic oxygen are significantly present in the spectrum. Even for a small oxygen admixture of 0.1 vol.%, the line $3\ ^5P \rightarrow 3\ ^5S$ (the ^5S state being metastable) at 777 nm is almost as intensive as the helium 706.5 nm line. The excited state $3\ ^5P$ of atomic oxygen is produced by the quenching of helium metastables by molecular oxygen [31]

$$O_2(X) + He^m \longrightarrow O(3\ ^5P) + O + He(1\ ^1S). \quad (3)$$

The development of the intensities of the helium line at 388.9 nm and the FNS of nitrogen, normalized on the respective maximum, is presented in the range 0–0.1 vol.% O_2 admixture at an applied voltage amplitude of 940 V in figure 8 (semi-logarithmic scale). The helium line emission increases exponentially with increasing oxygen concentration. However, the FNS emission drops to 5% of its maximal intensity in the pure helium discharge at 0.01 vol.% of oxygen admixture. Adding more oxygen results in a less rapid decrease of the FNS. The intensity is comparable with the background signal from 0.025 vol.% of oxygen admixture, therefore any observable trend is then within the experimental error.

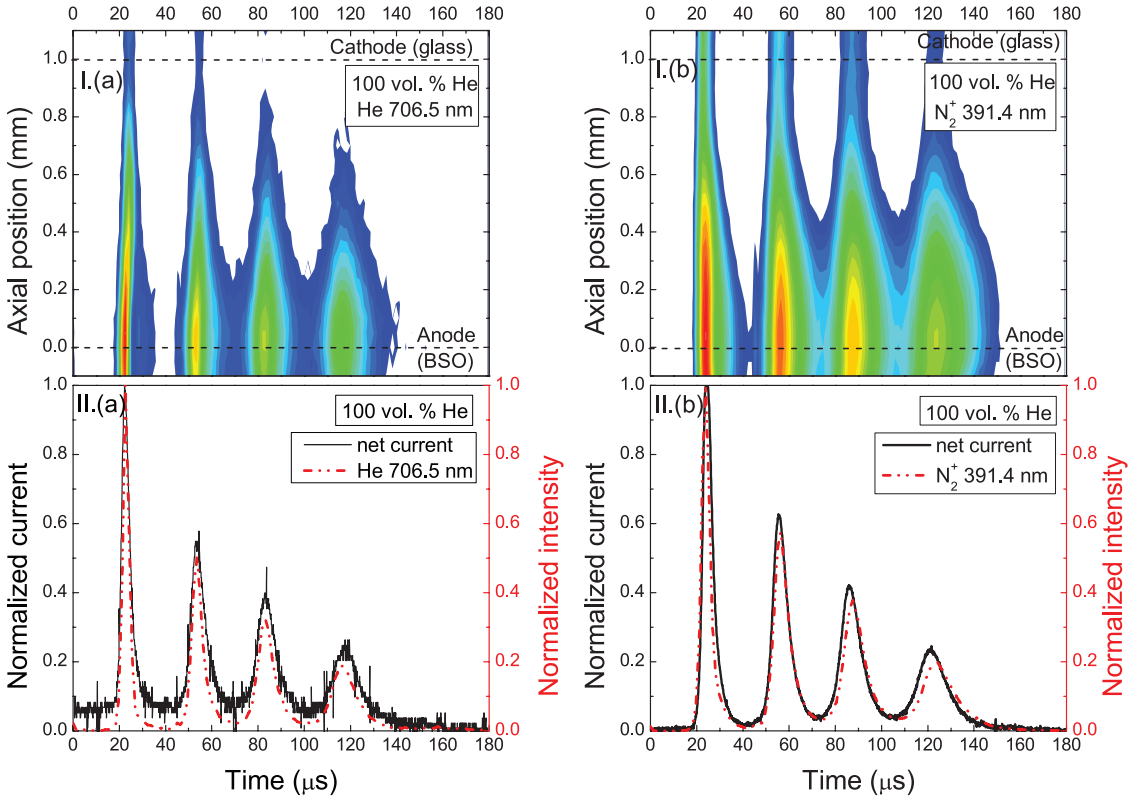

Figure 9. I. Spatiotemporally resolved emission from the diffuse helium discharge (impurities <10 ppm of nitrogen): (a) 706.5 nm He line, (b) the 0–0 band head of the N_2^+ FNS at 391 nm. The applied voltage amplitude is 910 V. II. Correlation between discharge net current and temporal development of discharge emission: (a) 706.5 nm He line, (b) the 0–0 band head of the N_2^+ FNS at 391 nm. Both, current and intensity, are normalized on their maximum. The radiation emission at the electrode positions is caused by the reflection on the transparent dielectric layers.

The decrease of the FNS intensity is probably due to the decrease of the electron temperature with adding oxygen into a pure helium discharge [32–34]. The electrons loose their energy in reactions with oxygen species such as ionization and dissociation of O_2 and excitation of vibrational-rotational O_2 states [23]. Then the electrons do not have sufficient energy to populate high-energetic helium metastable states ($\mathcal{E} \sim 20$ eV). The helium metastable atoms are also more effectively quenched by oxygen molecules than by nitrogen molecules due to the lower ionization energy of O_2 [14, 35]. Therefore, the crucial production process (1) of the FNS is attenuated.

Furthermore, the excited state of the nitrogen molecular ion $N_2^+(B\,^2\Sigma_u^+)$ is quenched by oxygen molecules as well [36]. However, the concentration of helium atoms in the discharge is much higher than the concentration of oxygen molecules. There are also other production channels of the FNS, namely ionization by electron impact from the ground state of N_2, direct electron excitation of N_2^+, or charge transfer from helium dimer ions He_2^+ [10]. Therefore the FNS is still observable in the spectrum.

3.3. Spatiotemporally resolved discharge radiation

The optical emission evolution in the diffuse discharge operated in pure helium and in helium with 0.1 vol.% oxygen admixture has been investigated by the single photon counting technique. The results are presented in figures 9 and 10. The FNS 0–0 band head at 391 nm and the helium line 706.5 nm were observed in the discharge operated in pure helium (see figure 9). The applied voltage amplitude was 910 V. The FNS emission was weak in the discharge with 0.1 vol.% oxygen admixture. Therefore, only the helium line at 706.5 nm as well as the oxygen atomic line at 777 nm were investigated (see figure 10). The applied voltage amplitude was increased up to 940 V. The temporal development of the net current and the optical emission intensity of He, N_2^+, and O are presented below the colour maps for comparison. The temporal intensity profiles were determined as the integral of the spatiotemporal emission development over the discharge gap.

Both discharges, in pure helium and helium with oxygen admixture, can be characterized by a maximum emission intensity in front of the anode. In combination with the duration of the current pulses of several tens of microseconds, these results confirm the generation of the APTD as shown in [17, 18] for He/N_2 mixtures. The temporal development of both emissions correlates with the current pulses of the accordant discharge breakdown. The emission starts in the moment when the electron density increases and the atoms are excited into the upper levels or ionized by energetic electrons. The excess of energy is then released in form of spontaneous emission. The radiative lifetimes of the upper state of N_2^+ 391 nm, He 706.5 nm and O 777 nm line are 62 ns [36], 64 ns [37] and 170 μs [38], respectively. The effective lifetimes are even shorter due to the collisional quenching [31].

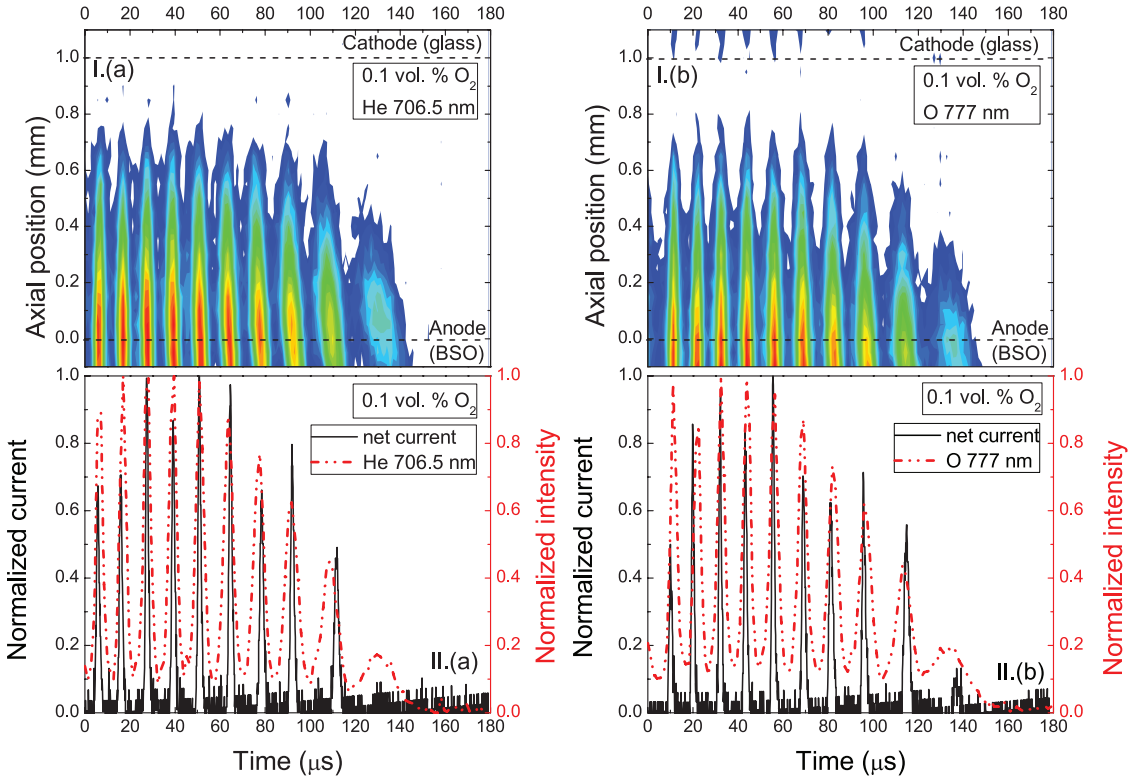

Figure 10. I. Spatiotemporally resolved emission from the diffuse helium discharge with 0.1 vol.% oxygen admixture: (a) 706.5 nm He line, (b) 777 nm O line. The applied voltage amplitude is 940 V. II. Correlation between discharge net current and temporal development of discharge emission: (a) 706.5 nm He line, (b)777 nm O line. Both, current and intensity, are normalized on their maximum. The radiation emission at the electrode positions is caused by the reflection on the transparent dielectric layers.

The ionization ratio of the nitrogen molecules is enhanced by helium metastables and therefore also the emission of the FNS in the region with low electron density [39, 40]. Thus, the FNS light comes from a larger volume in the discharge gap than the helium light in a pure helium discharge (figure 9). The radiative He($3\,^3$S) state is dominantly populated through electron impact excitation from the helium ground state as known from the literature [31]. Therefore, the intensity of the helium 706.5 nm line is maximal at the anode as expected for the APTD [6, 7]. The short gap distance of 1 mm prevents the evolution of the glow-like discharge.

The discharge becomes unstable with increasing oxygen admixture to helium. Therefore, the emission pulses are broader then the current pulses (figure 10). This is caused by the different collecting time periods of these signals. Whereas the emission signal was collected during several hours, the current signal was averaged only during several voltage periods. The difference in emission and current signal width is therefore also an indication of the discharge stability.

3.4. Phase resolved surface charge measurement

The results of the phase resolved and laterally averaged surface charge measurement are presented in figure 11 (part I) for pure helium and helium with 0.025 vol.% oxygen admixture. The temporal development of the net current and the transported charge calculated from the net current are also shown. The net current is determined from the measured total current by subtracting the displacement current. The latter is obtained from the applied voltage and the capacitance of the discharge cell. The temporal evolution of global transported charge density σ is calculated via integration of the net current $I(t)$

$$\sigma(t) = \frac{1}{A}\int_0^t I(t')\,\mathrm{d}t', \tag{4}$$

A denotes the area of the electrode where the discharge operates.

The applied voltage amplitude is decreased to 560 V in pure helium in order to ensure the stability of all the subsequent discharge breakdowns during the measurement. Under these conditions the discharge operates in the diffuse mode. As can be seen from the net current, three and four current pulses were observed in the positive and negative half period, respectively. Before the current pulses appear, the surface charges originating from the previous discharge breakdown are deposited on the BSO crystal. When the discharge ignites, the initial surface charge polarity changes to the opposite one by the accumulation of the transported charge on the dielectrics surface. The surface charge density remains constant between the discharge breakdowns. This behaviour was also observed and discussed in detail in [17]. The calculated transported charge corresponds very well with the deposited charge measured via the Pockels effect. The absolute value of the surface charge density is $|\sigma_+| = 1.26$ nC cm^{-2} for the positive half period and $|\sigma_-| = 2.18$ nC cm^{-2} for the negative one. Most likely, the asymmetry in both half cycles can be explained by the different dielectric materials, namely glass and BSO. The total transported charge is $\Delta Q = A \cdot \Delta\sigma = 6.1$ nC.

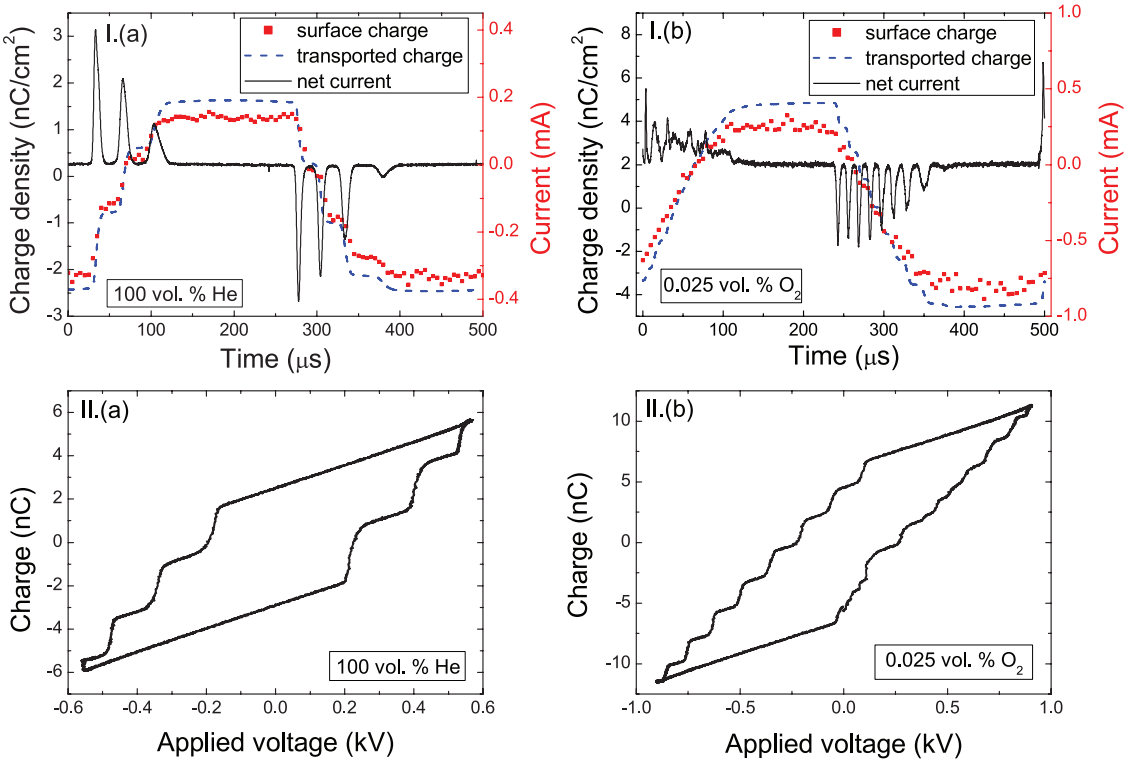

Figure 11. I. Phase resolved measurement of the laterally averaged surface charge density (squares) with the corresponding net current (solid line) and with the surface charge calculated from the net current (dashed line) over one period for (a) pure helium at the applied voltage amplitude of 560 V, (b) helium with 0.025 vol.% oxygen admixture at the applied voltage amplitude of 910 V. II. $Q - U$ diagrams, (a), (b) see I. part.

The temporal development of the surface charge density for the discharge in helium with 0.025 vol.% oxygen admixture shows in general the same behaviour. The applied voltage amplitude was 910 V. In the positive half period the discharge operates in the filamentary mode and in the negative one in the diffuse mode under these conditions. In the positive half period a large amount of filaments ignite over the entire discharge region as long as the applied voltage is rising. However, the temporal resolution of the measurement (5 μs) is long in comparison to the time between the discharge breakdowns. Therefore, the surface charge density in the positive half period is not increasing stepwise because the time intervals with constant surface charge density are not detected. The temporal resolution is limited by the camera exposure in compromise with a sufficient detection signal for measurement procedure. The calculated transported charge is in a good agreement with the measured deposited charge. The absolute value of the surface charge density is $|\sigma_+| = 3.80$ nC cm^{-2} for the positive half period and $|\sigma_-| = 3.65$ nC cm^{-2} for the negative one. This corresponds to the total transported charge of about 13.3 nC.

The discrepancy between the surface charge measurement and the calculated transported charge in both cases is probably due to the discharge expansion outside the small area of BSO surface which is analysed by the surface charge diagnostics. The multiple discharge breakdowns show a radial development [27]. Presumably, the surface charges have already covered the entire electrode area after the first breakdown. Therefore, the last breakdowns in the same half period do not occur within the small centred observation area of the surface charge measurement. Hence, the total amount of the transported charge is larger than the detected surface charge density.

The $Q - U$ diagrams represent another method to determine the transported charge (see figure 11 part II). The steep slopes of the $Q - U$ diagrams are connected with the transported charge in each discharge breakdown. For the discharge operated in pure helium at the applied voltage amplitude of 560 V the estimated total transported charge is $|\Delta Q| \approx (2.5 + 1.9 + 1.5)$ nC $= 5.9$ nC in the positive half period and $|\Delta Q| \approx (1.9 + 1.8 + 1.6 + 0.5)$ nC $= 5.8$ nC in the negative half period. In the case of the helium discharge with an admixture of 0.025 vol.% of oxygen at the applied voltage amplitude of 910 V the estimation of the total transported charge is $|\Delta Q| \approx (1.7 + 1.8 + 1.7 + 1.9 + 1.9 + 1.6 + 1.5 + 1.2)$ nC $= 13.3$ nC in the negative half period. The single current pulses cannot be clearly distinguished in the positive half period due to the filamentary discharge mode. The results are in a good agreement with the surface charge measurement.

4. Conclusion

This work is focused on the investigation of the barrier discharge in helium with small oxygen admixtures. The different discharge modes are studied in dependence on the various oxygen admixture and an applied voltage amplitude. The transition from the diffuse mode into the filamentary one is observed at a very low oxygen content (at 0.025 vol.%). Most

likely, due to the asymmetric discharge cell configuration the filamentary mode occurs firstly only in the positive half period. In the negative half period the APTD with characteristic current oscillations is established. The filamentary mode in both half periods is achieved at higher oxygen admixtures (about 0.5 vol.%). A similar behaviour was observed also in N_2/O_2 mixtures [11] where the discharge was still diffuse up to 0.05 vol.% of O_2 admixture at 1.1 mm discharge gap. The diffuse mode in He/O_2 mixture is no more sustainable at higher oxygen amount unlike the discharge generated in He/N_2 mixture [16]. Only the APTD mode is observed in the discharge cell configuration described here. The emission maximum is detected near the anode by means of spatiotemporally resolved optical emission spectroscopy. The number of current peaks per half period is increasing and their duration is decreasing with an increasing amount of oxygen in the discharge.

Further, the optical emission spectra are recorded to determine the main excited species and to investigate the crucial processes ongoing in the discharge. The Penning ionization of the nitrogen molecules by helium metastables dominates in the pure helium discharge. By adding O_2 the helium metastable atoms as well as the nitrogen excited species are very effectively quenched by oxygen molecules. Therefore, the radiation emission from N_2 and N_2^+ is almost diminished. O_2 molecules dissociate during these processes and the light emission of the oxygen atoms is then observed in the spectrum.

The phase resolved surface charge measurement over one discharge cycle by the electro-optic Pockels effect is also performed in this gas mixture. The calculated transported charge is in agreement with the measured deposited charge. The results of the surface charge measurements correspond well with former results in He/N_2 mixtures [17].

Acknowledgments

The work was supported by the Collaborative Research Center Transregio 24 'Fundamentals of Complex Plasmas' funded by the Deutsche Forschungsgemeinschaft, the grant No GA13-24635S of the Czech Science Foundation, the project 'R&D center for low-cost plasma and nanotechnology surface modifications' (No CZ.1.05/2.1.00/03.0086) funded by the European Regional Development Fund, and the project LO1411 (NPU I) funded by the Ministry of Education, Youth and Sports of the Czech Republic.

References

[1] Kogelschatz U 2003 *Plasma Chem. Plasma Process.* **23** 1–46
[2] Wagner H E, Brandenburg R, Kozlov K, Sonnenfeld A, Michel P and Behnke J 2003 *Vacuum* **71** 417–36
[3] Fridman G, Friedman G, Gutsol A, Shekhter A B, Vasilets V N and Fridman A 2008 *Plasma Process. Polym.* **5** 503–33
[4] Okazaki S, Kogoma M, Uehara M and Kimura Y 1993 *J. Phys. D: Appl. Phys.* **26** 889
[5] Kozlov K V and Wagner H E 2007 *Contrib. Plasma Phys.* **47** 26–33
[6] Massines F, Rabehi A, Decomps P, Gadri R B, Segur P and Mayoux C 1998 *J. Appl. Phys.* **83** 2950
[7] Massines F, Gherardi N, Naudé N and Ségur P 2005 *Plasma Phys. Control. Fusion* **47** B577
[8] Gherardi N, Gouda G, Gat E, Ricard A and Massines F 2000 *Plasma Sources Sci. Technol.* **9** 340
[9] Trunec D, Brablec A and Buchta J 2001 *J. Phys. D: Appl. Phys.* **34** 1697
[10] Golubovskii Y B, Maiorov V A, Behnke J and Behnke J F 2003 *J. Phys. D: Appl. Phys.* **36** 39
[11] Brandenburg R, Maiorov V A, Golubovskii Y B, Wagner H E, Behnke J and Behnke J F 2005 *J. Phys. D: Appl. Phys.* **38** 2187
[12] Kozlov K V, Brandenburg R, Wagner H E, Morozov A M and Michel P 2005 *J. Phys. D: Appl. Phys.* **38** 518
[13] Snyder H R and Anderson G 1998 *IEEE Trans. Plasma Sci.* **26** 1695–9
[14] Myers G and Cunningham A 1977 *J. Chem. Phys.* **67** 3352–9
[15] Velazco J E, Kolts J H and Setser D W 1978 *J. Chem. Phys.* **69** 4357
[16] Brandenburg R, Navrátil Z, Jánský J, St'ahel P, Trunec D and Wagner H E 2009 *J. Phys. D: Appl. Phys.* **42** 085208
[17] Bogaczyk M, Wild R, Stollenwerk L and Wagner H E 2012 *J. Phys. D: Appl. Phys.* **45** 465202
[18] Tschiersch R, Bogaczyk M and Wagner H E 2014 *J. Phys. D: Appl. Phys.* **47** 365204
[19] Kabouzi Y, Calzada M D, Moisan M, Tran K C and Trassy C 2002 *J. Appl. Phys.* **91** 1008–19
[20] Liu D X, Rong M Z, Wang X H, Iza F, Kong M G and Bruggeman P 2010 *Plasma Process. Polym.* **7** 846–65
[21] Yariv A 1989 *Quantum Electronics* (New York: Wiley)
[22] Bogaczyk M, Sretenović G B and Wagner H E 2013 *Eur. Phys. J.* D **67** 1–11
[23] Léveillé V and Coulombe S 2006 *Plasma Process. Polym.* **3** 587–96
[24] Lee D, Park J, Hong S and Kim Y 2005 *IEEE Trans. Plasma Sci.* **33** 949–57
[25] Descoeudres A, Sansonnens L and Hollenstein C 2003 *Plasma Sources Sci. Technol.* **12** 152
[26] Akishev Y S, Demyanov A V, Karalnik V B, Pankin M V and Trushkin N I 2001 *Plasma Phys. Rep.* **27** 164
[27] Mangolini L, Orlov K, Kortshagen U, Heberlein J and Kogelschatz U 2002 *Appl. Phys. Lett.* **80** 1722–4
[28] Stollenwerk L and Stroth U 2011 *Contrib. Plasma Phys.* **51** 61–7
[29] Howorth J R 1972 *J. Phys. B: At. Mol. Opt. Phys.* **5** 402
[30] Chiper A S, Rusu B G, Nastuta A V and Popa G 2009 *IEEE Trans. Plasma Sci.* **37** 2098–102
[31] Liu D W, Iza F and Kong M G 2009 *Appl. Phys. Lett.* **95** 031501
[32] Hagelaar G J M and Pitchford L C 2005 *Plasma Sources Sci. Technol.* **14** 722
[33] Alves L L *et al* 2013 *J. Phys. D: Appl. Phys.* **46** 334002
[34] Pitchford L C, Bordage M C, Hagelaar G J M, Pancheshnyi S, Biagi S F, Itikawa Y, Kochetov I, Napartovich A and Phelps A V 2012 *Proc. 65th Annual Gaseous Electronics Conf.* (*Austin, Texas, 22–26 October 2012*)
[35] Schmeltekopf A L and Fehsenfeld F C 1970 *J. Chem. Phys.* **53** 3173–7
[36] Pancheshnyi S, Starikovskaia S and Starikovskii A 1998 *Chem. Phys. Lett.* **294** 523–7
[37] Drake G 2006 NIST atomic spectra database (http://physics.nist.gov/asd.)
[38] Wells W C and Zipf E C 1974 *Phys. Rev.* A **9** 568–70
[39] Luo H, Liang Z, Lv B, Wang X, Guan Z and Wang L 2007 *Appl. Phys. Lett.* **91** 221504
[40] Massines F, Ségur P, Gherardi N, Khamphan C and Ricard A 2003 *Surf. Coat. Technol.* **174–5** 8–14

Eur. Phys. J. D **54**, 259–264 (2009)
DOI: 10.1140/epjd/e2009-00013-1

THE EUROPEAN PHYSICAL JOURNAL D

Regular Article

The influence of electrode gap width on plasma properties of diffuse coplanar surface barrier discharge in nitrogen

J. Čech[a], P. Šťahel, and Z. Navrátil

Department of Physical Electronics, Masaryk University, Kotlarska 2, Brno, 611 37, Czech Republic

Received 14 September 2008 / Received in final form 10 December 2008
Published online 6 February 2009 – © EDP Sciences, Società Italiana di Fisica, Springer-Verlag 2009

Abstract. In this work we have studied the influence of electrode gap width (inter-electrode distance) on plasma properties of the diffuse coplanar surface barrier discharge. The outer conditions and discharge configuration can substantially influence properties of the discharge. Better understanding of these effects can lead to optimization of the discharge parameters for industrial applications. In this work the discharge was operated in nitrogen at atmospheric pressure. The electrode gap width was varied in the range from 0.6 to 2.2 mm. The input voltage, electrode temperature and gas flow was kept constant for all cases. Plasma parameters were studied by the means of time and space resolved optical emission spectroscopy and oscilloscopic measurements. These measurements gave us time and space distribution of discharge luminosity (e.g. intensities of second positive and first negative systems of nitrogen) and 1D-spatial profiles of rotational and vibrational temperature of nitrogen.

PACS. 52.50.Dg Plasma sources – 52.25.-b Plasma properties – 52.70.Ds Electric and magnetic measurements – 52.70.Kz Optical (ultraviolet, visible, infrared) measurements

1 Introduction

Fast in-line plasma treatment of fabrics or large area substrates is of great importance in industry nowadays. The utilization of different types of dielectric barrier discharges (DBD) operated at atmospheric pressure [1] for these applications has been made with different success. The main problem of processing of substrates in most of DBD configurations stands is the inhomogeneity of DBD at atmospheric pressure (formation of plasma microchannels). This results in inhomogeneous treatment of the substrates and unintentional pin-holing of the substrates at high power densities that are necessary for rapid treatment.

These drawbacks are reduced in the diffuse coplanar surface barrier discharge (DCSBD), where plasma is generated in thin layer above the surface of dielectric and plasma microchannels are oriented parallel to dielectric surface. Due to small distance between electrodes the microchannel part of the discharge can be suppressed in order to increase the homogeneity of the treatment and suppress the pin-hole effects. Furthermore, the plasma microchannels of DCSBD move rapidly along the surface, which improves the homogeneity of the treatment [2,3]. For better utilization of the DCSBD for industrial purposes the influence of outer physical conditions and discharge geometry on the plasma parameters has to be studied.

In this paper the influence of electrode gap width on the plasma parameters of DCSBD with standard, multimicrodischarge, configuration was studied. 1D-spatial profiles of vibrational and rotational temperatures were obtained using spatially resolved spectroscopy. The rotational temperature was calculated from fully resolved second positive system of nitrogen (SPS) band 0-0 (337.1 nm). Vibrational temperature was estimated from SPS band 0-2 (380.5 nm). Rotational as well as vibrational temperature profiles were correlated with intensity profile of the second positive system of nitrogen. Time-space maps of intensities of second positive system of nitrogen (SPS – 337.1 nm) and first negative system of nitrogen (FNS – 391.5 nm) were also estimated. In addition to the optical measurements the influence of electrode gap width and input voltage frequency on the ignition and extinction voltages of DCSBD was investigated.

In [4] the DCSBD in single microdischarge – pin-to-pin electrode configuration was studied by the means of cross correlation spectroscopy. In that work Hoder et al. applied a model for estimation of the electron density and electric field in the discharge by measuring the discharge radiation intensities at specified wavelengths – second positive system of nitrogen (SPS – 377.1 nm) and first negative system of nitrogen (FNS – 391.5 nm). For our experiments we decided to use the same wavelengths as in [4] to be able to

[a] e-mail: cech@physics.muni.cz

compare our observations with those in [4] and see if there could be a correspondence between single-microdischarge and multi-microdischarge regimes of DCSBD.

2 Experimental setup

The experimental setup scheme is shown in Figure 1. It consisted of coplanar discharge cell, power supply unit and diagnostic instruments.

The discharge cell (see Fig. 2) was composed of two brass electrodes overlaid by dielectric plate and discharge chamber attached to the dielectric plate from opposite side from the electrodes. As the dielectric 96% alumina (Al_2O_3) plate of the thickness of 0.5 mm was used.

The electrodes formed rectangular inter-electrode space with the length of 30 mm. Gap between electrodes can be varied by movable electrode in the range of 0.1 to 5 mm. In this work the electrode gap width was changed in five steps: 0.6, 0.8, 1.2, 1.7 and 2.2 mm. The coplanar electrode system used in this work consisted of only one electrode pair, contrary to large area DCSBD [2,3].

The whole coplanar electrode system was dipped in electrically insulating oil bath and the grounded electrode was attached eventually to external cooler to keep it on the room temperature.

The discharge chamber had cylindrical shape with diameter of the chamber of 30 mm and the height of 30 mm. The discharge chamber enabled us to control the discharge atmosphere. The 99.996% pure nitrogen was flown through the chamber with constant flow rate of 3 slpm controlled with Vogtlin Instruments red-y GCR mass flow meter. The emission spectra and pictures of the discharge were taken through the quartz window on the top of the chamber (in Fig. 2 on the very bottom).

Discharge was powered by LIFETECH high voltage power supply unit with sinusoidal voltage output with the frequency of 35 to 37 kHz frequency (tuned to the resonance for each discharge gap width). In order to compare the results the voltage amplitude was kept constant at 15 kV. TTL triggering signal for time resolved spectroscopy was taken from the power supply function generator.

Electrical parameters of the discharge were measured by LeCroy WaveRunner 6100A digital storage oscilloscope (1 GHz/5 GSa). Input voltage was measured by Tektronix P6015A high voltage probe (1000:1). The discharge current was measured using HP 1160A (10:1) probe as a voltage drop on the 330 Ω resistor placed in the circuit in serie with the discharge cell.

Optical emission spectra were recorded with Horiba Jobin-Yvon FHR 1000 monochromator equipped with two gratings (2400 gr/mm and 3600 gr/mm). The optical signal was detected by Symphony CCD camera and i-Spectrum ICCD camera that was externally synchronized with applied voltage. Both of the cameras were cooled by means of cascaded Peltier cells.

The discharge emission pattern was projected by quartz lens on the adjustable slit. The light passing through

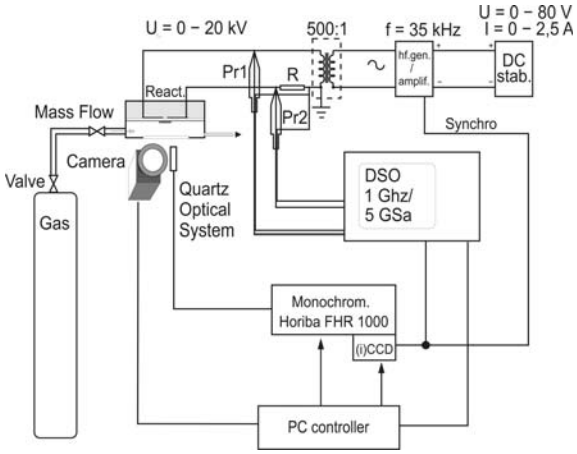

Fig. 1. Scheme of experimental setup with discharge cell and supporting and diagnostic units.

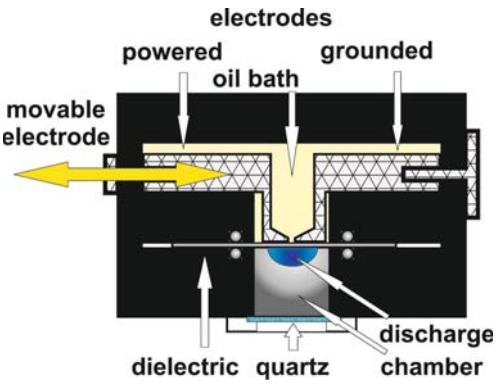

Fig. 2. (Color online) Detail of the discharge cell with coplanar electrode system. The dielectric plate, discharge chamber and movable electrode are labeled.

the slit was guided by the quartz optical fibre to the monochromator. The 1D-spatial profile of discharge emission was obtained by moving the slit in direction across the electrode gap. The optical resolution in the direction of scanning was set to 1 mm and the optical signal was gathered from the total area of approx. 5 mm^2 of the discharge in all cases (the scan track has width approx. 5 mm).

3 Experimental results and discussion

3.1 Visual appearance of the discharge and SPS intensity profiles

The visual appearance of the discharge is presented in Figure 3 together with schematic plot of electrode positions. The distinct pictures show discharge operated at different conditions. The horizontal axis represents increase of the inter-electrode distance (id) from 0.6 mm up to 2.2 mm.

The structure of the discharge pattern can be recognized combining discharge pictures in Figure 3 and corresponding intensity profiles of the SPS at 380.5 nm given

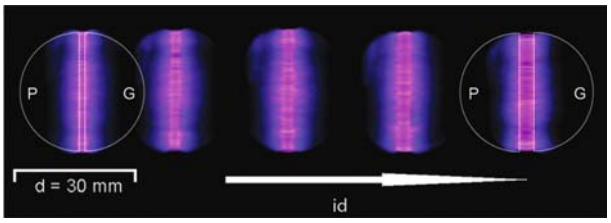

Fig. 3. (Color online) Set of discharge images taken at input voltage of 15 kV and exposure time $\tau = 1/25$ s. Inter-electrode distance (id) from left to the right is: 0.6, 0.8, 1.2, 1.7 and 2.2 mm. Semicircle electrodes positions are depicted – powered electrode P is under the left part of discharge pattern, grounded electrode G is under the right part of discharge pattern.

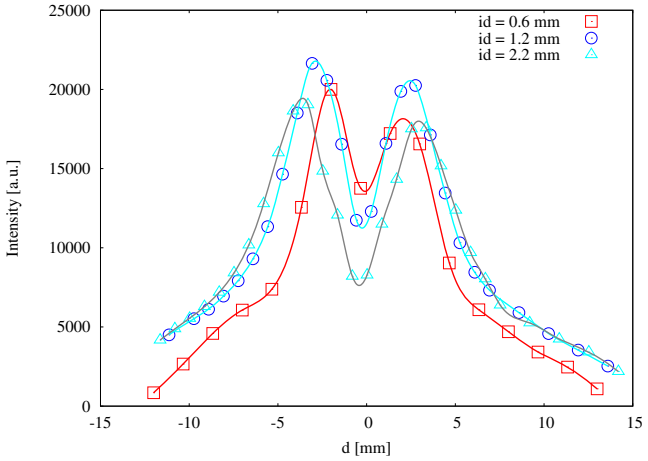

Fig. 4. (Color online) 1D-spatial profile of SPS integrated intensity ($\lambda = 380.5$ nm) for different inter-electrode distance – id. (For better clarity only three distances are depicted.) The quantity d represents the distance from the geometric axis of the electrode gap. Input voltage was kept at 15 kV.

in Figure 4. The DCSBD consisted of many single microdischarges moving rapidly along the electrodes. The single microdischarges are H-shaped with sharp narrow filamentary part above electrode gap and much wider diffuse part above electrode edges. As the effects of the spatio-temporal accumulation there are areas of lower intensities belonging to the filamentary part of microdischarges and brighter areas belonging to the diffuse parts of microdischarges. According to this, three discharge regions can be recognized on DCSBD pictures. The first (inner) region is formed by microchannels – filaments crossing the gap in between the electrodes and this is clearly visible for $id = 2.2$ mm as the darker region in the middle of the pattern. The second region is represented by the very bright areas just above the inner (straight) edge of electrodes. The outer edge of this second region can be recognized on the intensity profiles as the change of the profile slope due to large change of intensity. Third region is most clearly visible for the pictures with $id = 1.2$ or 1.7 mm and it appears as the diffuse light that is extended up to the outer (rounded) edge of the electrodes.

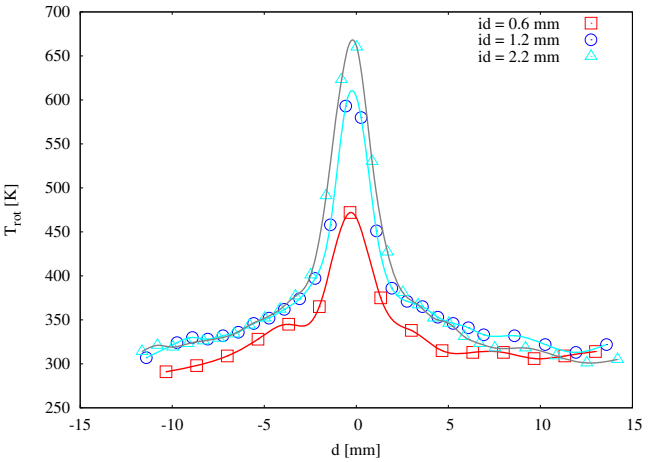

Fig. 5. (Color online) 1D-spatial profile of rotational temperature for different inter-electrode distances –id. (For better clarity only three distances are depicted.) The quantity d represents the distance from the geometric axis of the electrode gap. Input voltage kept at 15 kV. Errorbars are not shown for better clarity of figures. For discussion of errors see the text.

It can be seen in Figures 3 and 4 that inter-electrode distance influences substantially the discharge pattern and the corresponding intensity profiles. Most important effect is suppression of filamentary part of discharge with narrowing the electrode gap. The enhancement of diffuse like part of the discharge with electrode gap around 1 mm is also valuable observation.

3.2 Rotational temperature spatial profiles

The spatial profiles of rotational and vibrational temperature are useful characteristics for deducing the effects of plasma treatment of materials in DCSBD. The distribution of vibrational temperature (comparing with the intensity profiles) can give us the information about the "active area" involved in plasma treatment and the efficiency of this treatment. The distribution and the absolute values of the rotational temperature is on the other hand very important parameter in the case of plasma treatment of temperature sensitive materials, because the rotational temperature of SPS can be used as a measure of the neutral gas temperature. Thus the rotational temperature profile can be used for the estimation of the temperature stress of treated materials.

The evolution of spatial profiles of rotational temperature, with respect to the electrode gap width (inter-electrode distance) is given in Figure 5. For the estimation of rotational temperature the intensities of rotational lines $R_1(22–21)$ up to $R_1(17–16)$ of fully resolved rotational spectrum of second positive system of nitrogen $C^3\Pi_u \rightarrow B^3\Pi_g$ (337.1 nm) was used.

Two regions of the rotational temperature profile can be observed and can be correlated to the SPS intensity profile regions. In filamentary region the rotational temperature is considerably higher than in the second bright

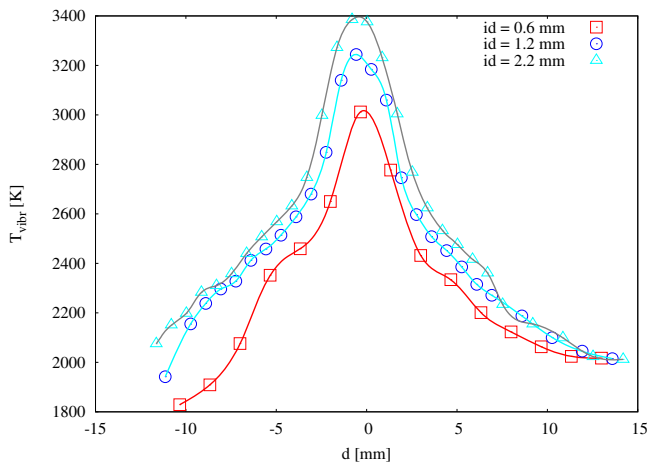

Fig. 6. (Color online) 1D-spatial profile of vibrational temperature for different inter-electrode distance – *id*. (For better clarity only three distances are depicted.) The quantity d represents the distance from the geometric axis of the electrode gap. Input voltage kept at 15 kV. Errorbars are not shown for better clarity of the figures. For discussion of errors see the text.

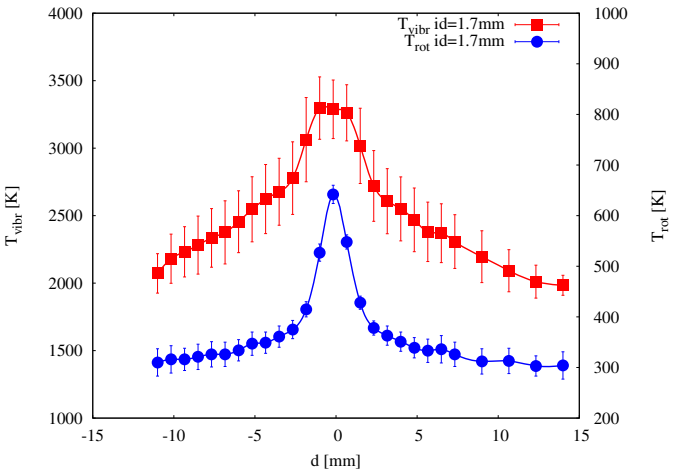

Fig. 7. (Color online) 1D-Spatial profiles of vibrational temperature together with rotational temperature for inter-electrode distance $id = 1.7$ mm.

one region. The temperature in the filamentary region peaks at almost 700 K, whereas the rotational temperature in the second region of the discharge, the bright one, has substantially lower values not higher than 350 K. There is a clear observation that the rotational temperature decreases with decreasing electrode gap. This is very important for temperature-sensitive materials treatment. The estimated statistical error of the rotational temperature is about 20 K (profile with errorbars can be seen in Fig. 7).

3.3 Vibrational temperature spatial profiles

The evolution of 1D-spatial profiles of vibrational temperature, with respect to the electrode gap width, is given in Figure 6. The vibrational temperature was estimated from the bands of SPS ($\Delta\nu = -2$, heads 0–2, 1–3, 2–4 starting at 380.5 nm).

Similar regions as in rotational temperature profiles can be observed also in the vibrational temperature profiles. There is a peak in vibrational temperature profile in the filamentary region of the discharge with values up to 3400 K. But in contrast to the rotational profile the high temperature region is considerably extended to the second discharge region. In the second region of the discharge there is still high vibrational temperature with the values about 2800 K. The statistical error of the vibrational temperature is about 200 K (profile with errorbars can be seen in Fig. 7).

The comparison of the rotational and vibrational temperature profiles is given in Figure 7, where the behavior described above can be seen. From the profiles in Figure 7 it can also be seen that the DCSBD creates highly non-equilibrium plasma with low rotational and high vibrational temperature.

If the SPS intensity profiles (Fig. 4) are considered together with the rotational (Fig. 5) and vibrational temperature (Fig. 6) profiles, the region of high SPS intensity with high vibrational and low rotational temperature can be observed. This is the case of the second, bright, discharge region above the electrode edges. The "hot" filamentary region has considerable lower SPS emission intensity.

These results are in good agreement with our plasma treatment experiments. We have observed that materials are better treated in the region above the electrode – the luminous (second) region, than above the inter-electrode region – the filamentary (first) region.

3.4 The time and space resolved intensity maps

In Figures 8 and 9 the time–space intensity maps of the SPS and FNS are given for electrode gap width of 0.6 mm, input voltage amplitude of 15 kV and frequency of 35 kHz. The anode and cathode are labeled for both input voltage periods and the electrode edges (electrode gaps) are denoted in both figures. Figure 8 represents the time and space distribution of intensity of the SPS accumulated over thousands of discharge periods and many statistically appearing filaments. Figure 9 represents the similar distribution, but for the FNS intensity. These maps are representing the average exposure of the treated samples during the potential plasma treatment. It can be observed that the large area of the electrodes is effectively irradiated during the voltage period. With this information we can deduce the plasma treatment efficiency, resp. how the changes of the discharge layout could influence this efficiency.

Keeping in mind different time scales and the effects of data accumulation, there is a correspondence of our measurements (Figs. 8 and 9) with the measurements of Hoder et al. [4]. In Figure 8 as in [4] SPS intensity maximum above anode edge is observed for both semi-periods of

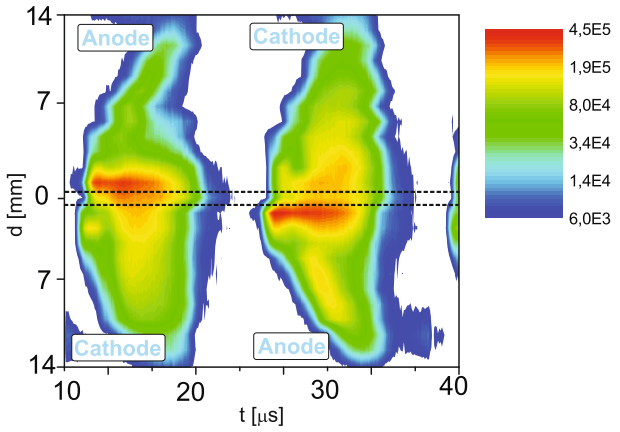

Fig. 8. (Color online) SPS intensity time-space map. The input voltage was 15 kV and the frequency of 35 kHz and electrode gap width was 0.6 mm. Dashed black lines denote electrode edges (electrode gap). The anode and cathode positions are labeled.

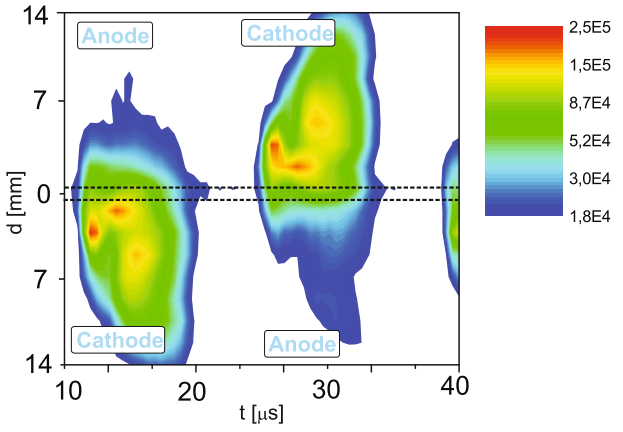

Fig. 9. (Color online) FNS intensity time-space map. The input voltage was 15 kV and the frequency of 35 kHz and electrode gap width was 0.6 mm. Dashed black lines denote electrode edges (electrode gap). The anode and cathode positions are labeled.

the discharge. Later broad second-maximum above cathode is observed in Figure 8 as well as side-maximum of SPS above anode in greater distance from the electrode gap (see Fig. 8). These phenomena are most likely synergic effect of the multi-microdischarge DCSBD configuration studied in this work and surface charge accumulation on the dielectric barrier influencing subsequent microdischarges in the discharge semi-period. In the case of FNS luminous regions can be distinguished above the cathode in both semi-periods of the discharge as in [4]. The statistical time-space distribution of single microdischarges in extended DSCDB configuration can be deduced from the maxima positions in Figure 9 by comparison with data given in [4]. There are three maxima of FNS intensity in each semi-period of discharge. The first FNS maximum in Figure 9, sorted by the time of occurrence, can be correlated to the head of the SPS main maximum (see Fig. 8). The last FNS maximum can be correlated to the SPS side-maximum, supporting the surface charge influence assumption.

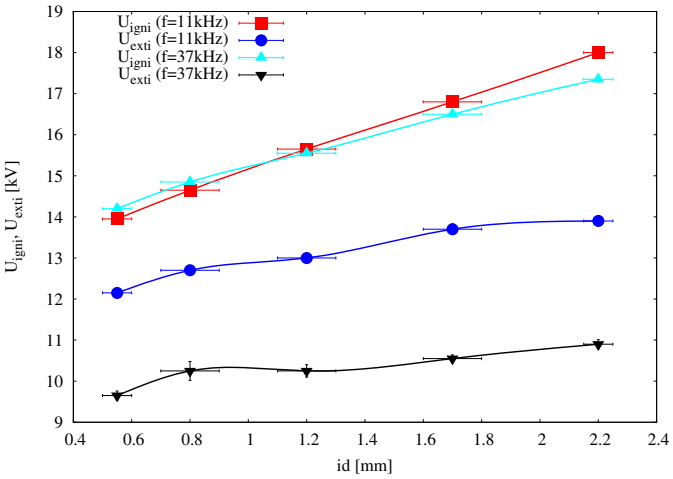

Fig. 10. (Color online) The dependence of ignition and extinction voltages amplitudes on the electrode gap width for the input voltage frequency of 11 kHz and 37 kHz.

3.5 The influence of electrode gap width on ignition/extinction voltage

The influence of electrode gap width and input voltage frequency on the ignition as well as extinction voltage was also studied and the results are given in Figure 10. The ignition voltage means the amplitude of the input voltage, when the discharge first appears if the amplitude is raised slowly from 0 V. It was found that the ignition voltage rises almost linearly as the electrode gap width increases, at least in the studied range of electrode gap widths. For the frequency of 11 kHz of input voltage the slope of this relation is slightly higher than for the frequency of 37 kHz.

The extinction voltage means the amplitude of input voltage below that the discharge disrupts. It can be seen, that for lower frequency of input voltage the extinction voltage is considerably higher, than for the higher frequency of input voltage. The difference of the extinction voltage values for frequencies of 11 and 37 kHz is almost 20%. This behaviour is in agreement with the explanation, that the subsequent periods of DCSBD could be governed by the active species developed and retained in the space above and on the surface of the dielectric barrier during previous period of the discharge. If assuming that the quenching rate of the active species is the same for both input voltage frequencies, the residence time of active species between the subsequent discharge periods are more than three times longer for the 11 kHz in comparison with the 37 kHz. Thus the amount of conserved active species just before the breakdown is considerably lower for the frequency of 11 kHz which results in higher extinction voltage than in the case of frequency of 37 kHz.

4 Conclusion

There is little systematic examination of outer physical conditions influence on the DCSBD. Research has been so far limited to the study of single microdischarge DCSBD. This paper gives first results on the influence of electrode gap width on parameters of DCSBD in standard configuration. It was find out that the electrode gap width is important parameter influencing not only the overall discharge pattern, but also rotational and vibrational temperatures and operating voltage of the DCSBD. By reduction of the electrode gap width the filamentary part of the discharge can be suppressed and the rotational temperature can be lowered substantially to ensure plasma treatment of temperature sensitive samples. It was find out that high radiation intensity regions above electrodes generate highly non-equilibrium plasma with low rotational temperature. That supports our experimental observations, that plasma treatment of materials is very efficient above electrodes. The spatio-temporally resolved spectroscopy was found useful for estimating effective time-space plasma coverage of electrodes during the discharge period. Improvements in this effective coverage could lead to increase of industrial fast in-line plasma treatment efficiency. However, the interpretation of obtained time and space resolved intensity maps is complicated by the fact, that the mechanisms of single microdischarge is not completely understood and the study of interactions between the concurrent and subsequent microdischarges of DCSBD is currently in the beginning.

This research has been supported by the Grant of Academy of Science CR KAN101630651 and the Long-term intent project No. MSM0021622411, Ministry of Education, Czech Republic.

References

1. K.H. Becker, W. Kogelschatz, K.H. Schvenbach, R.J. Bacher, *Non/Equilibrium Air Plasmas at Atmospheric Pressure, Series in Plasma Physics* (IOP, Bristol 2005)
2. M. Šimor, J. Rahel, P. Vojtek, A. Brablec, M. Černák, Appl. Phys. Lett. **81**, 2716 (2002)
3. M. Černák, J. Ráhel, D. Kovácik, M. Šimor, A. Brablec, P. Slavíček, Contrib. Plasma Phys. **44**, 504 (2004)
4. T. Hoder, M. Šíra, K.V. Kozlov, H.-E. Wagner, J. Phys. D: Appl. Phys. **41**, 035212 (2008)

Eur. Phys. J. Appl. Phys. (2016) 75: 24706
DOI: 10.1051/epjap/2016150538

THE EUROPEAN PHYSICAL JOURNAL APPLIED PHYSICS

Regular Article

Pre-breakdown phase of coplanar dielectric barrier discharge in helium*

Tomáš Morávek[a], Jan Čech, Zdeněk Navrátil, and Jozef Ráhel'

Masaryk University, CEPLANT – R&D Center for Low-Cost Plasma and Nanotechnology Surface Modification, Kotlářská 2, 61137 Brno, Czech Republic

Received: 28 October 2015 / Received in final form: 25 January 2016 / Accepted: 18 March 2016

Abstract. Coplanar barrier discharge in single-pair electrode configuration was used to study the formation of helium diffuse mode discharge. Transition from Townsend avalanching to the cathode and anode directed ionization waves was documented by high-speed camera imaging. When alumina dielectric barrier was coated by a thin layer of high permittivity coating (ε_r = 120–140), a new partial discharge preceding the Townsend avalanching phase was clearly visible. We suggest that this new pre-Townsend breakdown event is analogous to the known backward discharge of surface barrier discharge. Low magnitude of local electric field strength during the pre-Townsend breakdown reduces the number of competing electron collision excitation processes. This opens a new opportunity for studying optical emission from surface charge recombination processes.

1 Introduction

Non-thermal plasma generated at atmospheric pressure by dielectric barrier discharge (DBD) has already found a huge amount of applications in various fields: medicine [1,2], surface treatment [3,4], plasma display panels [5], pollution control [6,7], gas flow control [8], etc. DBD owes its non-thermal character to the dielectric barrier separating the metallic power electrodes from each other. Accumulation of surface charge on this dielectric barrier creates so called "memory voltage", which leads to a rapid extinction of formed micro-discharges. Accumulated localized surface charge determines the position of micro-discharge in the next half-cycle [9]. However, this intrinsic feature represents a problem for some applications. It spatially stabilizes the micro-discharge appearance [10,11], thus worsens the discharge macroscopic uniformity. Eventually it causes thermal damage of heat sensitive material by thermal built-up in stationary micro-discharge channel.

To address this issue it is necessary to get better understanding of processes involved in charge relaxation within the interim of two consequent discharge breakdowns. Some pioneering work on this topic has already been done for volume DBD by employing Pockels electro-optic effect on BSO ($Bi_{12}SiO_{20}$) crystal [12,13]. The measurements registered dynamics of charge relaxation; nevertheless they did not provide much information on actual pathways of energy released by the charge recombination process. In the present work we use coplanar geometry DBD to create two distinct, well defined regions of opposite polarity surface charge residing at the same dielectric plate. Using high-speed camera imaging, discharge formation dynamics on these pre-charged surface domains and more importantly processes that may be associated with the interim charge relaxation were studied. Planar geometry of coplanar discharge made the focusing of optical camera particularly convenient.

2 Experimental

Coplanar electrode discharge set-up is shown on Figure 1. Brass metal electrodes with adjustable rectangular electrode gap set to 4.7 mm were immersed into insulation oil and covered by alumina dielectric plate (96% Al_2O_3; thickness 0.6 mm). In one case the alumina dielectric was coated with a high permittivity dielectric coating (ESL 4113-H; ε_r = 120–140); in second case uncoated alumina was used. The motivation for using high permittivity coating was to increase the amount of charge involved in the relaxation processes. Discharge face of alumina plate was housed in a small chamber equipped with a quartz window for optical diagnostics. Helium with purity 5.0 was flowing through the chamber at flow rate of 555 sccm,

[a] e-mail: tomas1104@seznam.cz

* Contribution to the topical issue "6th Central European Symposium on Plasma Chemistry (CESPC-6)", edited by Nicolas Gherardi, Ester Marotta and Cristina Paradisi

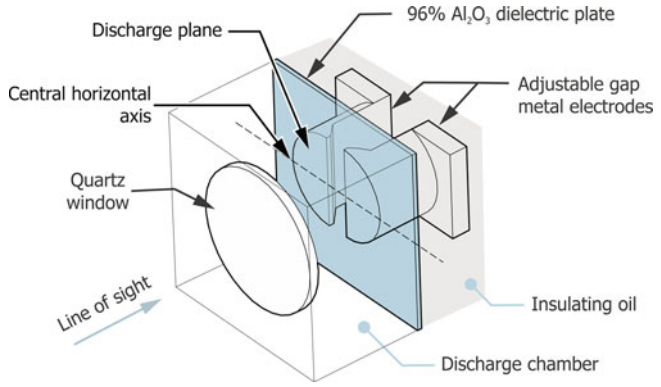

Fig. 1. Schematic view of discharge setup. Outer radius of metal electrode was 10 mm; electrode gap was set to 4.7 mm.

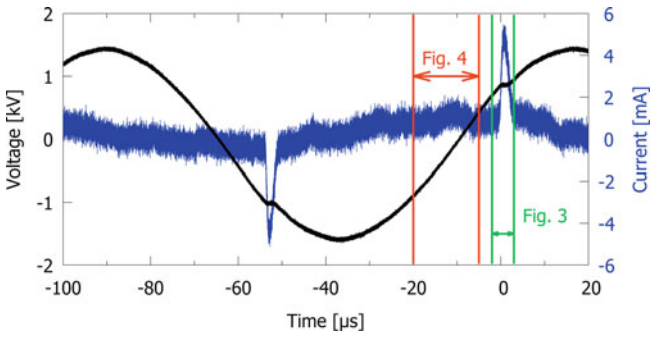

Fig. 2. Current and voltage waveforms for He diffuse mode on HPC surface with indicated time intervals corresponding to the figures in further text.

operating pressure was slightly above 1 atm. The volume of the discharge chamber was 5 cm^3. Discharge was driven by alternating voltage of frequency 9.4 kHz, generated with function generator (Agilent 33220A) and amplified to a high voltage signal with amplitude of 1.6 kV. The applied voltage and the discharge current were measured by HV probe P6015A (Tektronix) attached to a digital oscilloscope (Keysight DSO-S 204A). The discharge current was measured by Pearson monitor Model 2877. The jitter of discharge onset was approx. 100–200 ns FWHM, almost two orders less than the total lifetime of discharge breakdown. This enabled the adoption of highly accumulated hi-res 2D optical imaging of the phase evolution of the light emission from the discharge, using ICCD camera PI-MAX3-1024i-SR-46-CM (Princeton Instruments) equipped with true-macro objective telephotolens (SIGMA 105/2.8 MACRO).

3 Results and discussion

3.1 Phenomenological description

By keeping voltage slightly above the extinction voltage, a diffuse discharge in helium was established. Fine tuning of the frequency and voltage amplitude led to the discharge with single time-stable current peak per one half-cycle, suitable for investigation by ICCD camera. Figure 2 shows a typical current-voltage characteristics of the discharge with the high-permittivity coating (HPC). Integration of current waveform confirmed higher charge transfer due to HPC (10 nC vs. 6 nC at fixed operation voltage).

To get a more synoptic overview of dynamics of discharge evolution, images taken by ICCD were post-processed to create artificial streak camera-like record along the central horizontal axis of electrode setup (Fig. 3).

As expected, DBD on both types of dielectrics started by Townsend avalanching (TA) at the anode edge, with a slow gradual increase of light intensity there. Approx. 10 μs after the start of Townsend avalanching, space charge created distortion of electric field was sufficient to invoke propagation of two oppositely directed ionization waves – cathode directed (CDIW) and anode directed (ADIW). CDIW crossed the space above the inter-electrode gap at increasing speed in about 1 μs and continued to propagate along the instantaneous cathode at lower but constant speed. A more detail data on CDIW propagation, including spectrally resolved signals, are given in references [14,15]. ADIW propagated at similar speed to CDIW above the cathode. The existence of ADIW has been reported already e.g., in reference [16]. Pair comparison on tested materials showed that HPC formed more intense CDIW and ADIW, which however propagated at slightly lower velocities. We assume that the difference can be attributed to larger amount of charge being transported for HPC. It provided more radiative collisions, and more intense shielding by the space charge of positive ions.

Graphically determined average speed of CDIW above the cathode plane was 7 km/s and 4 km/s for bare alumina and HPC respectively. These relatively small velocities indicate that CDIW propagation is facilitated by the electron drift, not by extremely fast streamer mechanism breakdown characterized by velocities of thousands km/s. Our preliminary measurements of E/N at that position, from the ratio of helium lines at 668 and 728 nm according to [17] suggested, that the CDIW field is lower than 5 kV/cm (5–20 Td). This matched well the Laplacian electric field calculation at the breakdown voltage. Drift velocity of electrons at this E/N lays within the range of 12.5–50 km/s [18], which is considerably more that the speed of our CDIW. Hence drifting electrons are fully capable to mediate the CDIW propagation along the cathode plane, and it is safe to exclude streamer mechanism breakdown from our next considerations. The comparison of TA phases gave an impression of being slightly longer for HPC. But since the difference in signal intensity is only in units of photons, we cannot make any definite statement here.

3.2 Pre-breakdown event

Approximately 10 μs before the onset of Townsend avalanching an extremely weak but clearly detectable

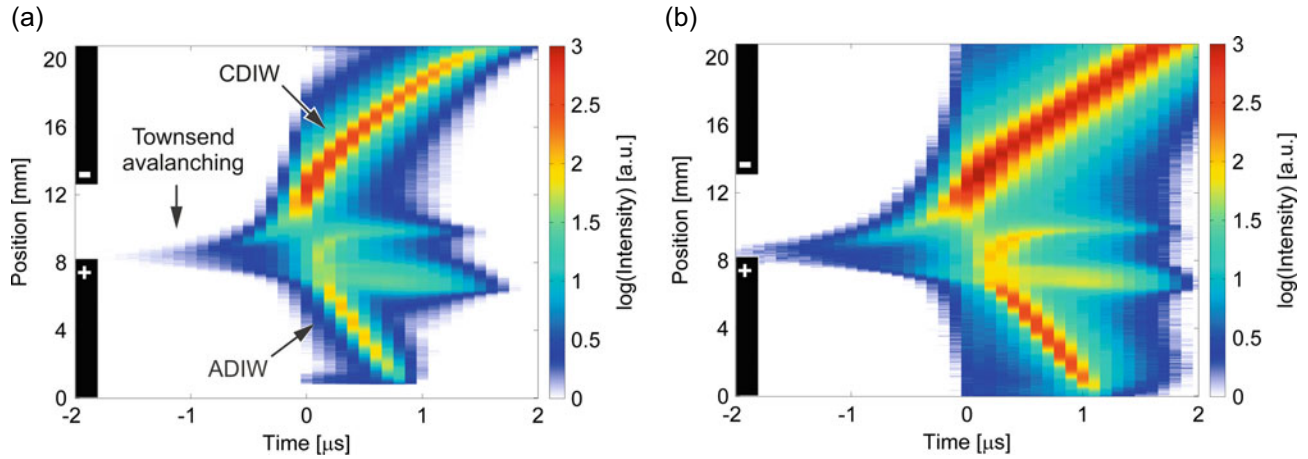

Fig. 3. Streak camera-like temporal evolution of light intensity along the central horizontal axis for: (a) alumina dielectric; (b) alumina with HPC. Absolute start of Townsend avalanching some 10 μs before the CDIW onset is not shown here.

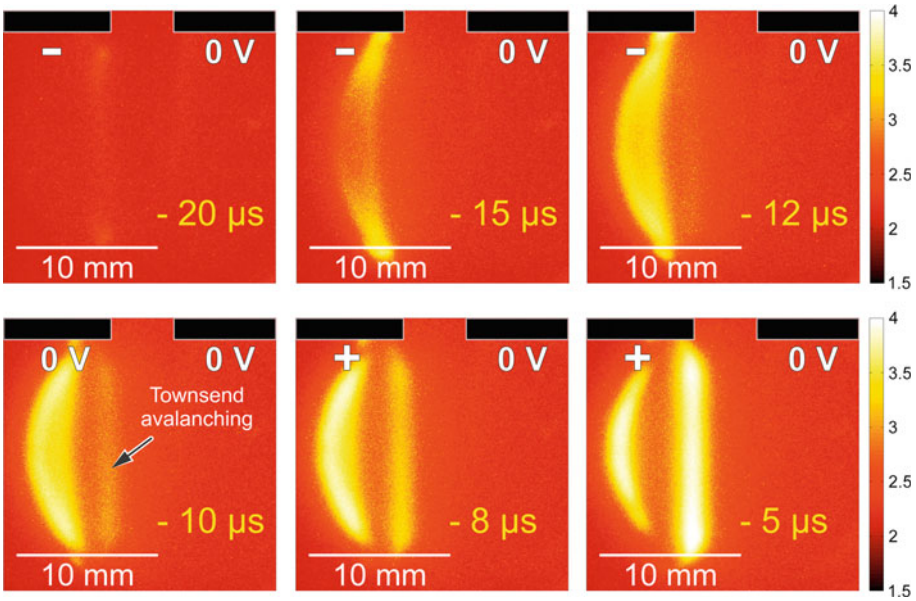

Fig. 4. ICCD plane view filmstrip of pre-breakdown event on HPC. $10^4\times$ higher sensitivity comparing to Figure 3. In -10 μs the formation of Townsend avalanching at anode edge (former cathode) can be recognized.

luminous wave appeared above the still negative electrode edge and spread laterally along its surface (Fig. 4). It started at the falling slope of voltage cycle, when the external voltage was roughly the same as in previous discharge onset. In about 10 μs the whole dielectric of cathode plane was covered, reaching its maximum of total light intensity – though almost 10^4 times lower than the intensity of CDIW. Such extremely weak intensity may explain, why we cannot see any corresponding electrical current in Figure 2. It was most likely below our sensitivity level. In case of HPC the appearance of pre-Townsend luminous wave was more pronounced (Fig. 5). This was due to contribution of two main factors: more charge being transported at HPC enhanced the emission intensity; and lower HPC background luminescence improved the image contrast.

From Figure 5, the velocity of pre-Townsend event was graphically determined as 0.8 km/s for HPC, which was significantly less than the CDIW top speed (7 km/s). Since the CDIW propagation by streamer mechanism has been excluded in our previous discussion, the result suggested, that the pre-Townsend event had occurred at lower E/N. Electron mobility in helium is nearly constant within the range of 1–100 Td [18]. Therefore from the plain ratio of velocities we could estimate that pre-Townsend luminous wave propagated at approx. 10 times lower electric field strength than CDIW.

Our explanation of the underlying physics of pre-Townsend breakdown event is based on its occurrence at moments close to the change of electrode polarity. It points out to the important role of surface charge memory voltage. It is known from the theory of surface barrier

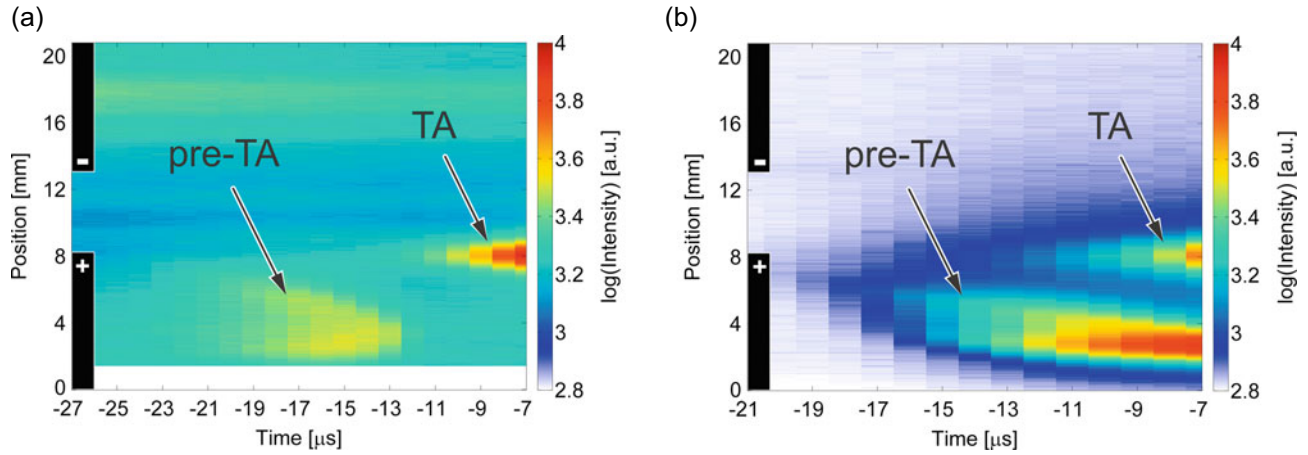

Fig. 5. Streak camera-like reconstruction of pre-breakdown event followed by initial stage of Townsend avalanching phase. Polarity of electrodes is given for times of TA. (a) Bare alumina dielectrics; (b) HPC. Signal from alumina exhibited a considerable dielectric fluorescence.

discharge (SBD) formation, that prior the onset of opposite polarity breakdown, so called "backward discharge" occurs [19]. When the magnitude of applied voltage decreases, at some point it is too small to counteract the attractive coulomb forces of deposited surface charge of opposite polarity. Consecutive "backward discharge" renders a partial charge recombination near the metallic electrode of SBD. To our best knowledge there is no published information on the intensity of light emission associated with the SBD's backward discharge. But based on our former experience we assume that eventual light emission would be very low. A helium charge transport recombination, although at slower time scale, was observed in reference [12] when both polarity charges were non-uniformly deposited on the same dielectric electrode. Still, no detectable radiation associated with the process was reported in reference [12]. Radiation-wise the situation is different for pulsed volume DBD. Measurements of [20] have shown that memory voltage of surface charge is sufficient to create highly luminous discharge breakdown of opposite polarity during the pulse falling slope. These three examples show convincingly, that regardless of geometry of dielectric barrier discharge, memory voltage induced by surface charge is capable to initiate drift of charge particles, in order to recombine with its opposite polarity counterpart. In favorable conditions (as in Ref. [20]) the drift may be even accompanied by excitation/ionization collisions.

Based on this analysis we assume that the observed pre-Townsend breakdown event is an equivalent to the backward discharge of surface barrier discharge, with fortunate combination of factors allowing the light emission. From the direction of pre-breakdown event propagation we have deduced following scenario: the fall of external voltage below some threshold value released weakly adsorbed electrons above the instantaneous anode, which started to move towards the positive charge at the cathode (soon to be anode). Light emission started from the place where positive charge had been deposited, i.e., from the edge of cathode, and decayed when the pool of positive charge was depleted. Observed light emission can be due to both excitation collisions caused by local increase of electric field, and/or to charge recombination radiation (homogeneous or heterogeneous). The presence of HPC made the phenomenon more visible, by reducing background material luminescence and by increasing the number of electrons participating in pre-breakdown processes. For further elaboration of above described scenario, thorough spectrally resolved measurements are still needed. Owing to the above mentioned low intensity of light emission this would be a particularly challenging task. Nevertheless it offers a new experimental window for assessing the processes of heterogeneous interactions of plasma species with dielectric surface, unobstructed by the radiation from the active plasma.

4 Conclusion

The use of high permittivity dielectric coating on helium coplanar barrier discharge enabled us to record a new pre-breakdown luminous wave, preceding the known Townsend avalanching phase. We suggest that this event is equivalent to the backward discharge of surface barrier discharge (SBD), known to partially remove or even change the polarity of deposited charge near the SBD metallic electrode. The wave is carried out by electrons, released from trapped state on the instantaneous anode dielectric plane, when the magnitude of external voltage falls below some threshold value. Although the light intensity of pre-breakdown luminous wave is extremely weak, it offers a new opportunity to experimentally asses processes of DBD surface charge interaction.

This research has been supported by the by the Czech Science Foundation, Contract No. GA13-24635S and by the Project CZ.1.05/2.1.00/03.0086 funded by European Regional Development Fund and Project LO1411 (NPU I) funded by Ministry of Education Youth and Sports of Czech Republic.

References

1. K.D. Weltmann et al., Pure Appl. Chem. **82**, 1223 (2010)
2. J. Vrajova et al., Eur. Phys. J. D **54**, 233 (2009)
3. D. Skacelova et al., Appl. Surf. Sci. **312**, 203 (2014)
4. P. Kral et al., Wood Sci. Technol. **49**, 319 (2015)
5. J.P. Boeuf, J. Phys. D: Appl. Phys. **36**, 53 (2003)
6. M. Hijosa-Valsero et al., J. Hazard. Mater. **262**, 664 (2013)
7. N. Osawa et al., Int. J. Plasma Environ. Sci. Technol. **6**, 119 (2012)
8. T.N. Jukes, Renew. Energy **80**, 644 (2015)
9. Y.S. Akishev et al., Eur. Phys. J. D **61**, 421 (2011)
10. M. Bogaczyk et al., J. Phys. D: Appl. Phys. **45**, 465202 (2012)
11. J. Cech et al., Open Chemistry **13**, 528 (2014)
12. R. Wild, J. Benduhnand, L. Stollenwerk, J. Phys. D: Appl. Phys. **47**, 435204 (2014)
13. R. Tschiersch, M. Bogaczyk, H.-E. Wagner, J. Phys. D: Appl. Phys. **47**, 365204 (2014)
14. T. Morávek et al., in *Proceedings of the International Symposium on High Pressure Low Temperature Plasma Chemistry, Zinnowitz, Germany, 2014*, pp. 98–102
15. T. Morávek, Z. Navrátil, J. Ráhel, J. Čech, in *Proceedings of the 27th Summer school and International Symposium on the Physics of Ionized Gases, Belgrade, Serbia, 2014*, pp. 371–374
16. T. Hoder, M. Černák, H.-E. Wagner, in *Book of Contributed Papers of HAKONE 12th, 2009*, pp. 207–211
17. S.S. Ivković et al., J. Phys. D: Appl. Phys. **47**, 055204 (2014)
18. IST-Lisbon database, `www.lxcat.net`, retrieved on January 19, 2016
19. V.I. Gibalov, G.J. Pietsch, J. Phys. D: Appl. Phys. **33**, 2618 (2000)
20. M. Kettlitz et al., J. Phys. D: Appl. Phys. **45**, 245201 (2012)

IOP Publishing Plasma Sources Science and Technology
Plasma Sources Sci. Technol. **26** (2017) 055025 (10pp) https://doi.org/10.1088/1361-6595/aa66b5

Diagnostics of pre-breakdown light emission in a helium coplanar barrier discharge: the presence of neutral bremsstrahlung

Zdeněk Navrátil[1], Tomáš Morávek[1], Jozef Ráheľ[1], Jan Čech[1], Ondřej Lalinský[2] and David Trunec[1]

[1] Department of Physical Electronics, Faculty of Science, Masaryk University, Kotlářská 2, 611 37 Brno, Czech Republic
[2] Institute of Scientific Instruments of the CAS, Královopolská 147, 612 64 Brno, Czech Republic

E-mail: zdenek@physics.muni.cz

Received 13 December 2016, revised 3 March 2017
Accepted for publication 14 March 2017
Published 24 April 2017

Abstract

Weak light emission ($\sim 10^{-3}$ of active discharge signal; average count rate ~ 1 photon s^{-1} nm^{-1}) associated with surface charge relaxation during the dark phase of a helium diffuse coplanar barrier discharge was studied by optical emission spectroscopy, using a technique of phase-resolved single photon counting. The optical emission spectra of the dark phase contained luminescent bands of the dielectrics used (Al_2O_3, AlN) and spectral lines from the gas constituents (OH^*, N_2^*, N_2^{+*}, He^*, He_2^*, O^*). During the charge relaxation event, a broad continuum appeared in the optical emission spectra, consisting of bremsstrahlung radiation and amplified luminescence of the dielectric barrier. The analysis presented suggests that the bremsstrahlung radiation originated from slow electrons colliding with neutral helium atoms. The fitting procedure we developed reproduced well the observed shape of the continuum. Moreover, it provided a method for the determination of electric field strength in the discharge during this particular phase. The electric field reached 1 kV cm^{-1} during the charge relaxation event.

Keywords: dielectric barrier discharge, helium, single photon counting, bremsstrahlung, electric field, backward discharge, surface charge

1. Introduction

Surface charge accumulation plays an important role in the formation dynamics of a dielectric barrier discharge (DBD). It facilitates a rapid build-up of a counter electric field, causing a prompt cessation of the DBD's microdischarge (MD) growth. Moreover it provides a so-called memory effect. Upon reversal of the polarity, the deposited surface charge lowers the inception voltage of successive MDs. This promotes reignition of the MD at the location of previous breakdown [1]. Furthermore, surface charge is claimed to influence the time jitter of the MD's actual appearance and its magnitude [2].

For typical conditions of DBD operation the interval between two successive MDs is at least an order of magnitude longer than the lifetime of a single MD. During this rather long dark phase, the charge deposited by the MD is free to migrate along the dielectric surface or to interact with ambient gas. Both processes lead to its gradual relaxation. Experimental assessment of unipolar surface charge dynamics made in Greifswald for a plane-parallel volume DBD in He, N_2 and their mixtures (involving the technique based on the Pockels electro-optic effect) showed a nearly constant level of surface charge density within the whole interval [1, 3]. This picture was changed dramatically when two adjacent charged domains of opposite polarity were created by a reverse breakdown on the same dielectric plane [4]. The presence of bipolar surface charging introduced a new attractive lateral force, which gave rise to charge transport along the dielectrics. Instead of a gradual removal of charge by its mutual recombination, an unexpected growth of surface charge density was observed. However, the analysis presented did not provide any information on light emission associated with the expected charge recombination.

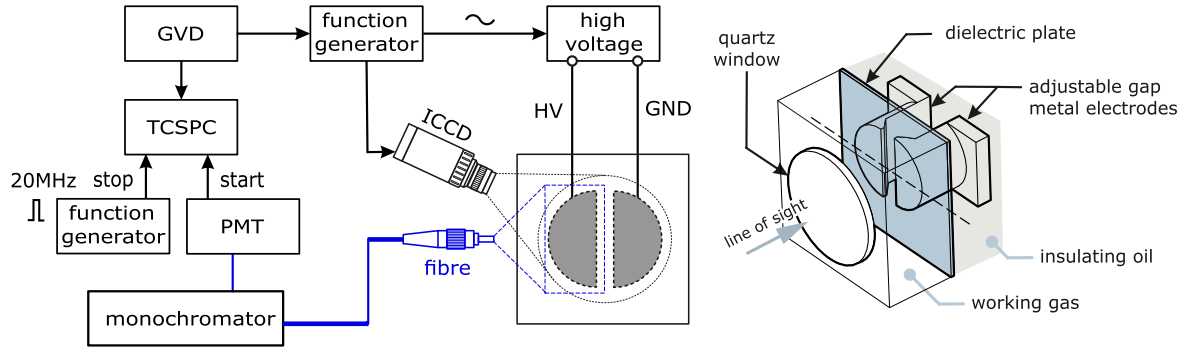

Figure 1. Scheme of experimental the setup. GVD—galvano controller B&H GVD-120, TCSPC—time-correlated single photon counter BH SPC-150, PMT—photomultiplier BH PMC-100-4, monochromator—JY HR-640, ICCD—PI MAX3 ICCD camera.

A periodic formation of well-defined opposite charge domains residing on the same dielectric plane occurs naturally in the coplanar DBD. The advantage of the coplanar electrode configuration is that it allows straightforward accumulation of the eventual optical emission signal. Recently, our investigation of the diffuse mode in a helium coplanar DBD revealed the presence of an extremely weak luminous event propagating along the driven electrode during the dark phase of the discharge [5]. The luminous event appeared shortly before reversal of the external voltage polarity, when the driven electrode was changing its polarity from negative to positive and its dielectric surface was still positively charged. The event vanished just before or simultaneously with (depending on the driving frequency) the onset of the Townsend avalanching phase of the consequent cathode-directed ionizing wave. Our phenomenological analysis in [5] led to the conclusion that the observed luminous event is the manifestation of surface charge relaxation (similar to the backward discharge in [6]) between the two oppositely charged surface domains, mediated by weakly bounded surface electrons. The work presented here offers further evidence to support this conclusion by providing temporally resolved spectral characterization via single photon counting of this luminous charge relaxation event (CRE).

2. Experimental setup

The coplanar electrode system consisted of a single pair of semicircular brass electrodes (20 mm diameter) separated by a 4.7 mm rectangular electrode gap (see figure 1). The electrodes were immersed in insulating oil and covered by a dielectric barrier plate of chosen material. The materials were: alumina (96% Al_2O_3; thickness 0.635 mm), aluminium nitride (AlN; thickness 0.635 mm) and 96% Al_2O_3 coated with a high-permittivity dielectric film (ESL 4113-H; $\varepsilon_r = 120$–140). The whole system was housed in a gas-tight plastic box with quartz optical window. The discharge was operated in flowing helium (gas purity 5.0) at 500 sccm and at atmospheric pressure. The discharge was driven by an alternating high voltage of frequency 9.5 kHz (20 kHz for discharge with high-permittivity dielectric film) and amplitude 1.6 kV. The sinusoidal waveform was generated with a function generator (Agilent 33220A) and amplified to the high-voltage signal by a high-voltage amplifier built in-house. The high-voltage signal was applied to one ('driven') electrode, the other was grounded. The stability and characteristics of electrical parameters were monitored by a digital oscilloscope (Keysight DSO-S 204A) using a Pearson current monitor (Model 2877) and Tektronix high-voltage probe (P6015A). The discharge was stabilized in its diffuse, non-filamentary operating mode that occurred slightly above the breakdown voltage.

The optical emission spectra were recorded by a method of phase-resolved single photon counting (PRSPC) in the spectral region of 250–800 nm. Photons emitted from the driven-electrode region and collected by an optical fibre located in front of the window were monochromatized (Jobin Yvon HR-640, grating 1200 grooves mm^{-1}, resolution used 4 nm) and counted by a time-correlated single photon counter (TCSPC Becker & Hickl SPC-150, PMT PMC-100-4). The reason for such low spectral resolution was the extremely low intensity of the CRE optical signal. The collection time for one wavelength was 100 s. In the past, the TCSPC technique was adopted for the sub-nanosecond diagnostics of barrier discharges by so-called cross-correlation spectroscopy (CCS), which correlates the counted photons with the stop signal taken from the overall discharge light pulse [7]. Since such high time resolution was not required in the present experiment, the stop signal for TCSPC was taken from an independent function generator producing rectangular pulses with frequency 20 MHz (see figure 1). Similar finesse had already been used, e.g., in [8]. The collected photons were phase-correlated with the voltage signal using a galvano controller card B&H GVD-120. Firstly, the card served as a source of the triggering waveform for the high-voltage power supply. Secondly, the card provided so-called pixel clock output, consisting of 512 equidistant rectangular TTL pulses per one period of the high-voltage signal. This output was read by the TCSPC to resolve the temporal position of the counted photons within the voltage period. The PRSPC method enabled us to measure the light signal over the entire period of 105 μs, i.e. also in the phases unreachable by CCS. The drawback was a lower time resolution of 0.2 μs given by the limits of the galvano controller card itself.

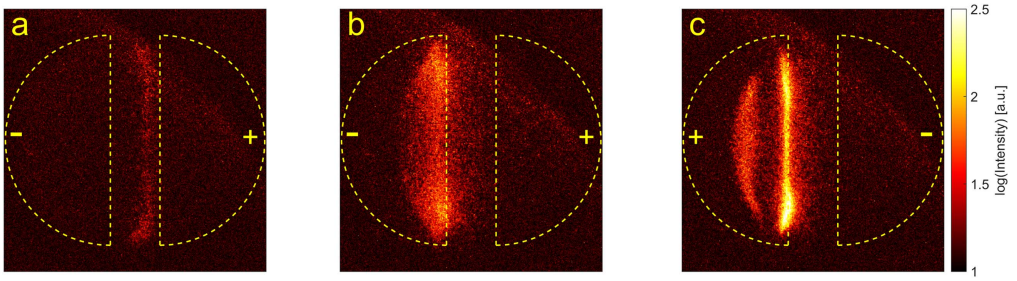

(a) $-13.5\,\mu$s (b) $-9\,\mu$s (c) $-4.4\,\mu$s

Figure 2. (a)–(c) ICCD images of a helium discharge on Al_2O_3 coated with the high-permittivity dielectric film, showing the evolution of the charge relaxation event. Collection time 500 ns, number of accumulations 10000, AC voltage frequency 20 kHz. The signs denote the instantaneous polarities of electrodes.

The measured spectra were corrected for the instrument sensitivity using a combined deuterium–halogen calibration lamp (AvaLight-DH-CAL). Supporting phase-resolved images of a helium discharge were captured using a PI-MAX3 ICCD camera.

Supplementary diagnostic techniques were applied to investigate the luminescence of ceramics used as a dielectric barrier. The cathodoluminescence (CL) spectra were studied under electron beam excitation using a CL apparatus described in [9]. Prior to the CL measurements, the ceramics were coated with a thin Al film of 50 nm to avoid surface charging by electron irradiation. The excitation part of the CL apparatus was made from a transmission electron microscope (Tesla BS-242) adjusted especially for CL studies. The ceramic sample was irradiated by a focused electron beam of 18 keV energy and 30 nA current. The electron beam created a round spot of diameter of 2 mm on the ceramic surface. The CL light was collected from the opposite side of the sample, and guided by optical fibre into the spectrometer (Horiba JY iHR 320) equipped with a photomultiplier (Hamamatsu R943-02). The measured spectra were corrected for the spectral transmittance of the apparatus and also for the spectral sensitivity of the detector.

For CL decay measurements, the electron beam was periodically deflected out of an aperture in order to create electron beam pulses with a duration of 50 ns and frequency 1 kHz. Instead of guiding the emitted light into the spectrometer, the light was directed to the photomultiplier tube (ET-Enterprises 9113WB) connected to the oscilloscope (Tektronix DPO7254). The CL decay measurement was spectrally integrated over the region 200–800 nm; the time resolution was 2 ns.

Photoluminescence (PL) spectra of ceramics were measured using a fluorescence spectrometer (FLS920, Edinburgh Instruments) working in a steady-state mode. The samples were irradiated by light from a built-in xenon lamp monochromatized in an excitation monochromator. The emitted luminescence light passed first through an optical filter that eliminated the scattered excitation light below 330 nm. The light was then spectrally resolved in the emission monochromator and detected using a single photon counting photomultiplier. The emission spectra were measured in the spectral range 340–750 nm with a spectral resolution of 1 nm.

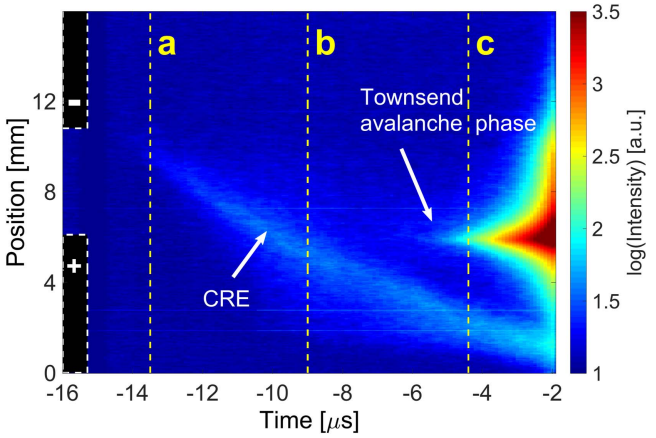

Figure 3. Streak camera-like image obtained from the ICCD images of the charge relaxation event on the high-permittivity dielectric film. The times of the ICCD images in figure 2 are indicated by symbols a–c. The plotted intensity was obtained by summing the pixel intensities vertically in a central image region. The marked polarity of the electrodes is valid for times later than $-8\,\mu$s.

3. Results and discussion

3.1. ICCD images

Recorded ICCD images of the charge relaxation event in a helium discharge on the Al_2O_3 dielectric coated with the high-permittivity film are shown in figures 2(a)–(c). This particular material provided the images with the best contrast. Zero time in these figures corresponds to the maximum of the discharge current pulse. A weak luminous event started above the grounded electrode (on the right) approximately 10 μs before the onset of the Townsend avalanching phase. At that moment, the grounded electrode was still the instantaneous anode with a deposited negative surface charge. Such an early phase of the event initiation was not resolved in our previous work [5]. The luminous event then crossed the interelectrode gap and propagated along the driven electrode (i.e. the instantaneous cathode with deposited positive surface charge). For a more synoptic perspective, a streak camera-like representation of this process in the central region along the horizontal axis is given in figure 3 (times corresponding to figures 2(a)–(c) are illustrated by dashed lines). Since the reversal of external voltage polarity occurred at a time

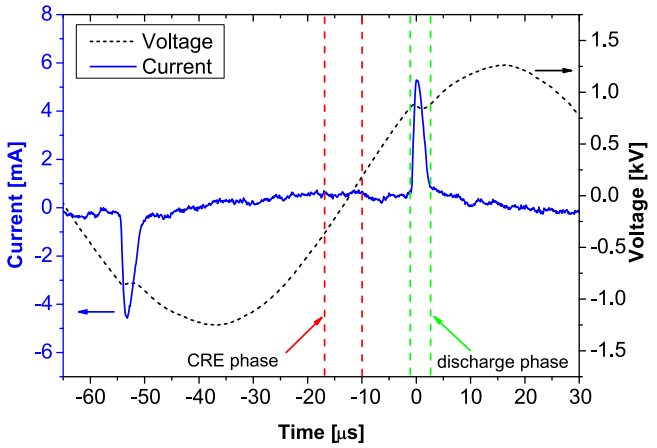

Figure 4. Current and voltage waveforms of a helium diffuse discharge on Al_2O_3 ceramics. The time intervals of the charge relaxation event and of the active discharge are indicated by red and green lines, respectively.

of -8μs (see figure 3), the driven electrode became the instantaneous anode during the final stages of the luminous event. Then the Townsend avalanching phase appeared there.

As can be seen in figure 4, no detectable current peak could be attributed to the relaxation event. Given the fact that the light intensity of the CRE was approximately three orders of magnitude lower than that of the active discharge, the expected associated current signal had to be well below the detection limit of the current probe used.

3.2. Phase-resolved optical emission spectra

Maps of phase-resolved optical emission spectra during the period of coplanar barrier discharge in helium are displayed for two different ceramics in figure 5. The colour scale was chosen so that the low-level light emissions during the dark phase (with intensities of hundreds of photons only) are clearly visible. The light emissions from the active discharge are then not to scale and their measured intensities (typically 5×10^5 counted photons per data point) are even saturated due to the limited count rate of the TCSPC instrument.

First, we shall discuss the light emission from gas constituents during the dark phase. Light emission from molecular spectral systems such as OH ($A\ ^2\Sigma^+ \rightarrow X\ ^2\Pi$), N_2^+ FNS system ($B\ ^2\Sigma_u^+ \rightarrow X\ ^2\Sigma_g^+$), N_2 SPS system ($C\ ^3\Pi_u \rightarrow B\ ^3\Pi_g$) and also the He_2 ($d\ ^3\Sigma_u^+ \rightarrow b\ ^3\Pi_g$) band at 640 nm can be clearly recognized. This is in agreement with observations in a helium volume barrier discharge [8]. Similarly, atomic lines of oxygen (at 777 nm) and even of helium (e.g. at 587.6, 667.8, 706.5 and 728.1 nm) are visible during the dark phase. The presence of the FNS system (radiative lifetime of the $B\ ^2\Sigma_u^+$ state is around 60 ns [7]) and of helium and oxygen lines in spectra at late times before the next breakdown reflects the presence of helium metastable species and ions in the gas, as expected in diffuse barrier discharges [10–12]. In helium plasmas at atmospheric pressure with the gas temperature below 2500 K, the He_2^+ molecular ion is the dominant ion [13]. However, the content of impurities in helium (N_2, O_2) must be kept below several ppm, otherwise He_2^+ ions are

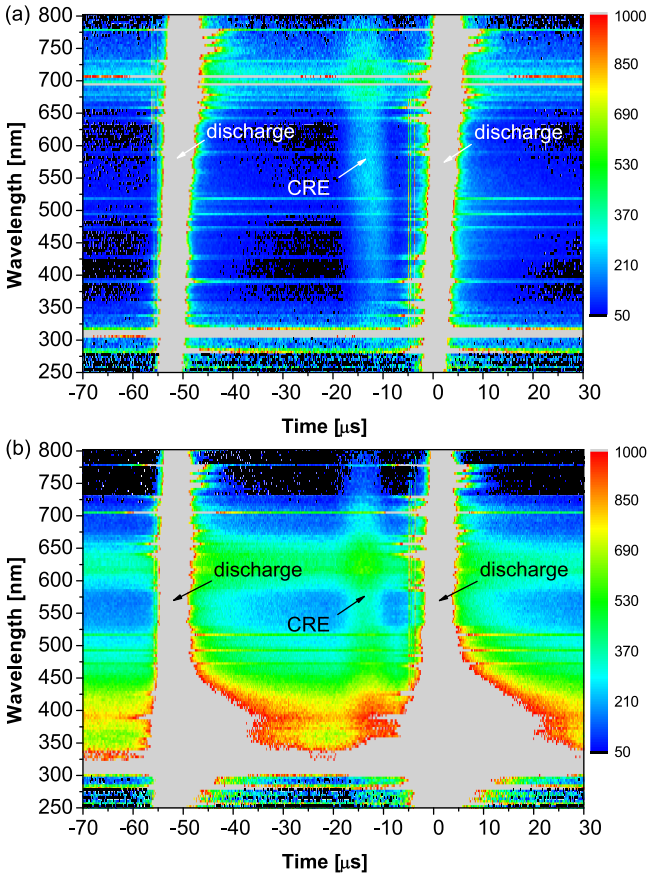

Figure 5. Time-resolved spectra of a helium coplanar discharge with (a) Al_2O_3 dielectric and (b) AlN dielectric. The charge relaxation event is marked with an arrow as CRE.

effectively converted to N_2^+ or O_2^+ by charge transfer reactions [14]. The He_2^+ ions recombine with electrons dissociatively, leaving one helium atom in an excited state. Although dissociative recombination from the ground state of the He_2^+ molecule is a slow process in comparison with other rare gases [15], dissociative recombination from higher vibrational states ($v \geqslant 3$) is much faster (2×10^{-7} cm^3 s^{-1}). Since it can even produce helium atoms in excited states with $n = 3, 4$ (see the discussion and the references in [16] for more information), helium atomic lines are observed in late-time spectra. Lines of atomic oxygen appear, e.g., as a consequence of Penning ionization of molecular oxygen by helium metastable species followed by dissociative recombination of O_2^+ ions into the $3p\ ^5P$ state.

Besides line emissions, continuous spectral bands were observed in the UV and red regions during the entire period. As will be shown in sections 3.2.1 and 3.2.2, they can be assigned to the luminescence of the dielectric. Moreover, weak light emission exhibiting a continuous spectrum over the whole measured region (250–800 nm) was observed just during the time of the charge relaxation event (see CRE in figure 5). The light was observable for about 8 μs. Afterwards, its intensity decreased and later the light emission from Townsend avalanching became visible.

In order to obtain the light attributable specifically to the charge relaxation event, spectra were summed in a time

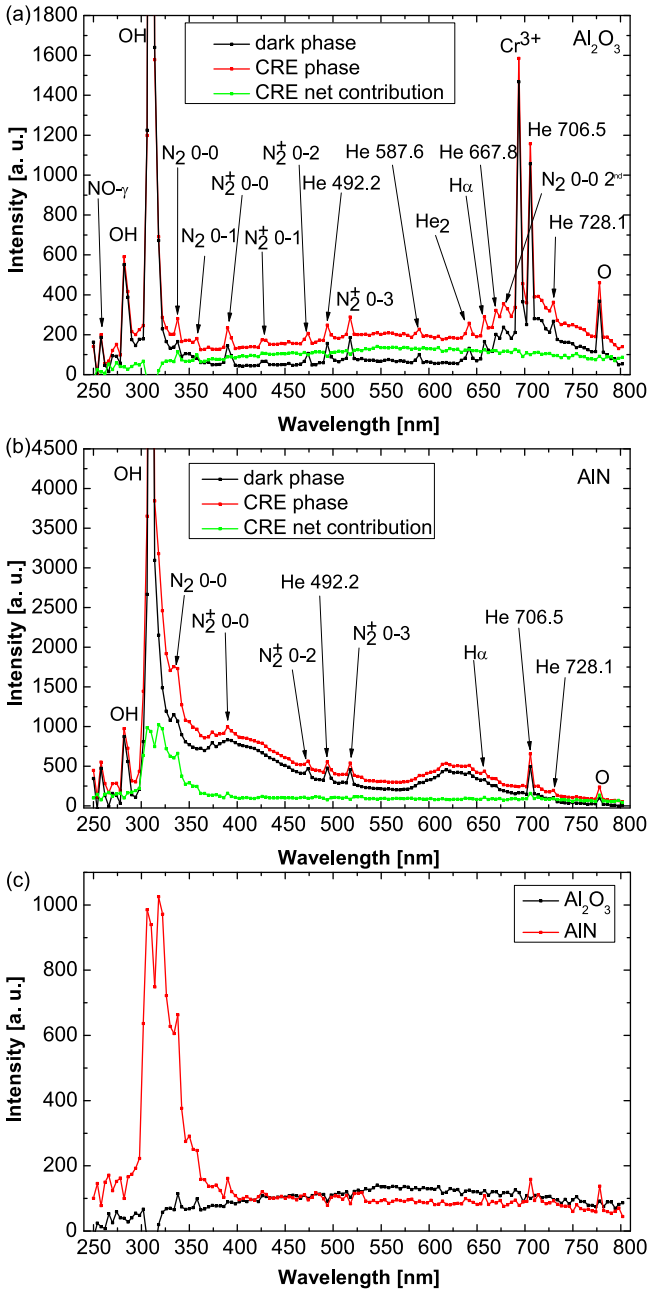

Figure 6. Spectra of the dark phase, CRE phase and CRE net contribution in a helium discharge on (a) Al_2O_3 dielectric and (b) AlN dielectric. (c) Pair comparison of net contributions of the charge relaxation event on Al_2O_3 and AlN.

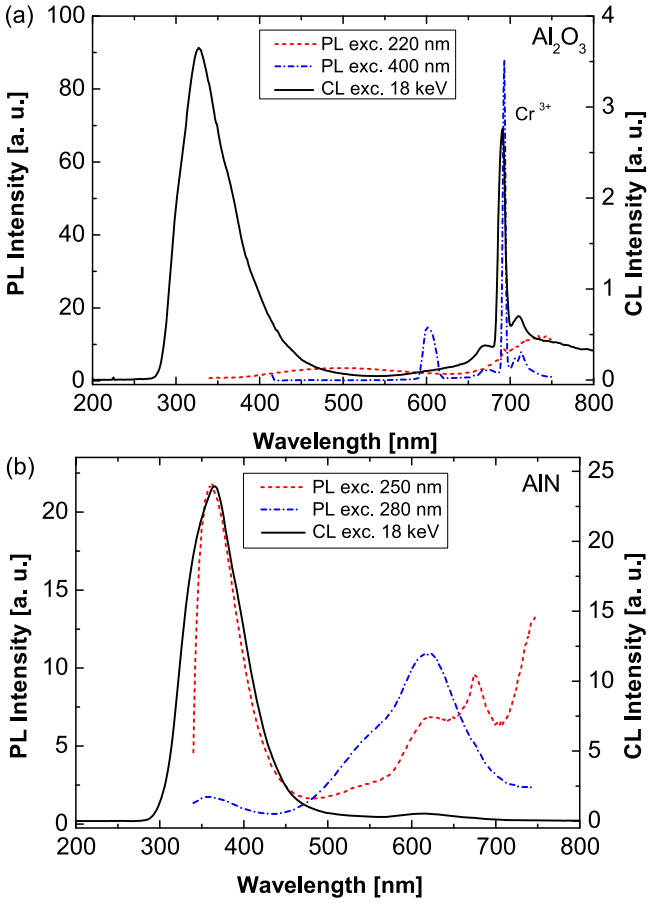

Figure 7. Photoluminescence and cathodoluminescence emission spectra of (a) Al_2O_3 and (b) AlN dielectric. The spectra were corrected for the spectral sensitivities of the apparatus. The intensities in PL spectra (or CL spectra) can be mutually compared.

interval of 7 μs during the CRE occurrence (or during CRE phase) as well as in an interval of 7 μs just preceding the CRE to get the dark phase background signal. The summed signals and their difference are depicted in figures 6(a) and (b) for discharges on Al_2O_3 and AlN dielectric, respectively. Since the contribution of dielectric luminescence to the optical signal has to be examined carefully, in the following the discharge spectra will be compared to luminescence spectra of a particular dielectric barrier obtained by independent measurements. In those measurements, ceramics were irradiated either by monochromatic light or by a controlled electron beam, and the photoluminescence (PL) or cathodoluminescence (CL) spectra were measured.

3.2.1. Al_2O_3. As mentioned in the discussion of the spectral maps, most of the lines in the spectrum of the dark phase in figure 6(a) can be easily associated with the emissions either from helium itself or from impurities present in the gas; the striking exception is a strong line at 694 nm. PL and CL emission spectra of the Al_2O_3 sample are depicted in figure 7(a). Since the light emission at 694 nm was clearly detected in both PL and CL spectra, the line at 694 nm had to originate from the ceramic and not from the gas. More specifically, the line was produced by emission on centres caused by Cr^{3+} impurity in the lattice of α-alumina [17]. In fact, the line is comprised of two lines at 692.9 and 694.3 nm (sometimes referred to as R lines) but they cannot be discerned, due to low resolution [18]. The Cr^{3+} ions are responsible also for two other relatively narrow peaks, located around the 694 nm line in the measured CL spectrum [19]. As stated in [20], these two lines are related to the same electronic transition as the line at 694 nm and arise from the creation or destruction of one or more quanta of lattice

vibrational energy (phonons or local modes) occurring simultaneously with the electronic transition.

Besides the Cr^{3+} line, weak wide bands at 270–370 nm and 650–800 nm are present in the spectra of both the dark phase and the phase of the charge relaxation event (CRE phase). These bands can also be assigned to the luminescence of the Al_2O_3 dielectric. In the case of Al_2O_3 cathodoluminescence, the CL spectrum is dominated by the emission band centred near 330 nm. This band might be caused by the oxygen vacancies forming F- and F^+-centres, as proven in Al_2O_3:C single crystals and in the nanostructured Al_2O_3 ceramic [21].

Photoluminescence spectra also exhibit increased intensity in the vicinity of the 694 nm peak. Low peaks at 713 nm and 668 nm can be clearly distinguished in emission spectra for excitation at 400 nm, which agrees well with the cathodoluminescence measurement. As explained above, these peaks are related to the Cr^{3+} impurity. The broad band at 650–750 nm observed in the spectra for excitation at 220 nm can be attributed to the presence of Ti^{3+} impurity [22].

On the other hand, both the Cr^{3+} line and the continuous bands in the UV and red parts of the spectrum of the dark phase are not present in the spectrum of the CRE net contribution. The CRE contribution is a flat continuum with a maximal intensity at 550 nm spreading over the whole measured region (250–800 nm). Hence the light specifically appearing during the relaxation event was not produced by any long-lasting luminescence of the ceramics but rather by a different process exhibiting a continuous spectrum.

3.2.2. AlN. The spectra of the discharge on AlN dielectric during the dark phase and the CRE phase are shown in figure 6(b). All the lines appearing in the raw CRE spectrum (spectrum of the CRE phase) can be assigned to emissions from the gas phase. Nevertheless, unlike in Al_2O_3, a strong continuous band at 300–550 nm and also an intense spectral region at 570–720 nm can be observed in the spectra of both the CRE phase and the preceding dark phase. Moreover, a part of the UV band below 400 nm appears also in the spectrum of the CRE net contribution, having its greatest intensity there.

The PL and CL emission spectra of the AlN sample are depicted in figure 7(b). In general, the spectra are stronger than the PL and CL spectra of Al_2O_3. The dominant peak with a maximum at 370 nm in both PL and CL spectra was attributed to the recombination process between two types of oxygen-related centres in the AlN lattice [23]. Furthermore, both PL and CL spectra exhibit an increase of intensity in the spectral region above 570 nm, which is probably connected to the accidental presence of Mn^{4+} ions substituting the Al^{3+} ones, as explained, e.g., in [23, 24].

Comparing the spectra of the discharge and the ceramic, one can assume that the luminescence of the AlN dielectric is the main source of light within the continuous spectrum during the dark phase. Furthermore, the AlN luminescence in the UV remains the dominant contributor to the net light emission of the charge relaxation event. Still, the CRE net light emission has the same flat continuous spectrum in the remaining spectral region of 400–800 nm as it had in the case of Al_2O_3.

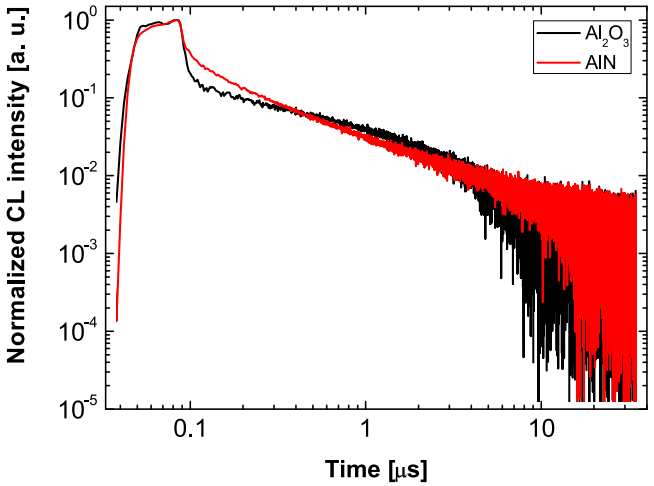

Figure 8. Spectrally unresolved cathodoluminescence decays of Al_2O_3 and AlN dielectrics under pulsed electron beam excitation.

The CL decay curves of both ceramics were recorded for 40 μs from the excitation pulse. This time corresponds to the typical timespan between the last discharge and the consequent relaxation event. As can be seen from figure 8, the CL decay curve of AlN exhibited a fast component and a slow one. The straight line in the presented log–log plot indicates a power-law dependence of the CL temporal development. According to [25, 26] this favours tunnel recombination between donor–acceptor centres with a random distribution of separation. The CL decay curve of Al_2O_3 is more complex, as it seems to be composed of at least three exponentials with different decay times. This indicates the presence of more types of luminescence centres of different origin. In any case, the curves in figure 8 confirmed the acceptable level of systematic error made by subtracting the background signal of a dark phase time that is different to the actual time of the CRE occurrence.

To conclude, the light emission associated with the charge relaxation event seems to consist of two main contributions: (1) dielectric luminescence, which is material-specific, and (2) material-independent broad continuous radiation with a maximum around 550 nm; see figure 6(c). The identification of the process responsible for the latter is provided in the next section.

3.3. The origin of broad continuum radiation

The observation of the broad continuum in discharges with different dielectrics favours a hypothesis in which the continuum light is produced by a process occurring in the gas phase. For the coplanar barrier discharge studied here, the following possible origins of continuous radiation were considered:

- **Molecular continua.** The Hopfield continuum emitted by neutral helium excimers He_2 ($A\ ^1\Sigma_u^+ \rightarrow X\ ^1\Sigma_g^+$) appears in

the vacuum UV (VUV, 60–120 nm) [27]. On the other hand, so-called third continua are observed in the UV–VIS region in rare gases due to transitions between states of singly charged molecular ions [28]. In the case of helium, the Huffmann–Tanaka continuum He_2^+ ($C\ ^2\Pi_u \rightarrow A\ ^2\Sigma_g^+$) has a maximum at 360 nm and decreases until 650 nm at 300 K [29]. As pointed out in [30], due to involvement of He_2^+ ions the continuum should be sensitive to admixture of another gas with a lower ionization energy (e.g. neon).

Since the discharge was burning in a controlled atmosphere but not in a vacuum cell, the role of impurities is minute but cannot be completely ruled out. However, the molecular continuum of NO_2 ($^2B_2 — X\ ^2A_1$), produced, for example, in the reaction between NO and O [31], appears above 400 nm and has a more pronounced shape than in the measurement presented in figure 6(c). The H_2 molecular continuum ($a\ ^3\Sigma_g^+ \rightarrow b\ ^3\Sigma_u^+$) is observed below 400 nm, clearly increasing towards the VUV region [32].

To sum up, light emission from typical molecules does not seem to be responsible for the observed continuum.

- **Recombination spectra: free–bound (f–b) transitions.** As mentioned in section 3.2, He_2^+ is the dominant ion in cold helium plasmas at atmospheric pressure. In contrast to atomic ions, the molecular ions recombine dissociatively, producing an atomic line spectrum. The continuous recombination spectrum of atomic He^+ ions in different conditions has been studied in [33]. The recombination continuum due to f–b transitions down to the 2 ^{3}P state was observed in the UV below 342 nm and was accompanied by atomic lines of transitions $n\ ^3$D–2 ^{3}P from highly excited states (n = 6–12) above this wavelength. Thus, even the shape and presence of highly excited states are different from the situation studied here.

  Since the atomic ions are not expected to be present in the gap at late times, it is possible to rule out also the recombination of atomic ions as a production channel of the observed continuum.
- **Bremsstrahlung: free–free (f–f) transitions.** Bremsstrahlung produced during electron elastic collisions on neutral atoms and ions has a continuous spectrum [34]. Since the ionization ratio is very low under the conditions studied, the dominant role of neutral atoms can be assumed. This is further justified by the observation of the relaxation event above the instantaneous anode with negatively charged dielectric (see the times before phase a in figure 3). Neutral bremsstrahlung has a continuous spectrum in the visible region in rare-gas glow discharges [35]. It has been observed recently in atmospheric pressure argon discharges operating under more or less similar conditions [36–38].

  Finally, neutral bremsstrahlung is a probable source of the observed continuous radiation. See similar discussions in [37, 38].

The hypothesis of the neutral bremsstrahlung being the main source of the continuous spectrum seems to be the most plausible for the coplanar barrier discharge situation studied here. At the moment of termination of the active discharge, the attractive Coulomb force between the surface charges of oppositely charged dielectric electrodes is surpassed by the tangential component of the applied external field. As the external voltage progresses to its zero value during the subsequent voltage swing, at some moment the attractive Coulomb force prevails. Some fraction of weakly bound electrons residing on the dielectric of the instantaneous anode can detach from the surface and propagate through the gap towards their positive counterparts on the instantaneous cathode surface, being accelerated by this surface charge field. Because the field is lower than the field expected during the current pulse [39], the electrons are not capable of exciting the same species as in the active discharge. Hence, only the products of elastic collisions with neutral atoms (neutral bremsstrahlung) and of collisions with the dielectric (cathodoluminescence of AlN) are observed.

A theory of neutral bremsstrahlung will be applied to the measured continuous radiation in the next section. The dependence of the bremsstrahlung continuum on electron energies enabled us to further test the bremsstrahlung hypothesis. Moreover, a small admixture of neon, which does not disrupt the diffuse character of the discharge, was added to helium to study the continuum behaviour. Since the large intensity of AlN luminescence complicated the investigation of the continuum, attention was paid only to measurements on Al_2O_3 dielectric.

3.4. Analysis of the measured continuum as the neutral bremsstrahlung

A survey of various formulae for intensity of bremsstrahlung continuum (BC) can be found, e.g., in [40]. Most of the calculations have utilized the bremsstrahlung differential cross section in a form [41]

$$\frac{\mathrm{d}\sigma(\varepsilon)}{\mathrm{d}\lambda} = \frac{4\alpha}{3\pi}\frac{\varepsilon}{m_e c^2 \lambda}\sqrt{1-\frac{h\nu}{\varepsilon}}\left(2-\frac{h\nu}{\varepsilon}\right)\sigma_m(\varepsilon),$$

where λ is the wavelength, α the fine-structure constant, ε the energy of the colliding electron and $h\nu$ the photon energy. When $h\nu \ll \varepsilon$, $\sigma_m(\varepsilon)$ is a momentum transfer cross section for electron collisions with helium atoms. In the visible region, where the energies of photon and electron are comparable, the bremsstrahlung cross section can be approximated with the same formula, replacing only $\sigma_m(\varepsilon)$ by the elastic cross section $\sigma_{el}(\varepsilon)$ [41]. The difference between $\sigma_m(\varepsilon)$ and $\sigma_{el}(\varepsilon)$ is below 16% for $\epsilon < 19$ eV for helium [42]. Therefore, $\sigma_m(\varepsilon)$ taken from [43] could be used in the calculations. Since the energy dependence of $\sigma_m(\varepsilon)$ is weak, it can even be assumed to be constant [40].

The spectral emission coefficient is calculated as

$$I(\lambda; E/N) = \frac{1}{4\pi} n_e N h\nu \sqrt{\frac{2}{m_e}} \int_{h\nu}^{\infty} \frac{\mathrm{d}\sigma(\varepsilon)}{\mathrm{d}\lambda} f(\varepsilon; E/N)\varepsilon\, \mathrm{d}\varepsilon,$$

where n_e is electron density, N helium atom density and $f(\varepsilon)$

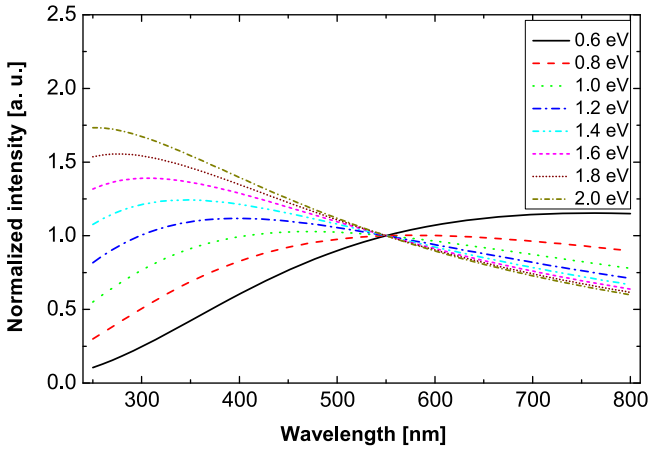

Figure 9. Calculated variation of the neutral bremsstrahlung continuum of electrons on helium atoms with electron temperature, assuming a Maxwellian EDF. The plot shows the normalized intensity $I(\lambda)/I(550\ \text{nm})$.

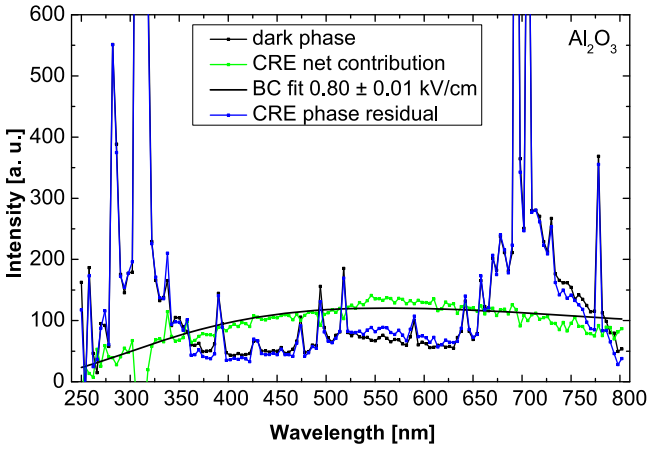

Figure 10. Example of the fit of the net contribution of the charge relaxation event in a pure helium discharge on Al_2O_3 dielectric with the model of neutral bremsstrahlung. The spectra of the dark phase, that of the net contribution of the charge relaxation event and the residual spectrum of the phase of the relaxation event after the subtraction of the bremsstrahlung continuum model are shown for comparison.

the electron distribution function (EDF). Since the EDF is non-Maxwellian under the conditions studied, a Boltzmann kinetic equation (BKE) for a stationary EDF was solved assuming the classical two-term approximation for the EDF for a specific reduced electric field E/N and a gas mixture (helium with a small neon admixture). The cross sections for binary elastic and inelastic electron collisions with ground-state atoms of helium and neon were taken from [43, 44]. The correctness of the BKE solver used was checked by comparing the EDF obtained to that of Bolsig+ [45]. Because the neon admixture was less than a few per cent, the bremsstrahlung of electrons colliding with neon atoms could be neglected.

The procedure described enabled us to fit the measured spectrum, i.e. the net contribution in figure 6(c), with the bremsstrahlung model $I(\lambda; E/N)$ using the least-squares method. In order to diminish the role of some long-lasting emissions still present to a small degree in the net contribution (such as OH, which decreases quickly and cannot be simply subtracted), weights inversely proportional to the intensity measured in the dark phase were introduced into the sum. A neutral gas temperature of 300 K was assumed in the calculations of the final electric field strength.

Examples of neutral bremsstrahlung continuum calculated with a Maxwellian EDF instead and for different electron temperatures are shown in figure 9. The curves were normalized to have unit intensity at 550 nm. As can be seen, the curves are flat with their maxima in the visible region when the electron temperature is around 1 eV. At higher and lower electron temperatures the maximum moves to the UV and IR regions, respectively.

3.4.1. Time-averaged spectra. The fit of the net contribution of the charge relaxation event in a pure helium discharge on Al_2O_3 dielectric with the model of neutral bremsstrahlung is displayed in figure 10. The model of the BC calculated for the electric field of 0.8 kV cm^{-1} and the residual spectrum of the phase of the relaxation event with the BC fit subtracted are

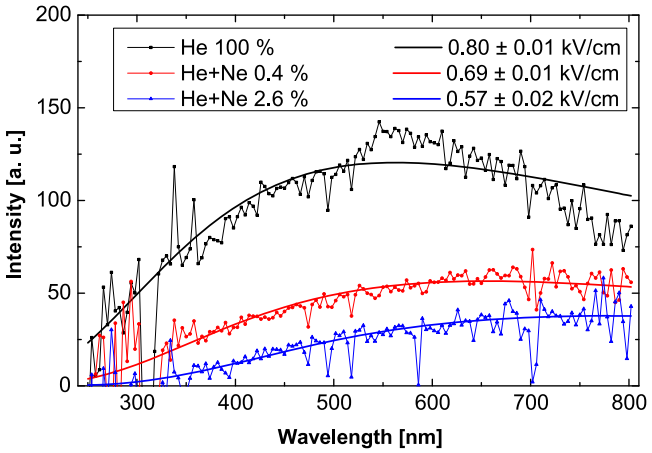

Figure 11. Fits of the summed CRE net-contribution spectra in discharges on Al_2O_3 in pure helium and in helium–neon mixtures with the model of neutral bremsstrahlung. Electric fields are calculated assuming a gas temperature of 300 K. Uncertainties are only statistical.

shown in addition to the curves shown already in figure 6(a). As can be seen, the BC with a flat maximum at 566 nm fits the measured spectrum well. In this sense, the BC fit served as a tool to probe the electric field strength in the gap. A small difference between the calculated residual spectrum and the measured spectrum of the dark phase suggests that, in practice, only the bremsstrahlung continuum is added to the background radiation by the charge relaxation event.

A comparison of fitted spectra of CRE net contributions in various neon admixtures is shown in figure 11. The admixture of a small amount of neon shifted the onset voltage of the discharge to lower values. The intensity of the continuum decreased slightly and its maximum shifted to the red region. Consequently, the electric fields obtained from the fit were lower in mixtures containing neon. The small alteration of the continuum caused by the neon admixture

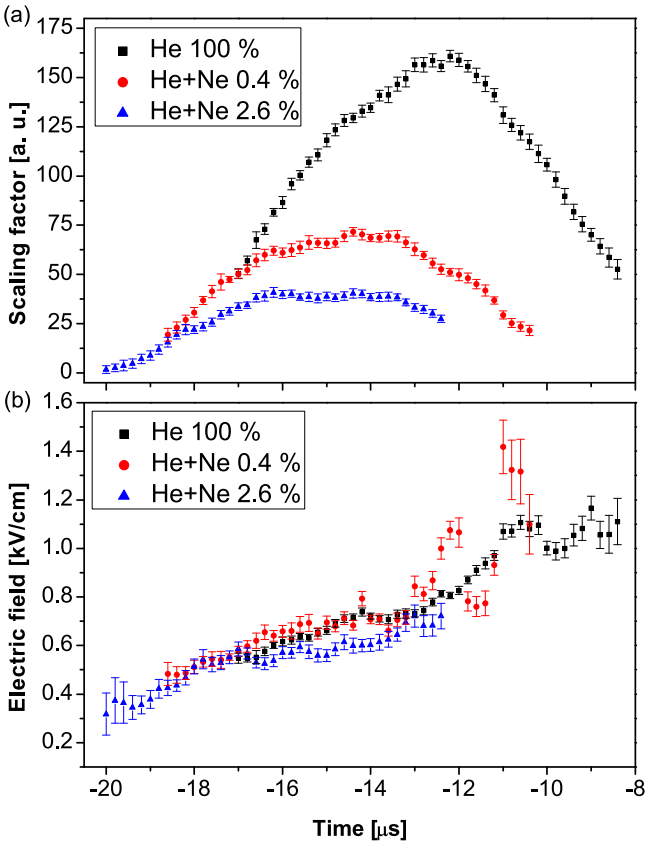

Figure 12. Time development of (a) scaling factor and (b) electric field during the development of the relaxation event in pure helium and two helium–neon mixtures on Al_2O_3 obtained from the fits of time-resolved net-contribution spectra. Uncertainties are only statistical.

suggests [30] that He_2^+ ions are not involved in the production of the continuous radiation.

3.4.2. Time-resolved spectra. As can be seen in figure 5, the CRE continuum was registered during the time interval of 8 μs, appearing in 40 measured spectra in total (each spectrum covered 0.2 μs of the high-voltage period). Therefore, the time development of the continuum could be investigated during the 8 μs interval. In order to overcome the low level of intensity in the spectra, the temporal development of the continuum was analysed from the signal moving average, created from the original series of spectra by averaging over three successive time steps. Similarly to the time-averaged spectra, the dark phase background was subtracted from the signal. The results of the final spectral fits are presented in figure 12 for different neon admixtures.

The development of the scaling factor, which adjusts the normalized intensity of the simulated BC to the measured values, is presented in figure 12(a). The continuum has the highest intensity in the pure helium discharge, as has already been shown in figure 11. It can also be seen that the admixture of neon resulted in a shift of the relaxation event (hence the appearance of BC) to earlier times.

The temporal development of the fitted electric fields is presented in figure 12(b). As can be seen, all three time developments follow the same linear trend. Such an exceptional coincidence derived from quite different shapes of BC (see figure 11) provides strong support for our neutral bremsstrahlung hypothesis. The trend has the same slope as the corresponding waveform of applied voltage in figure 4. Owing to the tiny number of electrons involved in the process of charge relaxation, the distortion of the global electric field by the charge relaxation event should be minimal. Therefore, one can reasonably interpret the trend of the electric field in figure 12 as the time development of the average field within the whole discharge space (note that the signal was collected from the whole driven-electrode region and was not spatially resolved). The external voltage reaches its zero value at the time of -14 μs in figure 12. For this particular moment, the electric field calculated from BC corresponds to the surface charge field only. The spatially averaged memory field is the same for all three gas mixtures investigated, and is some 0.6–0.7 kV cm^{-1}.

4. Conclusion

The phase-resolved single photon spectroscopy of light emission during the dark phase of a helium diffuse coplanar barrier discharge revealed the presence of ongoing background dielectric luminescence and gas-phase light emissions. When the charge relaxation event appeared at times close to the reversal of electrode polarity, the light emission in the dark phase was extended by a very broad continuum. In the case of AlN, the relaxation event also caused some enhancement of the dielectric luminescence.

The most probable origin of the observed broad continuum is the bremsstrahlung of slow electrons colliding with neutral helium atoms. The fitting procedure developed on the basis of the bremsstrahlung model reproduced well the observed shape of the continuum and also provided a method for determination of the electric field in the discharge during the relaxation event. At those times, the electric fields reached 1 kV cm^{-1}. A natural, but extremely challenging next step is to employ the bremsstrahlung continuum to obtain the spatially resolved development of the electric field.

Acknowledgments

This research has been supported by the Czech Science Foundation, contract No. GA13-24635S and by the project CZ.1.05/2.1.00/03.0086 funded by European Regional Development Fund and project LO1411 (NPU I) funded by Ministry of Education, Youth and Sports of the Czech Republic. The authors would like to express their gratitude to Mgr. Ján Krausko for performing the photoluminescence measurements.

References

[1] Bogaczyk M, Wild R, Stollenwerk L and Wagner H-E 2012 *J. Phys. D: Appl. Phys.* **45** 465202
[2] Akishev Y, Aponin G, Balakirev A, Grushin M, Karalnik V, Petryakov A and Trushkin N 2011 *Plasma Sources Sci. Technol.* **20** 024005
[3] Tschiersch R, Bogaczyk M and Wagner H-E 2014 *J. Phys. D: Appl. Phys.* **47** 365204
[4] Wild R, Benduhn J and Stollenwerk L 2014 *J. Phys. D: Appl. Phys.* **47** 435204
[5] Morávek T, Čech J, Navrátil Z and Ráhel' J 2016 *Eur. Phys. J. Appl. Phys.* **75** 24706
[6] Gibalov V I and Pietsch G J 2012 *Plasma Sources Sci. Technol.* **21** 024010
[7] Kozlov K V, Wagner H-E, Brandenburg R and Michel P 2001 *J. Phys. D: Appl. Phys.* **34** 3164
[8] Navrátil Z, Brandenburg R, Trunec D, Brablec A, St'ahel P, Wagner H-E and Kopecký Z 2006 *Plasma Sources Sci. Technol.* **15** 8
[9] Bok J and Schauer P 2014 *Meas. Sci. Technol.* **25** 075601
[10] Kogelschatz U 2002 *IEEE Trans. Plasma Sci.* **30** 1400
[11] Brandenburg R, Navrátil Z, Jánský J, St'ahel P, Trunec D and Wagner H E 2009 *J. Phys. D: Appl. Phys.* **42** 085208
[12] Massines F, Gherardi N, Naudé N and Ségur P 2009 *Eur. Phys. J. Appl. Phys.* **47** 22805
[13] Jonkers J, van de Sande M, Sola A, Gamero A, Rodero A and van der Mullen J 2003 *Plasma Sources Sci. Technol.* **12** 464
[14] Murakami T, Niemi K, Gans T, O'Connell D and Graham W G 2013 *Plasma Sources Sci. Technol.* **22** 015003
[15] Ivanov V A 1992 *Usp. Fiz. Nauk* **162** 35
[16] Pedersen H B *et al* 2005 *Phys. Rev.* A **72** 012712
[17] Chapoulie R, Capdupuy C, Schvoerer M and Bechtel F 2010 *Phys. Status Solidi* A **171** 613
[18] Snytnikov V N, Stoyanovskii V O, Ushakov V A and Parmon V N 2005 *Kinetics and Catalysis* **46** 260
[19] Kiiko V S, Makurin Yu N, Safronov A A, Enyashin A N and Ivanovskii A L 2003 *Refract. Ind. Ceram.* **44** 94
[20] Nelson D F and Sturge M D 1965 *Phys. Rev* **137** A1117
[21] Kortov V S, Ermakov A E, Zatsepin A F and Nikiforov S V 2008 *Radiat. Meas.* **43** 341
[22] Powell R C, Venikouas G E, Xi L, Tyminski J K and Kokta M R 1986 *J. Chem. Phys.* **84** 662
[23] Trinkler L and Berzina B 2014 *Phys. Status Solidi* B **251** 542
[24] Benabdesselam M, Iacconi P, Lapraz D, Grosseau P and Guilhot B 1995 *J. Phys. Chem.* **99** 10319
[25] Jain M, Guralnik B and Andersen M T 2012 *J. Phys.: Condens. Matter.* **24** 385402
[26] Huntley D J 2006 *J. Phys.: Condens. Matter* **18** 1359
[27] Carman R J, Ganesan R and Kane D M 2016 *J. Phys. D: Appl. Phys.* **49** 085201
[28] Boichenko A M, Tarasenko V F and Yakovlenko S I 1999 *Laser Phys.* **9** 1004
[29] Hill P C 1991 *Phys. Rev.* A **43** 2546
[30] Lissovski A and Treshchalov A 2003 *ICPIG 26th Proc.* vol 3 *(Greifswald)* p247
[31] Adler-Golden S M 1989 *J. Phys. Chem.* **93** 691
[32] Fantz U, Schalk B and Behringer K 2000 *New J. Phys.* **2** 7.1
[33] Ohno Y, Nezu A, Matsuura H and Akatsuka H 2015 *Prog. Nucl. Energy* **82** 130
[34] Biberman L M and Norman G E 1967 *Sov. Phys. Usp.* **10** 52
[35] Rutscher A and Pfau S 1976 *Physica* C **81** 395
[36] Park S, Choe W, Moon S Y and Park Y 2014 *Appl. Phys. Lett.* **104** 084103
[37] Bazinette R, Paillol J and Massines F 2015 *Plasma Sources Sci. Technol.* **24** 055021
[38] Nikiforov A Y, Ionita E-R, Dinescu G and Leys C 2016 *Plasma Phys. Control. Fusion* **58** 014013
[39] Ivković S S, Sretenović G B, Obradović B M, Cvetanović N and Kuraica M M 2014 *J. Phys. D: Appl. Phys.* **47** 055204
[40] Burm K T A L 2004 *Plasma Sources Sci. Technol.* **13** 387
[41] Kas'yanov V and Starostin A 1965 *Sov. Phys - JETP* **21** 193
[42] Nesbet R K 1979 *Phys. Rev.* A **20** 58
[43] Biagi-v7.1 database www.lxcat.net (Accessed: 11 May 2016)
[44] Biagi-v8.9 database www.lxcat.net (Accessed: 11 May 2016)
[45] Hagelaar G J M and Pitchford L C 2005 *Plasma Sources Sci. Technol.* **14** 722

IOP Publishing Plasma Sources Science and Technology
Plasma Sources Sci. Technol. **27** (2018) 105002 (13pp) https://doi.org/10.1088/1361-6595/aade41

2D-resolved electric field development in helium coplanar DBD: spectrally filtered ICCD camera approach

Jan Čech, Zdeněk Navrátil, Michal Štipl, Tomáš Morávek and Jozef Ráheľ

Department of Physical Electronics, Faculty of Science, Masaryk University, Kotlářská 2, 611 37 Brno, Czech Republic

E-mail: cech@physics.muni.cz

Received 24 April 2018, revised 17 August 2018
Accepted for publication 31 August 2018
Published 9 October 2018

Abstract

Electric field strength in diffuse coplanar barrier discharge in helium at atmospheric pressure, driven by AC voltage (amplitude 1.5 kV, frequency 10 kHz), was measured by optical emission spectroscopy. Two helium singlet lines at 667.8 nm (He I 2 ^{1}P–3 ^{1}D) and 728.1 nm (He I 2 ^{1}P–3 ^{1}S) were recorded within the discharge space and period with a high spatial (20 μm) and temporal (50 ns) resolution and analyzed with the line intensity ratio method developed by Ivković *et al* 2014. A novel experimental approach, based on a direct observation of the discharge by ICCD camera through two interference filters, was developed to obtain 2D spatially resolved distributions of the electric field. The obtained results proved the existence of several developing regions of high electric field, namely the cathode-directed and anode ionization waves. The electric field in the cathode-directed wave peaked at 32 kV/cm during the first contact of the wave with the cathode's dielectrics, followed by a decrease to values of 15–25 kV/cm above the electrode. The electric field in the anode-directed wave was lower, reading some 15 kV/cm. The performed 'sensitivity analysis' pointed out the crucial importance of precise temporal and spatial synchronization for the techniques based on the intensity ratio of two spectral lines. Artificially introduced 50 ns misalignment between the measured data of both spectral lines resulted in the substantial distortion of the electric field map. Reduction of the temporal resolution from 50 to 100 ns led to the decrease of electric field maxima by 30%. The reduction of the spatial resolution from 20 to 40 μm decreased the maximal field value by 10%.

Supplementary material for this article is available online

Keywords: electric field, dielectric barrier discharge, coplanar, helium, ICCD, 2D, intensity ratio

1. Introduction

The magnitude of local reduced electric field (E/N) is the principal parameter controlling the outcome of the major processes of electrical gas discharges. These include the initiation and dynamics (propagation) of electrical breakdown, shape of electron energy distribution function, spectral emission characteristics of ionized gas, etc. Owing to the similarity law, the driving processes of high-pressure dielectric barrier discharges (DBDs) are constricted to the volumes of only several tens of μm characteristic size. Moreover, the characteristic time domain of the active phase of DBDs is frequently only a few ns [1]. The resulting experimental obstacles have stimulated an unceasing search for new, highly resolved (both spatially and temporally) techniques for the measurement of local E/N development (see e.g. [2]).

The nature of DBDs does not permit us to use the classical technique of electrical probe measurement (see e.g. [3]), mainly due to the unacceptable disturbance of the measured plasma system. On the other hand, passive optical probing via optical emission spectroscopy (OES) avoids any external

disturbance of the investigated plasma system. In the literature, two major groups of optical probing techniques for measuring the electric field in plasmas can be distinguished: a) the '*ab initio*' methods utilizing mainly the Stark effect, i.e. shift of individual atomic lines induced by the presence of external electric field; and b) the 'intensity ratio' methods utilizing the relation between the spectral distribution of the plasma emission (i.e. the relative populations of energy states of emitting atoms and/or molecules) and the local electric field. Both groups of techniques require spectrally resolved signal. Spatially resolved E/N measurements have to be done either by the point-to-point (0D) or line-to-line (1D) approach, which is not only exceedingly time consuming, but may be a serious source of detrimental measurement artefacts. One of the goals of the presented paper is to present a simple experimental variation of the 'intensity ratio' method, which allows highly resolved 2D imaging of the electric field evolution and better control over the output analysis.

Considering the plasma diagnostic techniques, there is always a trade-off between the accuracy, sensitivity, versatility and speed of the data acquisition. The *ab initio* methods of electric field measurement based on quantum-mechanical effects seem to be the most plausible, since they can provide direct and absolute dependencies of spectral attributes on the electric field. Using the Stark effect, the electric field is typically evaluated from a splitting or shifting of spectral lines of hydrogen or helium [4–6]. The so-called Stark polarization OES, developed originally for electric field measurement in low-pressure helium discharge [7], has also been used for the electric field measurement at atmospheric pressure in helium volume DBD [8], in an ionizing wave/streamer in 13 or 30 kHz helium atmospheric pressure plasma jets [9, 10] or in a γ-mode sheath of atmospheric pressure radio-frequency discharge [11]. The method has supplied valuable experimental data for the direct comparison of the electric field in helium atmospheric pressure discharges to the outputs of numerical studies, see e.g. [12–14].

For low-pressure discharges, the laser-assisted method of Stark shift measurement exhibiting high temporal resolution and superb sensitivity to the electric field (10 V cm^{-1}) was developed [15]. However, such an order of sensitivity is completely unavailable at atmospheric pressure. As known from the Stark effect theory and experiments, the sensitivity of the energy level (and then also of the spectral line originating from this level) to the electric field increases with the principal quantum number (see e.g. [16] for the case of helium). This is what mostly limits the method sensitivity at higher pressure, since the highly excited states are effectively quenched. The most sensitive lines are therefore not observed. Moreover, pressure broadening of spectral line profiles hinders the precise measurement of spectral line positions at atmospheric pressure. Another drawback of the Stark method is in the high spectral resolution that is necessary to accurately determine subtle changes of spectral line profiles due to varying electric field. This limits considerably their throughput, especially for highly spatially resolved measurements, which are needed for proper DBD characterization. Therefore, the indirect intensity ratio methods, which do not require such high spectral resolution, are of considerable interest.

The intensity ratio methods are based on collisional-radiative (CR) modeling [17]. Due to the variation of electron distribution function and of the rates of electron excitation processes with the reduced electric field strength (E/N), the light emission rates from excited states are dependent on the electric field. Although this approach presents the possibility of comparing the intensities on absolute scale or to fit the full emission spectrum to obtain the E/N (see e.g. [18, 19]), mostly the ratio of intensities of two carefully selected lines (or bands) is taken as the spectral marker. This approach greatly simplifies the measurement, but at the cost of reliability of the method. The critical point of the method lies in the assessment of this calibration function, binding the local E/N magnitude with the line intensity ratio. The validity constraints placed by the used CR model or the necessity of precise experimental calibration using a plasma source with known E/N limits their usage to a narrow range of discharge conditions. Still, the intensity ratio methods represent a well-established tool for E/N characterization in atmospheric pressure DBDs of nitrogen/oxygen gas mixture [20–22], or recently of argon mixtures [22] and helium [23].

The intensity ratio method developed by Ivković *et al* [23] utilizes two helium singlet lines, 667.8 nm (HeI 2 ^{1}P–3 ^{1}D) and 728.1 nm (HeI 2 ^{1}P–3 ^{1}S), as the spectral marker of the local electric field in helium discharges. Using the CR model validated through the Stark polarization spectroscopy, the calibration curve between the intensity ratio $R = I_{667}/I_{728}$ and the strength of the electric field was obtained in the range 3–40 kV cm^{-1} for $T = 310$ K.

$$E(R) = 2.224 - 20.18 \times R + 45.07 \times R^2 - 19.98 \times R^3 + 3.369 \times R^4, \quad [E] = \text{kV cm}^{-1}. \tag{1}$$

However, stepwise excitation from metastables to the observed levels introduces extra dependence of the intensity ratio on the metastable density, being critical below 3 kV cm^{-1}. The method enabled direct observation of cathode fall formation in atmospheric pressure helium volume DBD [23]. In this case, 1D spatial resolution was obtained by a projection of the discharge onto the entrance slit of the imaging spectrometer.

In the presented article, we are reporting on our attempt to further test this method of the electric field measurement in non-filamentary mode of coplanar barrier discharge in helium [24, 25]. Besides plasma-assisted applications [26], the unique feature of coplanar geometry arrangement is that the formation of the whole discharge breakdown can be observed at the same plane. The planar configuration composed of two electrodes embedded in the dielectric allowed several unique observations of fundamental atmospheric pressure discharge phenomena in air, nitrogen and rare gases in the past [24, 25, 27–33].

A novel experimental approach is presented in this work for 2D spatially resolved mapping of the electric field using the line ratio method, which employs an ICCD camera equipped with a pair of bandpass interference filters for both spectral

lines. The performed measurements provided detailed spatio-temporal distributions of the electric field (section 3). The following method sensitivity analysis investigated experimental aspects, important for valid interpretation of E field results from intensity ratio class methods (section 4).

2. Experimental

A single-electrode pair coplanar DBD developed earlier [29] was used for the measurement. Semi-circular brass electrodes of 20 mm radius with a parallel gap footprint were immersed in an insulating oil bath connected to an external cooling system at room temperature. The electrodes were covered with a 96% Al_2O_3 dielectric plate of $50 \times 50 \times 0.63$ mm^3. The discharge was generated in flowing helium (550 sccm, purity grade 5.0, i.e. 99.999%) at atmospheric pressure on the top of the dielectric plate. The distance between the electrodes was set to 4.75 mm.

The whole setup was housed inside the gas-tight polymeric chamber. Discharge emission was observed through the quartz glass window. The diameter of the visible area was 20 mm. To allow highly accumulated ICCD measurements, the discharge was stabilized in its non-filamentary mode [24, 25]. This mode is also referred to in the literature as a diffuse mode, where the term 'diffuse' means that the 'surface cross-section is covered by the discharge more or less entirely, although the plasma is not necessarily homogeneous in the axial direction' [34]. The discharge was powered by the sine-wave high voltage of 1.6 kVmax, 10.3 kHz. The HV generator was triggered by an Agilent 33220A arbitrary function generator. The V-A discharge characteristics were monitored by a 4-channel digital storage oscilloscope Keysight DSO-S 204A (2GHz@10GSa/s) equipped with an HV probe Tektronix P6015A and Pearson 2877 current monitor.

Optical emission from the discharge plane was recorded by the high-speed ICCD camera (Princeton Instruments PI-MAX3 + SIGMA 105/2.8 EX DG MACRO lens). The camera was clocked by the same function generator as the HV source. The actual gating of the camera's photocathode, provided by the internal digital delay generator, was monitored by the oscilloscope to check the phase-resolved measurement of discharge emission. For the presented high-resolution electric field imaging, the discharge emission on the 667.8 and 728.1 nm spectral lines was recorded subsequently through bandpass filters (Thorlabs FL670-10 and FL730-10 with FWHM of 10 nm and central wavelengths of 670 and 730 nm), attached directly to the lens of the camera. This approach enables precise spatially resolved imaging, but special care had to be taken to ensure spatial alignment and correct time synchronization of both image stacks (see the discussion in section 4). A special optical path was used for the precise time synchronization (see figure 1). In this setup, the camera was focused through the pair of bandpass interference filters mounted at the output of the binocular optical setup (Bino-box). This allowed simultaneous observation of the discharge in two spectral regions, which made it possible

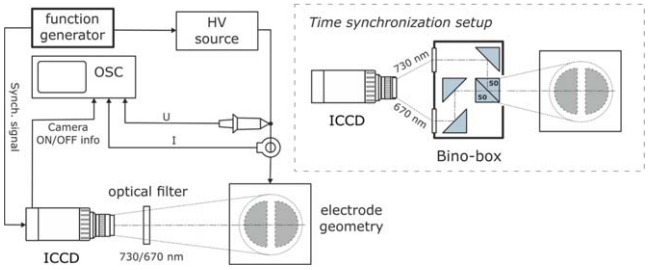

Figure 1. Sketch of the experimental setup for E field measurement. ICCD camera looking directly through a single interference filter at the discharge during the E field measurement. Binocular optical setup was used for precise temporal calibration.

to synchronize the image stacks of both wavelengths. Due to limited spatial resolution and laborious alignment, the Bino-box was used for the temporal synchronization only.

The spatial stabilization of the measurement was ensured by mounting all the optical components as well as the discharge chamber to the optical table. The focusing and positioning to the acquired area was done by the precise motorized linear positioning stages (Zaber T-LSQ 150B in 'xy' + 'z' setup). Temporal stabilization of the discharge appearance was achieved through the selection of the discharge conditions slightly above the extinction voltage, where the discharge breakdown exhibits the lowest averaged jitter of $\approx$50 ns (3σ interval). Owing to this unavoidable jitter, the time step of our E/N evolution measurement was chosen to be 50 ns (3σ interval of the jitter).

In order to check the performance of the used bandpass interference filters in isolating the desired helium lines out of the discharge spectra, the overall discharge spectra were measured with or without filters included into the optical path by an optical emission spectrometer with a CCD detector (Jobin-Yvon HR640, 1200 gr/mm). The spectra can be compared in figure 2. We found that without the filters there was only a weak parasitic emission around the 728.1 nm line, but intensive lines e.g. of O and N_2 close to the 667.8 nm line. The inclusion of the interference filters provided satisfactory isolation of the helium lines in the spatio-temporally-averaged discharge spectra.

In order to determine the total spectral sensitivity of the system, the optical setup was mounted with either filter 1 or filter 2 and the intensities of the reference calibrated spectral lamp (Avantes AvaLight-DH-CAL) were acquired with the ICCD camera. Then, the spectral transmittances of the filters were measured for both filters. Using the calibration curve of the spectral lamp, the total irradiance of the lamp on the entrance lens of the ICCD camera was calculated for both filters. With these factors, a relative spectral correction coefficient was determined for the measured signals of both wavelengths. Finally, the ratio of the helium 667.8 and 728.1 nm lines was obtained for each pixel of the ICCD image as the element-wise division of respective background-corrected pixel intensities acquired using the first and second optical filter and divided by the relative spectral sensitivity correction coefficient—see figure 3.

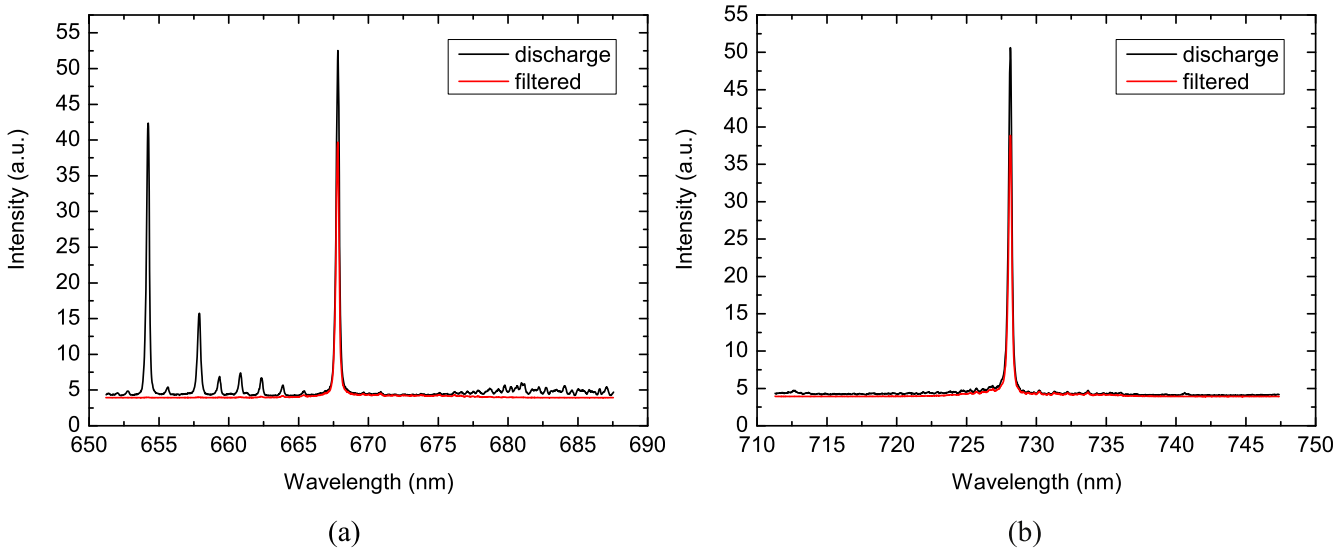

Figure 2. Isolation of helium spectral lines at (a) 667.8 and (b) 728.1 nm by interference filters from the total discharge spectrum. Discharge spectra were measured by spectrometer with a CCD detector.

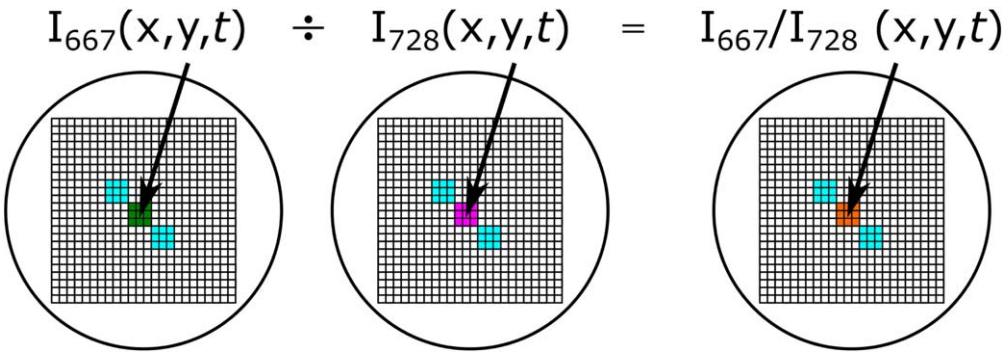

Figure 3. Stacks of time-sliced image frames for the line intensity ratio construction.

3. Results and discussion

3.1. General description

The standard regime of discharge operation of coplanar DBD is the filamentary discharge. Even when generated in pure helium, the onset regime of coplanar DBD is the filamentary one. But when we widened the electrode gap to several millimeters and gradually lowered the operating voltage amplitude to the values close to the extinction voltage (1.6 kV), the discharge transited from the filamentary regime with clearly visible multiple filaments to a homogeneous regime, where no branching filament structures can be distinguished even in single-shot ICCD images (see figure 4). The studied discharge mode was almost similar to the 'atmospheric pressure glow discharge' (APGD), known from the volume configuration of DBD generated in helium (see e.g. [35]). Similar to the APGD of volume DBD, the regime exhibited a broad current peak (2–5μs FWHM), stable with respect to the voltage phase, with the rising edge slope of approximately 1–2 mA/μs (see again figure 4(a)). The chief advantage of the homogeneous discharge regime was the high spatio-temporal stability of the discharge, which enabled us to perform highly accumulated, gated 2D optical observations with the ICCD camera. The slow nature of helium discharge evolution enabled a clear resolution of all discharge phases, even with a 50 ns gate-time window (see figure 4(b) and the discussion in the next section).

3.2. 2D-resolved electric field

The 2D spatially resolved evolution of the electric field, calculated from the I_{667}/I_{728} ratio according to (1), is shown in figure 5. The evolution of the total light intensity at the same time moments is plotted in figure 4(b) for comparison. Intensity distributions of the helium 667.8 and 728.1 nm lines were similar to that of the total light intensity and they are therefore not shown.

The discharge starts with a Townsend phase of accumulation of space charge in front of the anode. The electric current and the intensities of the helium lines are low, insufficient for the determination of the electric field from the

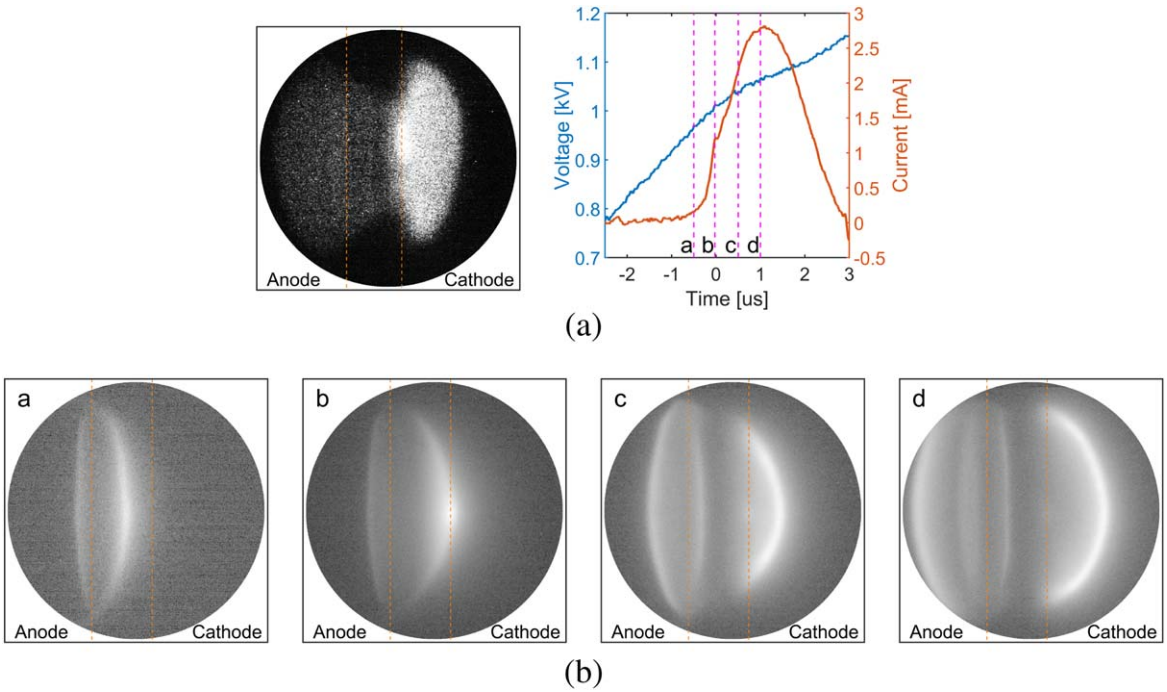

Figure 4. (a) Single-shot ICCD image (gate time 1 μs) and current–voltage characteristics of homogeneous helium coplanar barrier discharge. Blue—voltage, red—current. (b) 2D-resolved temporal development of the total light emission (gate time 50 ns, 10000 accumulations). Letters denote the times marked on the current curve in figure 4(a). Diameter of the visible area was 20 mm.

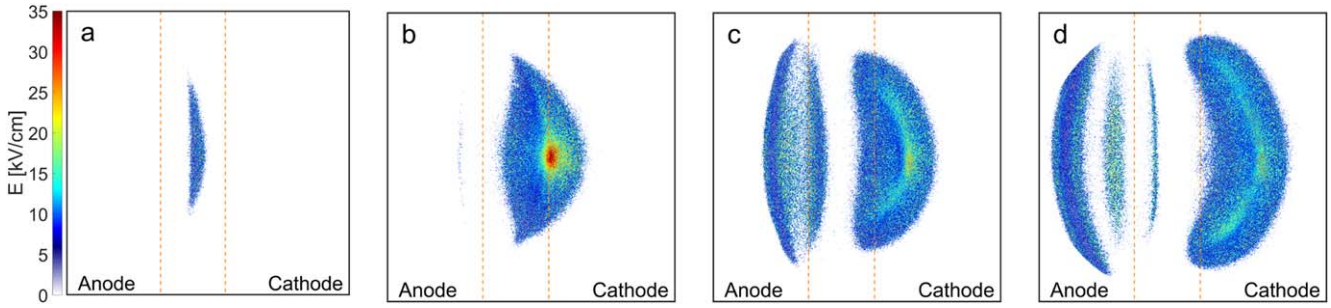

Figure 5. 2D-resolved temporal development of the electric field calculated from the I_{667}/I_{728} ratio. Letters denote the times marked on the current curve in figure 4(a). Diameter of the visible area was 20 mm.

ratio (not shown). Then, the propagation phase starts, manifesting itself by a cathode-directed ionization wave (CDIW[1]), see figure 5(a). The electric field strength is elevated to the value of 10 kV/cm in the wavefront. When the wave reaches the cathode dielectrics, a bright spot with the electric field of ≈32 kV/cm is formed at the central horizontal axis (b). The moment of this 'first touch' is also manifested by a small current peak on the rising slope of the discharge current pulse. Simultaneously, several ionization waves start propagating in the anode region. Their electric field is lower, around 10 kV/cm (c, d). In the meantime, the CDIW continues sliding away from the gap center, leaving deposited surface charges on the alumina dielectric plate. The electric field in the wavefront remains slightly enhanced at the central horizontal axis (20–25 kV/cm), with a value of 15–20 kV/cm outside. Finally, the whole discharge is quenched after approximately 3–4 μs.

The ionization wavefronts were slightly non-uniform in the direction perpendicular to the wave propagation, with a dominant route of propagation along the central horizontal axis. Therefore, the acquired optical signal (pixel intensities) could be vertically binned (several rows of image matrix adjacent to this axis) in order to increase the signal-to-noise ratio and to obtain the electric field during weakly emitting discharge phases (see next section). Besides, the resulting integrated data, plotted in a way which mimic the streak-camera output along the discharge's central horizontal axis, provided the possibility to compare our 2D results to 1D measurements, obtained e.g. from the technique of cross-correlation spectroscopy [27].

[1] The term cathode-directed ionization wave (CDIW), resp. anode-directed ionization wave (ADIW), is used here with the general meaning as in [27] to emphasize that the wave formation is clearly a space-charge-dominated event, with no intention to classify the CDIW/ADIW as a streamer according to Raether–Meek streamer criterion.

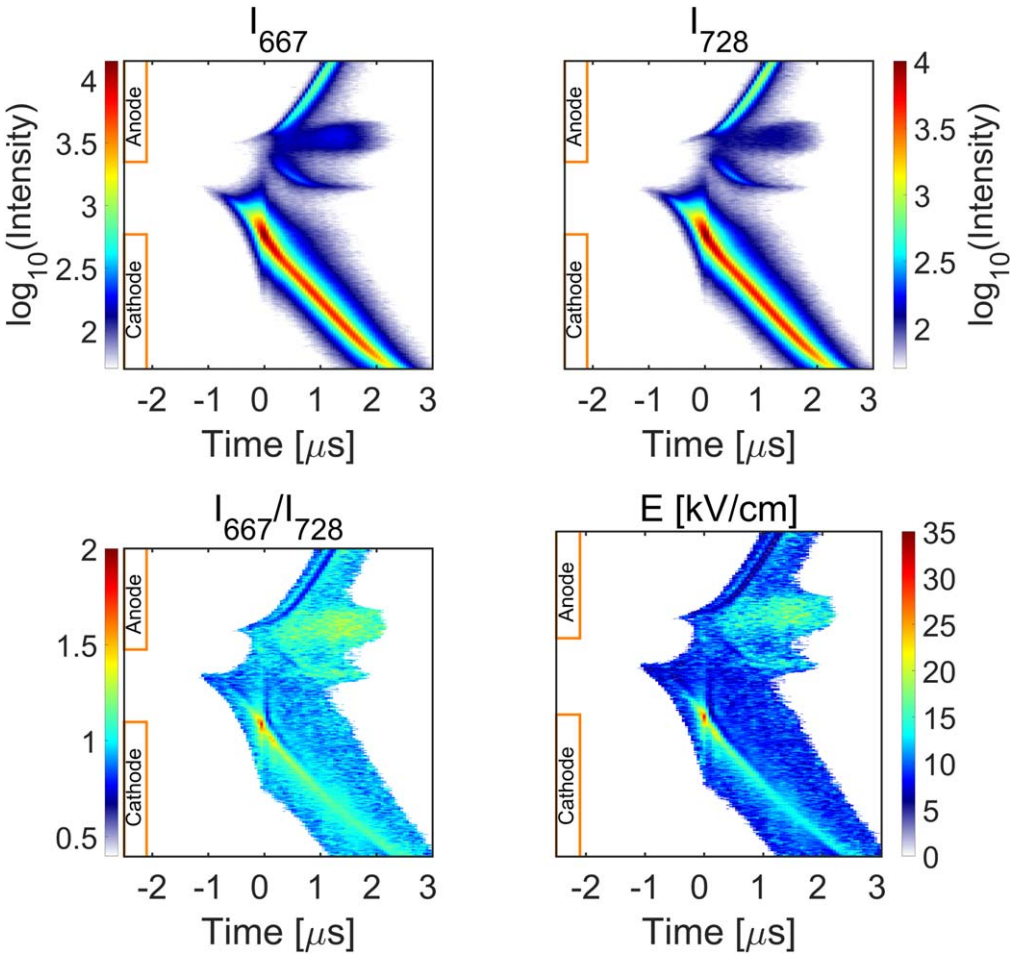

Figure 6. Spatio-temporal development of the intensities of the 667.8 and 728.1 nm lines, of their intensity ratio and of the electric field, all in streak-camera-like representation.

3.3. Integrated development

Figure 6 shows the integrated 1D development of the 667.8 and 728.1 nm helium line intensities along the central horizontal line, together with the constructed line intensity ratio and calculated electric field. The observed spatio-temporal development resembles qualitatively the development of the coplanar discharge in air [27]. The typical 'long nose', i.e. Townsend avalanching phase just preceding the CDIW formation, was more visible in the total light emission pattern (not shown).

In the resulting spatio-temporal electric field maps, we can identify two high-field domains. The first and most prominent domain belongs to the CDIW. This is visible as the red line, originating in the center of the images and propagating to the right-bottom corner. The peak electric field in this domain was found to be around 15–32 kV/cm (60–130 Td). The second domain belongs to anode-ionizing wave(s) situated in the upper part of the images. The peak electric field is lower there, reading some 15 kV/cm (60 Td).

The wave propagation velocities and electric field values are, however, substantially smaller than those in discharge in air (see figure 7). The velocity of the waves was determined in this work from the three frame time steps (i.e. from 150 ns steps). The average CDIW propagation velocity was about

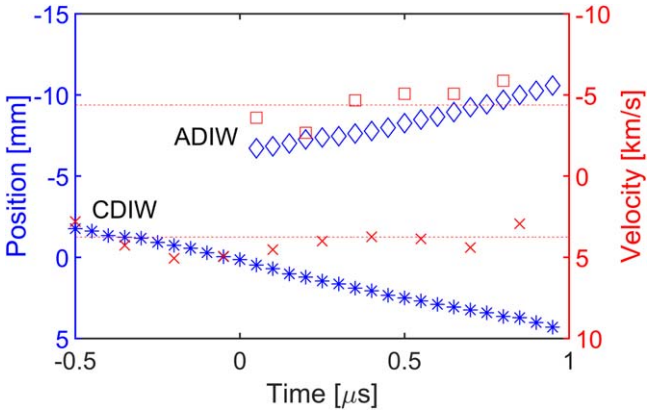

Figure 7. Propagation velocity of the cathode-directed wave (bottom) and anode-directed wave (top) as a function of time. Instantaneous positions of the wave heads for those times are shown for comparison.

3.7 km/s. The propagation velocity of ADIW develops with the position, having the average value slightly higher (4.4 km/s). These values are lower than the electron drift velocity expected at the respective field, e.g. ≈300 km/s at 25 kV/cm. Such a low value can be explained by considering the direction of the electric field. The value of the electric field

determined from the intensity ratio method is the magnitude of the electric field. Above the coplanar electrodes, however, the major component of the electric field is its normal component, directing towards/outwards the dielectric plate. The tangential electric field component directing along the dielectric is substantially smaller. It is this smaller component of electric field, which is responsible for the propagation of the discharge along the electrodes. The propagation of the CDIW can also be viewed as a slow displacement of the formed cathode fall.

On the other hand, propagation velocities in air coplanar DBD are in the order of 10^6 m/s and the electric field reaches 200–1200 Td (for 30 kPa [28]). The cited values were also obtained from the intensity ratio method, but using the molecular band of the second positive system of N_2 (at 337.1 nm) and of the first negative system of N_2^+ (at 391.5 nm) [20]. Because of very different energies of N_2 and N_2^+ states, the spatio-temporal intensity maps of both bands are substantially different [27]. On the other hand, excitation energies of upper states 3 ^{1}S and 3 ^{1}D of both helium lines used in this work are quite similar, being 22.92 and 23.07 eV. Therefore, their spatio-temporal developments in figure 6 are also similar.

3.4. Discussion

The use of calibration (1) for electric field determination from the obtained line intensity ratio maps requires careful consideration of its applicability with respect to the experimental circumstances and the validity of model prerequisites.

First, the role of metastables becomes dominant at low electric field values, causing the strong rise of the calibration curve back to high ratio values at fields of 1–2 kV/cm. Such a final increase of the intensity ratio was indeed observed experimentally, forming a 'moat' following the high electric field region (see figure 6), in agreement with similar observations in [23]. However, electric field determination in this region is hindered owing to the lack of metastable density.

Second, the applied method of filtering the light using bandpass filters may fail outside the high-field region. For the 670 nm filter, a parasitic emission (see section 2) can cause the overestimation of the He 667.8 nm line intensity and the electric field. The intensity during the active phase of discharge development (i.e. when the electric field and emission from helium are high), can be overestimated by some units of percent. However, during the passive phases of the discharge, when the helium lines are weak, the parasitic emission may play an important role. When comparing the minimum values of R ratio in the experiment (around 0.6) with the curves presented in [23], an absolute difference up to 0.1 is found, which could lead to the electric field overestimation of up to 3–4 kV/cm.

Another limitation also arises from the CR model [23]. Since the model takes electron impact excitation from the ground and metastable states as the only sources of excitation, the applicability of the method is limited only to regions, where these processes prevail. The mean electron energy of ≈2 eV expected at electric fields around 1 kV/cm (measured in the dark phase of the discharge [25]), suggests that the

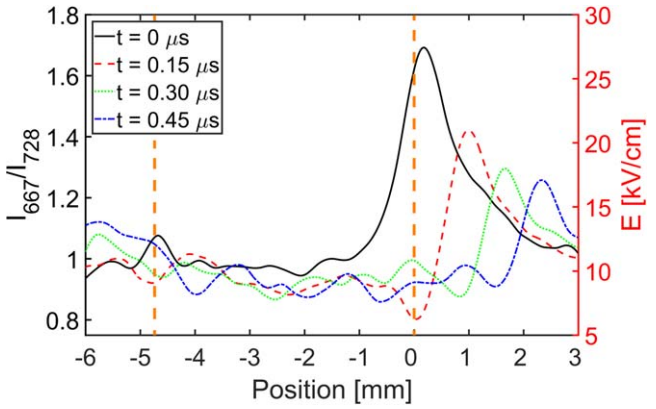

Figure 8. Ionization wave head as reflected in the measured line intensity ratio and the calculated electric field. CDIW reaches the cathode dielectrics at zero time. Noise in the calculated intensity ratio data was partially suppressed using a robust local regression with a weighted second degree polynomial model.

stepwise excitation of 3 ^{1}S and 3 ^{1}D levels via metastable states (threshold energies 2.3 and 2.5 eV, respectively) is still possible during the decay phase of the discharge development. The light emissions on the helium lines were indeed observed during the entire voltage period [25]. However, other processes such as dissociative recombination of He_2^+ ions can contribute to the population of the excited states in this region as well [25, 36]. The amount of this contribution varies with the gas purity, since the presence of impurities can substantially influence the He_2^+ density through the charge exchange collisions [37]. To sum up, the reliable values of electric field can be expected only in high electric field regions, where the concurrent processes, neglected in the model, are of no great importance.

The applicability of the used CR model may also be influenced by the time to settle the excited-level equilibrium populations. The used CR model [23] finds the stationary solution. When the rate equations are solved in time, the intensity ratio R is stabilized in about 5 ns, but its value may be considerably increased during this time [36].

The obtained maximum value of the electric field of 32 kV/cm in the CDIW approaching the cathode is higher than previously measured in helium barrier discharges at atmospheric pressure. Since this value comes from the above-mentioned 'first touch' spot, the value may suffer from a possible spatial spot instability. Also, fast varying electric fields may be overestimated due to the above-mentioned non-equilibrium of the excited-level populations. On the other hand, the intensity ratio measured in the spot is consistent with the values measured at later times (see figure 8). Besides, fields higher than 30–60 kV/cm can still occur in helium atmospheric pressure discharges, as in constricted radio-frequency discharge with metallic electrodes [11].

Up to now, we have not been aware of any published experimental or simulated work on electric field in helium coplanar discharge. In the original application of the line ratio method, fields up to 11 kV/cm were found in the cathode region of the volume helium DBD, at the time of the maximal current [23]. This measurement was validated by

the measurement using the Stark effect. Such a field is similar to our value measured in the CDIW propagating between the electrodes, but differs substantially from E values obtained during the contact with the dielectrics and subsequent propagation along the dielectric surface. Besides the differences between the configurations as the field geometry and the possibility for the ionization wave to propagate after reaching the electrode, the presence of the dielectrics alone could be the important factor, since at a close distance to the (charge populated) front of the CDIW and the dielectric barrier, the local field is enhanced due to a 'charge mirroring' effect. Considering the narrow gap between the propagating CDIW front and the surface of the dielectric and also the fact that the ratio of relative permittivity of alumina and helium gas is approximately 9, the effect of 'charge mirroring' on the interface of the gas–solid phases can be substantial. The described effect is also better experimentally observable in coplanar geometry than in volume geometry, because in coplanar geometry the 'contact' area of discharge with the dielectric surface is directly facing the ICCD camera.

The fields of 15–25 kV/cm measured in the ADIW and the CDIW later above the electrodes are comparable with the published electric field data obtained in various atmospheric pressure plasma jets. For example, electric fields up to 10, 20 and 18 kV/cm were measured in ionizing waves ('plasma bullets'), formed outside the nozzle of the jet, using the Stark effect [9, 10]. An electric field strength above 10 kV/cm in the head of the positive streamer propagating in the helium jet was obtained from the modeling [12]. Higher values in the range of 15–30 kV/cm were found off axis of the jet in the jet luminous ring [13]. In that work, the calculated streamer velocities were at least one order higher than the velocity of our CDIW. On the other hand, the streamer velocities decreased with the decreased slope of the voltage rise and the input slope values >3 kV/500 ns were more than two orders higher than in our experiment.

4. The method sensitivity analysis

To assess the method sensitivity to various experimental errors and/or technical limitations, we have performed a simulated 'sensitivity analysis' on the acquired data, i.e. on the 1D streak-camera representation of measured data for clearer comparison. The measured data were artificially distorted in order to see the resulting deviation of the output electric field values with respect to those measured. The results are presented using two representations: (i) streak-camera-like maps of the electric field strength, where the sensitivity to spatial distortion of the calculated electric field can be easily tracked, and (ii) histograms of the electric field values, constructed from the pixel values in the area of the CDIW, which can track the sensitivity of the E field absolute value distribution. For the comparison, the streak-camera-like maps are accompanied with the derived maximal and average values of electric field at current data processing settings. The maximum value (labeled 'MAX') and the average value (labeled 'AVG') were calculated from the CDIW/ADIW region, which was assessed from the valid data of a '500 count' threshold. The histograms of E field values were constructed using regularly spaced bins of 5 kV/cm width and for better comparison the displayed E field range was limited to a maximum 50 kV/cm. The axes and color bars of the E field maps are the same as in figure 6 but have been omitted for better readability of the figures.

Since the line intensity ratio method is reliably applicable only in high electric field regions with strong light emission, generally important aspects such as selection of the threshold intensity or threshold signal-to-noise ratio for calculation of the field will not be presented here. Attention will be paid namely to the role of temporal and spatial misalignment and resolution.

4.1. Temporal misalignment

The 'misalignment' (both temporal and/or spatial) of recorded image stacks for respective spectral lines is expected to have a substantial influence on the actual quantification of the electric field E. We begin with the analysis of temporal misalignment, i.e. the time de-synchronization. In the performed sensitivity analysis, we have purposely introduced a series of time offsets between the recorded image stacks of respective spectral lines, ranging from −50 to +100 ns.

It can clearly be seen from the results shown in figures 9 and 10, that the precise time-domain alignment is the decisive parameter of the method. This critical time-shift sensitivity was indeed the reason for the construction of the mentioned Bino-box optical setup, which enabled us to precisely synchronize the measured image stacks. The time-domain misalignment of the image stacks by even a single frame (i.e. by 50 ns only) results in substantial distortion of the E field map (figure 9). If the misalignment was greater than two frames (±100 ns), the maximum values of the line intensity ratio would result in unphysically high values of the electric field. When looking at the histogram representation (figure 10(a)), we may expect that the correct time alignment of the frames can be estimated from minimizing the maximal R ratio (or E field) value. Although this would provide a correct magnitude of the measured E field, it is still not a sufficient condition to determine the precise time alignment. The pair comparison of misalignment of +50 ns with the correct one (0 ns) gives a similarly minimized value of E. However, the development of the electric field for +50 ns in figure 9 shows that the domain of maximum E lags behind the CDIW ionizing front, which is in conflict with the physical reality.

4.2. Spatial misalignment

An analogous sensitivity analysis was done through the purposeful introduction of spatial de-coherence between the respective image stacks. The analysis showed that the precise spatial alignment is the equally decisive parameter of the method, chiefly due to the highly narrow space into which the CDIW is confined. The lateral misalignment was introduced in the direction of the CDIW propagation; the influence of a few pixel shift in both opposing directions is displayed in figure 11. The shift of more than 1 pixel had a substantial

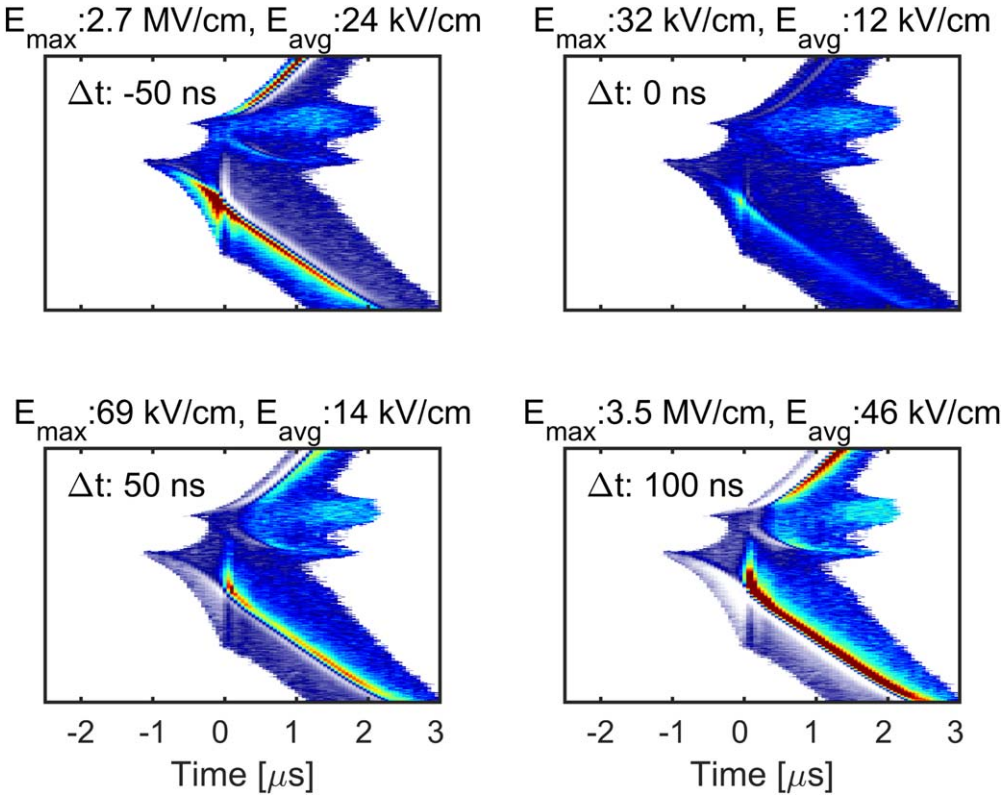

Figure 9. Influence of temporal misalignment on the derived E field values.

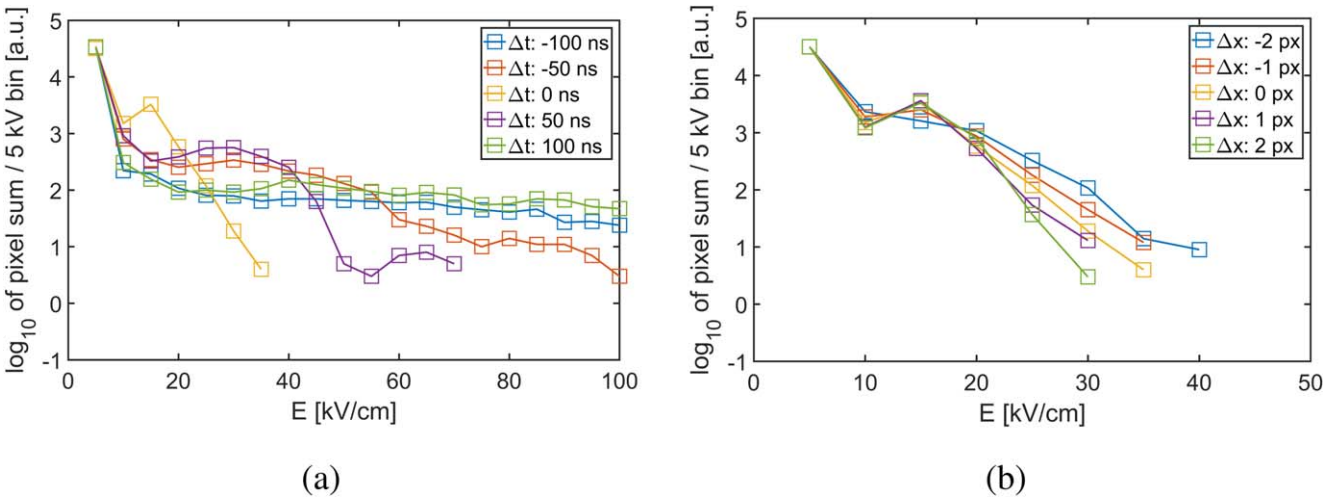

Figure 10. Histograms of the number of pixels with respect to the E field values for different (a) temporal misalignment, (b) spatial misalignment.

influence on the distortion of the histograms of the E values (figure 10(b)). A monotonic growth of E field is apparent on the histogram, when the image stack for 728.1 nm is spatially shifted behind the stack of 667.8 nm (negative pixel shift). The shift in the opposite direction had no such effect. Therefore, we could not identify a simple 'thumb rule' (e.g. minimal/maximal value) for the proper pixel shift dependency. However, the pixel shift in the positive direction resulted in the general decrease of the E field values. In addition to the change of E field absolute values, we observed a loss of contrast in the anode region in some experiments.

4.3. Temporal resolution

A further parameter that we analyzed was the choice of temporal resolution of acquired images. The temporal resolution limit of the equilibrium line ratio method depends on the settlement time, which is around 5 ns (see the discussion in section 3.4). As mentioned in section 2, the measurement suffered from the presence of discharge jitter. Using the current–voltage measurements, we found the discharge jitter to be approximately 50 ns (3σ interval). Since the presented method used the phase-locked ICCD camera accumulations to

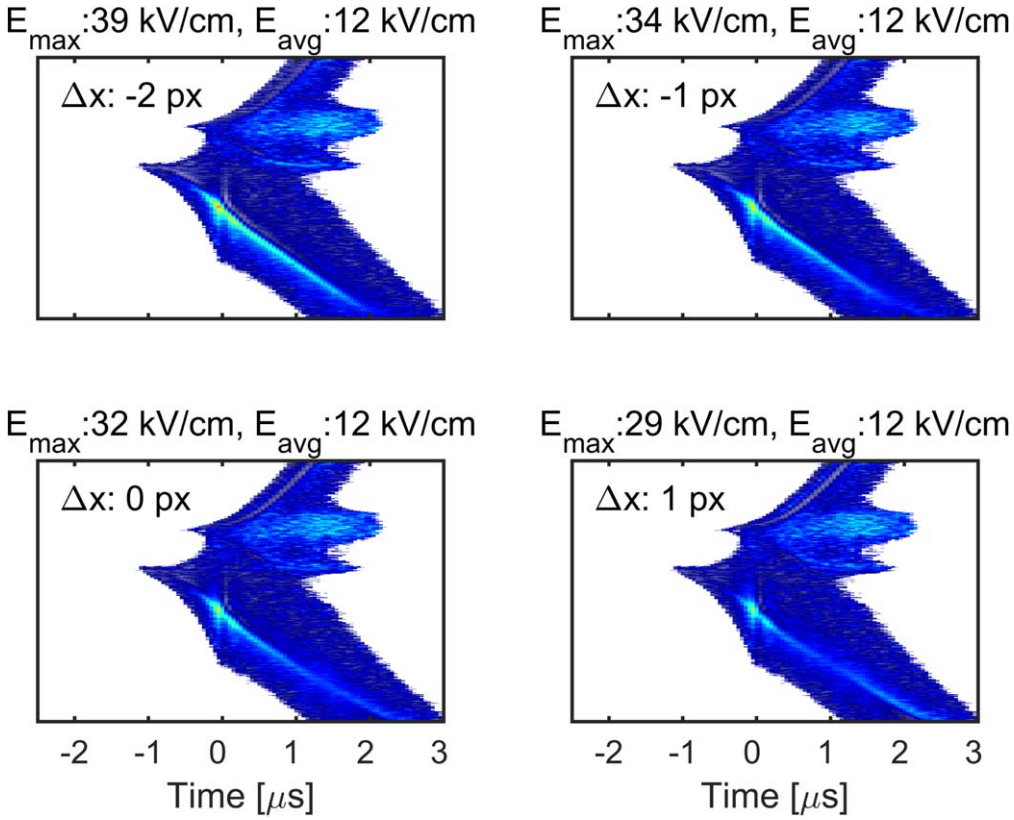

Figure 11. Influence of spatial misalignment on the derived E field values.

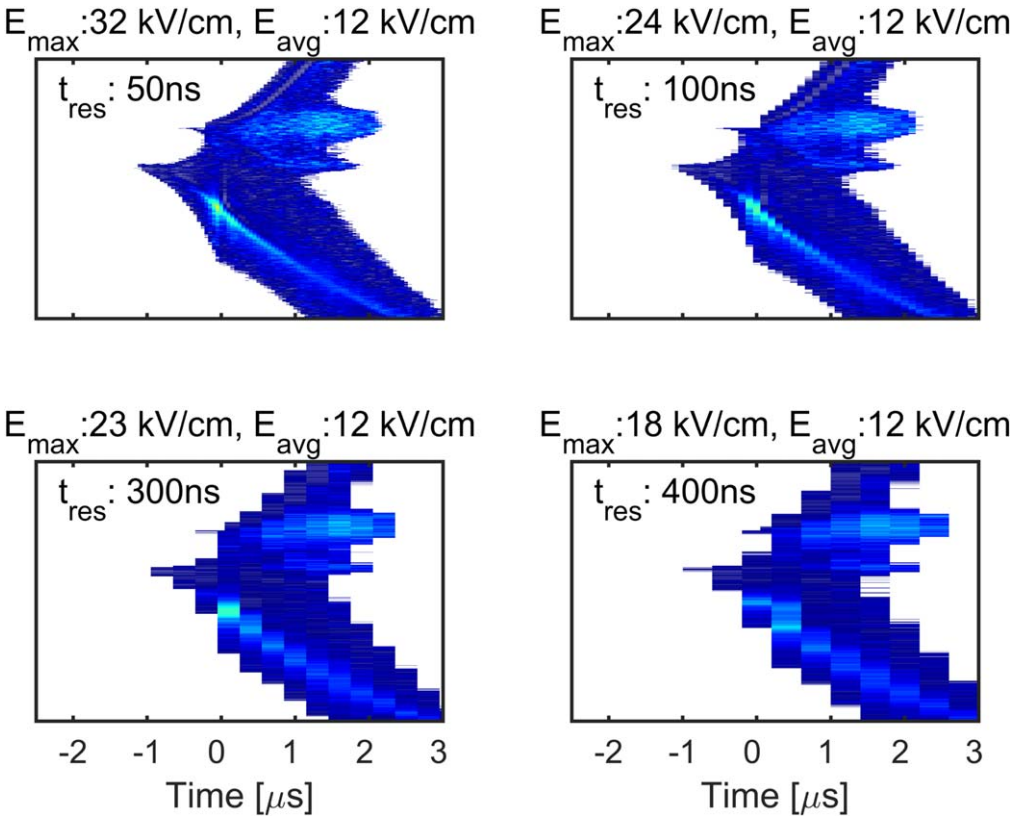

Figure 12. Influence of decreasing temporal resolution on the derived E field values.

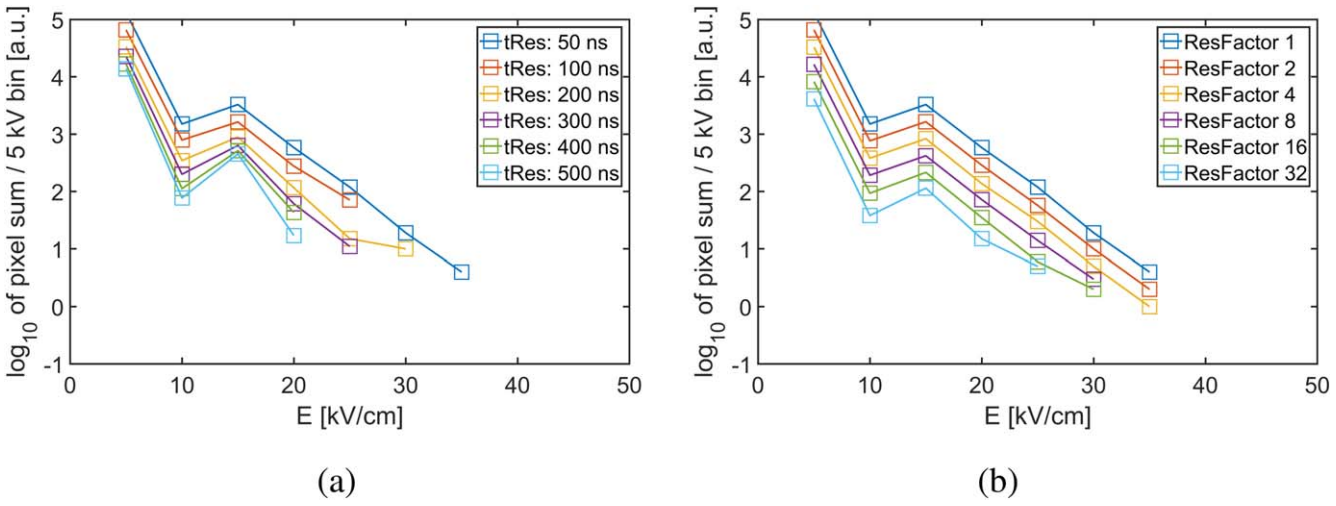

Figure 13. Histograms of the number of pixels with respect to the E field values for decreased (a) temporal resolution, (b) spatial resolution.

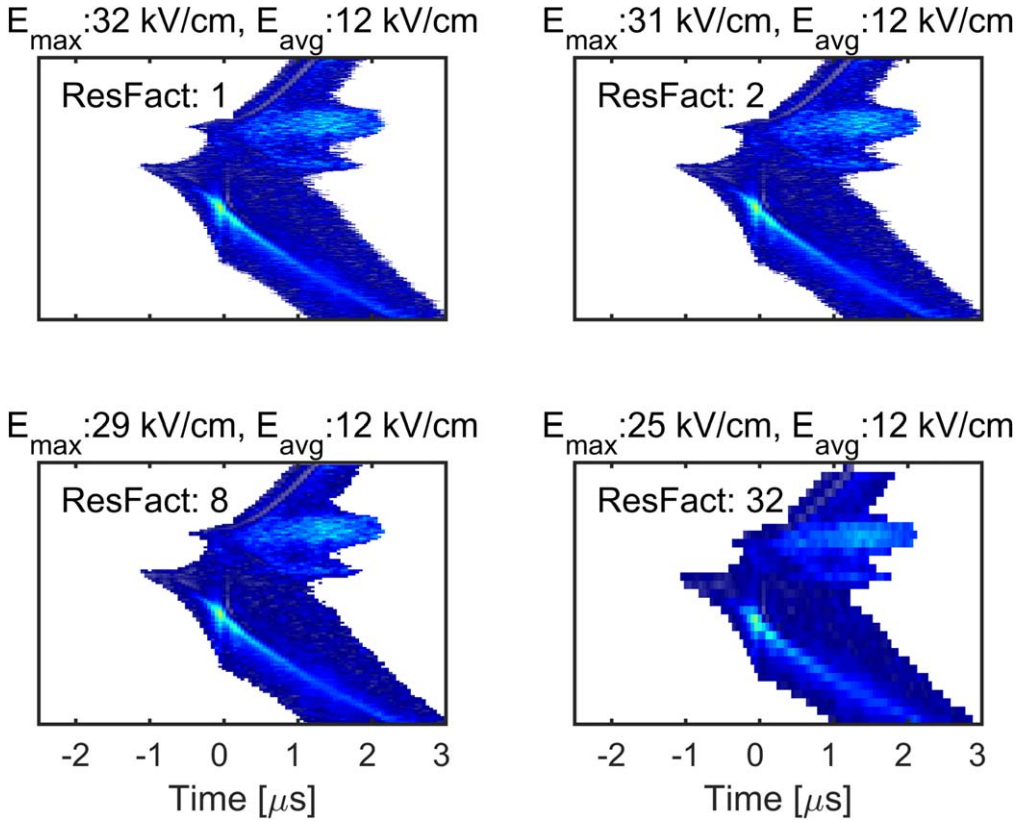

Figure 14. Influence of decreasing spatial resolution on the derived E field values.

track the discharge evolution, the discharge jitter constituted the main limit for the temporal resolution of the measurement. To be within the 'margin of safety', we have chosen the gate time and time steps of 50 ns, which resulted in slightly lower effective temporal resolution due to discharge jitter (1σ being around 15 ns). Thus, the presented measurements represent the average values of the electric field within the respective time intervals. Improvement of the temporal resolution (e.g. by decreased discharge jitter) may provide even higher values of the instantaneous electric field.

When we artificially lowered the temporal resolution (by aggregation of the image stack at the time-domain direction) the qualitative picture of the E field development remained unaltered (figure 12). However, the maximal values of the E field were highly influenced. Lowering the resolution effectively averaged the investigated E, incorporating the instants when the E is not as high as during the presence of a relatively fast and narrow CDIW front. Halving the resolution led to the decrease of E field maxima by 30% (figure 13(a)). Therefore, when a similar DBD is investigated at a lower temporal

resolution, maximum E field values can be underestimated (even by a factor as high as 2, when 400 instead of 50 ns is used). This could be especially pronounced when the highly transient events in the discharge evolution are studied, such as the CDIW/ADIW. Less pronounced effects are expected on the E values in the discharge channel, where the channel evolves in a much longer time domain. Comparing our results from the coplanar DBD to [23], where the volume DBD was investigated under comparable discharge conditions, we could deduce that our 2× higher temporal resolution could be one of the reasons behind the higher E values in CDIW in our experiments.

4.4. Spatial resolution

The lowering of spatial resolution led to a similar effect (figures 13(b) and 14). With a lower spatial resolution, the E field development remained qualitatively the same, but with the exception of the loss of the details in the anode area. However, the maximal E values were also lowered due to the spatial averaging. Our actual hardware limitations allowed us to follow the discharge with the spatial resolution no better than 20 × 20 μm. When the resolution was decimated to the squares of 40 × 40 μm, the fine anodic structures were preserved, but the maximal E value decreased by 10%. Therefore, it may be possible that better spatial resolution will lead to even higher peak E values.

5. Conclusion

A novel experimental approach of the helium line intensity ratio method of E field measurement [23], based on the direct observation of the discharge by ICCD camera through two interference filters, was successfully applied for the E field determination of coplanar discharge in helium. The obtained results proved the existence of several developing regions of high electric field, namely of CDIWs and ADIWs. Similar behavior, although at very different absolute values of time and electric field, was observed earlier in the coplanar discharge in air [27]. Electric field of 15–25 kV/cm in the CDIW, already sliding on the electrode's dielectrics, is close to the electric fields obtained from the Stark effect in helium plasma jets. However, a higher electric field of 32 kV/cm was measured during the first contact of the wave with the cathode's dielectrics. A number of discussed experimental and theoretical constraints limit the applicability and accuracy of the method only to the regions of the high electric field, as already stated by the authors of the line ratio method in [23]. Attention must also be paid to the purity of the gas as the method [23] expects quenching of excited states by helium ground-state atoms only. The impact of the impurities on the excited-state populations has to be incorporated into the model prior to any application in mixed gas atmospheres.

The performed sensitivity analysis pointed out the crucial importance of precise temporal and spatial synchronization and of high discharge stability for the techniques based on the intensity ratio of two spectral lines. Although the helium coplanar discharge is manifested by a broad current peak with approximately 2 μs FWHM, the high electric field wavefront of the CDIW persists at one place only for a very short time of less than 50 ns. The introduced 50 ns misalignment between the measured data of the 667.8 and 728.1 nm line then resulted in the substantial distortion of the E field map; 100 ns misalignment produced unphysically high values of the electric field. Halving the temporal resolution from 50 to 100 ns led to the decrease of E field maxima by 30%. Halving the spatial resolution from 20 to 40 μm decreased the maximal E value by 10%. Improvement of the temporal and spatial resolution and of the discharge stability may provide even higher values of the electric field. However, due to the high sensitivity of the measurement to the spatial and temporal alignment, it would be a challenging task to maintain the spatio-temporal coherence of the measurement on the μm and ns scale.

The speed and substantially improved control over the spatio-temporal coherence of collected optical signals are the main reasons for employing the presented two-filter ICCD method and/or its binocular variation. The method provides critical information on the minimum spatial and temporal resolution required for an accurate assessment of conditions inside the highly transient environment of the ionizing wavefront. Analysis of the obtained 2D emission maps allows us to identify regions where (and only where) the given line intensity ratio model can be applied unambiguously. Its application before commencing temporally better resolved but extremely lengthy and tedious point-to-point (0D) or line-to-line methods (1D) can dramatically improve the efficacy of data acquisition, and mitigate the risk of their unphysical interpretation. The presented method should be considered as a useful supportive or a cross-checking tool to these conventional reduced dimensionality sets of the line intensity ratio electric field measurements.

Acknowledgments

This research has been supported by the project LO1411 (NPU I) funded by the Ministry of Education, Youth and Sports of the Czech Republic. The authors would like to express their gratitude to Nikola Cvetanović for fruitful discussion on the helium collisional-radiative model.

ORCID iDs

Jan Čech https://orcid.org/0000-0002-4900-6011

References

[1] Kogelschatz U 2003 *Plasma Chem. Plasma Process.* **23** 1
[2] Hoder T, Šimek M, Bonaventura Z, Prukner V and Gordillo-Vázquez F J 2016 *Plasma Sources Sci. Technol.* **25** 045021

[3] Huddlestone R H and Leonard S L 1965 *Plasma Diagnostic Techniques* (New York: Academic)
[4] Videnović I R, Konjević N and Kuraica M M 1996 *Spectrochimica Acta Part* B **51** 1707
[5] Wujec T, Janus H W and Jeleński W 2003 *J. Phys. D: Appl. Phys.* **36** 868
[6] Cvetanović N, Martinović M M, Obradović B M and Kuraica M M 2015 *J. Phys. D: Appl. Phys.* **48** 205201
[7] Kuraica M M and Konjević N 1997 *Appl. Phys. Lett.* **70** 1521
[8] Obradović B M, Ivković S S and Kuraica M M 2008 *Appl. Phys. Lett.* **92** 191501
[9] Sretenović G B, Krstić I B, Kovačević V V, Obradović B M and Kuraica M M 2014 *J. Phys. D: Appl. Phys.* **47** 102001
[10] Sobota A, Guaitella O, Sretenović G B, Krstić I B, Kovačević V V, Obrusník A, Nguyen Y N, Zajíčková L, Obradović B M and Kuraica M M 2016 *Plasma Sources Sci. Technol.* **25** 065026
[11] Navrátil Z, Josepson R, Cvetanović N, Obradović B M and Dvořák P 2016 *Plasma Sources Sci. Technol.* **25** 03LT01
[12] Naidis G V 2011 *J. Phys. D: Appl. Phys.* **44** 215203
[13] Boeuf J-P, Yang L L and Pitchford L C 2013 *J. Phys. D: Appl. Phys.* **46** 015201
[14] Viegas P, Péchereau F and Bourdon A 2018 *Plasma Sources Sci. Technol.* **27** 025007
[15] Czarnetzki U, Luggenhölscher D and Döbele H F 1999 *Plasma Sources Sci. Technol.* **8** 230
[16] Windholz L, Wasowicz T J, Drozdowski R and Kwela J 2012 *J. Opt. Soc. Am.* B **29** 934
[17] van der Sijde B, van der Mullen J J A M and Schram D C 1984 *Beitr. Plasmaphys.* **24** 447
[18] Navratil Z, Dvorak P, Brzobohaty O and Trunec D 2010 *J. Phys. D: Appl. Phys.* **43** 505203
[19] Navrátil Z, Dosoudilová L, Hnilica J and Bogdanov T 2013 *J. Phys. D: Appl. Phys.* **46** 295204
[20] Kozlov K V, Wagner H-E, Brandenburg R and Michel P 2001 *J. Phys. D: Appl. Phys.* **34** 3164
[21] Paris P, Aints M, Valk F, Plank T, Haljaste A, Kozlov K V and Wagner H-E 2005 *J. Phys. D: Appl. Phys.* **38** 3894
[22] Goekce S, Peschke P, Hollenstein C, Leyland P and Ott P 2016 *Plasma Sources Sci. Technol.* **25** 045002
[23] Ivković S S, Sretenović G B, Obradović B M, Cvetanović N and Kuraica M M 2014 *J. Phys. D: Appl. Phys.* **47** 055204
[24] Morávek T, Čech J, Navrátil Z and Ráheľ J 2016 *Eur. Phys. J. Appl. Phys.* **75** 24706
[25] Navrátil Z, Morávek T, Ráheľ J, Čech J, Lalinský O and Trunec D 2017 *Plasma Sources Sci. Technol.* **26** 055025
[26] Černák M, Kováčik D, Ráheľ J, St'ahel P, Zahoranová A, Kubincová J, Tóth A and Černáková L 2011 *Plasma Phys. Control. Fusion* **53** 124031
[27] Hoder T, Šíra M, Kozlov K V and Wagner H-E 2008 *J. Phys. D: Appl. Phys.* **41** 035212
[28] Hoder T, Synek P, Chorvát D, Ráheľ J, Brandenburg R and Černák M 2017 *Plasma Phys. Control. Fusion* **59** 074001
[29] Čech J, St'ahel P and Navrátil Z 2009 *Eur. Phys. J.* D **54** 259
[30] Šimek M, Ambrico P F and Prukner V 2011 *Plasma Sources Sci. Technol.* **20** 025010
[31] Nakamiya T, Mitsugi F, Suyama S, Ikegami T, Sonoda Y, Iwasaki Y and Tsuda R 2016 *J. Adv. Oxid. Technol.* **13** 43–9
[32] Boeuf J P 2003 *J. Phys. D: Appl. Phys.* **36** R53
[33] Gibalov V I and Pietsch G J 2012 *Plasma Sources Sci. Technol.* **21** 024010
[34] Brandenburg R 2017 *Plasma Sources Sci. Technol.* **26** 053001
[35] Massines F, Gherardi N, Naudé N and Ségur P 2009 *Eur. Phys. J. Appl. Phys.* **47** 22805
[36] Cvetanović N 2017 Private communication
[37] Murakami T, Niemi K, Gans T, O'Connell D and Graham W G 2013 *Plasma Sources Sci. Technol.* **22** 015003

IOP Publishing
Fast Track Communications
Plasma Sources Science and Technology
Plasma Sources Sci. Technol. **23** (2014) 042001 (5pp)
doi:10.1088/0963-0252/23/4/042001

Fast Track Communication

Diffuse α-mode atmospheric pressure radio-frequency discharge in neon

Z Navrátil, L Dosoudilová, R Josepson, P Dvořák and D Trunec

Department of Physical Electronics, Faculty of Science, Masaryk University, Kotlářská 2, 611 37 Brno, Czech Republic

E-mail: zdenek@physics.muni.cz

Received 18 March 2014, revised 21 May 2014
Accepted for publication 16 June 2014
Published 7 July 2014

Abstract

In this work, a radio-frequency (RF) atmospheric pressure glow discharge burning in neon between planar metal electrodes is achieved for the first time. The RF discharge can operate in two stable modes: in a diffuse α-mode with uniformly covered electrode surfaces and in a constricted γ-mode. Similarities are revealed when the discharge is compared against the RF atmospheric pressure glow discharge in helium, namely both discharges show a discontinuity and a hysteresis in the current–voltage characteristic at the mode transition; the spatio-temporal profiles of the light emission in the α-mode from neon, helium and atomic oxygen are also similar.

Keywords: radio frequency capacitive discharge, atmospheric pressure, neon, helium

(Some figures may appear in colour only in the online journal)

Recently, the generation of large homogeneous non-thermal gas discharges at atmospheric pressure has received significant interest [1, 2]. Using a dielectric barrier in a discharge gap, a homogeneous (or diffuse) barrier discharge (BD), called an atmospheric pressure glow discharge (APGD), can be generated in helium or neon [3, 4]. Another type of homogeneous BD, namely atmospheric pressure Townsend-like discharge, is obtained in nitrogen [5]. These BDs are supplied by an AC power source with frequencies in the range from several kilohertz to tens of kilohertz. Another homogeneous discharge, operating at atmospheric pressure in a planar electrode configuration, can be obtained with bare metal electrodes and a radio-frequency (RF; 13.56 MHz) power source in helium [6, 7], named RF atmospheric pressure glow discharge (RF APGD). When the applied power is low, the discharge operates in a diffuse, so-called α-mode. The breakdown voltage in this discharge is lower than in the BDs due to the higher applied-voltage frequency [8] and due to the absence of dielectric barriers in the gap. At higher voltage, the RF APGD transits into a γ-mode, similarly to intermediate pressure capacitive RF discharges [7, 9]. The γ-mode discharge produces a localized, constricted plasma at atmospheric pressure. The RF APGD in helium in the planar electrode gap has been a subject of numerous investigations [10–15]. It has already been applied in materials science, e.g. for carbon nanotube deposition in $He/H_2/CH_4$ gas mixtures [16].

A constricted γ-mode discharge or arc is usually observed in other gases. The α-mode RF discharge has rarely been obtained in argon or air in a planar electrode gap [17–19]. A constricted γ-mode in a planar electrode configuration has been reported in nitrogen, air and helium–air mixtures [18, 20]. Helium, neon, argon and nitrogen have also been used to generate RF glow discharges on microstructured electrode arrays with electrode gaps tens of micrometers wide [21]. As shown in that work, the neon profits from the low voltage necessary for breakdown. Due to an decrease of the breakdown voltage and an increase of the total ionization coefficient in mixtures with xenon, neon is used as a buffer gas in applications such as plasma display panels, high pressure excimer lasers, mercury-free fluorescent lamps, etc [22–24]. Neon discharges operated at atmospheric pressure also have potential applications as sources of extreme ultraviolet radiation from neon excimers [25].

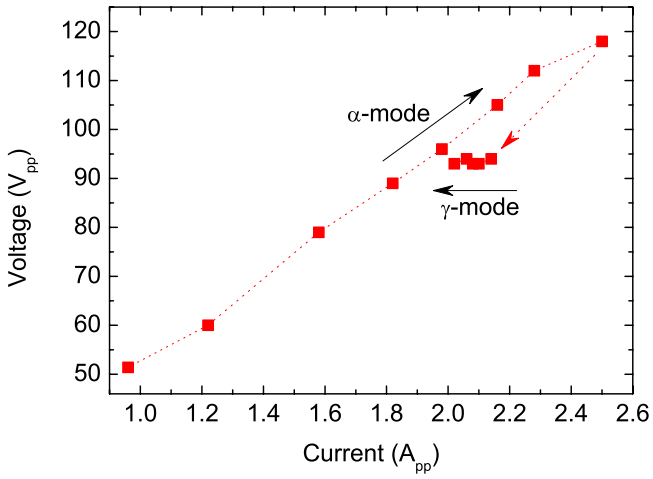

Figure 1. Current–voltage characteristic of a neon RF discharge at atmospheric pressure. The discharge gap was 2 mm.

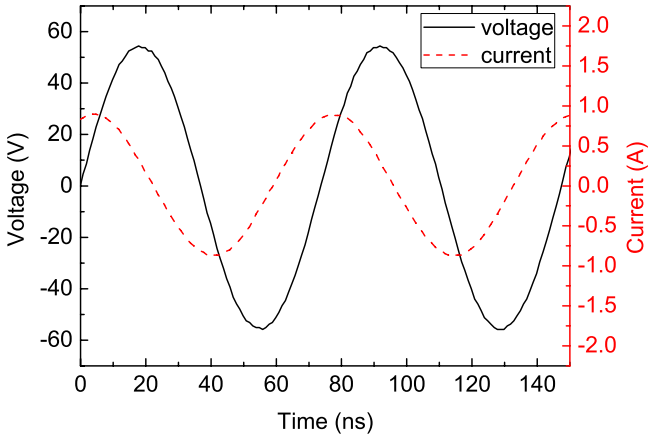

Figure 2. Time dependences of the applied voltage and discharge current of neon α-mode RF discharge within two voltage cycles. The discharge gap was 2 mm; the generator RF power was 10 W.

BDs burning in neon and helium and operated at frequencies of several kilohertz were compared in [26, 27]. In this work, we report a first experimental study of α-mode RF APGD discharge in neon and we compare its properties to those of helium α-mode discharge.

The RF discharge was generated in a parallel plate electrode gap. The electrodes, made of brass and 40 mm in diameter, were placed into a steel vacuum chamber. The discharge gap was 2 or 4 mm. The chamber was firstly evacuated down to 5 Pa by means of a rotary oil pump and then filled with a working gas (neon, helium; gas purity 5.0) up to atmospheric pressure. A gas flow of 400 sccm was maintained during the measurements using a membrane pump. The harmonic 13.56 MHz signal was generated by a function generator (Agilent 33220A) and amplified with an RF power amplifier (Hüttinger TIS 0.5/13560). The electrical parameters were monitored using a digital storage oscilloscope (LeCroy WaveRunner 6100A). The vacuum chamber was equipped with two quartz windows. One window served for time-resolved imaging of the RF discharge with an intensified charge-coupled device camera (ICCD camera, Princeton Instruments PI-MAX3). The gate of the ICCD camera was gradually delayed from the synchronization signal of the function generator to scan, with a 2 ns step, through the whole RF period. The gate width was 2.74 ns, the gate rate reached 848 kHz and 65 535 gating events were accumulated. Band-pass or interference filters introduced into the optical path provided spectral resolution into blue (<500 nm), red (>610 nm) and oxygen atomic line (≈845 nm) wavelength regions. The second window was used for spatially resolved, but temporally unresolved optical emission spectroscopy (Horiba FHR 1000 with a CCD detector) in the UV–visible range (200–750 nm). A spatial resolution of 0.04–0.08 mm was achieved by projecting the discharge via a quartz lens onto a movable slit, with optical fiber located beyond it.

A current–voltage (I–V) characteristic of an RF discharge burning in neon at atmospheric pressure is shown in figure 1. When the discharge gap is below 4 mm, the discharge starts in the α-mode. The discharge is stable and uniformly covers part of the discharge electrodes. With further increase of the power, the discharge quickly occupies all of the electrodes, and the voltage and current increase linearly as in abnormal glow discharges [12]. When the RF power is raised above a critical level, the discharge transits into the constricted γ-mode. This transition is represented by a discontinuity in the I–V curve; both voltage and current decrease (the matching circuit was not readjusted). Then, if the power is decreased, the discharge current also decreases, and the applied voltage remains almost constant. The discharge turns finally again into the α-mode. The form of the I–V curve of the neon discharge is very similar to that of the helium RF APGD discharge [7, 11], but shifted to lower values of voltage and current.

The time dependences of the applied voltage and the current of the α-mode discharge are shown in figure 2. A low distortion of the voltage and the current waveforms by higher harmonic frequencies was checked using Fourier analysis. The ratio of the amplitudes of the higher harmonics to the amplitude of the fundamental component (13.56 MHz) of the discharge voltage or current waveforms was well below 1%; only the third harmonic had a amplitude of a few per cent of the fundamental component. Even harmonics were significantly weaker than odd harmonics due to the opposing action of the two sheaths in a symmetrically driven discharge [28]. The amplitudes of the higher harmonic frequencies of the discharge voltage and the current are known to decrease sharply with increasing pressure due to the damping of current oscillations by electron–neutral collisions [29, 30]. In spite of this, the existence of higher harmonics was predicted theoretically even in atmospheric pressure discharges [31] and the measurement presented in this work confirms the theoretical prediction.

The most intense optical emissions in the spectra of neon α-mode discharge (not shown here) were Ne I atomic lines ($3p \rightarrow 3s$) at 585–745 nm, the OH band ($A\,^2\Sigma^+ \rightarrow X\,^2\Pi$) at 311 nm, the second positive system of N_2 ($C\,^3\Pi_u \rightarrow B\,^3\Pi_g$; SPS) with a maximal intensity at 337 nm and the H_α line at 656 nm. Spatial intensity profiles (time averaged) of selected spectral lines are shown in figure 3. The line intensities were corrected for the instrument spectral sensitivity. The neon atomic lines were the most intense close to the electrodes and their intensities were very low in the center of the discharge

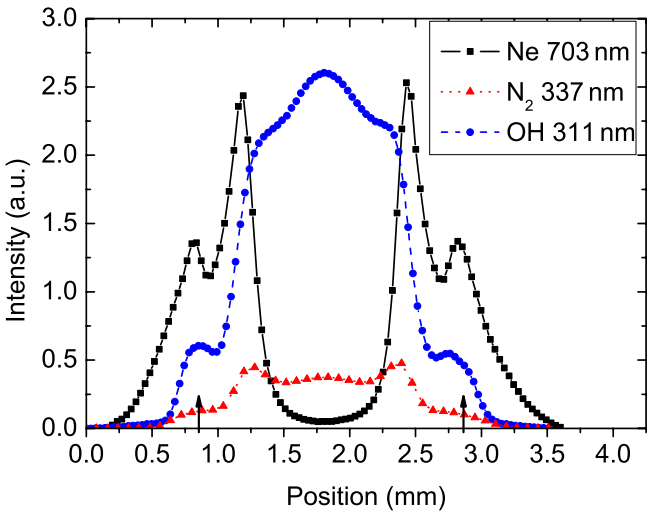

Figure 3. Spatial intensity profiles of selected spectral lines of neon α-mode RF discharge. The discharge gap was 2 mm; the generator RF power was 10 W. The intensities were corrected for the instrument spectral sensitivity. The arrows indicate the positions of electrodes.

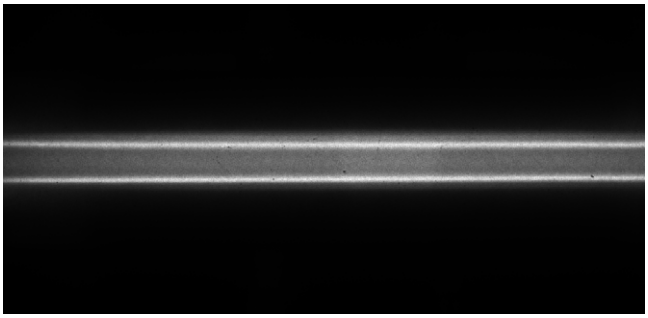

Figure 4. Time-averaged ICCD image of neon atmospheric pressure α-mode RF discharge. The discharge gap was 2 mm; the generator RF power was 10 W.

gap, like for helium discharge [7, 11]. In contrast, the most intense OH emission was observed in the discharge gap center. The SPS of nitrogen had a low intensity, almost constant across the discharge gap, with less pronounced maxima at the electrodes.

The spectral band of OH $A\,^2\Sigma^+, v' = 0 \rightarrow X\,^2\Pi, v'' = 0$, measured at the position of maximal intensity of the atomic lines for the generator RF power of 10 W, was used for the determination of the rotational temperature of the OH molecules in the $A\,^2\Sigma^+$ state. Since the OH rotational temperature calculated from rotational lines between states with low rotational quantum numbers often reproduces a neutral gas kinetic temperature [32, 33], the value $T_r \approx (350 \pm 20)$ K obtained clearly indicates the non-thermal character of the neon α-mode discharge.

A typical time-averaged image of the neon discharge taken with the ICCD camera is shown in figure 4. The discharge burned in the α-mode, homogeneously covering the whole electrode area. Temporally and spatially resolved emission patterns obtained from time-resolved ICCD images are shown in figure 5. Both neon and helium discharges were measured. The emissions of the helium discharge were recorded for comparison and the results obtained were in a good agreement with the findings of previous investigations [13]. The atomic lines of neon and helium were monitored using the red filter (figures 5(a), (d), (e), (h)). Since helium atoms were found to be excited inside the sheath of the helium discharge [13], the similar emission patterns of the helium and neon lines (figures 5(a), (e)) suggest the same behavior for neon. Indeed, the direct excitation of neon states of the 3p configuration requires electrons with high energy $\epsilon > 18$ eV. However, high electric fields were identified at the center of the helium discharge during the phases of maximum current [15]. Moreover, the radiating states can be excited by stepwise excitation through metastable states by low energy electrons ($\epsilon > 2$ eV for neon). Therefore, some excitation can be observed also outside the electrode sheaths. The time shift between the neon and helium intensity maxima can be explained by the different phase angles between the voltage and the current waveforms. Comparing the atomic emission patterns in the 2 and 4 mm discharge gaps (see figures 5(d), (h)), no substantial difference is observed between the figures.

Molecular emissions were recorded using the blue filter. The spatio-temporal emission pattern of the N_2^+ first negative system ($B\,^2\Sigma_u^+ \rightarrow X\,^2\Sigma_g^+$; FNS), recorded with this filter in the helium discharge (see figure 5(f)), was explained in terms of Penning ionization of nitrogen by helium metastables and by successive excitation by low energy electrons in the time between the sheath formations [13]. No FNS was registered and only a weak SPS was measured in the optical emission spectra of the neon discharge (not shown here). Thus, mostly SPS is shown in the spatio-temporal emission pattern in figure 5(b), using the blue filter. Neon metastables with energies 16.6 and 16.7 eV are capable of Penning ionization of nitrogen molecules (ionization energy 15.6 eV), but this process is less efficient than in helium [34]. Moreover, neon metastables cannot produce the N_2^+ ions in the $B\,^2\Sigma_u^+$ state (the upper state of the FNS), since this requires more energy (18.7 eV). The upper state of the SPS ($C\,^3\Pi_u$) can be excited in collisions with electrons with energies $\epsilon > 11$ eV. Since these energies are available, namely inside the electrode sheaths, the SPS emission maxima are localized into the same regions as the maxima of the neon emission. The nearly constant emission patterns of the atomic oxygen line at 844.6 nm during the whole RF period (see figures 5(c), (g)), observed previously for helium [13] and appearing also for neon, reveal a role of long-lived metastables. The effective lifetime of the upper state 3p ^{3}P of the 844.6 nm line is about 5 ns at atmospheric pressure due to quenching by helium [14]. The excited states 3p ^{3}P and 3p ^{5}P of atomic oxygen, emitting lines at 844.6 nm and 777.3 nm, respectively, are produced by the quenching of helium and neon metastables by molecular oxygen [13, 35].

Helium and neon are, up to now, the only rare gases in which diffuse barrier and RF APGDs have been easily generated. The diffuse mode for neon and helium BDs was explained by ion trapping, by Penning ionization of impurities by metastables and by surface emission of electrons from a dielectric [36]. These processes maintain collectively a sufficient pre-breakdown plasma density, favoring the formation of many small electron avalanches under low electric

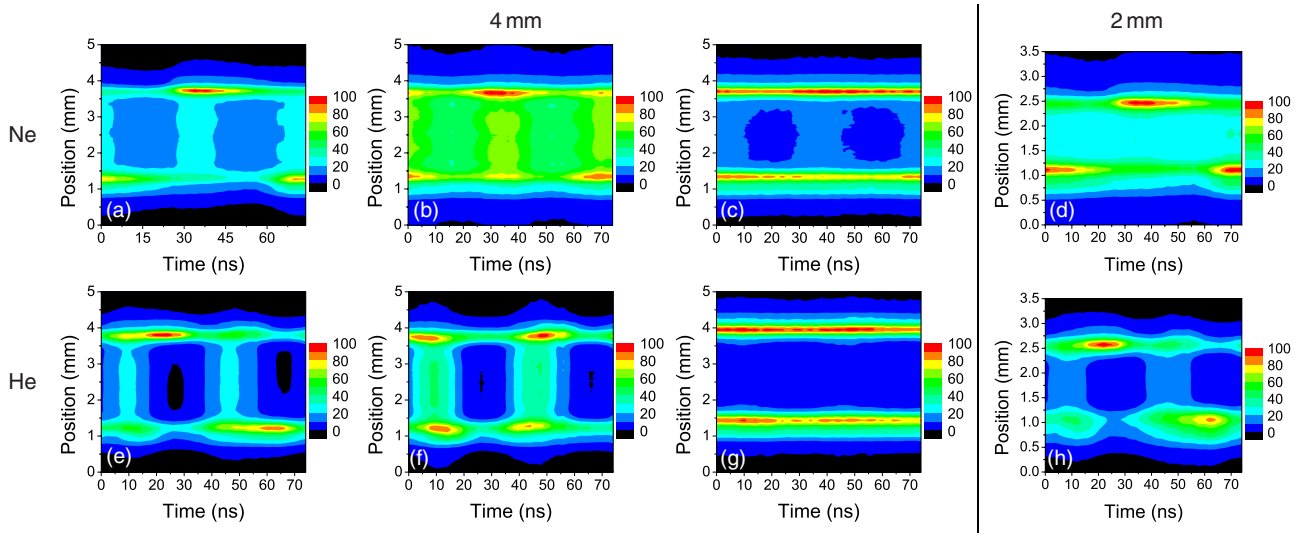

Figure 5. Temporally and spatially resolved light emissions of the α-mode discharge in neon (upper figures) and helium (lower figures) in different spectral regions. The discharge gaps were 2 and 4 mm. Filters used: (*a*), (*d*), (*e*), (*h*) red filter, atomic lines; (*b*), (*f*) blue filter, N_2 and N_2^+ in neon and helium, respectively; (*c*), (*g*) 845 nm interference filter, oxygen line.

field and generation of a homogeneous discharge. On the other hand, the diffuse α-mode RF discharge in helium is sustained by the ionization by electrons heated at sheath edges or in low conduction bulk under high electric field [13, 15]. The role of Penning ionization for the generation of the homogeneous RF discharge is less important, as compared to BDs operating at frequencies of several kilohertz, since the electron density is maintained at a sufficient level during the short RF period (74 ns). The minor role of impurity nitrogen in neon discharge is even supported by low N_2 SPS and FNS emission. The effect of surface emission from metal is negligible in the diffuse α-mode. The role of surface emission is enhanced when sheath breakdown occurs and avalanches develop inside the RF sheaths [9]. The discharge then operates in the constricted γ-mode. Other parameters such as gas heat conductivity can also play important roles [37].

We have shown that homogeneous atmospheric pressure RF discharge can also be generated in neon. The neon discharge exhibits similar phenomena to helium atmospheric pressure RF discharge, namely they have diffuse α-modes with uniformly covered electrode surfaces and constricted γ-modes, similar I–V curves with discontinuity at the mode transition and similar spatio-temporal emission patterns of the atomic lines in α-mode discharge.

Acknowledgments

The present work was supported by grant No GA13-24635S of the Czech Science Foundation, by the project 'R&D center for low-cost plasma and nanotechnology surface modifications' (No CZ.1.05/2.1.00/03.0086) funded by the European Regional Development Fund, and by the program 'Employment of newly graduated doctors of science for scientific excellence' (No CZ.1.07/2.3.00/30.0009) co-financed by the European Social Fund and the state budget of the Czech Republic.

References

[1] Fridman A, Chirokov A and Gutsol A 2005 *J. Phys. D: Appl. Phys.* **38** R1
[2] Tendero C, Tixier C, Tristant P, Desmaison J and Leprince P 2006 *Spectrochim. Acta Part* B **61** 2
[3] Kanazawa S, Kogoma M, Moriwaki T and Okazaki S 1988 *J. Phys. D: Appl Phys.* **21** 838
[4] Trunec D, Brablec A and Buchta J 2001 *J. Phys. D: Appl. Phys.* **34** 1697
[5] Gherardi N, Gouda G, Gat E, Ricard A and Massines F 2000 *Plasma Sources Sci. Technol.* **9** 340
[6] Blades M W 1994 *Spectrochim. Acta* **49B** 47
[7] Park J, Henins I, Herrmann H W, Selwyn G S and Hicks R F 2001 *J. Appl. Phys.* **89** 20
[8] Park J, Henins I, Herrmann H W and Selwyn G S 2001 *J. Appl. Phys.* **89** 15
[9] Raizer Y 1995 *Radio-Frequency Capacitive Discharges* (Boca Raton, FL: CRC Press)
[10] Yuan X and Raja L L 2003 *IEEE Trans. Plasma Sci.* **31** 495
[11] Yang X, Moravej M, Nowling G R, Babayan S E, Panelon J, Chang J P and Hicks R F 2005 *Plasma Sources Sci. Technol.* **14** 314
[12] Moon S Y, Rhee J K, Kim D B and Choe W 2006 *Phys. Plasmas* **13** 033502
[13] Liu D W, Iza F and Kong M G 2009 *Appl. Phys. Lett.* **95** 031501
[14] Waskoenig J, Niemi K, Knake N, Graham L M, Reuter S, Schulz-von der Gathen V and Gans T 2010 *Plasma Sources Sci. Technol.* **19** 045018
[15] Hemke T, Eremin D, Mussenbrock T, Derzsi A, Donkó Z, Dittmann K, Meichsner J and Schulze J 2013 *Plasma Sources Sci. Technol.* **22** 015012
[16] Nozaki T, Ohnishi K, Okazaki K and Kortshagen U 2007 *Carbon* **45** 364
[17] Shi J J and Kong M G 2007 *Appl. Phys. Lett.* **90** 111502
[18] Wang H B, Sun W T, Li H P, Bao C Y, Gao X and Luo H Y 2006 *Appl. Phys. Lett.* **89** 161504
[19] Schwab H A 1971 *Proc. IEEE* **59** 613
[20] Wang H B, Sun W T, Li K P, Bao C Y and Zhang X Z 2006 *Appl. Phys. Lett.* **89** 161502
[21] Baars-Hibbe L Sichler P, Schrader C, Gericke K-H and Büttgenbach S 2005 *Plasma Process. Polym.* **2** 174

[22] Boeuf J P 2003 *J. Phys. D: Appl. Phys.* **36** R53
[23] Abramczyk H 2005 *Introduction to Laser Spectroscopy* (Amsterdam: Elsevier) p 88
[24] Kogelschatz U 2003 *Plasma Chem. Plasma Process.* **23** 1
[25] Fedenev A, Morozov A, Krücken R, Schoop S, Wieser J and Ulrich A 2004 *J. Phys. D: Appl. Phys.* **37** 1586
[26] Navrátil Z, Brandenburg R, Trunec D, Brablec A, St'ahel P, Wagner H-E and Kopecký Z 2006 *Plasma Sources Sci. Technol.* **15** 8
[27] Gagnon H, Piyakis K and Wertheimer M R 2014 *Plasma Process. Polym.* **11** 106
[28] Lieberman M A 1988 *IEEE Trans. Plasma Sci.* **16** 638
[29] Mussenbrock T and Brinkmann R P 2006 *Appl. Phys. Lett.* **88** 151503
[30] Dvořák P 2010 *Plasma Sources Sci. Technol.* **19** 025014
[31] Dvořák P 2013 *Plasma Sources Sci. Technol.* **22** 045016
[32] Pellerin S, Cormier J M, Richard F, Musiol K and Chapelle J 1996 *J. Phys. D: Appl. Phys.* **29** 726
[33] Bruggeman P, Schram D, González M Á, Rego R, Kong M G and Leys C 2009 *Plasma Sources Sci. Technol.* **18** 025017
[34] West W P, Cook T B, Dunning F B, Rundel R D and Stebbings R F 1975 *J. Chem. Phys.* **63** 1237
[35] Mueller D and Krenos J 1993 *J. Phys. Chem.* **97** 2106
[36] Massines F, Gherardi N, Naudé N and Séguer P 2009 *Eur. Phys. J. Appl. Phys.* **47** 22805
[37] Staack D, Farouk B, Gutsol A and Fridman A 2008 *Plasma Sources Sci. Technol.* **17** 025013

Atmospheric Pressure RF Discharge in Neon and Helium

Raavo Josepson, Zdeněk Navrátil, Lenka Dosoudilová, Pavel Dvořák, and David Trunec

Abstract— **Radio frequency (13.56 MHz) capacitive discharges at atmospheric pressure in neon and helium were studied by ICCD imaging. The discharges were generated between parallel plate metal electrodes with a gap of 2 mm. At certain conditions, a homogeneous discharge burning in α-mode can be generated both in helium and neon. The time-resolved images of discharges reveal similarities in atomic excitation mechanism in both gases.**

Index Terms— **Atmospheric-pressure plasmas, neon and helium, radio frequency capacitive discharge.**

RECENTLY, radio frequency (RF) capacitive discharges operated at atmospheric pressure have gained interest in material processing [1]. Similarly to low pressure RF discharges, the RF discharges at elevated pressures can be operated in two modes: α- or γ-mode [2]. The homogeneous α-mode has been so far observed in helium at atmospheric pressure [3], [4]; filamentary γ-mode is usually observed in other gases. In this paper, we report on the homogeneous α-mode in neon and we compare the discharges in neon and helium using a full-color ICCD imaging.

The RF discharges were generated in parallel plate electrode setup. The electrodes, made of brass and 40 mm in diameter, were placed at a distance of 2 mm into a steel vacuum chamber. The chamber was evacuated down to 5 Pa by a rotary oil pump and then filled with helium or neon (gas purity 5.0) up to atmospheric pressure. A gas flow of 400 sccm was kept during the measurements using a membrane pump. The harmonic 13.56-MHz signal was generated by a function generator (Agilent 33220A) and then amplified (by Hüttinger TIS 0.5/13560). Electrical parameters were monitored using a digital storage oscilloscope (LeCroy WaveRunner 6100 A). Time-resolved pictures of the RF discharge were taken by ICCD camera (PI-MAX3). The ICCD gate was gradually delayed from the synchronization signal of the function generator to scan with 2-ns step through the RF period. The gate width was 2.74 ns, gate rate reached 850 kHz, and 65 535 gating events were accumulated. Three RGB bandpass filters introduced into the optical path provided pictures in blue (<500 nm), green (510–570 nm), and red (>610 nm) wavelength region. Three pictures with the same delay were then assembled into one full-color picture. A sensitivity of the optical setup was balanced using a photograph taken with a full-color camera (Nikon 1). By scaling the RGB channels of time-integrated ICCD image up to the values of the photograph, correction factors for the RGB channels were obtained. Then, the factors were applied to the RGB channels of time-resolved ICCD images.

Time-resolved ICCD images of RF discharge burning in helium and neon at atmospheric pressure are shown in Fig. 1. At applied voltage of ~100–200 V (peak-to-peak), both discharges burned in α-mode and they were homogeneous along the electrodes. A remarkable changing of color and structure was observed within the series of images of the helium discharge. An emission spectrum of helium discharge (not shown here) consisted of helium atomic lines (587.6, 667.8, and 706.5 nm), hydrogen atomic lines H_α, H_β, and of nitrogen molecular systems ($N_2C^3\Pi_u \rightarrow B^3\Pi_g$, $N_2^+B^2\Sigma_u^+ \rightarrow X^2\Sigma_g^+$) in visible region. Light emission of OH and O was observed in UV and IR, respectively. Thus, sharp red lights at the electrodes show the regions of He excitation, while blue and green areas represent regions in which light emission from N_2^+ dominates. The alternating excitation of N_2^+ and He has been already observed and explained [4]. While helium atoms are excited only inside the sheath under high electric field, excited N_2^+ can be produced in low electric field regions at the time of sheath formation and collapse. In neon, a periodical fade in and out of sharp areas at the electrodes was observed in red, and the light emission in blue and green was weak and almost homogenous both in space and time. Since the red spectral region includes strong neon lines (585–743 nm), neon atoms are, as the atoms of helium, excited inside the sheath. The homogeneous weak light shows, that impurities as N_2 are excited in the whole discharge gap.

Manuscript received November 2, 2013; accepted February 16, 2014. Date of publication March 4, 2014; date of current version October 21, 2014. This work was supported in part by the Czech Science Foundation under Grant GA13-24635S, in part by the European Regional Development Fund under Project CZ.1.05/2.1.00/03.0086, and in part by the Program under Grant CZ.1.07/2.3.00/30.0009 through the European Social Fund and the State Budget of the Czech Republic.

The authors are with the Department of Physical Electronics, Masaryk University, Kotlářská 2, Brno 611 37, Czech Republic (e-mail: raavo.josepson@ttu.ee; zdenek@physics.muni.cz; ldosoudi@mail.muni.cz; pdvorak@physics.muni.cz; trunec@physics.muni.cz).

Color versions of one or more of the figures in this paper are available online at http://ieeexplore.ieee.org.

Digital Object Identifier 10.1109/TPS.2014.2307080

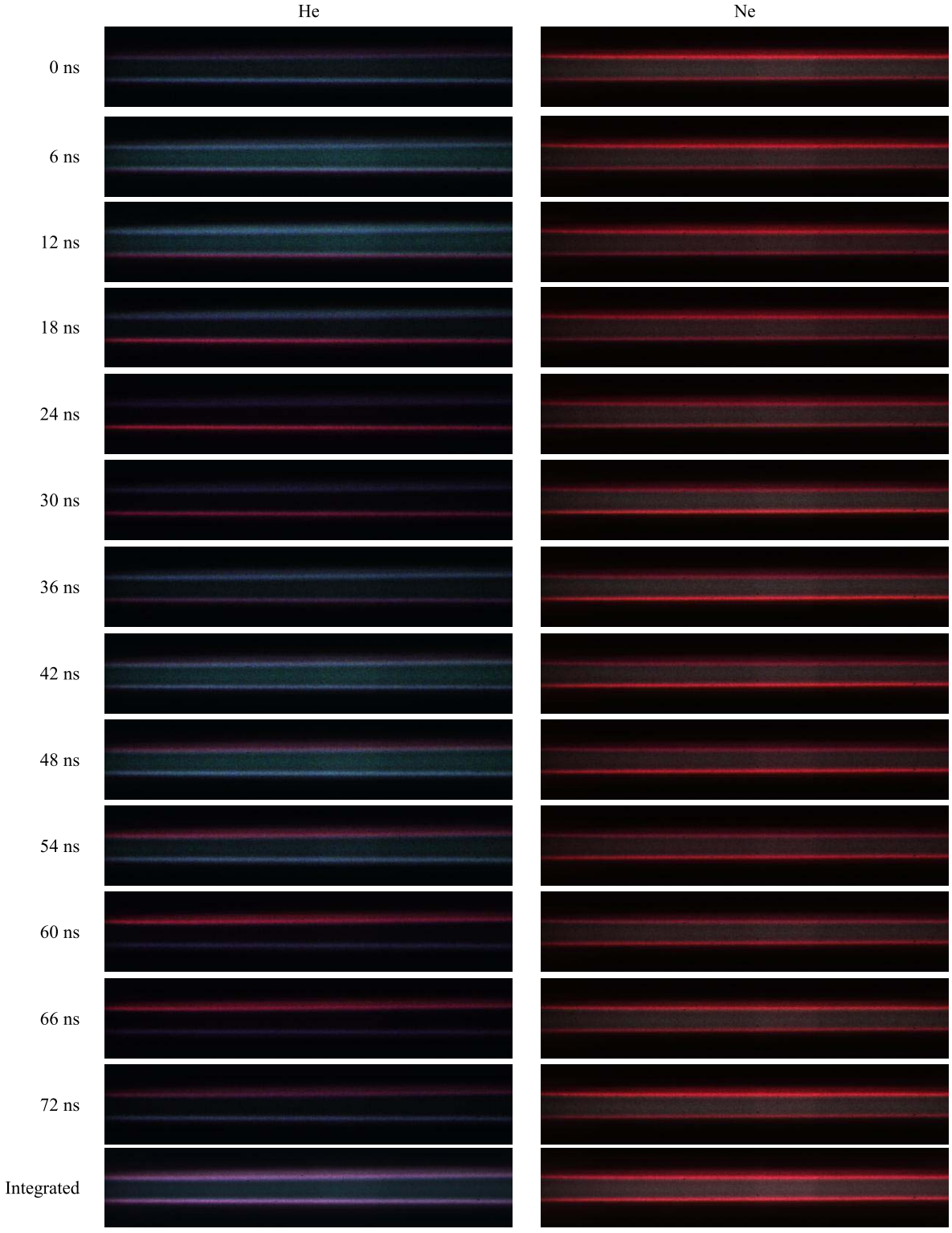

Fig. 1. α-mode RF discharge at atmospheric pressure in helium and neon developing within one RF period of 74 ns. The images were taken with time step of 2 ns, so every third image is shown. The integrated images were obtained by averaging over all time-resolved images.

REFERENCES

[1] T. Nozaki, S. Yoshida, T. Karatsu, and K. Okazaki, "Atmospheric-pressure plasma synthesis of carbon nanotubes," *J. Phys. D, Appl. Phys.*, vol. 44, no. 17, p. 174007, 2011.

[2] Y. Raizer, *Radio-Frequency Capacitive Discharges*. Cleveland, OH, USA: CRC Press, 1995.

[3] J. Park, I. Henins, H. W. Herrmann, and G. S. Selwyn, "Gas breakdown in an atmospheric pressure radio-frequency capacitive plasma source," *J. Appl. Phys.*, vol. 89, no. 1, pp. 15–19, 2001.

[4] D. W. Liu, F. Iza, and M. G. Kong, "Electron avalanches and diffused γ-mode in radio-frequency capacitively coupled atmospheric-pressure microplasmas," *Appl. Phys. Lett.*, vol. 95, pp. 031501-1–031501-3, 2009.

Letters

IOP Publishing

Plasma Sources Science and Technology

Plasma Sources Sci. Technol. **25** (2016) 03LT01 (6pp)

doi:10.1088/0963-0252/25/3/03LT01

Letter

Electric field development in γ-mode radiofrequency atmospheric pressure glow discharge in helium

Zdeněk Navrátil[1], Raavo Josepson[1], Nikola Cvetanović[2], Bratislav Obradović[3] and Pavel Dvořák[1]

[1] Department of Physical Electronics, Faculty of Science, Masaryk University, Kotlářská 2, 611 37 Brno, Czech Republic

[2] Faculty of Transport and Traffic Engineering, University of Belgrade, Vojvode Stepe 305, 11000 Belgrade, Serbia

[3] Faculty of Physics, University of Belgrade, Studentski trg 12, 11001 Belgrade, Serbia

E-mail: zdenek@physics.muni.cz and raavo.josepson@ttu.ee

Received 11 May 2015, revised 27 January 2016
Accepted for publication 4 February 2016
Published 16 March 2016

Abstract

Time development of electric field strength during radio-frequency sheath formation was measured using Stark polarization spectroscopy in a helium γ-mode radio-frequency (RF, 13.56 MHz) atmospheric pressure glow discharge at high current density (3 A cm^{-2}). A method of time-correlated single photon counting was applied to record the temporal development of spectral profile of He I 492.2 nm line with a sub-nanosecond temporal resolution. By fitting the measured profile of the line with a combination of pseudo-Voigt profiles for forbidden (2 ^{1}P–4 ^{1}F) and allowed (2 ^{1}P–4 ^{1}D) helium lines, instantaneous electric fields up to 32 kV cm^{-1} were measured in the RF sheath. The measured electric field is in agreement with the spatially averaged value of 40 kV cm^{-1} estimated from homogeneous charge density RF sheath model. The observed rectangular waveform of the electric field time development is attributed to increased sheath conductivity by the strong electron avalanches occurring in the γ-mode sheath at high current densities.

Keywords: radiofrequency discharge, atmospheric pressure, electric field, helium

(Some figures may appear in colour only in the online journal)

1. Introduction

Radio-frequency atmospheric pressure plasmas have become a useful tool in various plasma processing applications [1]. Using bare metal planar electrodes and a radio-frequency (RF) power source, a non-thermal, so-called radio-frequency atmospheric pressure glow discharge (RF APGD) can be easily obtained in helium, neon and argon [2–5]. When a discharge gap is below several millimetres and the applied RF power is low, the discharge operates in a homogeneous α-mode. The RF APGD transits into γ-mode at a higher RF power. Although the discharge is constricted to a smaller electrode area and the neutral gas temperature is increased in the γ-mode, it is an efficient source of charged particles, metastables and reactive species [6, 7].

RF APGD in helium in the planar electrode gap was a subject of numerous studies [4, 8–19]. Since the direct measurement of the electric field in RF APGD is difficult, the electric field was obtained by a numerical modelling or estimated from the measurement of the applied voltage and of the discharge current. The electric field of 1–3 kV cm^{-1} was identified in an α-mode discharge bulk [4, 18]. The time averaged electric

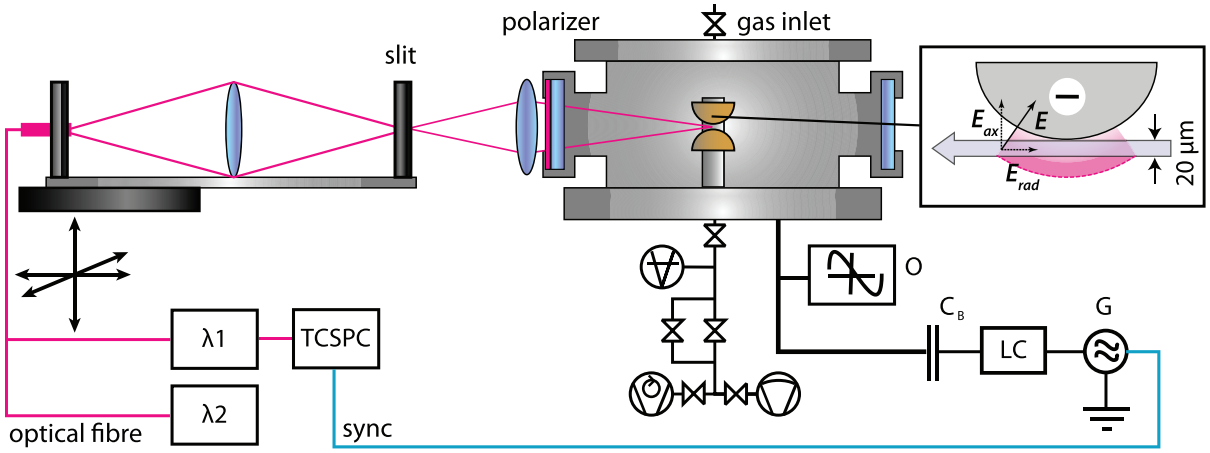

Figure 1. Scheme of experimental set-up. G—13.56 MHz generator, O—oscilloscope LeCroy WaveRunner 6100 A, λ1—monochromator JY HR-640, TCSPC—time correlated single photon counter BH SPC-150, λ2—Horiba FHR-1000 spectrometer with CCD. The curvatures in the zoomed figure are largely exaggerated.

field, obtained from the modelling, reached 5 kV cm^{-1} in α-mode RF sheath, decreasing linearly from the electrode [6]. The evaluation of the electric field in γ-mode discharge from electrical measurement is even more complicated because of discharge non-uniformity, uncertain electrode coverage and also RF sheath thickness decreasing to about 100 μm and less at high current densities [4, 6]. The time-averaged electric field calculated with a 1D model for a current density of 106 mA cm^{-2} reached 12 kV cm^{-1} in γ-mode RF sheath, also decreasing linearly from the electrode [6].

Since electron impact excitation occurs inside the sheath of γ-mode discharges [16], the light emission from the γ-mode RF sheath is significant and the electric field in the sheath can be determined from Stark splitting of atomic spectral lines using optical emission spectroscopy. In case of RF electric field (13.56 MHz), the high frequency Stark effect observed in microwave electric fields [21] does not occur and the Stark shift dependence on instantaneous electric field is the same as in the DC field [20]. In this work, we applied a method of Stark polarization spectroscopy of helium 492.2 nm line for the time-resolved measurement of electric field in RF sheath of γ-mode RF APGD. Splitting of hydrogen atomic lines [22] could not be used due to their low intensity in the discharge and their excitation mechanism [23, 24]. Helium 492.2 nm line has already been applied for the electric field measurement in cathode fall of low pressure DC glow discharge and of atmospheric pressure diffuse barrier discharge [25, 26, 28]. Stark broadening of the same line can be used for electron density measurement for values of density higher than 10^{16} cm^{-3} [27].

2. Experimental setup

The stable γ-mode RF APGD was generated between hemispherical bare metal electrodes inside a steel vacuum chamber (see figure 1). The electrodes were made of brass, 8 mm in diameter and they were cooled by oil-cooling circuit. The chamber was evacuated first down to 5 Pa by a rotary oil pump and then filled with helium (gas purity 5.0) up to atmospheric pressure. A gas flow of 200 sccm was kept constant during the measurements using a membrane pump. The discharge gap was 2 mm. The harmonic 13.56 MHz signal was generated by a function generator (Agilent 33220A) and amplified with RF power amplifier (Hüttinger TIS 0.5/13560). Electrical parameters were monitored by a digital storage oscilloscope (LeCroy WaveRunner 6100A). The use of hemispherical electrodes decreased the voltage needed for α-γ mode transition. The amplitudes of voltage and current were 240 V and 0.6 A, respectively.

The vacuum chamber was equipped with quartz windows for optical diagnostics. A glass polarizer introduced into the optical path extracted the light polarized in the direction of the interelectrode axis. A spatial resolution of the optical measurements was achieved by projecting the discharge with unit magnification by a quartz lens onto a 20 μm slit, with an optical fibre located beyond it. The slit was located at the position of the maximum intensity of He I 492.2 nm line at the driven electrode. Temporally resolved optical emission spectroscopy was performed by the method of time-correlated single photon counting (TCSPC). The light collected by the optical fibre was first spectrally resolved (Jobin Yvon HR-640, grating 1200 gr mm^{-1}, instrumental FWHM 0.075 nm) and then analyzed by a single photon counter (Becker and Hickl SPC-150) with a photomultiplier working in a photon counting mode (PMC-100-4). Arrivals of the individual photons were correlated with the RF signal, taken from the function generator, with a temporal resolution of 0.8 ns. The monochromator scanned slowly over the spectral profile at 492.2 nm with a step of 0.02 nm. Temporally unresolved optical emission spectra were recorded by Horiba FHR-1000 spectrometer (grating 2400 gr mm^{-1}, instrumental FWHM 0.005 nm, CCD detector).

3. Results and discussions

Temporally unresolved spectral profiles of He I 492.2 nm line measured with the CCD at varied RF power at the driven electrode are displayed in figure 2. The measured profiles consist of uncommonly broad allowed (2 ^{1}P–4 ^{1}D) and forbidden

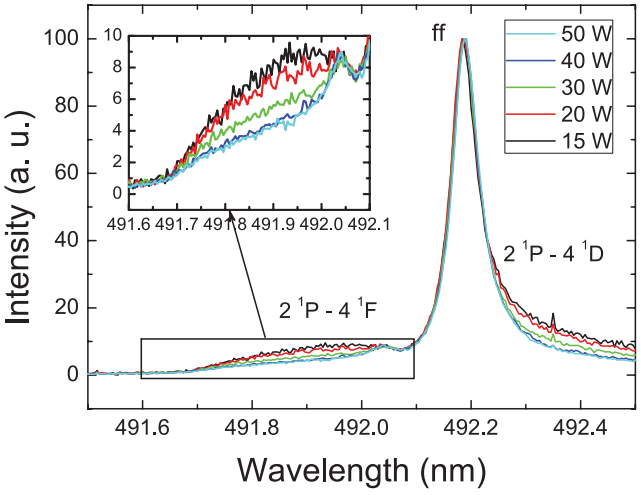

Figure 2. Time-unresolved spectral profiles of He I 492.2 nm line in γ-mode discharge measured at the driven electrode for varied RF power. The spectral profiles were normalized according to the maximum. The forbidden component is shown magnified in a smaller plot.

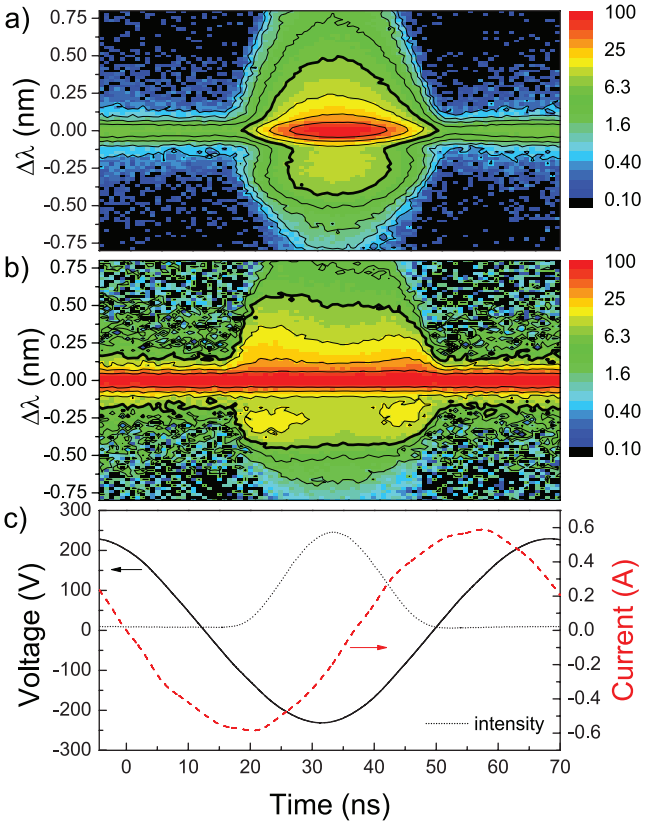

Figure 3. Time-resolved spectral profile of He I 492.2 nm line measured with TCSPC during the sheath formation in γ-mode discharge at the driven electrode. (a)—global intensity normalization in the plot, (b)—each spectral profile normalized separately. Thick line denotes an intensity of half maximum of the forbidden component. (c)—time-development of voltage, current and line intensity integrated over the spectral profile. Time 0 ns corresponds to the time of the discharge current inversion.

(2 ^{1}P–4 ^{1}F) helium line. Time averaging and limited space resolution led to inclusion of components from different sheath regions into the measured profile (see zoomed drawing in figure 1). The field strength distribution in the measured regions is then reflected as the distribution of wavelength shift. Since the forbidden component is emitted only in the high field regions due to the braking of selection rules in the dipole approximation, the result is a broad line. On the other hand, since the allowed line is emitted in all of the sheath regions, the result is a large wing on the red side of the measured profile, instead of a single shifted line. The wing appears as a part of a non-shifted peak of the allowed line at the central wavelength of 492.19 nm, which corresponds to radiation from low field regions (so-called field-free or ff component) [28].

When the RF power is low, a broad peak of the forbidden line is observed shifted at wavelengths 491.7–492.1 nm. The increase of RF power (and current) decreases the sheath thickness [6, 12] and the observed spatial region becomes a region of lower electric field. The broad forbidden line therefore disappears and only a small narrow peak appears instead at 492.04 nm (approximately at zero-field wavelength of the forbidden line). The measured FWHM of the field-free component of 0.06 nm does not vary with increased power, since a negligible impact of Stark broadening is expected under the studied conditions [27]. The most important broadening mechanisms, van der Waals and resonance broadening by helium ground state atoms, broaden the allowed component to FWHM of 0.055 nm, in agreement with the measured value.

The time evolution of spectral profile of He I 492.2 nm line measured with TCSPC at the driven electrode is shown in figure 3(a). Most of the light is emitted within 30 ns during the sheath formation, when the voltage on the driven electrode is the most negative (compare with figure 3(c)). When the voltage on the driven electrode is positive, the light intensity maximum is located at the other (grounded) electrode. The non-zero intensity of ff component ($\Delta\lambda = 0$ nm) observed in times between the intensity maxima is then mostly due to reflected light originally emitted at the grounded electrode. In the late phase of the emission maximum, the ff component decays exponentially with a decay time of about 3.6 ns , the forbidden and the allowed components decrease even somewhat faster (decay time about 2 ns). The radiative lifetimes of helium 4 ^{1}D and 4 ^{1}F states are 36 and 67 ns, respectively [29]. However, 4 P, 4 D and 4 F levels are strongly coupled by excitation transfer induced by collisions with helium ground state atoms [30, 31]. Quenching of 4 ^{1}D and 4 ^{1}F states by helium atoms [31] results in decay times of 38 and 75 ps, respectively. It may be concluded that the intensity of He I 492.2 nm line always follows the instantaneous discharge development. On the other hand, the time resolution of electric field measurement is not limited by the lifetimes of the excited states, since the delay in photon emission does not influence the photon wavelength dictated by instantaneous Stark shift during the photon emission.

The time evolution of spectral profile of He I 492.2 nm line, but with each spectral profile normalized independently, is shown in figure 3(b). The appearance of the forbidden line during the intensity maximum confirms the existence of a region with a high electric field strength, i.e. of the sheath region. Outside this region the electric field is small and cannot be measured. Two small maxima appear during this forbidden

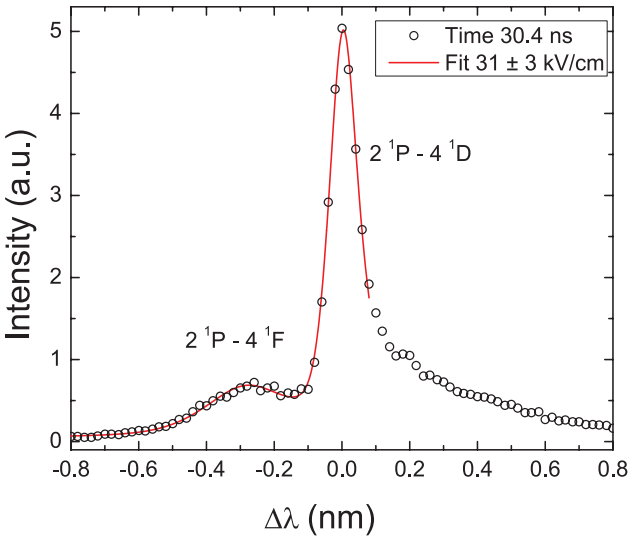

Figure 4. Fitted time-resolved He I 492.2 nm spectral profile measured with TCSPC at time 30.4 ns at the driven electrode. Only the forbidden and field-free component were included in the fitting domain.

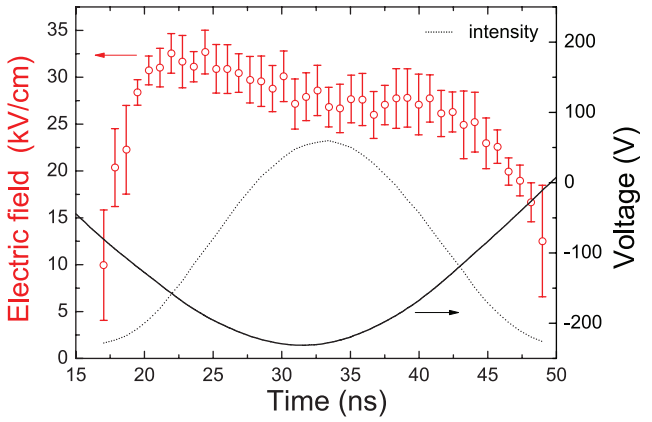

Figure 5. Time-development of electric field strength at the driven electrode obtained from the fit of forbidden and field-free component. Solid and the dotted line denote the applied RF voltage development and the development of intensity integrated over the spectral profile, respectively.

line development. The line intensity obtained as an integral over the spectral profile is displayed together with the voltage and current waveforms in figure 3(c). The intensity reaches maximum approximately at the time when the electrode is the most negative, as simulated in [16]. A small delay 2.2 ns of the intensity is comparable to the experimental error of signal correlation. The phase shift between the voltage and current is around 60°, but the current is distorted by higher harmonics as predicted in atmospheric pressure RF discharges [32].

An example of time-resolved spectral profiles slotted in figure 3 is shown in figure 4. The time-resolved profiles are broader in contrast to the observations in atmospheric pressure barrier discharges [26]. As explained, this can be due to insufficient spatial resolution and/or presence of non-axial electric field (see zoomed drawing in figure 1). The sheath thickness below 100 μm [6] is comparable with the expected spatial resolution (optical slit width was 20 μm). The spatial resolution is further reduced due to the use of round electrodes for discharge stabilization, since the curvature of the discharge near the electrodes leads to inclusion of different regions along the optical path into the measured profile.

The measured allowed component was very broad and could not be used for field determination. For this reason a fitting method based on wavelength distance between the forbidden component (emitted only in the high field regions) and the field-free (non-shifted) component was developed. Namely, the fitting function is a superposition of two pseudo-Voigt profiles and the shift of the forbidden component is directly related to the field strength via dependence given in [28]. The intensities of two components and their widths are free fitting parameters while the field strength is directly obtained from the fit. In this case, the shifted allowed line is excluded from the fitting domain (see figure 4).

Whereas the width of the ff component obtained from fitting agrees with value calculated from expected broadening mechanisms and instrumental width (≈0.1 nm), the forbidden component is much wider than expected (≈0.3 nm). Since this suggests, that the forbidden line still contains light emission from regions with various electric fields, the electric field strengths obtained from the fit should be taken only as an average value of the field in the cathode sheath.

The time-development of electric field strength, determined from the fits of the time resolved spectral profiles, together with the development of He I 492.2 nm line intensity and applied RF voltage is shown in figure 5. The electric field time development has almost a rectangular shape reaching 32 kV cm^{-1}. The field is slightly higher at the beginning and the end of the sheath formation, which can be seen from the two maxima appearing in the forbidden line time development (see figure 3(b))). As mentioned, large broadening of the forbidden line introduces an uncertainty in the field determination and implies the presence of a wider range of the electric field strengths. Since the field strengths of ≈30 kV cm^{-1} shown here should be taken as average field values inside the cathode sheath, the maximum field strength at the cathode is expected to be at least twice higher, $E \gtrsim 60$ kV cm^{-1}. The large width of the forbidden line also did not allow the measurement of the electric field lower than about 10 kV cm^{-1}.

A direct comparison of the measured electric field with the results of previous numerical modelling as in [6] is not possible due to a large difference in current density. The time-averaged electric field at the driven electrode, calculated from the presented time-resolved electric field development (figure 5), is 11.3 kV cm^{-1}. This value was obtained as the time average of the measured field over the whole voltage period with assumed zero field outside the measured time interval. On the other hand, the electric field of 6 kV cm^{-1}, averaged in time and over the sheath, was calculated for the much lower RMS current density of 106 mA cm^{-2} [6] compared to the current density $j_{\mathrm{RMS}} \approx 3$ A cm^{-2} in the presented measurement. These electric field values are at least consistent taking into account the trend of increasing electric field with the increasing current density [6].

The measured development of the electric field can be explained by a simple RF sheath model. The current density j

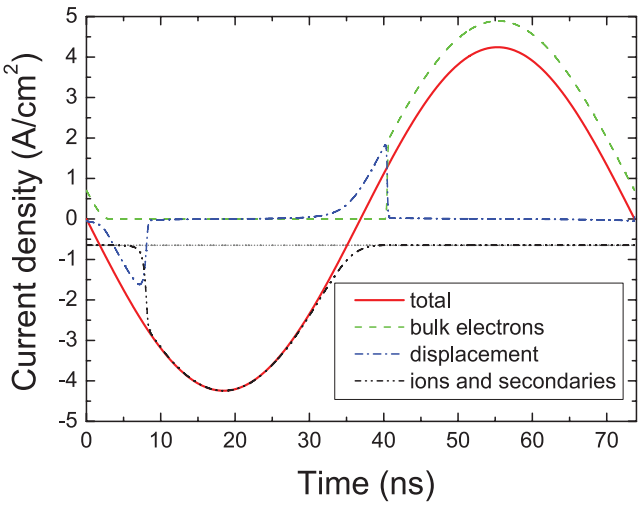

Figure 6. Modelled densities of currents flowing from the electrode: total current (red), current of ions and secondary electrons (black, the Bohm flow of ions from bulk plasma is depicted by a grey dotted line), current of electrons from bulk plasma (green), displacement current (blue). Total RMS current density was set 3 A cm^{-2} according to the experimental value. Time 0 ns corresponds to the time of the total discharge current inversion.

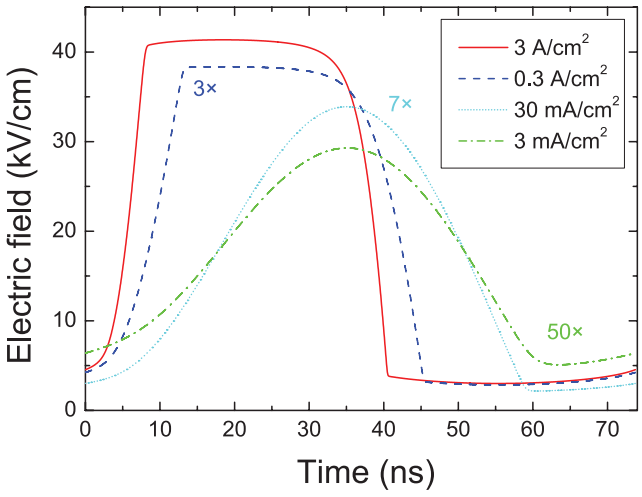

Figure 7. Modelled average electric field strengths for constant ratio j_{RMS}/n and various total discharge current densities j_{RMS}: 3 A cm^{-2} (red), 300 mA cm^{-2} (blue, 3 × increased), 30 mA cm^{-2} (turquoise, 7 ×) and 3 mA cm^{-2} (green, 50 ×). The field strength is spatially averaged over the RF sheath, having half the maximum value at the electrode.

flowing from the electrode surface can be expressed as a sum of the displacement current density $\varepsilon_0 \mathrm{d}E/\mathrm{d}t$, ion current density j_{i}, current density of secondary electrons γj_{i} and flux of electrons from the bulk plasma. The flux of ions flowing through the plasma-sheath boundary ($-nv_{\mathrm{B}}$, where $v_{\mathrm{B}} = \sqrt{kT_{\mathrm{e}}/m_{\mathrm{i}}}$ is the Bohm velocity, T_{e} electron temperature and m_{i} ion mass) is in the sheath amplified due to ionization caused by avalanches ignited by secondary electrons. The resulting amplified ion current density at the electrode can be expressed by

$$j_{\mathrm{i}} = \frac{-nev_{\mathrm{B}}}{1-\gamma\left[\mathrm{e}^{\int_0^s \alpha(x)\mathrm{d}x}-1\right]}, \qquad (1)$$

where n is the bulk electron density and s is actual sheath thickness. Townsend ionization coefficient ($\alpha = Ap\,\mathrm{e}^{-Bp/E}$, $A = 2.1$ m^{-1} Pa^{-1}, $B = 25.5$ Vm^{-1} Pa^{-1}, E is the electric field strength), and secondary electron emission coefficient ($\gamma = 0.01$) were taken in the same form as in [12]. Assuming homogeneous ion density in the sheath n and much shorter ion transport time through the sheath compared to the RF period (which is justified by the small sheath thickness in the γ-mode), the total current density can be written as

$$j(t) = -ne\frac{\mathrm{d}s(t)}{\mathrm{d}t} - \frac{nev_{\mathrm{B}}(1+\gamma)}{1-\gamma\left[\mathrm{e}^{\int_0^{s(t)}\alpha(x,t)\mathrm{d}x}-1\right]} + \frac{1}{4}ne\sqrt{\frac{8kT_{\mathrm{e}}}{\pi m_e}}\,\mathrm{e}^{-eU_{\mathrm{sh}}(t)/(kT_{\mathrm{e}})}, \qquad (2)$$

where m_e is the electron mass and $U_{\mathrm{sh}} \approx nes^2/(2\varepsilon_0)$ is the actual sheath voltage.

The equation (2) was solved numerically for sinusoidal current density j together with the condition, that sheath voltages at the beginning and at the end of the period must be equal (identical in our case with the condition of zero DC current flowing through the sheath). The waveforms of current density components, obtained from the model for the total current density $j_{\mathrm{RMS}} = 3$ A cm^{-2} taken from the experiment, are shown in figure 6. When the sheath voltage increases sufficiently, the sheath conductivity rises sharply due to the increase of the term $\gamma\left[\mathrm{e}^{\int_0^s \alpha(x)\mathrm{d}x}-1\right]$. As a result, most of the current is taken over by secondary avalanches, whereas the displacement current ($-ne\,\mathrm{d}s/\mathrm{d}t$) is stopped, preventing the sheath voltage from further growth. A similar situation occurs in the second half of the period, when the sheath voltage is very small and the sheath conductivity is high due to the electron current, which has to compensate the high ion current from the first half of the RF period.

Several examples of the modelled electric field strength for different current densities, obtained by solution of equation (2) and then spatially averaged over the sheath, are shown in figure 7. The development of the electric field strength for the conditions closest to the presented experiment is depicted by the curve calculated for the highest discharge current density $j_{\mathrm{RMS}} = 3$ A cm^{-2}; the used bulk electron density $n = 10^{13}$ cm^{-3} [6] is only a rough estimate. As concluded from figure 6, strong electron avalanches initiated by γ processes in high current γ-mode RF sheath can cause a strong increase of sheath conductivity in most of the discharge period. Consequently, the growth of the sheath thickness is stopped and the sinusoidal waveform of electric field strength is replaced with the rectangular one (see figure 7). The maximum electric field strength of 80 kV cm^{-1} at the electrode (twice the average value in homogeneous charge density model) corresponds well to the maximal Stark shift of the forbidden component observed in figures 2 and 3. The calculated maximum sheath thickness of 45 μm obtained for the presented discharge conditions is in agreement with the small sheath thickness expected in the γ-mode discharge [6, 19].

4. Conclusion

In conclusion, time development of electric field strength during radio-frequency sheath formation was measured using Stark polarization spectroscopy in helium γ-mode radio-frequency atmospheric pressure glow discharge. Instantaneous, but spatially averaged electric fields up to 32 kV cm^{-1} were measured in the γ-mode RF cathode sheath, roughly in agreement with the result of the RF sheath modelling (space averaged 40 kV cm^{-1}). The observed rectangular waveform of the electric field was attributed to the strong increase of the sheath conductivity due to electron avalanches initiated by the γ processes at high current densities. Improved spatial resolution of the measurement may reveal a higher maximal electric field strength at the electrode, as expected from the RF sheath modelling.

Acknowledgments

The present work was supported by grant GA13-24635S of Czech Science Foundation, project CZ.1.05/2.1.00/03.0086 funded by European Regional Development Fund, project CZ.1.07/2.3.00/30.0009 co-financed from European Social Fund and the state budget of the Czech Republic and project LO1411 (NPU I) funded by Ministry of Education, Youth and Sports of the Czech Republic. The authors also want to express their gratitude to Prof M S Dimitrijević for helpful discussion on Stark effect in high frequency electric field.

References

[1] Laroussi M and Akan T 2007 *Plasma Process. Polym.* **4** 777
[2] Park J, Henins I, Herrmann H W, Selwyn G S and Hicks R F 2001 *J. Appl. Phys.* **89** 20
[3] Navrátil Z, Dosoudilová L, Josepson R, Dvořák P and Trunec D 2014 *Plasma Sources Sci. Technol.* **23** 042001
[4] Laimer J and Störi H 2006 *Plasma Process. Polym.* **3** 573
[5] Li S-Z, Wu Q, Wang D and Uhm H S 2011 *Phys. Lett.* A **375** 598
[6] Shi J and Kong M G 2005 *IEEE Trans. Plasma Sci.* **33** 624
[7] Schröder D, Burhenn S, Kirchheim D and Schulz-von der Gathen V 2013 *J. Phys. D: Appl. Phys.* **46** 464003
[8] Park J, Henins I, Herrmann H W and Selwyn G S 2001 *J. Appl. Phys.* **89** 15
[9] Yuan X and Raja L L 2003 *IEEE Trans. Plasma Sci.* **31** 495
[10] Yang X, Moravej M, Nowling G R, Babayan S E, Panelon J, Chang J P and Hicks R F 2005 *Plasma Sources Sci. Technol.* **14** 314
[11] Shi J and Kong M G 2005 *J. Appl. Phys.* **97** 023306
[12] Moon S Y, Rhee J K, Kim D B and Choe W 2006 *Phys. Plasmas* **13** 033502
[13] Shi J J and Kong M G 2007 *Appl. Phys. Lett.* **90** 111502
[14] Iza F, Lee J K and Kong M G 2007 *Phys. Rev. Lett.* **99** 2
[15] Schulz-von der Gathen V, Buck V, Gans T, Knake N, Niemi K, Reuter S, Schaper L and Winter J 2007 *Contrib. Plasma Phys.* **47** 510
[16] Liu D W, Iza F and Kong M G 2009 *Appl. Phys. Lett.* **95** 031501
[17] Niemi K, Waskoenig J, Sadeghi N, Gans T and O'Connell D 2011 *Plasma Sources Sci. Technol.* **20** 055005
[18] Hemke T, Eremin D, Mussenbrock T, Derzsi A, Donkó Z, Dittmann K, Meichsner J and Schulze J 2013 *Plasma Sources Sci. Technol.* **22** 015012
[19] Kawamura E, Lieberman M A, Lichtenberg A J, Chabert P and Lazzaroni C 2014 *Plasma Sources Sci. Technol.* **23** 035014
[20] Sobelman I I 1996 *Atomic Spectra and Radiative Transitions* (New York: Springer)
[21] Hicks W W, Hess R A and Cooper W S 1972 *Phys. Rev.* A **5** 490
[22] Videnović I R, Konjević N and Kuraica M M 1996 *Spectrochim. Acta* B **51** 1707
[23] Navrátil Z, Brandenburg R, Trunec D, Brablec A, St'ahel P, Wagner H-E and Kopecký Z 2006 *Plasma Sources Sci. Technol.* **15** 8
[24] Ivković S S, Obradović B M and Kuraica M M 2012 *J. Phys. D: Appl. Phys.* **45** 275204
[25] Kuraica M M and Konjević N 1997 *Appl. Phys. Lett.* **70** 1521
[26] Obradović B M, Ivković S S and Kuraica M M 2008 *Appl. Phys. Lett.* **92** 191501
[27] Lara N, González M Á and Gigosos M A 2012 *Astron. Astrophys.* **542** A75
[28] Cvetanović N, Martinović M M, Obradović B M and Kuraica M M 2015 *J. Phys. D: Appl. Phys.* **48** 205201
[29] Khayrallah G A and Smith S J 1978 *Phys. Rev.* A **18** 559
[30] Shaw M J and Webster M J 1976 *J. Phys. B: At. Mol. Phys.* **9** 2839
[31] Catherinot A and Dubreuil B 1981 *Phys. Rev.* A **23** 763
[32] Dvořák P 2013 *Plasma Sources Sci. Technol.* **22** 045016